



**HAL**  
open science

# Systèmes à $N$ fermions corrélés. Les modèles de champ moyen pour la physique des noyaux et d'autres systèmes à $N$ corps

M. Grasso

► **To cite this version:**

M. Grasso. Systèmes à  $N$  fermions corrélés. Les modèles de champ moyen pour la physique des noyaux et d'autres systèmes à  $N$  corps. Physique Nucléaire Théorique [nucl-th]. Université Paris Sud - Paris XI, 2009. tel-00450182

**HAL Id: tel-00450182**

**<https://theses.hal.science/tel-00450182>**

Submitted on 25 Jan 2010

**HAL** is a multi-disciplinary open access archive for the deposit and dissemination of scientific research documents, whether they are published or not. The documents may come from teaching and research institutions in France or abroad, or from public or private research centers.

L'archive ouverte pluridisciplinaire **HAL**, est destinée au dépôt et à la diffusion de documents scientifiques de niveau recherche, publiés ou non, émanant des établissements d'enseignement et de recherche français ou étrangers, des laboratoires publics ou privés.

**Mémoire**  
présenté par

**MARCELLA GRASSO**

pour obtenir  
**L'Habilitation à Diriger des Recherches**  
**en sciences physiques**  
**de l'Université Paris Sud 11**

Sujet : **Systemes à N fermions corrélés.**  
**Les modèles de champ moyen pour la physique des noyaux et d'autres systemes à N**  
**corps**



**Systemes à N fermions corrélés.  
Les modèles de champ moyen pour la  
physique des noyaux et d'autres  
systemes à N corps**

**Habilitation à Diriger des Recherches  
Marcella Grasso (IPN Orsay)**

**Soutenue le 19 octobre 2009**

**Jury :**

**M. Francesco Catara**

**M. Philippe Chomaz**

**M. Jacek Dobaczewski**

**M. Jacques Meyer**

**M. Nguyen Van Giai**

**M. Andrea Vitturi**

**Rapporteur**

**Rapporteur**

**Président**

**Rapporteur**



# Table des matières

## Chapitre 1

### Introduction

- 1.1 Introduction 6
- 1.2 Le problème à N corps 8
- 1.3 Modèles basés sur le champ moyen 10
- 1.4 Les équations Hartree-Fock-Bogoliubov ou Bogoliubov-de Gennes 13

## Chapitre 2

### Les noyaux exotiques décrits par les modèles de champ moyen

- 2.1 Introduction 20
- 2.2 L'interaction nucléaire 21
- 2.3 La fonctionnelle de Skyrme 22
- 2.4 Les équations Skyrme-HFB en symétrie sphérique 24
- 2.5 Evolution de la structure en couches et noyaux-bulle (effets du terme tenseur) 25

- *M. Grasso, Z.Y Ma, E. Khan, J. Margueron, and N. Van Giai 30*  
*Evolution of the proton sd states in neutron-rich Ca isotopes*  
*Phys. Rev. C 76 (2007), 044319*

- *M. Grasso, L. Gaudefroy, E. Khan, T. Nikšić, J. Piekarewicz, O. Sorlin, N. Van Giai, and D. Vretenar 36*  
*Nuclear "bubble" structure in  $^{34}\text{Si}$*   
*Phys. Rev. C 79 (2009), 034318*

- *E. Becheva, et al. 44*  
 *$N=14$  Shell Closure in  $^{22}\text{O}$  Viewed through a Neutron Sensitive Probe*  
*Phys. Rev. Lett. 96 (2006), 012501*

- 2.6 Halos dans les noyaux de masse intermédiaire 48

- *M. Grasso, S. Yoshida, N. Sandulescu, and N. Van Giai 50*  
*Giant neutron halos in the non-relativistic mean field approach*  
*Phys. Rev. C 74 (2006), 064317*

- 2.7 Interaction d'appariement et vibrations d'appariement 57

- *E. Khan, M. Grasso, and J. Margueron 59*  
*Constraining the nuclear pairing gap with pairing vibrations*

*arXiv:0905.4108, soumis Phys. Rev. C, rapport reçu, quelques modifications apportées, version resoumise*

## **2.8 Termes non standard dans l'interaction de Skyrme : termes dépendant de la densité de spin 67**

- *J. Margueron, S. Goriely, M. Grasso, G. Colò, and H. Sagawa 69*  
*Extended Skyrme interaction: ground state of nuclei and of nuclear matter*  
*arXiv:0906.3508, soumis J. Phys. G, rapport reçu, quelques modifications apportées, version resoumise*

## **2.9 Les résultats microscopiques de champ moyen : ingrédients importants dans les études de réaction 87**

- *Dao. T. Khoa, Hoang Sy Than, Tran Hoai Nam, M. Grasso, and N. Van Giai 88*  
*Microscopic calculation of the interaction cross section for stable and unstable nuclei based on the nonrelativistic nucleon-nucleon  $t$  matrix*  
*Phys. Rev. C 69 (2004), 044605*

## **2.10 Applications d'intérêt astrophysique. Les étoiles à neutrons 100**

- *M. Fallot, M. Grasso, E. Khan, and J. Margueron 102*  
*Neutron stars and nuclei: two dense systems*  
*Nucl. Phys. News 17, n. 4 (2007), 31*
- *M. Grasso, E. Khan, J. Margueron, and N. Van Giai 108*  
*Low-energy excitations in nuclear systems : From exotic nuclei to the crust of neutron stars*  
*Nucl. Phys. A 807 (2008), 1*

# **Chapitre 3**

## **Extensions de la méthode des phases aléatoires. Corrélations dans l'état fondamental**

### **3.1 Introduction.**

Nécessité d'aller au-delà de l'approximation de quasiboson (QBA) 120

### **3.2 Les règles de somme. Inclusion des configurations particule-particule et trou-trou 122**

- *Danilo Gambacurta, Francesco Catara, and Marcella Grasso 124*  
*Self consistent extension of random phase approximation enlarged beyond particle hole configurations*  
*Phys. Rev. C 80 (2009), 014303*

### **3.3 Les états à multiphonons 130**

- *M. Grasso, F. Catara, and M. Sambataro* **131**  
*Boson-mapping-based extension of the random-phase approximation in a three-level Lipkin model*  
*Phys. Rev. C* 66 (2002), 064303

- *D. Gambacurta, M. Grasso, F. Catara, and M. Sambataro* **138**  
*Extension of the second random-phase approximation*  
*Phys. Rev. C* 73 (2006), 024319

## Chapitre 4

### Les paires de Cooper dans les gaz atomiques ultra-froids

**4.1** Les gaz fermioniques ultra-froids piégés **146**

**4.2** Champ moyen à température finie et procédure de régularisation **147**

- *Marcella Grasso and Michael Urban* **148**  
*Hartree-Fock-Bogoliubov theory versus local-density approximation for superfluid trapped fermionic atoms*  
*Phys. Rev. A* 68 (2003), 033610

**4.3** Appariement non-standard : la phase LOFF **158**

- *Paolo Castorina, Marcella Grasso, Micaela Oertel, Michael Urban, and Dario Zappalà* **159**  
*Non-standard pairing in asymmetric trapped Fermi gases*  
*Phys. Rev. A* 72 (2005), 025601

**4.4** Les états excités dans les gaz superfluides **163**

- *M. Grasso, E. Khan, and M. Urban* **164**  
*Temperature dependence and finite-size effects in collective modes of superfluid trapped Fermi gases*  
*Phys. Rev. A* 72 (2005), 043617

## Chapitre 5

### Conclusions et perspectives pour les études de physique nucléaire

**5.1** Contexte actuel **174**

**5.2** Au-delà du champ moyen. Quelques perspectives **176**

## Références **181**



# **Chapitre 1**

## **Introduction**

## 1.1 Introduction

Ce mémoire est une synthèse, sous forme de sélection d'articles, des travaux développés depuis la soutenance de ma thèse en 2001. De nombreuses lignes de recherche se sont dégagées dans les années qui ont suivi ma thèse et mes activités scientifiques se sont développées en suivant différentes directions.

Le domaine de la physique nucléaire, et notamment la réflexion autour des propriétés des noyaux instables, est l'activité qui absorbe prioritairement mes intérêts scientifiques ; elle se situe en continuité thématique par rapport à une partie de mon travail de thèse. Le noyau atomique est un système quantique composé par  $N$  fermions qui nécessite un traitement théorique basé sur des modèles microscopiques. Les travaux développés et l'expérience acquise dans ce domaine se prêtent donc de manière très naturelle à des extensions interdisciplinaires pour l'étude d'autres systèmes quantiques formés par  $N$  fermions comme, par exemple, les agrégats métalliques ou les gaz d'atomes fermioniques piégés. J'ai exploré quelques-uns de ces liens interdisciplinaires et je me suis intéressée aux propriétés de l'état fondamental et des états excités des gaz atomiques et des agrégats métalliques en utilisant des méthodes analogues à celles adoptées en physique nucléaire.

En ce qui concerne les gaz d'atomes, je me suis intéressée surtout aux propriétés liées à la superfluidité et à ses effets sur l'état fondamental (gap d'appariement et température critique) et sur les modes d'excitation (modes de respiration). La superfluidité analysée dans ces systèmes est celle de la phase BCS dans la région où la longueur de diffusion est négative. La formation de paires de Cooper dans ce régime est tout à fait analogue au phénomène de superfluidité qui se manifeste dans certains noyaux atomiques.

Les agrégats métalliques ont été choisis comme systèmes où effectuer des tests des nouvelles méthodes introduites pour améliorer et étendre l'approximation des phases aléatoires (random-phase approximation, RPA). Ces systèmes présentent une structure en couches avec des nombres magiques correspondants aux fermetures des couches [Kn84] comme les noyaux. À la différence des noyaux, l'interaction entre leurs constituants est bien connue, c'est l'interaction coulombienne. Avec l'approximation du jellium, leur structure ionique est gelée et décrite avec un fond de densité constante positivement chargé. Dans ce cadre simplifié, les  $N$  corps à traiter microscopiquement sont les électrons de valence délocalisés. Les états collectifs, dits plasmons dipolaires, ont été analysés avec des extensions de la RPA. D'autres applications dans des modèles de Lipkin à deux ou trois niveaux ont été aussi effectuées pour réaliser des tests des extensions de la RPA introduites.

L'ensemble de ces activités a contribué à former ma vision générale du problème à  $N$  corps. Les études des propriétés et des analogies qui existent entre des systèmes en principe très différents les uns des autres par taille, composition, échelles d'énergie et

techniques d'analyse expérimentale ont fait mûrir la compréhension et la maîtrise d'un certain nombre de modèles et approches théoriques utilisés dans différents domaines de la physique. Cela a par ailleurs enrichi et élargi mes perspectives de recherche en physique nucléaire.

Dans la suite, je décrirai quelques études réalisées dans les trois domaines d'activités, que je regrouperai en trois chapitres.

La première et la plus longue partie de ce mémoire, le Chapitre 2, sera consacrée à la réflexion autour des noyaux exotiques effectuée avec des modèles de champ moyen pour étudier : l'évolution de la structure loin de la stabilité et les phénomènes exotiques liés à cette évolution comme les structures à bulle, les corrélations d'appariement et les vibrations d'appariement, les halos, l'effet sur les propriétés de l'état fondamental du terme tenseur et d'autres termes non standards dans l'interaction de Skyrme. Des applications dans les domaines des réactions et de l'astrophysique nucléaire seront aussi discutées.

Le Chapitre 3 sera consacré à la présentation de quelques extensions de la méthode RPA. L'objectif de ces travaux sera détaillé : cet objectif est formel et vise à une formulation complètement auto-consistante de la méthode pour un meilleur traitement des corrélations dans l'état fondamental des systèmes à N corps. Des applications dans des modèles de Lipkin exactement solubles seront discutées. Récemment, nous avons par ailleurs commencé à réaliser des applications de ces méthodes à l'étude des systèmes nucléaires faiblement liés où le traitement des corrélations pourrait se révéler particulièrement important. Ce sera discuté à la fin du mémoire et fait partie de mes travaux en cours.

Le Chapitre 4 collecte et décrit quelques analyses autour des gaz atomiques ultra-froids piégés, particulièrement fascinants parce qu'ils sont les seuls systèmes à N corps qui permettent, entre autres, l'observation et l'étude des corrélations associées à la superfluidité en fonction de l'intensité de l'interaction, de la température et de la taille du système. Les méthodes microscopiques de champ moyen, amplement utilisées en physique nucléaire, sont les outils théoriques que j'ai adoptés pour analyser ces systèmes.

Un dernier chapitre de conclusions et perspectives dans le cadre de la physique nucléaire clôture cette collection de publications. Les limites de validité de l'approximation de champ moyen sont mises en évidence dans ce chapitre et un certain nombre de possibilités d'amélioration du pouvoir prédictif et de raffinement des modèles sont présentées et discutées.

Les articles présentés sont précédés et reliés les uns aux autres par des sections qui définissent la trame et le fil logique de chaque chapitre.

Dans la suite de ce premier chapitre, j'introduis le problème à N corps de manière générale en mentionnant très brièvement quelques-unes des étapes fondamentales qui

ont rendu possible, au cours du siècle dernier, sa formulation et son traitement dans le cadre de la physique quantique (Section 1.1). Quelques modèles basés sur l'approximation de champ moyen sont présentés de manière très générale dans la Section 1.2. Les équations Hartree-Fock-Bogoliubov sont dérivées dans la Section 1.3.

## 1.2 Le problème à N corps

La compréhension d'un système quantique à N corps est un des problèmes les plus riches et complexes face auxquels nous sommes confrontés en physique et offre la possibilité de tisser des liens interdisciplinaires entre différents domaines scientifiques comme ceux de la physique des solides, de la physique nucléaire, de la physique atomique et de la chimie quantique [Ma67, FW71, RS80]. Le monde qui nous entoure présente, à différentes échelles, une variété énorme de systèmes à N corps de composition et propriétés diverses, noyaux, atomes, molécules, systèmes atomiques, nanoparticules, agrégats, solides, systèmes planétaires, galaxies, etc. Notre observation et notre compréhension des phénomènes physiques doivent donc se baser très souvent sur l'analyse des propriétés de ces systèmes ayant un nombre incroyablement élevé de degrés de liberté. Le problème se complique ultérieurement pour les systèmes dont la nature quantique ne peut pas être négligée. À l'exception de très peu de cas triviaux, la solution exacte du problème à N corps n'est pas accessible.

En principe, la fonction d'onde  $\Psi$  qui décrit un système à N corps et contient toutes les informations sur ses degrés de liberté, peut être déterminée comme solution (dans les cas non-relativistes) de l'équation de Schroedinger,

$$H\Psi = E\Psi, \quad (1.1)$$

où l'Hamiltonien s'écrit, en seconde quantification, comme

$$H = \sum_{\alpha\beta} a_{\alpha}^{+} \langle \alpha | T | \beta \rangle a_{\beta} + \frac{1}{2} \sum_{\alpha\beta\gamma\delta} a_{\alpha}^{+} a_{\beta}^{+} \langle \alpha\beta | V | \gamma\delta \rangle a_{\delta} a_{\gamma} + \dots, \quad (1.2)$$

où  $a_{\alpha}^{+}, a_{\alpha}$  sont les opérateurs de création et d'annihilation d'une particule dans un état  $\alpha$ . Le premier terme de cette équation décrit la partie cinétique et un éventuel potentiel externe à 1 corps qui agit sur le système, tandis que le deuxième terme, à 2 corps, représente l'interaction entre les particules. En principe, l'Hamiltonien devrait contenir aussi des termes à 3, 4, ..., N corps, mais il s'avère que, dans la plupart des cas qui nous intéressent, l'interaction entre les constituants est suffisamment bien décrite par le terme à 2 (et éventuellement à 3) corps. A cause de l'énorme complexité du problème due à la présence de ce terme d'interaction dans l'Hamiltonien, la solution de l'équation de Schroedinger peut se réaliser seulement en ayant recours à des approximations.

Les approches semiclassiques ont l'avantage de simplifier de manière importante le problème à traiter. Cependant, cela se fait en négligeant complètement ou partiellement la nature quantique du système et, pour cette raison, ces approches ne sont pas adaptées à l'étude de certains systèmes et de certaines propriétés, lorsque les aspects quantiques sont la clé pour les décrire.

Dans certains cas, il est raisonnable de fixer des échelles d'énergies, de masses, etc., qui permettent d'établir une hiérarchie entre les degrés de liberté et de réduire ainsi le nombre de constituants pour lesquels un traitement quantique est nécessaire. Les autres constituants sont décrits avec des approches semiclassiques. Tel est le cas, par exemple, de l'approximation adiabatique de Born-Oppenheimer [AM76] utilisée couramment dans la physique des systèmes à  $N$  électrons comme les agrégats métalliques.

La formulation des méthodes pour traiter le problème à  $N$  corps quantique a commencé à se développer très tôt, pendant les premières années où la physique quantique elle-même était en train de se bâtir, dans la première moitié du siècle dernier. Dans la suite, je mentionne, à titre d'exemples, deux méthodes introduites au cours du siècle dernier et amplement utilisées dans la physique des systèmes à  $N$  corps : le modèle microscopique de champ moyen Hartree-Fock (HF) et la théorie de la fonctionnelle de la densité (DFT).

En 1927, à Cambridge, Hartree introduisait pour la première fois le concept innovateur de champ moyen appuyé sur l'approximation des particules indépendantes. Dans les années qui suivirent, Slater et Fock complétèrent ce modèle variationnel avec un ansatz sur la fonction d'onde d'état fondamental dans les systèmes fermioniques, qui incluait correctement le Principe de Pauli. L'état fondamental était choisi comme produit antisymétrisé de fonctions d'onde à 1 particule, un déterminant de Slater (Slater, 1929 ; Fock, 1930). La méthode d'HF était formalisée mais il fallut attendre les années 50 pour pouvoir effectuer en pratique les premières applications numériques. Cette méthode, qui a vu le jour dans le cadre de la physique des systèmes à  $N$  électrons, se diffusa bientôt dans d'autres domaines de la physique. A la fin des années 50 et dans les années qui suivirent, des applications en physique nucléaire furent possibles grâce aux avancées dans la compréhension des propriétés de l'interaction nucléaire. L'introduction d'interactions effectives phénoménologiques permettait de réaliser les premiers calculs numériques [Sk56, Sk59, VB72, Go75, Ne82]. Entre-temps, l'accès au problème à  $N$  corps quantique avait été grandement facilité grâce à l'introduction du formalisme de seconde quantification et à l'utilisation des fonctions de Green. Il ne faut pas oublier, par ailleurs, que le formalisme de seconde quantification est essentiel pour la formulation relativiste du problème à  $N$  corps nucléaire qui a été abordée pour la première fois par Walecka en 1974 [Wa74].

Dans les années 60, la théorie de la DFT était introduite, elle aussi dans le cadre de la physique des systèmes à  $N$  électrons où la structure électronique était traitée dans l'approximation de Born-Oppenheimer. Cette approche variationnelle s'appuie sur deux théorèmes démontrés par Hohenberg et Kohn en 1964 [HK64]. Très peu après, les équations de Kohn et Sham furent proposées [KS65]. Dans les fonctionnelles de la densité utilisées, il y a typiquement deux termes : une partie directe d'Hartree et une

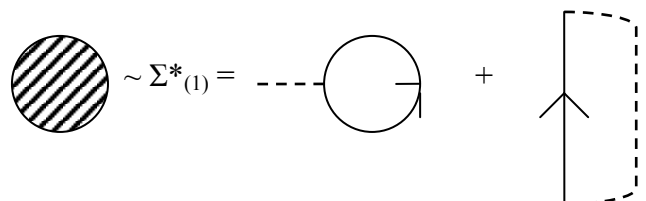
partie d'échange-corrélation qui décrit de manière approximée le terme d'échange et la présence de quelques corrélations dans l'état fondamental. La DFT est couramment appliquée, par exemple, pour calculer les énergies de liaison des molécules en chimie et la structure à bandes en physique des solides [DR90, Ko06].

Ces dernières années, en physique nucléaire, beaucoup d'efforts sont consacrés à l'application des concepts de la DFT aux études de structure nucléaire [Do07, Be08, Ca08, Du08, Ko08, Be09, La09].

Les fonctionnelles de la densité sont d'ailleurs bien connues en physique nucléaire. Dans le cadre du champ moyen non relativiste avec des interactions de type Skyrme, par exemple, la densité d'Hamiltonien  $\mathcal{H}$  (qui est dérivée de manière variationnelle à partir de l'interaction de Skyrme et qui, intégrée, donne l'énergie de l'état fondamental) est une fonctionnelle de la densité locale (fonctionnelle de Skyrme). Comme ces fonctionnelles permettent d'accéder à l'énergie de l'état fondamental, on parle souvent en physique nucléaire de EDFT (Energy Density Functional Theory). Dans le cadre des théories relativistes, un certain nombre de travaux sont également orientés vers l'analyse des fonctionnelles EDF [Ni08]. Des modèles de EDF relativiste inspirés de la QCD de basse énergie ont été introduits assez récemment [Fi03, Fi04, Fi06, Fi07]. De manière générale, les efforts sont orientés vers la recherche et la formulation d'une fonctionnelle universelle, qui puisse reproduire les propriétés de l'état fondamental de tous les noyaux de la charte, stables ou instables, jusqu'aux drip lines nucléoniques.

### 1.3 Modèles basés sur le champ moyen

Les modèles employés dans mes travaux sont basés sur l'approximation de champ moyen qui s'inspire à son tour de l'approximation de particules indépendantes. L'approximation de particules indépendantes est valable lorsque, dans un système à N corps, le libre parcours moyen des constituants est au moins comparable à la taille du système. Dans ces conditions, qui sont très bien vérifiées, par exemple, dans les noyaux et dans les gaz atomiques dilués et piégés, il est raisonnable de simuler l'interaction de la particule  $i$  avec les autres N-1 particules par un potentiel moyen qui agit sur la particule  $i$  et décrit de manière effective la présence des autres N-1 particules. Le problème est équivalent à celui d'un système de particules indépendantes soumises à un potentiel externe et le terme à 2 corps de l'éq. (1.2) est approximé par un terme à 1 particule. En termes de diagrammes de Feynman, cette approximation correspond à considérer le premier ordre dans l'auto-énergie propre  $\Sigma^*$ ,



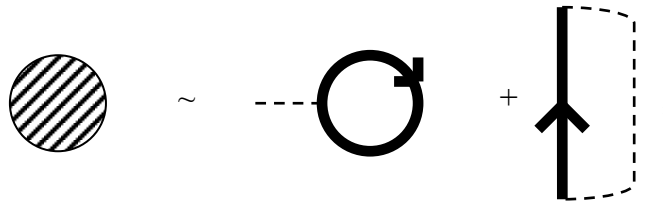
où les lignes solides représentent la fonction de Green non perturbée  $G_0$  et les tirets l'interaction. Le premier diagramme décrit le terme direct et le deuxième le terme d'échange pour l'auto-énergie propre.

Sur l'approximation des particules indépendantes sont fondés, par exemple, la méthode de champ moyen d'HF et le modèle en couches nucléaire. Comme déjà mentionné dans la Section 1.1, le potentiel moyen HF est construit de manière variationnelle en imposant que l'état fondamental soit un déterminant de Slater,

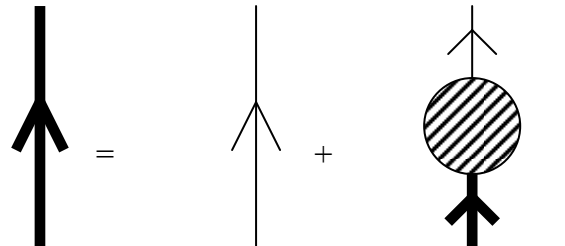
$$|\text{HF}\rangle = \prod_{i=1}^N a_i^+ |-\rangle, \quad (1.3)$$

où  $|-\rangle$  est l'état du vide et  $N$  le nombre de constituants dans le système.

La procédure pour la construction de ce potentiel moyen est auto-consistante et le problème est résolu de manière itérative jusqu'à l'obtention de la solution. Cela signifie que l'auto-énergie propre est exprimée par les diagrammes suivants :



où les lignes plus épaisses représentent la fonction de Green exacte  $G$ . Avec cette auto-énergie propre, l'équation de Dyson pour  $G$  est résolue :



ce qui peut s'écrire comme,

$$\left\{ -\frac{\hbar^2}{2m} \Delta + \Gamma_H(\vec{r}) \right\} \varphi_k(\vec{r}) + \int d\vec{r}' \Gamma_{\text{Ex}}(\vec{r}, \vec{r}') \varphi_k(\vec{r}') = \varepsilon_k \varphi_k(\vec{r}), \quad (1.4)$$

où

$$\Gamma_H(\vec{r}) = \int d\vec{r}' v(\vec{r}, \vec{r}') \rho(\vec{r}'), \quad (1.5)$$

et

$$\Gamma_{\text{Ex}}(\vec{r}, \vec{r}') = -v(\vec{r}, \vec{r}')\rho(\vec{r}, \vec{r}'), \quad (1.6)$$

$\rho(\vec{r})$  et  $\rho(\vec{r}, \vec{r}')$  étant les densités locale et non locale. Les équations (1.4) sont les équations HF et  $\Gamma_{\text{H}}$  et  $\Gamma_{\text{Ex}}$  sont respectivement les potentiels directs et d'échange. Les équations (1.4) sont écrites, pour simplicité de notation, dans le cas d'un potentiel à deux corps local qui ne dépend pas du spin et de l'isospin.

\*\*\*\*

Dans l'état fondamental HF, qui est un déterminant de Slater, les corrélations sont complètement absentes par construction. Une première extension naturelle d'HF est la méthode Hartree-Fock-Bogoliubov (HFB) ou Bogoliubov-de Gennes [dG66, RS80], où les corrélations d'appariement sont introduites dans le même schéma autoconsistant. Ces corrélations, responsables de la formation des paires de Cooper dans les systèmes superfluides, sont prises en compte formellement en définissant le concept de quasiparticule à travers les transformations unitaires de Bogoliubov. Avec ces transformations, les opérateurs de quasiparticule  $\beta$  sont définis comme des combinaisons d'opérateurs  $\gamma^+$  et  $\gamma$  de création et d'annihilation de particules,

$$\begin{aligned} \beta_{k\uparrow} &= \sum_n \left( u_{nk} \gamma_{n\uparrow} - v_{nk}^* \gamma_{n\downarrow}^+ \right) \\ \beta_{k\downarrow} &= \sum_n \left( u_{nk} \gamma_{n\downarrow} + v_{nk}^* \gamma_{n\uparrow}^+ \right) \end{aligned} \quad (1.7)$$

où les symboles  $\uparrow$  et  $\downarrow$  indiquent génériquement deux états renversés par rapport au temps.

L'état fondamental n'est plus un déterminant de Slater de particules indépendantes, mais un déterminant de Slater de quasi-particules indépendantes. Cette extension permet donc de considérer dans l'état fondamental un certain type de corrélations liées à la superfluidité. Cependant, comme le modèle HF, cette méthode néglige tout autre type de corrélations et elle est basée, encore une fois, sur une procédure variationnelle qui permet de dériver un potentiel moyen effectif en simulant le terme d'interaction à 2 corps dans l'Hamiltonien par un terme à 1 particule. Les équations HFB, qui décrivent l'état fondamental, ont la forme compacte suivante :

$$\begin{pmatrix} W & \Delta \\ \Delta & -W \end{pmatrix} \begin{pmatrix} u \\ v \end{pmatrix} = E \begin{pmatrix} u \\ v \end{pmatrix}, \quad (1.8)$$

où  $W$  contient la partie cinétique, le champ moyen et un éventuel potentiel externe à 1 corps et  $\Delta$  représente le champ d'appariement, qui est supposé réel. Les solutions de ces équations sont les énergies de quasiparticule  $E$  et les fonctions d'onde à deux composantes  $u$  et  $v$ , introduites par les transformations de Bogoliubov. Ces équations seront dérivées dans un cadre simplifié dans la section suivante.

Si on impose que le champ d'appariement couple seulement des états reliés par renversement du temps, une simplification de HFB est obtenue qui correspond exactement au modèle BCS introduit par Bardeen, Cooper et Schrieffer pour décrire les paires de Cooper d'électrons dans les supraconducteurs [BCS57]. Dans cette simplification, les quasiparticules de Bogoliubov ont l'expression suivante :

$$\begin{aligned}\beta_{n\uparrow} &= u_{nn}\gamma_{n\uparrow} - v_{nn}^*\gamma_{n\downarrow}^+, \\ \beta_{n\downarrow} &= u_{nn}\gamma_{n\downarrow} + v_{nn}^*\gamma_{n\uparrow}^+.\end{aligned}\tag{1.9}$$

\*\*\*\*

Une autre extension naturelle pour le champ moyen est son application à l'étude de l'évolution dynamique des systèmes à N corps à travers les théories de champ moyen dépendant du temps. Les équations HF ou HFB dépendantes du temps (TDHF ou TDHFB) doivent être résolues dans ce cas. Ces équations peuvent être simplifiées dans le cadre de la théorie de la réponse linéaire, et des équations du mouvement peuvent être dérivées qui décrivent les modes d'excitation du système dans la limite d'oscillations de petite amplitude. Cette procédure correspond à l'approximation des phases aléatoires (Random Phase Approximation, RPA). Les équations de la RPA (QRPA si on inclut l'appariement), furent introduites il y a quelques décennies et leurs premières applications furent réalisées dans les années 50 par Bohm et Pines pour étudier les oscillations d'un gaz d'électrons [BP52]. Les équations (Q)RPA peuvent être dérivées à partir des équations TDHF(B) en ajoutant une faible perturbation externe au champ moyen et en considérant des variations de la densité  $\rho$  (HF), ou de la densité généralisée  $R$  (HFB), linéaires dans la perturbation externe. Ces méthodes pour la description des états excités sont donc basées, elles aussi, sur l'approximation de champ moyen.

Les limites de validité de l'approximation de champ moyen sont mises en évidence dans le Chapitre 5 de ce mémoire. Par ailleurs, dans le Chapitre 3, des pistes d'amélioration et la formulation d'approches qui vont au-delà du champ moyen sont explorées : sont proposés des extensions de la RPA où l'approximation de quasiboson n'est pas appliquée et des corrélations sont introduites explicitement dans l'état fondamental.

## 1.4 Les équations Hartree-Fock-Bogoliubov ou Bogoliubov-de Gennes

Je montre dans cette section une des manières possibles d'introduire les équations HFB (mieux connues en physique atomique comme équations Bogoliubov-de Gennes). Une procédure très élégante pour dériver ces équations peut se réaliser dans un cas

simplifié : (i) symétrie sphérique ; (ii) deux états de spin schématiquement indiqués comme  $\uparrow$  et  $\downarrow$  ; (iii) interaction de portée nulle qui agit seulement entre deux spins opposés. Si l'intensité de l'interaction est  $V$  et si nous supposons que l'interaction est suffisamment bien décrite par un terme à deux corps, l'Hamiltonien du système est écrit comme la somme d'un terme à un corps :

$$H_1 = \int d^3\vec{r} \sum_{\alpha} \Psi^+(\vec{r}\alpha) U_1 \Psi(\vec{r}\alpha), \quad (1.10)$$

et d'un terme à deux corps :

$$H_2 = \frac{1}{2} V \int d^3\vec{r} \sum_{\alpha\beta} \Psi^+(\vec{r}\alpha) \Psi^+(\vec{r}\beta) \Psi(\vec{r}\beta) \Psi(\vec{r}\alpha), \quad (1.11)$$

où  $\alpha$  et  $\beta$  décrivent les deux états de spin  $\uparrow$  et  $\downarrow$ .  $U_1$  est la somme de la contribution cinétique et d'un éventuel potentiel externe à un corps. L'approximation de champ moyen correspond à introduire un Hamiltonien effectif ayant la forme suivante :

$$H_{\text{eff}} = \int d^3\vec{r} \left\{ \sum_{\alpha} \Psi^+(\vec{r}\alpha) H_e(\vec{r}) \Psi(\vec{r}\alpha) + W(\vec{r}) \Psi^+(\vec{r}\alpha) \Psi(\vec{r}\alpha) + \Delta(\vec{r}) \Psi^+(\vec{r}\uparrow) \Psi^+(\vec{r}\downarrow) + \Delta^*(\vec{r}) \Psi(\vec{r}\downarrow) \Psi(\vec{r}\uparrow) \right\} \quad (1.12)$$

où  $H_e$  est défini par la relation :

$$H_1 - \lambda N = \sum_{\alpha} \int d^3\vec{r} \Psi^+(\vec{r}\alpha) H_e \Psi(\vec{r}\alpha). \quad (1.13)$$

$N$  est l'opérateur nombre de particules :

$$N \equiv \sum_{\alpha} \int d^3\vec{r} \Psi^+(\vec{r}\alpha) \Psi(\vec{r}\alpha) \quad (1.14)$$

et  $\lambda$  est le potentiel chimique.

Puisque l'Hamiltonien  $H_{\text{eff}}$  est une forme quadratique en  $\Psi$  et  $\Psi^+$ , il peut être diagonalisé par une transformation unitaire, comme les transformations de Bogoliubov,

$$\begin{aligned} \Psi(\vec{r}\uparrow) &= \sum_n \left( u_n(\vec{r}) \gamma_{n\uparrow} - v_n^*(\vec{r}) \gamma_{n\downarrow}^+ \right) \\ \Psi(\vec{r}\downarrow) &= \sum_n \left( u_n(\vec{r}) \gamma_{n\downarrow} + v_n^*(\vec{r}) \gamma_{n\uparrow}^+ \right) \end{aligned} \quad (1.15)$$

du même type que les équations (1.7). Les transformations de Bogoliubov diagonalisent  $H_{\text{eff}}$  :

$$H_{\text{eff}} = \varepsilon_0 + \sum_{n\alpha} \varepsilon_n \gamma_{n\alpha}^+ \gamma_{n\alpha} , \quad (1.16)$$

où  $\varepsilon_0$  et  $\varepsilon_n$  sont, respectivement, les énergies de l'état fondamental et de l'état excité  $|n\rangle$ . L'équation (1.16) peut être écrite de manière équivalente comme,

$$[H_{\text{eff}}, \gamma_{n\alpha}] = -\varepsilon_n \gamma_{n\alpha} , \quad (1.17)$$

$$[H_{\text{eff}}, \gamma_{n\alpha}^+] = \varepsilon_n \gamma_{n\alpha}^+ .$$

Nous calculons maintenant  $[\Psi, H_{\text{eff}}]$  en utilisant l'expression de  $H_{\text{eff}}$ , Eq. (1.12), et les propriétés d'anticommutation des opérateurs  $\Psi$  :

$$\begin{aligned} [\Psi(\vec{r} \uparrow), H_{\text{eff}}] &= (H_e + W(\vec{r}))\Psi(\vec{r} \uparrow) + \Delta(\vec{r})\Psi^+(\vec{r} \downarrow), \\ [\Psi(\vec{r} \downarrow), H_{\text{eff}}] &= (H_e + W(\vec{r}))\Psi(\vec{r} \downarrow) - \Delta^*(\vec{r})\Psi^+(\vec{r} \uparrow). \end{aligned} \quad (1.18)$$

Si maintenant nous utilisons les transformations de Bogoliubov et les éqs. (1.17), nous obtenons les équations HFB à partir des équations (1.18) :

$$\begin{aligned} \varepsilon u(\vec{r}) &= [H_e + W(\vec{r})]u(\vec{r}) + \Delta(\vec{r})v(\vec{r}), \\ \varepsilon v(\vec{r}) &= -[H_e^* + W(\vec{r})]v(\vec{r}) + \Delta^*(\vec{r})u(\vec{r}). \end{aligned} \quad (1.19)$$

Dans ces équations,  $W$  est le champ moyen et  $\Delta$  le champ d'appariement qui sont évalués avec une procédure variationnelle. Nous imposons que l'énergie libre  $F$  soit stationnaire :

$$0 = \delta F = \delta \langle H \rangle - T \delta S, \quad (1.20)$$

où la moyenne de  $H$  est définie comme :

$$\langle H \rangle \equiv \frac{\sum_{\phi} \langle \phi | H | \phi \rangle \exp(-\beta E_{\phi})}{\sum_{\phi} \exp(-\beta E_{\phi})}, \quad \beta = \frac{1}{K_B T}. \quad (1.21)$$

En calculant  $\langle H \rangle = \langle H_1 + H_2 \rangle$  (Eqs. (1.10) et (1.11)) et en utilisant le théorème de Wick, nous obtenons :

$$\begin{aligned}
\delta F = \int d^3\vec{r} & \left\{ \sum_{\alpha} \delta \langle \Psi^+(\vec{r}\alpha) H_e \Psi(\vec{r}\alpha) \rangle \right. \\
& + V \sum_{\alpha\beta} \langle \Psi^+(\vec{r}\alpha) \Psi(\vec{r}\alpha) \rangle \delta \langle \Psi^+(\vec{r}\beta) \Psi(\vec{r}\beta) \rangle \\
& - V \sum_{\alpha} \langle \Psi^+(\vec{r}\alpha) \Psi(\vec{r}\alpha) \rangle \delta \langle \Psi^+(\vec{r}\alpha) \Psi(\vec{r}\alpha) \rangle \\
& \left. + V \left[ \langle \Psi^+(\vec{r}\uparrow) \Psi^+(\vec{r}\downarrow) \rangle \delta \langle \Psi(\vec{r}\downarrow) \Psi(\vec{r}\uparrow) \rangle + \text{C.C.} \right] \right\} - T\delta S.
\end{aligned} \tag{1.22}$$

Nous imposons que  $F_1 = \langle H_{\text{eff}} \rangle - TS$  soit stationnaire par rapport aux variations  $\delta u$  et  $\delta v$  puisque nous supposons que l'énergie libre  $F_1$  calculée avec les états qui diagonalisent  $H_{\text{eff}}$  est stationnaire :

$$\begin{aligned}
0 = \delta F_1 = \int d^3\vec{r} & \left\{ \sum_{\alpha} \delta \langle \Psi^+(\vec{r}\alpha) (H_e + W(\vec{r})) \Psi(\vec{r}\alpha) \rangle \right. \\
& \left. + \left[ \Delta(\vec{r}) \delta \langle \Psi^+(\vec{r}\uparrow) \Psi^+(\vec{r}\downarrow) \rangle + \text{C.C.} \right] \right\} - T\delta S.
\end{aligned} \tag{1.23}$$

En comparant les équations (1.22) et (1.23) nous concluons que  $F$  est stationnaire si :

$$\begin{aligned}
W(\vec{r}) &= V \langle \Psi^+(\vec{r}\uparrow) \Psi(\vec{r}\uparrow) \rangle = V \langle \Psi^+(\vec{r}\downarrow) \Psi(\vec{r}\downarrow) \rangle, \\
\Delta(\vec{r}) &= V \langle \Psi(\vec{r}\downarrow) \Psi(\vec{r}\uparrow) \rangle = -V \langle \Psi(\vec{r}\uparrow) \Psi(\vec{r}\downarrow) \rangle.
\end{aligned} \tag{1.24}$$

Cela nous mène à définir les densités de particule,

$$\rho(\vec{r}) \equiv \langle \Psi^+(\vec{r}\alpha) \Psi(\vec{r}\alpha) \rangle = \sum_n \left[ (1 - f_n) v_n^2(\vec{r}) + f_n u_n^2(\vec{r}) \right], \tag{1.25}$$

et d'appariement,

$$\tilde{\rho}(\vec{r}) \equiv \langle \Psi(\vec{r}\downarrow) \Psi(\vec{r}\uparrow) \rangle = -\sum_n \left[ (1 - 2f_n) v_n^*(\vec{r}) u_n(\vec{r}) \right], \tag{1.26}$$

où :

$$f_n = \frac{1}{\exp(\beta \varepsilon_n) + 1} \tag{1.27}$$

est la fonction de Fermi qui décrit la dépendance en température.

La procédure variationnelle a donc permis de dériver les expressions suivantes pour le champ moyen et le champ d'appariement écrits en fonction des densités de particule et d'appariement :

$$W(\vec{r}) = V\rho(\vec{r}), \quad (1.28)$$

$$\Delta(\vec{r}) = V\tilde{\rho}(\vec{r}). \quad (1.29)$$



# **Chapitre 2**

## **Les noyaux exotiques décrits par les modèles de champ moyen**

## 2.1 Introduction

Les noyaux instables sont des systèmes quantiques faiblement liés qui n'existent pas naturellement sur Terre. Leur étude systématique a débuté il y a une quinzaine d'années quand leur production a été rendue possible grâce à l'exploitation des faisceaux radioactifs dans les accélérateurs. Dans quelques cas, des régions de la carte des noyaux situées loin de la vallée de la stabilité ont été explorées et les drip lines nucléoniques ont été approchées. Alors que les drip lines protoniques se situent près de la vallée de stabilité, l'interaction coulombienne répulsive ne permettant pas de lier des noyaux trop riches en protons, les drip lines neutroniques sont prévues très loin des noyaux stables. Cela explique pourquoi les drip lines ont pu être approchées et parfois atteintes expérimentalement seulement pour certains noyaux riches en protons ou pour des noyaux légers riches en neutrons.

Les modèles théoriques prévoient pour les noyaux faiblement liés des propriétés assez différentes de celles des noyaux stables : des structures à halo pour les noyaux légers, des peaux de neutrons pour les noyaux plus lourds, des changements dans la séquence des nombres magiques et donc de la structure en couches, des modes d'excitation nouveaux, ... Certains de ces phénomènes, comme les halos dans les noyaux légers [Ta85], la modification des nombres magiques [So08] ou l'existence de nouveaux modes d'excitation de basse énergie (excitations pygmées) [Ad05], ont été mis en évidence expérimentalement. Cela crée un scénario exotique où les théoriciens sont impliqués dans le choix et la formulation des méthodes les mieux adaptées. Ce cadre de travail pour les théoriciens se situe dans un contexte très dynamique lié aux projets de construction d'accélérateurs de nouvelle génération dans différents laboratoires dans le monde. Ces installations vont permettre bientôt la production de faisceaux radioactifs avec des intensités plus élevées que les intensités disponibles dans les accélérateurs actuels. RIBF à Riken commence déjà à fonctionner. Spiral2 à Ganil et FAIR au GSI seront disponibles dans quelques années et, à plus long terme, le projet européen EURISOL va démarrer. Cela permettra d'une part de mieux connaître les propriétés de noyaux qui ont déjà été observés et, d'autre part, d'explorer de nouvelles régions de la carte des noyaux.

Un jeu subtil de différents types de corrélations détermine le comportement des noyaux exotiques. Les corrélations d'appariement, entre autres, qui dans les noyaux stables ne donnent pas un apport très important à l'énergie de liaison, se révèlent être, dans les noyaux faiblement liés, une contribution parfois fondamentale pour la description des drip lines. Les noyaux situés à proximité d'une drip line sont très faiblement liés : l'énergie de Fermi des neutrons ou des protons est voisine de zéro et, pour ces systèmes, l'interaction attractive d'appariement peut jouer un rôle fondamental pour les maintenir liés. De plus, les corrélations d'appariement peuvent faire diffuser très facilement des paires de neutrons ou de protons vers les états du continuum qui sont assez proches des derniers états occupés. Le traitement correct des corrélations d'appariement et

l'inclusion des états du continuum sont donc deux aspects très importants pour une bonne description de ces systèmes [Gr01].

## 2.2 L'interaction nucléaire

Une des difficultés majeures dans le problème à N corps nucléaire réside dans le fait que l'interaction nucléaire dans le noyau n'est pas connue, bien qu'un certain nombre de ses propriétés aient été analysées et soient maintenant bien comprises.

Le point de départ dans une démarche complètement microscopique est l'interaction nucléon-nucléon nue. Des interactions réalistes sont obtenues avec des ajustements phénoménologiques pour reproduire à la fois les déphasages dans les collisions nucléon-nucléon et la spectroscopie des systèmes très légers. La grande difficulté est le passage du système nucléon-nucléon libre au système composé par des nucléons dans un milieu. L'existence d'un cœur dur infiniment répulsif rend le problème impossible à résoudre. Une manière de surmonter cette difficulté est proposée par la méthode de Brueckner-HF (ou Dirac-Brueckner-HF dans le cas relativiste), où l'interaction est remplacée par une interaction effective à travers l'utilisation de la matrice G de Brueckner. Des applications sont faites surtout dans la matière nucléaire [Ba99]. Pour le traitement des noyaux légers, les interactions réalistes sont amplement utilisées dans les méthodes *ab-initio*, telles que l'approche 'No-Core Shell Model' [Fo05, Ro09], le modèle de 'Coupled Cluster' [Ha08] ou la méthode de 'Green's function MonteCarlo' [Wi02].

Comme déjà mentionné, les interactions réalistes sont ajustées en imposant des contraintes sur les déphasages dans les collisions nucléon-nucléon. Ces interactions ont des composantes de haut moment. En employant des techniques issues des théories des groupes de renormalisation, une interaction 'universelle' de bas moment ( $V_{\text{low-k}}$ ) peut être introduite à partir de ces interactions réalistes [Bo01, Bo03a, Bo03b]. Les composantes de haut moment sont intégrées et seulement des composantes jusqu'à un cutoff  $\Lambda$  sont présentes. L'interaction nucléon-nucléon  $V_{\text{low-k}}$  peut être utilisée directement dans la matière ou les noyaux sans devoir recourir à des resommations avec une matrice G et cela ouvre d'intéressantes perspectives pour des applications dans des systèmes nucléaires. Il faut mentionner, cependant, que l'inclusion de l'interaction à 3N est indispensable pour obtenir un point de saturation raisonnable dans la matière nucléaire avec  $V_{\text{low-k}}$ .

La dérivation naturelle de l'interaction nucléon-nucléon et la compréhension profonde de ses propriétés devraient se faire en considérant la nature sous-jacente du problème et en partant donc de la structure en quarks des nucléons. Cependant, les liens avec la QCD sont très difficiles à tisser puisque la physique qui nous intéresse est à basse énergie. Aux échelles typiques de la physique nucléaire, la constante de couplage fort

est  $\sim 1$  et le problème est non perturbatif. À travers l'introduction d'une théorie des champs effective, toutefois, il est toujours possible de baser la formulation du problème (par exemple, dans le cadre de l'introduction d'un Lagrangien dans une théorie relativiste) sur certaines symétries de la QCD, comme la symétrie chirale. Ces pistes sont de plus en plus explorées depuis quelques années [Ep08].

Les calculs de QCD sur réseau bénéficient par ailleurs des avancées formidables de ces dernières années qui ont fait augmenter énormément la puissance de calcul. Des premières tentatives de calculer des potentiels nucléaires ont été réalisées avec ces calculs *ab initio* à partir du Lagrangien de la QCD [La08].

Une manière complémentaire d'attaquer le problème est l'utilisation d'interactions phénoménologiques qui permettent de réaliser beaucoup plus facilement des calculs numériques sophistiqués pour des noyaux de masses intermédiaires ou lourdes. Les interactions phénoménologiques, comme celle de Gogny [Go75] ou celle de Skyrme [Sk56, Sk59], sont en effet amplement utilisées dans le cadre des applications des modèles de champ moyen à l'étude des noyaux de masses intermédiaires et lourdes. Elles sont construites à travers des ajustements phénoménologiques globaux d'un certain nombre de paramètres, de manière à reproduire les propriétés de quelques noyaux sphériques (énergies de liaison et rayons) et de la matière nucléaire.

Le fondement de l'interaction de Gogny est plus microscopique que celui de l'interaction de Skyrme, puisque la première a été introduite à partir d'une matrice  $G$  réaliste. Dans le même esprit, d'autres travaux ont été effectués dans les années 70 visant à construire des interactions phénoménologiques à partir d'une matrice  $G$ . Je mentionne l'étude de Negele et Vautherin de 1972 [NV72] où les techniques d'expansion de la matrice densité (DME) sont utilisées pour déduire une interaction phénoménologique (une densité d'Hamiltonien) à partir d'une matrice  $G$  réaliste. Ces auteurs ont montré que la densité d'Hamiltonien  $\mathcal{H}$ , qui est dérivée avec les techniques de DME, est analogue à celle obtenue avec une interaction de Skyrme. De plus, la plupart des paramètres ajustés pour les interactions de Skyrme ne sont pas très différents de ceux qu'on obtient avec une linéarisation de la densité d'Hamiltonien DME autour de la densité de saturation. Cette étude permet donc de baser l'interaction de Skyrme sur des fondements formels plus microscopiques.

## 2.3 La fonctionnelle de Skyrme

Dans le cadre du champ moyen non relativiste, les interactions effectives phénoménologiques se regroupent en deux catégories, les interactions de portée finie comme celle de Gogny, et les interactions de portée nulle comme les interactions de Skyrme.

La forme standard de l'interaction de Skyrme est :

$$\begin{aligned}
V(\vec{r}_1, \vec{r}_2) &= t_0(1 + x_0 P_\sigma) \delta(\vec{r}) \\
&+ \frac{1}{2} t_1(1 + x_1 P_\sigma) \left[ \vec{P}'^2 \delta(\vec{r}) + \delta(\vec{r}) \vec{P}'^2 \right] + t_2(1 + x_2 P_\sigma) \vec{P}' \cdot \delta(\vec{r}) \vec{P}' \\
&+ \frac{1}{6} t_3(1 + x_3 P_\sigma) \left[ \rho(\vec{R}) \right]^\alpha \delta(\vec{r}) \\
&+ i W_0 \sigma \cdot \left[ \vec{P}' \times \delta(\vec{r}) \vec{P}' \right]
\end{aligned} \tag{2.1}$$

avec un terme central, un terme qui simule une portée finie avec une dépendance en moments, un terme dépendant de la densité et un terme qui représente la partie de spin-orbite. La notation est celle habituellement rencontrée dans la littérature (voir par exemple [Me03]).

La densité d'Hamiltonien qui est dérivée à partir de cette interaction en supposant un modèle de champ moyen est :

$$\mathcal{H} = \mathcal{H}_0 + \mathcal{H}_3 + \mathcal{H}_{eff} + \mathcal{H}_{fin} + \mathcal{H}_{so}, \tag{2.2}$$

où  $\mathcal{H}_0$  et  $\mathcal{H}_3$  proviennent des termes en  $t_0$  et  $t_3$ , respectivement,  $\mathcal{H}_{eff}$  et  $\mathcal{H}_{fin}$  sont les termes de masse effective et de taille finie et  $\mathcal{H}_{so}$  décrit le couplage de spin-orbite. Un dernier terme en  $\vec{J}^2$  est souvent omis, où  $\vec{J}^2 = \sum_{\mu\nu} J_{\mu\nu} J_{\mu\nu}$  est le tenseur courant de spin.

Dans tout ce qui suit, nous travaillons en symétrie sphérique. Dans ce cas, le tenseur courant de spin est facilement écrit en fonction de la densité de spin-orbite dont l'expression est :

$$J_q(r) = \frac{1}{4\pi r^3} \sum_{lj} (2j+1) \left[ j(j+1) - l(l+1) - \frac{3}{4} \right] \phi_{lj,q}^2(r), \tag{2.3}$$

où  $\phi$  est la fonction d'onde radiale.

Le terme de la densité d'Hamiltonien provenant des contributions en  $\vec{J}^2$  est égal à :

$$\frac{1}{2} \alpha (J_n^2 + J_p^2) + \beta J_n J_p, \tag{2.4}$$

où :

$$\alpha = \alpha_C + \alpha_T \text{ et } \beta = \beta_C + \beta_T ; \tag{2.5}$$

$\alpha_C$  et  $\beta_C$  décrivent la contribution centrale non-locale et sont écrits en fonction des autres paramètres de la force de Skyrme,

$$\alpha_C = \frac{1}{8}(t_1 - t_2) - \frac{1}{8}(t_1 x_1 + t_2 x_2), \quad (2.6)$$

$$\beta_C = -\frac{1}{8}(t_1 x_1 + t_2 x_2). \quad (2.7)$$

Ces termes ont été inclus lors des ajustements de certaines paramétrisations de Skyrme comme SLy5 [Ch98];  $\alpha_T$  et  $\beta_T$  sont les paramètres qui décrivent la contribution tensorielle, qui a été prise en compte dans des paramétrisations plus récentes [Le07].

D'autres termes non standards peuvent être ajoutés. Un exemple en est donné dans la section 2.7 où des termes dépendant de la densité de spin sont introduits et leur effet est analysé.

## 2.4 Les équations Skyrme-HFB en symétrie sphérique

Dans le cas où la symétrie sphérique est imposée et que l'interaction de Skyrme est utilisée, les équations HFB ont la forme suivante :

$$\left[ -\frac{d}{dr} \mu \frac{d}{dr} + U + \mu \frac{l(l+1)}{r^2} + \mu' \frac{1}{r} + U_{so} \right] \begin{pmatrix} u_1 \\ u_2 \end{pmatrix} = E \begin{pmatrix} u_1 \\ u_2 \end{pmatrix}, \quad (2.8)$$

où  $u_i$  sont les parties radiales multipliées par  $r$  des fonctions d'onde  $\varphi_i$  :

$$\varphi_i(E, \vec{r}\sigma) = u_i(nlj, r) \frac{1}{r} Y_{lm}(\theta, \varphi) \begin{pmatrix} l m \frac{1}{2} \sigma | JM \end{pmatrix}, \quad i=1, 2. \quad (2.9)$$

Dans l'équation (2.8) :

$$\mu = \begin{pmatrix} M & \tilde{M} \\ \tilde{M} & -M \end{pmatrix}, \quad (2.10)$$

$$U = \begin{pmatrix} U - \lambda & \tilde{U} \\ \tilde{U} & -U + \lambda \end{pmatrix}, \quad (2.11)$$

$$U_{so} = \begin{pmatrix} B & \tilde{B} \\ \tilde{B} & -B \end{pmatrix} \frac{1}{r^2} \left( j(j+1) - l(l+1) - \frac{3}{4} \right). \quad (2.12)$$

Les expressions des paramètres d'inerties  $M$  et  $\tilde{M}$ , des potentiels  $U$  et  $\tilde{U}$ , et des facteurs de forme de spin-orbite  $B$  et  $\tilde{B}$  sont données dans l'Appendice A de l'article [Do84]. Nous reportons ici les expressions pour  $M$ ,  $U$  et  $B$  dans le cas où les termes en  $J^2$  sont négligés dans la densité d'Hamiltonien :

$$M_q(\vec{r}) = \frac{\hbar^2}{2m} + \frac{1}{4}t_1 \left\{ \left(1 + \frac{1}{2}x_1\right)\rho - \left(x_1 + \frac{1}{2}\right)\rho_q \right\} + \frac{1}{4}t_2 \left\{ \left(1 + \frac{1}{2}x_2\right)\rho + \left(x_2 + \frac{1}{2}\right)\rho_q \right\}, \quad (2.13)$$

$$\begin{aligned} U_q(\vec{r}) = & \frac{1}{2}t_0 \left[ (2 + x_0)\rho - (1 + 2x_0)\rho_q \right] \\ & + \frac{1}{24}t_3 \left\{ (2 + x_3)(2 + \alpha)\rho^{\alpha+1} - (2x_3 + 1) \left[ 2\rho^\alpha\rho_q + \alpha\rho^{\alpha-1}(\rho_p^2 + \rho_n^2) \right] \right\} \\ & + \frac{1}{8} \left[ t_1(2 + x_1) + t_2(2 + x_2) \right] \tau + \frac{1}{8} \left[ t_2(2x_2 + 1) - t_1(2x_1 + 1) \right] \tau_q \\ & + \frac{1}{16} \left[ t_2(2 + x_2) - 3t_1(2 + x_1) \right] \nabla^2\rho + \frac{1}{16} \left[ 3t_1(2x_1 + 1) + t_2(2x_2 + 1) \right] \nabla^2\rho_q, \end{aligned} \quad (2.14)$$

$$B_q(\vec{r}) = \frac{1}{2}W_0(\nabla\rho + \nabla\rho_q), \quad (2.15)$$

où  $\tau$  est la densité d'énergie cinétique,  $q$  distingue entre neutrons et protons et les quantités sans  $q$  dénotent les densités totales.

## 2.5 Évolution de la structure en couches et noyaux-bulle (effets du terme tenseur)

Si l'étude des noyaux se révèle un exercice complexe à cause de la difficulté de traiter ces systèmes à  $N$  corps et de détailler la nature de l'interaction nucléaire, le problème se complique ultérieurement lorsqu'on s'éloigne de la vallée de stabilité et que l'on veut traiter les noyaux exotiques situés dans des régions inexplorées de la carte.

C'est un défi très important : d'une part, les données expérimentales concernant les noyaux exotiques sont encore très peu nombreuses et, d'autre part, les extrapolations aux noyaux instables, à partir des propriétés bien connues pour les noyaux stables, peuvent être trompeuses. Une réflexion s'impose pour comprendre quel est actuellement le pouvoir prédictif des modèles couramment utilisés et comment, éventuellement, nous

pourrions améliorer ce pouvoir de prédiction par leur raffinement ou par la conception de nouveaux modèles. Ces considérations seront discutées dans le Chapitre 5.

À la fin de cette Section, j'inclus les articles [Gr07a], [Gr09] et [Be06] que je décris brièvement dans la suite.

\*\*\*\*

### [Gr07a] Évolution des états individuels (terme tenseur)

Une première étude systématique que nous avons effectuée concerne l'évolution de la structure en couches dans les isotopes de Ca [Gr07a]. Nous avons analysé, dans le cadre du modèle HF non relativiste et Hartree relativiste (que nous appellerons RMF dans la suite), l'évolution des états protoniques  $2s1/2$  et  $1d3/2$ . Les différentes contributions aux énergies individuelles de ces états, cinétique, centrale, spin-orbite et tensorielle, ont été isolées. Le rôle joué par le spin-orbite dans l'évolution de la structure était déjà bien connu : le développement d'une peau de neutrons dans les isotopes riches en neutrons génère une modification du potentiel spin-orbite qui est lié à la dérivée de la densité (voir Eqs. 2.15) [Do94]. Nous avons voulu analyser aussi les autres contributions de manière systématique.

Analogies et différences entre différents modèles ont été mises en évidence. Une propriété commune qui a été observée avec tous les modèles utilisés est la tendance à une inversion entre les deux états individuels autour du  $^{48}\text{Ca}$  et dans les isotopes très riches en neutrons. En particulier, nous avons montré que, autour du  $^{48}\text{Ca}$ , cette tendance est due au terme central et est favorisée par le terme tenseur. Dans cette analyse, un accent spécial est mis justement sur la contribution tensorielle, très discutée depuis les travaux d'Otsuka dans le contexte du modèle en couches [Ot05]. Dans le cadre du champ moyen, l'effet du tenseur provient des contributions  $\pi$ -nucléon et  $\rho$ -nucléon au terme d'échange [Lo06]. Il peut être pris en compte dans les interactions phénoménologiques comme celles de Skyrme [Sk59, St77]. Des analyses de ses effets et des paramétrisations pour le champ moyen avec Skyrme ont été proposées récemment [Br07, Co07, Le07].

Pour illustrer quelques résultats de notre travail, je montre dans la Figure 2.1 la différence des énergies individuelles des états protoniques  $2s1/2$  et  $1d3/2$  obtenue avec différents modèles non relativistes (sans contribution tensorielle). On observe la tendance commune à tous les modèles qui prédisent un rapprochement des deux états autour du  $^{48}\text{Ca}$  et pour les isotopes plus riches en neutrons. Dans certains cas, les deux états se croisent et une inversion a lieu. Des résultats tout à fait analogues sont obtenus avec les modèles relativistes.

L'effet du terme tensoriel, qui favorise l'inversion entre les deux états, peut être estimé dans la Figure 2.2, où la même différence d'énergies est montrée avec le modèle SLy5-HF qui contient les termes en  $J^2$ . Les valeurs des deux paramètres  $\alpha_T$  et  $\beta_T$ , Eq. (2.5), sont les mêmes que dans l'article [Co07].

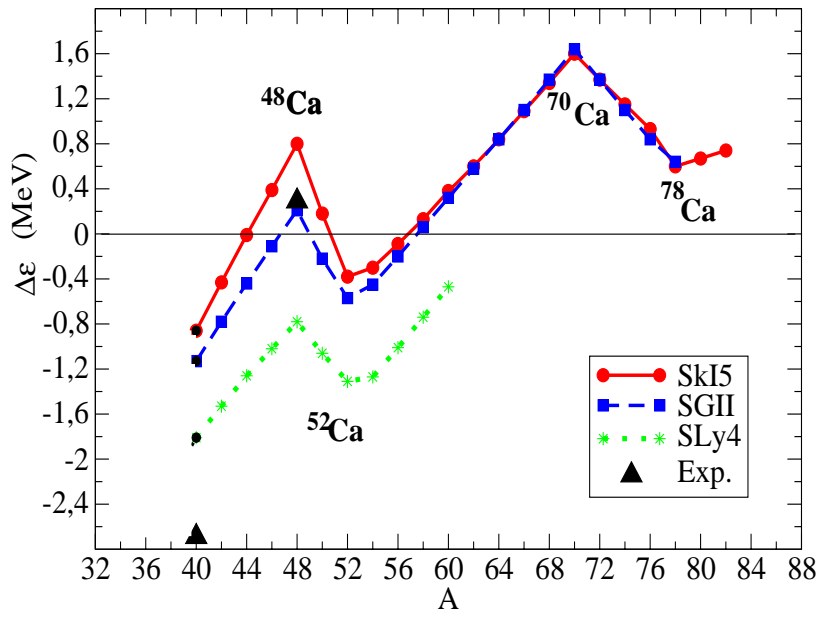


**Fig. 2.1.** Différence des énergies individuelles des états protoniques  $2s_{1/2}$  et  $1d_{3/2}$  obtenue avec différents modèles Skyrme-HF pour les isotopes de Ca.

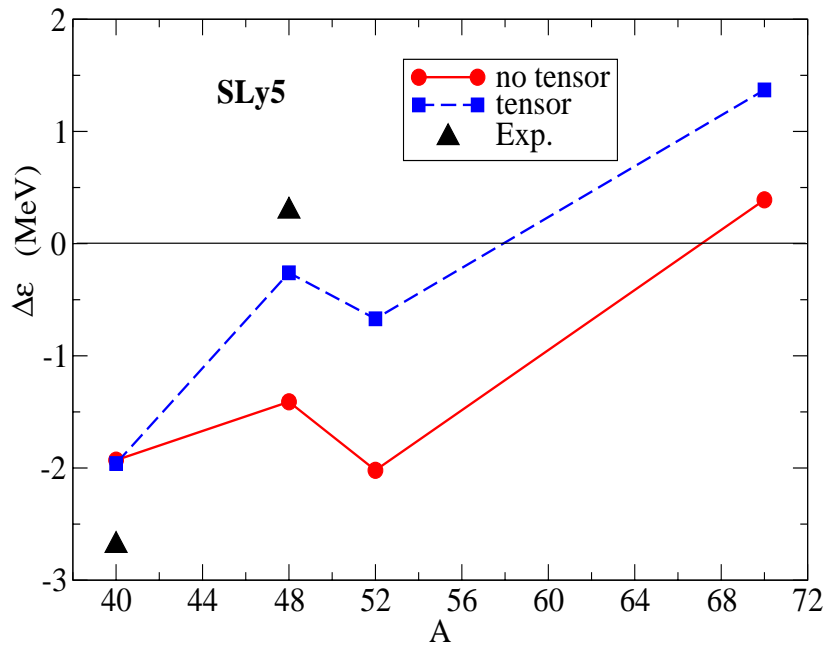


**Fig. 2.2.** Différence des énergies individuelles des états protoniques  $2s_{1/2}$  et  $1d_{3/2}$  obtenue avec SLy5-HF pour les isotopes de Ca avec (carrés) et sans (cercles) tenseur.

\*\*\*\*

## [Gr09] Noyaux-bulles

Le même comportement qui se manifeste autour du  $^{48}\text{Ca}$  et pour les isotopes de Ca très riches en neutrons est prédit aussi dans les isotopes d'Ar (autour du  $^{46}\text{Ar}$  et pour les isotopes très riches en neutrons). Dans les noyaux d'Ar, l'inversion éventuelle entre les deux états protoniques de particule individuelle (prédite par certains modèles) favoriserait la formation de structures qu'on appelle 'à bulle' caractérisées par des densités protoniques fortement creusées à l'intérieur du noyau [To04, Kh08]. Ces profils creusés au centre sont reliés au dépeuplement de l'orbitale  $2s1/2$ . Les résultats obtenus pour les isotopes d'Ar restent toutefois difficiles à interpréter. Les structures à bulles pour ces noyaux sont prédites seulement par les modèles où les corrélations d'appariement sont négligées. En effet, ces corrélations peuvent atténuer très fortement le phénomène des bulles en promouvant le peuplement de l'état  $s$ . À cause du fait que les états  $2s1/2$  et  $1d3/2$  sont très proches en énergie, presque dégénérés [Ga06c], nous nous attendons à ce que les corrélations d'appariement ne soient pas négligeables dans le noyau  $^{46}\text{Ar}$ . Par ailleurs, les isotopes d'Ar plus exotiques, où les modèles théoriques prévoient que l'appariement soit moins actif parce que les deux états individuels sont plus éloignés l'un de l'autre, ne pourront pas être produits dans un futur proche.

À la suite de ce travail nous avons voulu analyser plus en détail les prédictions théoriques sur l'existence éventuelle d'autres candidats pour des structures à bulles. Nous nous sommes concentrés sur le noyau  $^{34}\text{Si}$  qui semblerait être un excellent candidat grâce à la fermeture de sous-couche  $Z=14$  très marquée qui le caractérise. Ce noyau se comporte pratiquement comme un noyau magique et les corrélations sont presque absentes. Les résultats de cette analyse sont illustrés dans l'article [Gr09]. Dans ce travail, la quantité qui est utilisée pour définir une bulle est :

$$F \equiv \frac{\rho_{\max} - \rho_C}{\rho_{\max}}, \quad (2.16)$$

où  $\rho_{\max}$  et  $\rho_C$  sont, respectivement, les valeurs maximum et centrale de la densité. En s'appuyant sur le modèle en couches et sur différents modèles de champ moyen relativiste et non relativiste, une valeur de  $F$  de  $\sim 25\%$  est prédite pour la densité de charge dans le noyau  $^{34}\text{Si}$ .

A titre d'exemple, dans la figure 2.3 le profil radial de la densité de charge calculée avec SLy4-HF pour  $^{34}\text{Si}$  est présenté. Dans la même figure, on dessine aussi, pour comparaison, la densité de charge du noyau  $^{36}\text{S}$  (où l'état  $s$  est rempli).

La preuve expérimentale directe sur l'existence éventuelle de ces structures à bulle pour les densités devrait se réaliser en principe avec de la diffusion d'électrons qui permettrait de sonder directement la distribution de charge. Cependant, le noyau  $^{34}\text{Si}$  est un noyau instable et cette diffusion peut se réaliser seulement dans des anneaux de stockage qui ne sont pas disponibles à l'heure actuelle.

Une manière moins directe d'accéder à cette information serait de mesurer le facteur spectroscopique (pourcentage d'occupation) de l'état  $s$ . Une valeur proche de zéro serait un signal très fort de la présence d'une structure à bulle dans le noyau.

Une expérience de knockout de protons pour sonder le facteur spectroscopique de l'état  $s$  dans le noyau  $^{34}\text{Si}$  a été acceptée au MSU et sera réalisée l'année prochaine.

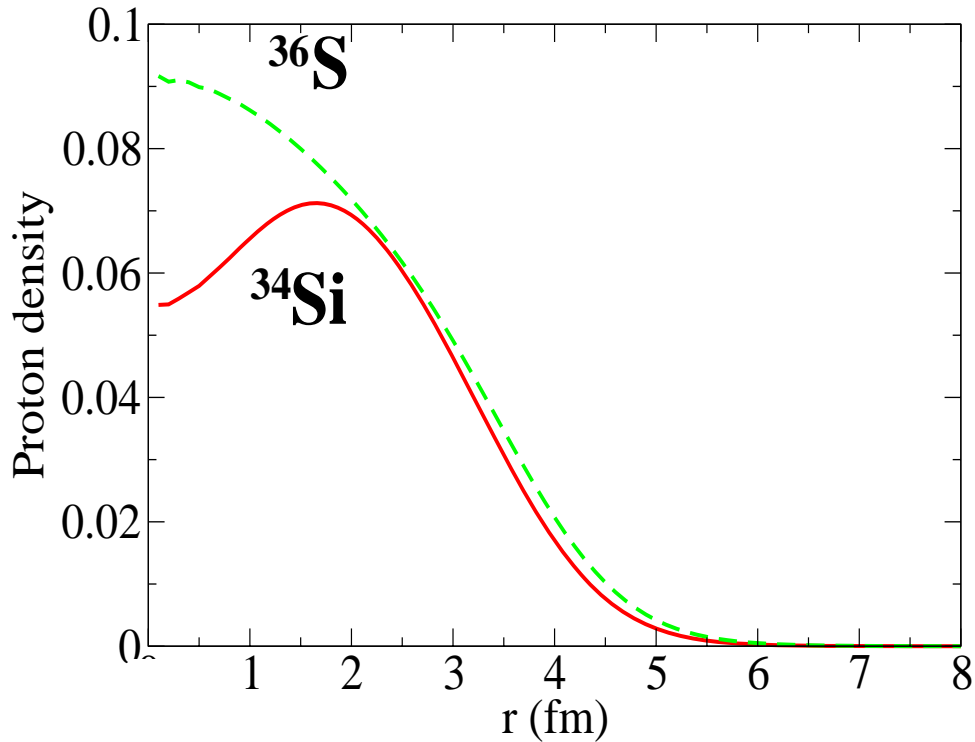


**Fig. 2.3.** Densités de charge de  $^{34}\text{Si}$  et  $^{36}\text{S}$  calculées avec *SLy4-HF*

\*\*\*\*

#### [Be06] Nouvelle fermeture de couche N=14

Le noyau  $^{34}\text{Si}$  est un candidat idéal pour une structure à bulle grâce à son comportement comparable à celui d'un noyau magique. Si la fermeture  $N=20$  pour les neutrons est attendue selon la structure en couches habituelle, la fermeture  $Z=14$  est un nouveau phénomène qui caractérise certains noyaux exotiques [So08]. Je mentionne à ce propos un travail où l'existence de ce nouveau nombre magique 14 dans les noyaux instables a été mise en évidence expérimentalement pour le noyau  $^{22}\text{O}$  [Be06]. Dans ce cas, la nouvelle fermeture de couche se manifeste pour les neutrons. Dans ce travail, j'ai contribué à l'analyse microscopique effectuée dans le cadre du modèle Skyrme-HFB avec continuum. Les densités de particule obtenues dans HFB avec continuum ont été utilisées pour l'évaluation du potentiel optique microscopique avec un modèle de folding.

## Evolution of the proton $sd$ states in neutron-rich Ca isotopes

M. Grasso

*Institut de Physique Nucléaire, Université Paris-Sud, IN2P3-CNRS, F-91406 Orsay Cedex, France and  
Dipartimento di Fisica e Astronomia and INFN, Via Santa Sofia 64, I-95123 Catania, Italy*

Z. Y. Ma

*China Center of Advanced Science and Technology (World Laboratory), Beijing 100080, People's Republic of China and  
China Institute of Atomic Energy, Beijing 102413, People's Republic of China*

E. Khan, J. Margueron, and N. Van Giai

*Institut de Physique Nucléaire, Université Paris-Sud, IN2P3-CNRS, F-91406 Orsay Cedex, France*

(Received 11 May 2007; published 23 October 2007)

We analyze the evolution with increasing isospin asymmetry of the proton single-particle states  $2s1/2$  and  $1d3/2$  in Ca isotopes, using nonrelativistic and relativistic mean-field approaches. Both models give similar trends and it is shown that this evolution is sensitive to the neutron shell structure, the two states becoming more or less close depending on the neutron orbitals that are filled. In the regions where the states get closer some parametrizations lead to an inversion between them. This inversion occurs near  $^{48}\text{Ca}$  as well as very far from stability where the two states systematically cross each other if the drip line predicted in the model is located far enough. We study in detail the modification of the two single-particle energies by using the equivalent potential in the Schrödinger-like Skyrme-Hartree-Fock equations. The role played by central, kinetic, and spin-orbit contributions is discussed. We finally show that the effect of a tensor component in the effective interaction considerably favors the inversion of the two proton states in  $^{48}\text{Ca}$ .

DOI: [10.1103/PhysRevC.76.044319](https://doi.org/10.1103/PhysRevC.76.044319)

PACS number(s): 21.10.Pc, 21.60.Jz

### I. INTRODUCTION

Novel properties and new scenarios are expected for nuclei situated far from stability. The new generation of radioactive beam facilities will allow us to answer many open questions about the peculiarities of these unstable systems. One of the major issues in the physics of exotic nuclei is the study of shell structure and magicity evolution when approaching the drip lines [1,2]. From a theoretical point of view, two aspects have been underlined as mainly responsible for the evolution of single-particle energies far from stability, the one-body spin-orbit potential that is strongly modified when the surface becomes more diffuse [1] and the tensor force between neutrons and protons in valence subshells [3].

Recently, the  $N = 28$  shell closure has been experimentally analyzed in the  $^{46}\text{Ar}(d, p)^{47}\text{Ar}$  transfer reaction [4]. A strong reduction of the neutron  $p$  spin-orbit splitting has been observed in  $^{47}\text{Ar}$  with respect to the isotope  $^{49}\text{Ca}$ . Because  $p$  states are mainly localized in the interior of the nucleus, this strong reduction cannot be justified by the presence of a diffuse surface that would affect only high- $l$  states mainly concentrated at the surface. A theoretical analysis based on the relativistic mean field (RMF) approach has been proposed by Todd-Rutel *et al.* [5]. A strong reduction of the spin-orbit splitting for neutron  $2p$  states is found in  $^{46}\text{Ar}$  as compared to  $^{48}\text{Ca}$ . At  $Z = 20$ , the state  $2s1/2$  is usually located between  $1d5/2$  and  $1d3/2$ . In the RMF calculations of Ref. [5], however,  $2s1/2$  is less bound than  $1d3/2$  in both  $^{46}\text{Ar}$  and  $^{48}\text{Ca}$  ( $2s1/2$ - $1d3/2$  inversion). In this scenario,  $2s1/2$  is empty in  $^{46}\text{Ar}$  and occupied in  $^{48}\text{Ca}$ : thus, the proton density profile in  $^{46}\text{Ar}$  presents a strong depletion in the interior of the

nucleus. This reduction of the charge density in the center would be responsible for the modification of the spin-orbit in the nuclear interior and, hence, for the reduction of the neutron  $2p$  splitting.

This problem of  $2s1/2$ - $1d3/2$  inversion of the proton states has been already analyzed by Campi and Sprung [6] within the Hartree-Fock (HF) + BCS model with an interaction derived from a  $G$  matrix [7].  $^{36}\text{Ar}$  was found as a candidate for this inversion. Skyrme forces do not lead to any inversion in this nucleus. It is thus worthwhile to revisit the problem for other nuclei in this region of the nuclear chart in the framework of the Skyrme-HF model.

In this work, we analyze the evolution of the  $s$ - $d$  proton single-particle states in Ca isotopes and the possible  $2s1/2$ - $1d3/2$  inversions. We also present some comparisons with the corresponding results obtained within RMF. We neglect pairing in our treatment because Ca isotopes are proton closed-shell nuclei. We have checked that, within RMF the inclusion of neutron pairing does not modify in a significant way the evolution of the proton states we are interested in. The only important effect due to pairing is the shift of the drip line toward heavier isotopes (for example, the drip line is shifted from  $^{60}\text{Ca}$  to  $^{76}\text{Ca}$  with the parametrization NL3 [8]). However, this aspect is not relevant in the present analysis, which is not intended to make any prediction on the drip line position. We choose the Ca isotopes because experimental signals for the inversion phenomena have been found at least in one of these isotopes,  $^{48}\text{Ca}$ : the ground state of  $^{47}\text{K}$  (one proton less than  $^{48}\text{Ca}$ ) is  $1/2^+$  with a large spectroscopic factor [9] and the single-particle spectrum of  $^{48}\text{Ca}$  has been measured, the

proton state  $1d3/2$  being more bound than  $2s1/2$  by about 300 keV [10]. We mention that proton centroids extracted from  $(d, 3H)$  reactions show that the two states are almost degenerate [11]. In our analysis, we explore all the contributions, kinetic, central, spin-orbit, and tensor, which can modify the single-particle energies with increasing  $A$  and we show that not only the spin-orbit and tensor terms are determinant. The role of the central mean-field term is in particular discussed. Within the models that lead to the crossing between the two states, we show that this inversion occurs near  $^{48}\text{Ca}$  as well as in very neutron-rich nuclei close to the drip line.

The article is organized as follows. In Sec. II we study the evolution with increasing  $A$  of the difference  $\Delta\epsilon$  between the  $2s1/2$  and  $1d3/2$  energies obtained within nonrelativistic and relativistic approaches. In Sec. III we concentrate on the nonrelativistic case and perform a detailed analysis of the results. The different contributions to  $\Delta\epsilon$  are isolated by analyzing them with the equivalent potential in the Schroedinger-like HF equations. In Sec. IV the effect of the tensor force is estimated in the framework of the SLy5-HF [12] model. Finally, conclusions are drawn in Sec. V.

## II. EVOLUTION OF $2s1/2$ AND $1d3/2$ PROTON STATES WITHIN SKYRME-HF AND RMF

We first perform a preliminary study with HF calculations of  $^{48}\text{Ca}$  using different Skyrme interactions. We then choose three representative forces: SkI5 [13], which gives a  $2s1/2$ - $1d3/2$  inversion with an energy difference  $\Delta\epsilon$  of  $\sim 800$  keV; SGII [14], which also reproduces the inversion ( $\Delta\epsilon \sim 200$  keV); and SLy4 [12] for which there is no inversion. With the three selected parametrizations we have systematically analyzed the Ca isotopes from  $^{40}\text{Ca}$  up to the HF two-neutron drip line. We recall that, in the three considered Skyrme parametrizations there is no explicit tensor force.

We show in Fig. 1 the difference  $\Delta\epsilon$  between the energies of the proton states  $2s1/2$  and  $1d3/2$  for the three Skyrme forces. The inversion takes place where  $\Delta\epsilon$  is positive. Corrections to the individual energies due to the coupling of single-particle motion with collective vibrations, which are neglected in our

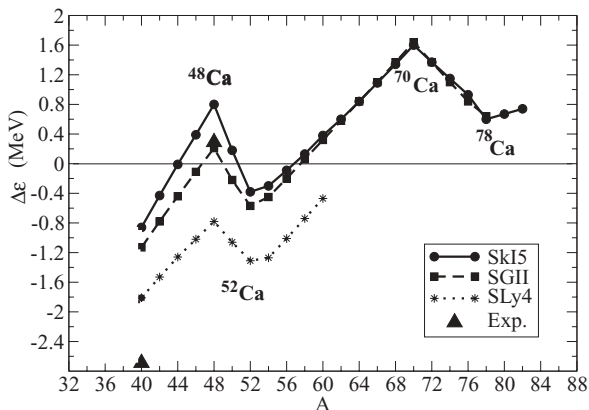


FIG. 1. Difference between the energies of the  $2s1/2$  and  $1d3/2$  proton states calculated with the Skyrme interactions SkI5, SGII, and SLy4 for Ca isotopes.

treatment, should be expected (see, for instance, Ref. [15]). However, by considering the energy difference instead of the individual single-particle energies the effects of these corrections should be reduced, the coupling to vibrations having the tendency of shifting upward the energies of both occupied states.

We observe that the SLy4-HF calculations never lead to the  $2s1/2$ - $1d3/2$  inversion. However, both SkI5-HF and SGII-HF models present this inversion around  $^{48}\text{Ca}$  as well as for more neutron-rich isotopes starting from  $^{58}\text{Ca}$  up to the drip line. The HF two-neutron drip line is located at  $^{82}\text{Ca}$ ,  $^{78}\text{Ca}$ , and  $^{60}\text{Ca}$  with SkI5, SGII, and SLy4, respectively. The two experimental points for  $^{40}\text{Ca}$  and  $^{48}\text{Ca}$  are also included in the figure. These points represent the energy splitting between the  $1/2^+$  and  $3/2^+$  states in  $^{39}\text{K}$  and  $^{47}\text{K}$ , respectively. The three sets of results globally present the same behavior. Indeed, in all three cases the quantity  $\Delta\epsilon$  starts from a negative value and increases from  $A = 40$  to  $A = 48$ . This generates a  $2s1/2$ - $1d3/2$  inversion with SkI5 (in  $^{46}\text{Ca}$ ,  $^{48}\text{Ca}$ , and  $^{50}\text{Ca}$ ) and with SGII (in  $^{48}\text{Ca}$ ). Going from  $^{48}\text{Ca}$  up to  $^{52}\text{Ca}$  the states cross again with SkI5 and SGII, whereas the distance between them increases with SLy4. These results agree with the experimental indications related to first-forbidden  $\beta$ -decay measurements [16]: the ground state of  $^{50}\text{K}$  has been assigned as  $J^\pi = 0^-$  and low-energy levels in  $^{50}\text{K}$  are dominated by the  $(\pi d3/2)^{-1} (\nu p3/2)^1$  configuration. This is an indication that the inversion is not present at  $N = 31$  in the K chain and, thus, at  $N = 32$  in the Ca chain. Beyond  $^{52}\text{Ca}$   $\Delta\epsilon$  increases again with the three parametrizations. This generates another inversion with SkI5 and SGII starting from  $^{58}\text{Ca}$ . We notice also that the nuclei for which  $\Delta\epsilon$  presents maxima or minima are the same for the three Skyrme forces.

A natural question to ask is whether the above general trends are specific of the Skyrme-HF approach. It is well known that the RMF approach gives a spin-orbit potential whose (N-Z) dependence is somewhat different from that of Skyrme-HF models [17]. We have performed RMF calculations with different parametrizations for the same set of Ca isotopes using the parametrizations DDME1 [18], NL3 [8], and NLB2 [19]. The latter one is chosen as an example of RMF model that does not lead to a  $2s1/2$ - $1d3/2$  level inversion. The calculated values of  $\Delta\epsilon$  are shown in Fig. 2 up to  $^{60}\text{Ca}$  which is the two-neutron drip line isotope predicted by DDME1 and NL3. Globally, we observe for  $\Delta\epsilon$  the same trend as that obtained within the nonrelativistic HF, with maxima and minima corresponding to the same nuclei,  $^{48}\text{Ca}$  and  $^{52}\text{Ca}$ . Because comparable trends are obtained in both nonrelativistic and relativistic approaches we conclude that the calculated evolution of  $2s1/2$  and  $1d3/2$  states is a generic behavior. We can thus explore more in detail the results by considering only the nonrelativistic case.

## III. ANALYSIS OF THE CONTRIBUTIONS TO $\Delta\epsilon$

We now concentrate on the maxima and minima of  $\Delta\epsilon$ . They correspond to nuclei with neutron closed shells or subshells: the maximum at  $^{48}\text{Ca}$  corresponds to the closure of the neutron  $1f7/2$  orbital, whereas the minimum at  $^{52}\text{Ca}$

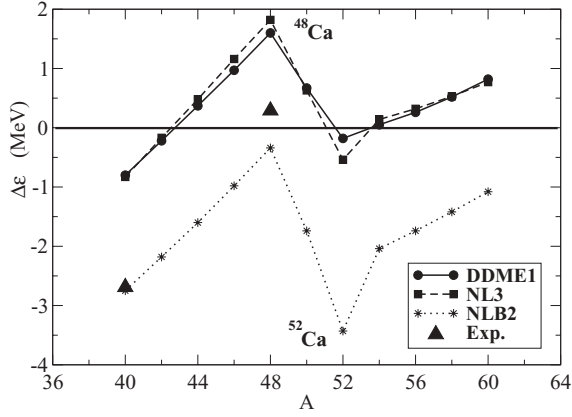


FIG. 2. Difference between the energies of the  $2s_{1/2}$  and  $1d_{3/2}$  proton states in Ca isotopes calculated in RMF with the parametrizations DDME1, NL3, and NLB2.

corresponds to the filling of the neutron  $2p_{3/2}$  state. In the nonrelativistic Skyrme-HF model the radial HF equations can be expressed in terms of an energy-dependent equivalent potential  $V_{\text{eq}}^{lj}$ :

$$\frac{\hbar^2}{2m} \left[ -\frac{d^2}{dr^2} \psi(r) + \frac{l(l+1)}{r^2} \psi(r) \right] + V_{\text{eq}}^{lj}(r, \epsilon) \psi(r) = \epsilon \psi(r), \quad (1)$$

where

$$V_{\text{eq}}^{lj}(r, \epsilon) = V_{\text{eq}}^{\text{centr.}} + \frac{m^*(r)}{m} U_{\text{so}}^{lj}(r) + \left[ 1 - \frac{m^*(r)}{m} \right] \epsilon, \quad (2)$$

with  $U_{\text{so}}^{lj}(r) = U_{\text{so}}(r) \times [j(j+1) - l(l+1) - 3/4]$ .  $U_{\text{so}}(r)$  is the spin-orbit HF potential and  $V_{\text{eq}}^{\text{centr.}}$  is

$$V_{\text{eq}}^{\text{centr.}} = \frac{m^*(r)}{m} U_0(r) - \frac{m^{*2}(r)}{2m\hbar^2} \left[ \frac{\hbar^2}{2m^*(r)} \right]^2 + \frac{m^*(r)}{2m} \left[ \frac{\hbar^2}{2m^*(r)} \right]'' , \quad (3)$$

where  $U_0(r)$  is the central HF potentials and  $m^*(r)$  is the effective mass [12]. For protons  $U_0$  includes the Coulomb potential. Up to a normalization factor the HF radial wave function  $\phi$  of energy  $\epsilon$  is related to the solution  $\psi$  of Eq. (1) by the relation  $\psi = (m^*/m)^{1/2} \phi$ . From Eqs. (1)–(3) we can write  $\Delta\epsilon$  as

$$\Delta\epsilon = \left[ \frac{\langle T \rangle_s}{\langle m^*/m \rangle_s} - \frac{\langle T \rangle_d}{\langle m^*/m \rangle_d} \right] + \left[ \frac{\langle V_{\text{eq}}^{\text{centr.}} \rangle_s}{\langle m^*/m \rangle_s} - \frac{\langle V_{\text{eq}}^{\text{centr.}} \rangle_d}{\langle m^*/m \rangle_d} \right] - \frac{\langle (m^*/m) U_{\text{so}}^{d3/2} \rangle}{\langle m^*/m \rangle_d}, \quad (4)$$

where  $T$  is the kinetic contribution. The three terms of the right-hand side of Eq. (4)—kinetic, central, and spin-orbit—are plotted in Fig. 3 for the force SkI5 and the nuclei  $^{40}\text{Ca}$ ,  $^{48}\text{Ca}$ ,  $^{52}\text{Ca}$ , and  $^{70}\text{Ca}$ . Similar results are obtained with SLy4 and SGII. We mention that the mean value of the effective mass in the denominators of Eq. (4) has very little  $A$  dependence from  $^{40}\text{Ca}$  to  $^{70}\text{Ca}$ . From Fig. 3, one notices that the spin-orbit

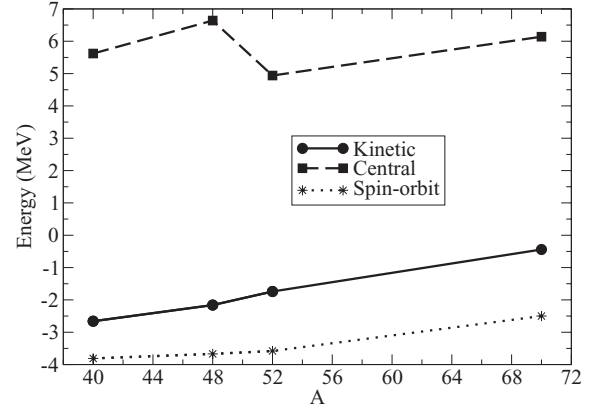
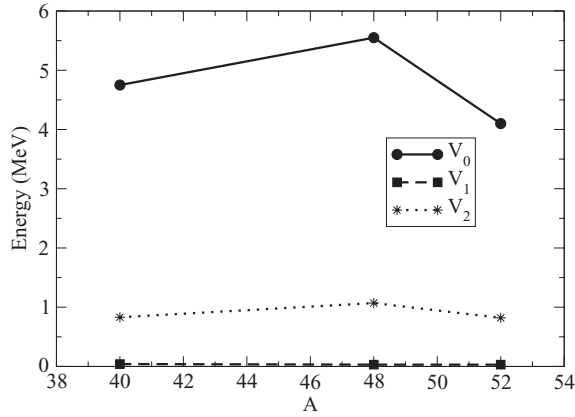


FIG. 3. Kinetic, central, and spin-orbit contributions of Eq. (4) for SkI5 in  $^{40}\text{Ca}$ ,  $^{48}\text{Ca}$ ,  $^{52}\text{Ca}$ , and  $^{70}\text{Ca}$ .

and kinetic terms present a regular behavior as a function of  $A$ . Both of them are weakened with increasing isospin asymmetry favoring the inversion in very neutron-rich isotopes. The spin-orbit term is weakened because the neutron surface becomes more diffuse with increasing  $A$ . In general, the kinetic energy of an orbital depends on the mean distance between its single-particle energy and the bottom of the potential in the region where the wave function is localized. For the two states  $2s_{1/2}$  and  $1d_{3/2}$  we can look at the difference  $\epsilon_{lj} - V_{\text{eq}}^{lj}(r_0)$ , where  $r_0$  is the rms radius of the corresponding wave function. The evolution of  $V_{\text{eq}}^{lj}$  with increasing  $A$  is governed by two effects: (i) the lowering of the proton potential due to the symmetry term and (ii) the formation of a neutron skin that modifies the proton distribution by pulling it toward larger radii. The intensity of these two effects depends on the quantum numbers of the neutron orbitals that are filled and of the proton wave function under study. As an illustration, we consider  $^{52}\text{Ca}$  and  $^{70}\text{Ca}$ . The rms radii  $r_0$  and the values  $\epsilon_{lj} - V_{\text{eq}}^{lj}(r_0)$  are shown in Table I for the  $2s_{1/2}$  and  $1d_{3/2}$  states. From  $^{52}\text{Ca}$  to  $^{70}\text{Ca}$  the difference  $\epsilon_{lj} - V_{\text{eq}}^{lj}(r_0)$  is reduced more for  $1d_{3/2}$  (4.9%) than for  $2s_{1/2}$  (0.4%). This analysis is confirmed by the evolution of the two rms radii. It is evident that, going from  $^{52}\text{Ca}$  to  $^{70}\text{Ca}$ , the  $1d_{3/2}$  wave function is more affected than  $2s_{1/2}$  by the enlarging of the potential due to the formation of a thick neutron skin. This explains the increase of the kinetic contribution to  $\Delta\epsilon$  with the neutron number. We consider now the central term of Eq. (4) that is responsible for the maxima and minima of  $\Delta\epsilon$ , and concentrate on the maximum at  $^{48}\text{Ca}$ . We mention that the major role played by the central term in

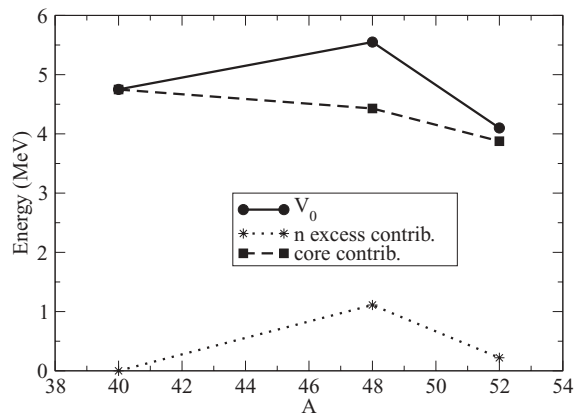
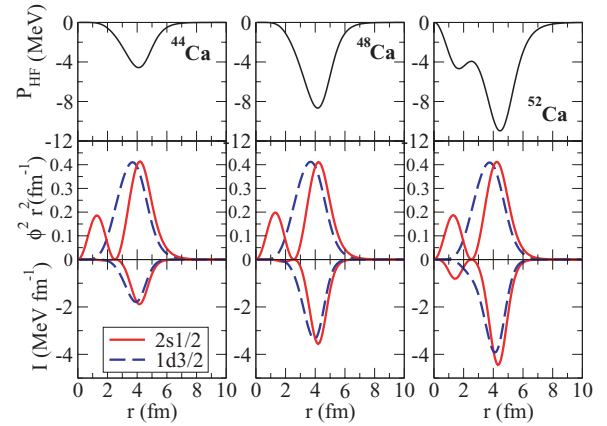
TABLE I. The values of  $r_0$  and  $\epsilon - V_{\text{eq}}^{lj}(r_0)$ , for the states  $2s_{1/2}$  and  $1d_{3/2}$  in  $^{52}\text{Ca}$  and  $^{70}\text{Ca}$ . The interaction is SkI5.

$A$	$r_0$ (fm)	$r_0$ (fm)	$\epsilon - V_{\text{eq}}^{lj}(r_0)$ (MeV)	$\epsilon - V_{\text{eq}}^{lj}(r_0)$ (MeV)
	$2s_{1/2}$	$1d_{3/2}$	$2s_{1/2}$	$1d_{3/2}$
52	3.71	3.70	23.11	19.73
70	3.81	3.89	23.01	18.76

FIG. 4.  $V_0$ ,  $V_1$ , and  $V_2$  calculated with SkI5 in  $^{40}\text{Ca}$ ,  $^{48}\text{Ca}$ , and  $^{52}\text{Ca}$ .

modifying the single-particle energies has been also underlined by Gaodefroy *et al.* [4]. We introduce the quantities  $V_0$ ,  $V_1$ , and  $V_2$  that correspond to the contributions of the three terms of Eq. (3). They are plotted in Fig. 4 for  $^{40}\text{Ca}$ ,  $^{48}\text{Ca}$ , and  $^{52}\text{Ca}$ . It turns out that the term mainly affected by the neutron shell structure is  $V_0$ , which contains the Hartree-Fock potential.

We can separate the energy contributions of the  $N = Z = 20$  core from those of the excess neutrons. For instance, the total nucleon density  $\rho$  is a sum of  $\rho_{\text{core}}$  and  $\rho_{\text{excess}}$ , and similarly for the other types of densities. Then, for any HF quantity the core contribution is obtained by replacing in its expression the total densities by core densities, whereas the neutron excess contribution corresponds to the rest. We show in Fig. 5 the core and neutron excess contributions to  $V_0$ . It is clear that the change of slope at  $^{48}\text{Ca}$  is mainly due to the neutron excess contribution. We have further verified that the term mainly responsible is the  $t_0$  term of the Skyrme force. The density-dependent term ( $t_3$  term) is also sensitive to the neutron shell structure but with an opposite behavior reducing the effect due to the  $t_0$  term. Hence, the main parameters that influence the behavior of  $\Delta\epsilon$  are  $x_0$  and  $t_0$  as well as  $x_3$ ,  $t_3$ , and  $\alpha$ . We have checked that the role played by the other terms of the HF potential is negligible.

FIG. 5. Core and neutron excess contributions to  $V_0$  for SkI5 in  $^{40}\text{Ca}$ ,  $^{48}\text{Ca}$ , and  $^{52}\text{Ca}$ .FIG. 6. (Color online) Potential  $P_{\text{HF}}$  (see text) (top), square of  $1d3/2$  and  $2s1/2$  radial wave functions times  $r^2$  (middle) and their product (bottom) calculated with SkI5 in  $^{44}\text{Ca}$ ,  $^{48}\text{Ca}$ , and  $^{52}\text{Ca}$ .

To complete our analysis we consider separately the two single-particle energies  $2s1/2$  and  $1d3/2$ . We have verified that the maximum of  $\Delta\epsilon$  at  $^{48}\text{Ca}$  is mostly due to the energy of the  $1d3/2$  state that decreases less rapidly from  $^{48}\text{Ca}$  to  $^{52}\text{Ca}$  than from  $^{40}\text{Ca}$  to  $^{48}\text{Ca}$ . This behavior is explained in Fig. 6. In the top panels the neutron excess contribution  $P_{\text{HF}}$  to the HF potential due to the  $t_0$  and  $t_3$  terms is plotted for  $^{44}\text{Ca}$ ,  $^{48}\text{Ca}$ , and  $^{52}\text{Ca}$  (see, e.g., Ref. [12] for the expressions in terms of the Skyrme force parameters). In the middle panels we show the squares of the  $1d3/2$  and  $2s1/2$  radial wave functions multiplied by  $r^2$ . In the bottom panels the products  $P_{\text{HF}}|\phi|^2r^2$  are shown. Because  $P_{\text{HF}}$  is negative (the  $t_0$  contribution is negative and the largest in absolute value) the proton single-particle energies are lowered with increasing  $N-Z$ , as expected. We observe that in  $^{44}\text{Ca}$  and  $^{48}\text{Ca}$  the potential related to the neutron excess ( $1f7/2$  neutron orbital) is concentrated in the region where the  $1d3/2$  wave function is localized. The overlap with this wave function is thus the largest and this explains why the filling of the neutron  $1f7/2$  orbital has an important effect on the proton  $1d3/2$  energy that is strongly lowered. However, when the neutron  $2p3/2$  orbital is filled (from  $^{48}\text{Ca}$  to  $^{52}\text{Ca}$ ) the potential changes very little in the region where the  $1d3/2$  wave function is appreciable. This explains why the  $1d3/2$  energy decreases more from  $A = 44$  to  $48$  than from  $A = 48$  to  $52$ . The energy of the  $2s1/2$  proton state is much less sensitive to the neutron shell structure in these isotopes and it decreases rather monotonically from  $A = 44$  to  $52$ .

#### IV. TENSOR FORCE EFFECT

The tensor force plays certainly a role in the evolution of single-particle states. This is discussed, e.g., in the framework of the shell model in Ref. [3]. In a mean-field approach, the tensor effect originates from the  $\pi$ -nucleon and  $\rho$ -nucleon contributions to the Fock terms [20,21], and it can be introduced phenomenologically in the parametrizations of effective interactions built for HF models [22–24]. Recent progress have been made in determining the tensor terms of

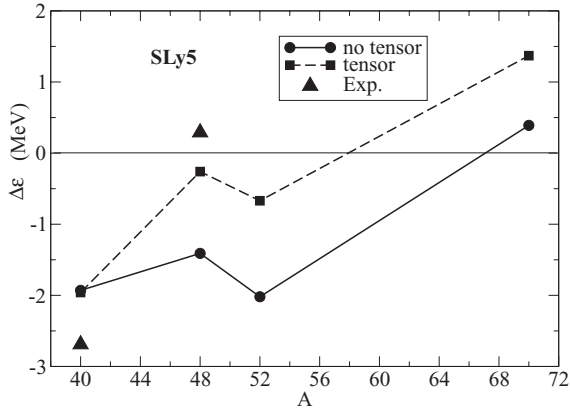


FIG. 7. Difference between the energies of  $2s_{1/2}$  and  $1d_{3/2}$  proton states in  $^{40}\text{Ca}$ ,  $^{48}\text{Ca}$ ,  $^{52}\text{Ca}$ , and  $^{70}\text{Ca}$  calculated with SLy5 with and without the tensor contribution.

Skyrme interactions [25,26] by adjusting the single-particle spectra measured in  $N = 82$  isotones and  $Z = 50$  isotopes [27].

When this force is included the spin-orbit potential presents an additional term depending on the spin density  $J$ , namely,

$$U_{\text{so}}^q = \frac{W_0}{2} (\nabla\rho + \nabla\rho_q) + \alpha J_q + \beta J_{q'}, \quad (5)$$

where  $q$  stands for neutrons (protons) and  $q'$  for protons (neutrons),  $\alpha$  and  $\beta$  consist of a sum of central and tensor contributions:  $\alpha = \alpha_C + \alpha_T$ ,  $\beta = \beta_C + \beta_T$ . The central contributions depend only on the velocity-dependent part of the Skyrme force, whereas the tensor contributions are generated by the tensor component of the Skyrme force [23,26]. To estimate the effect of the tensor force in our case we use the Skyrme force SLy5 that already contains in the fitting protocol the terms  $\alpha_C$  and  $\beta_C$ . For  $\alpha_T$  and  $\beta_T$  we adopt the values determined in Ref. [25] by comparing the Skyrme-HF predictions with the data of Ref. [27]. These values are  $\alpha_T = -170 \text{ MeV fm}^5$  and  $\beta_T = 100 \text{ MeV fm}^5$ . We expect that the tensor force favors the inversion in  $^{48}\text{Ca}$  (see, for instance, Fig. 4 of Ref. [3]). Actually, from  $^{40}\text{Ca}$  to  $^{48}\text{Ca}$  the  $1f_{7/2}$  neutron orbital is filled. The interaction between the proton orbital  $1d_{3/2}$  and the neutron orbital  $1f_{7/2}$  is attractive and its effect is to lower the energy of  $1d_{3/2}$ , thus favoring the crossing with  $2s_{1/2}$ . As an illustration we performed SLy5-HF calculations for  $^{40}\text{Ca}$ ,  $^{48}\text{Ca}$ ,  $^{52}\text{Ca}$ , and  $^{70}\text{Ca}$  ( $^{70}\text{Ca}$  is still bound within SLy5-HF). We show in Fig. 7 the values of  $\Delta\epsilon$  obtained with and without the tensor contribution. As expected, the tensor force increases the slope going from  $^{40}\text{Ca}$  to  $^{48}\text{Ca}$ , bringing the two states close together and improving the agreement with the experimental data. The improvement is quite strong because the value of  $\Delta\epsilon$  in  $^{48}\text{Ca}$  is equal to  $-0.26 \text{ MeV}$  and  $-1.41 \text{ MeV}$  with and without the tensor contribution, respectively. We can also expect that, by adding the tensor contribution within, for instance, the SkI5 model, the

value of  $\Delta\epsilon$  at  $^{48}\text{Ca}$  (Fig. 1) would be further increased and this result would be more similar to the relativistic case DDME1 or NL3 (Fig. 2). However, a precise conclusion cannot be drawn because, to perform a proper calculation, including the tensor effect in the SkI5 model, all the other parameters of the force should be also readjusted.

## V. SUMMARY

In this article we have analyzed the modification of the proton single-particle states  $2s_{1/2}$  and  $1d_{3/2}$  in Ca isotopes within the nonrelativistic Skyrme-HF and the relativistic RMF models. Pairing effects have been neglected because Ca isotopes are proton closed-shell. We are interested in the evolution of proton states and the inclusion of neutron pairing does not affect significantly the global trend of our results. Both models, HF and RMF, lead to the same evolution with increasing  $A$  for the difference  $\Delta\epsilon$  of the energies of the two states. This evolution depends on the neutron orbitals that are filled,  $\Delta\epsilon$  presenting maxima and minima corresponding to neutron shell or subshell closures. In particular, going from  $^{40}\text{Ca}$  to  $^{48}\text{Ca}$  the two proton states come closer to each other and they can sometimes cross in some models. By performing an analysis based on the equivalent potential in the nonrelativistic Skyrme-HF approach, we have shown that the kinetic and spin-orbit contributions present quite a regular behavior with increasing  $A$ . They both strongly favor the inversion of the two states in very neutron-rich nuclei. We have also verified that the contribution that is mostly responsible for the maximum of  $\Delta\epsilon$  at  $^{48}\text{Ca}$  (and leading to an inversion for some models) is the central HF potential and, in particular the  $t_0$  and  $t_3$  terms. The former term favors the crossing of the two states near  $^{48}\text{Ca}$ , whereas the latter acts against it. The net effect is that the two states get closer and can cross each other in some models.

We have finally analyzed the role of the tensor force within the SLy5-HF model and found that its contribution goes in the same direction as the  $t_0$  term of the HF potential, favoring the inversion of the states near  $^{48}\text{Ca}$ .

Our analysis was restricted to a purely mean-field picture. Work should be done to include effects beyond mean field. For instance, particle-phonon coupling, which has been neglected here, is expected to improve the quality of the theoretical results in the study of single-particle states evolution.

## ACKNOWLEDGMENTS

The authors thank K. Bennaceur, A. Bhagwat, G. Colò, L. Gaudefroy, H. Sagawa, and O. Sorlin for valuable discussions. Z.Y.M. and N.V.G. acknowledge the partial support of CNRS-IN2P3 (France) under the PICS program, of the National Natural Science Foundation of China under Nos. 10475116 and 10535010 and the European Community project Asia-Europe Link in Nuclear Physics and Astrophysics CN/Asia-Link 008(94791).

- [1] J. Dobaczewski, I. Hamamoto, W. Nazarewicz, and J. A. Sheikh, Phys. Rev. Lett. **72**, 981 (1994).
- [2] E. Becheva *et al.*, Phys. Rev. Lett. **96**, 012501 (2006).
- [3] T. Otsuka, T. Suzuki, R. Fujimoto, H. Grawe, and Y. Akaishi, Phys. Rev. Lett. **95**, 232502 (2005).
- [4] L. Gaudefroy *et al.*, Phys. Rev. Lett. **97**, 092501 (2006).
- [5] B. G. Todd-Rutel, J. Piekarewicz, and P. D. Cottle, Phys. Rev. C **69**, 021301(R) (2004).
- [6] X. Campi and D. W. L. Sprung, Phys. Lett. **B46**, 291 (1973).
- [7] D. W. L. Sprung and P. K. Banerjee, Nucl. Phys. **A168**, 273 (1971).
- [8] G. A. Lalazissis, J. König, and P. Ring, Phys. Rev. C **55**, 540 (1997).
- [9] C. A. Ogilvie *et al.*, Nucl. Phys. **A465**, 445 (1987).
- [10] Database of the National Nuclear Data Center, Brookhaven; T. W. Burrows, Nuclear Data Sheets Update for  $A = 47$ . Nucl. Data Sheets **74**, 1 (1995); J. S. Hanspal *et al.*, Nucl. Phys. **A436**, 236 (1985); S. Fortier *et al.*, *ibid.* **A311**, 324 (1978).
- [11] P. D. Cottle and K. W. Kemper, Phys. Rev. C **58**, 3761 (1998).
- [12] E. Chabanat *et al.*, Nucl. Phys. **A627**, 710 (1997); **A635**, 231 (1998); **A643**, 441 (1998).
- [13] P.-G. Reinhard and H. Flocard, Nucl. Phys. **A584**, 467 (1995).
- [14] N. V. Giai and H. Sagawa, Phys. Lett. **B106**, 379 (1981); N. V. Giai and H. Sagawa, Nucl. Phys. **A371**, 1 (1981).
- [15] P. Donati, T. Dossing, Y. R. Shimizu, S. Mizutori, P. F. Bortignon, and R. A. Broglia, Phys. Rev. Lett. **84**, 4317 (2000).
- [16] P. Baumann *et al.*, Phys. Rev. C **58**, 1970 (1998).
- [17] G. A. Lalazissis, D. Vretenar, W. Pöschl, and P. Ring, Phys. Lett. **B418**, 7 (1998); G. A. Lalazissis, D. Vretenar, and P. Ring, Phys. Rev. C **57**, 2294 (1998).
- [18] T. Nikšić, D. Vretenar, P. Finelli, and P. Ring, Phys. Rev. C **66**, 024306 (2002).
- [19] A. Boussy, S. Marcos, and J.-F. Mathiot, Nucl. Phys. **A415**, 497 (1984); A. Boussy, S. Marcos, and Pham van Thieu, *ibid.* **A422**, 541 (1984).
- [20] W. H. Long, N. Van Giai, and J. Meng, Phys. Lett. **B640**, 150 (2006).
- [21] W. H. Long, H. Sagawa, J. Meng, and N. Van Giai, arXiv:nucl-th/0609076.
- [22] T. H. R. Skyrme, Nucl. Phys. **9**, 615 (1959).
- [23] Fl. Stancu, D. M. Brink, and H. Flocard, Phys. Lett. **B68**, 108 (1977).
- [24] T. Otsuka, T. Matsuo, and D. Abe, Phys. Rev. Lett. **97**, 162501 (2006).
- [25] G. Colò, H. Sagawa, S. Fracasso, and P. F. Bortignon, Phys. Lett. **B646**, 227 (2007).
- [26] D. M. Brink and Fl. Stancu, Phys. Rev. C **75**, 064311 (2007).
- [27] J. P. Schiffer *et al.*, Phys. Rev. Lett. **92**, 162501 (2004).

Nuclear “bubble” structure in  $^{34}\text{Si}$ M. Grasso,<sup>1</sup> L. Gaudefroy,<sup>2</sup> E. Khan,<sup>1</sup> T. Nikšić,<sup>3</sup> J. Piekarewicz,<sup>4</sup> O. Sorlin,<sup>5</sup> N. Van Giai,<sup>1</sup> and D. Vretenar<sup>3</sup><sup>1</sup>*Institut de Physique Nucléaire, Université Paris-Sud, IN2P3-CNRS, F-91406 Orsay Cedex, France*<sup>2</sup>*CEA, DAM, DIF, F-91297 Arpajon, France*<sup>3</sup>*Physics Department, Faculty of Science, Zagreb University, HR-10000 Zagreb, Croatia*<sup>4</sup>*Florida State University, Tallahassee, Florida 32306, USA*<sup>5</sup>*Grand Accélérateur National d'Ions Lourds (GANIL), CEA/DSM-CNRS-IN2P3, Boulevard Henri Becquerel, Boîte Postale 55027, F-14076 Caen Cedex 5, France*

(Received 22 September 2008; revised manuscript received 10 February 2009; published 26 March 2009)

Bubble nuclei are characterized by a depletion of their central density. Their existence is examined within three different theoretical frameworks: the shell model and nonrelativistic and relativistic microscopic mean-field approaches. We analyze  $^{34}\text{Si}$  and  $^{22}\text{O}$  as possible candidates for proton and neutron bubble nuclei, respectively. In the case of  $^{22}\text{O}$ , we observe a significant model dependence, thereby calling into question the bubble structure of  $^{22}\text{O}$ . In contrast, an overall agreement among the models is obtained for  $^{34}\text{Si}$ . Indeed, all models predict a central proton density depletion of about 40% and a central charge density depletion of 25%–30%. This result provides strong evidence in favor of a proton bubble in  $^{34}\text{Si}$ .

DOI: [10.1103/PhysRevC.79.034318](https://doi.org/10.1103/PhysRevC.79.034318)

PACS number(s): 21.10.Ft, 21.60.-n, 25.30.Bf, 27.30.+t

## I. INTRODUCTION

The “bubble” structure of atomic nuclei is characterized by a depleted central density. Although it is somewhat unexpected that a “hole” can be made in a nuclear system where nuclear forces generate a saturation density ( $\rho_0 \sim 0.16 \text{ fm}^{-3}$ ), this phenomenon has been discussed for many decades. Indeed, the possibility of bubble nuclei started with the pioneering work of Wilson in the 1940s [1], who studied the low-energy excitations of a thin spherical shell, up to the first microscopic calculations of Campi and Sprung in the 1970s [2]. More recently, bubbles have been discussed in superheavy and hyperheavy nuclei [3,4]. The promise of producing more exotic nuclei with the new generation of RIB facilities has revived interest in this subject.

Owing to the absence of a centrifugal barrier,  $s$  orbitals have radial distributions peaked in the interior of the nucleus, with their corresponding wave function extending further into the surface depending on the number of nodes. In contrast, orbitals with nonzero angular momenta are suppressed in the nuclear interior and do not contribute to the central density. Therefore, any vacancy of  $s$  orbitals is expected to produce a depletion of the central density. By using electron scattering from  $^{206}\text{Pb}$  and  $^{205}\text{Tl}$  up to large momentum transfers, the radial distribution of the  $3s$  proton orbital was experimentally mapped and shown to closely resemble the one predicted by an independent particle model. The agreement extends from the center of the  $^{206}\text{Pb}$  nucleus all the way to the surface and reproduces accurately the nodal structure of the wave function [5,6]. Differences in the charge density between  $^{206}\text{Pb}$  and  $^{205}\text{Tl}$  revealed that about 80% of the proton removal strength came from the  $3s$  state, thereby leading to a depletion of the proton density in the nuclear interior. Specifically, the depletion fraction, defined as

$$F \equiv \frac{\rho_{\text{max}} - \rho_c}{\rho_{\text{max}}}, \quad (1)$$

amounts to  $F = 11(2)\%$ . In this equation  $\rho_c$  and  $\rho_{\text{max}}$  represent the values of the central and maximum charge density in  $^{205}\text{Tl}$ , respectively. Yet the small energy difference between the  $3s_{1/2}$  and the  $2d_{3/2}$  proton orbitals plus the coupling of the  $3s_{1/2}$  proton to collective excitations in  $^{206}\text{Pb}$  yield a proton hole strength in  $^{205}\text{Tl}$  that is shared among the  $3s_{1/2}$  and  $2d_{3/2}$  orbitals, with the former carrying about 70% of the strength and the latter the remaining 30%. Consequently, the central depletion in  $^{205}\text{Tl}$  relative to  $^{206}\text{Pb}$  is not as large as if the full hole strength would have been carried by the  $3s$  orbital. Using similar arguments, one can conclude that the depletion at the center of  $^{204}\text{Hg}$  is not expected to be very large, as the two-proton hole strength will be again shared among the  $3s_{1/2}$  and  $2d_{3/2}$  orbitals. Therefore, the search for the best bubble candidates should be oriented toward nuclei with an  $s$  orbital well separated from its nearby single-particle states and where correlations are weak. This latter feature arises mainly for nuclei located at major shell closures.

Recently, the formation of a proton bubble resulting from the depletion of the  $2s_{1/2}$  orbital was investigated in  $^{46}\text{Ar}$  [7, 8] and in the very neutron rich Ar isotopes [8]. In  $^{46}\text{Ar}$  the proton  $2s_{1/2}$  and  $1d_{3/2}$  orbitals are almost degenerate: As in the case of  $^{206}\text{Pb}$ , pairing correlations will lead to a significant occupancy of the  $2s_{1/2}$  orbital [9], thus weakening the bubble effect. This weakening will continue to hold for any  $N = 28$  isotone between  $Z = 20$  and  $Z = 14$  as long as the  $2s_{1/2}$  and  $1d_{3/2}$  orbitals remain degenerate, as shown for instance in Fig. 3 of Ref. [10]. For very neutron rich Ar isotopes, such as  $^{68}\text{Ar}$ , the  $s_{1/2}$  proton orbital is predicted to move significantly above the  $d_{3/2}$  state, hindering the role of pairing correlations [8,11]. Unfortunately, the production of this exotic nucleus is far beyond the present and near-future capabilities of RIB facilities.

A more suitable region of the chart of the nuclides to search for a proton bubble is that of the  $N = 20$  isotones. Between  $Z = 20$  and  $Z = 16$  the  $s_{1/2}$  orbital is located about 6.5 MeV above the  $d_{5/2}$  orbital and about 2.5 MeV below the  $d_{3/2}$  orbital,

thereby forming two subshell closures at  $Z = 14$  and  $Z = 16$ , respectively [12]. In addition, the  $N = 20$  shell closure is rigid enough to hinder significant coupling to collective states. If one assumes a sequential filling of proton orbitals, the  $2s_{1/2}$  orbital should be completely empty in  $^{34}\text{Si}$  but fully filled in  $^{36}\text{S}$ . This may lead to an important change in the proton density distribution between  $^{36}\text{S}$  and  $^{34}\text{Si}$ , making  $^{34}\text{Si}$  an excellent candidate for a bubble nucleus. Concomitantly, both Skyrme and Gogny Hartree-Fock-Bogoliubov models predict a spherical shape for  $^{34}\text{Si}$  [13,14]. Other possible candidates in the Si-isotopic chain, such as  $^{28}\text{Si}$  and  $^{42}\text{Si}$ , are not optimal as they are deformed [15,16]. For these nuclei several correlations hinder the development of a bubble. The mirror system of ( $^{36}\text{S}$ ,  $^{34}\text{Si}$ ), ( $^{36}\text{Ca}$ ,  $^{34}\text{Ca}$ ), could not be studied at present because the  $^{34}\text{Ca}$  nucleus has not been observed so far.

A neutron bubble may be found in the oxygen chain, where large  $N = 14$  (between  $d_{5/2}$  and  $s_{1/2}$ ) and  $N = 16$  (between  $s_{1/2}$  and  $d_{3/2}$ ) subshell gaps of about 4.2 MeV [17,18] and 4 MeV [19], respectively, have been determined. Combined with the large proton gap at  $Z = 8$ ,  $^{22}\text{O}$  [17,20,21] and  $^{24}\text{O}$  [18,19,22] therefore behave as doubly magic nuclei. In this case the change in the occupancy of the  $2s_{1/2}$  neutron orbital will occur between  $^{22}\text{O}$  and  $^{24}\text{O}$ , making  $^{22}\text{O}$  a good candidate for a neutron bubble nucleus.

The present article aims at determining whether  $^{34}\text{Si}$  and  $^{22}\text{O}$  could be considered as good proton and neutron bubble nuclei, respectively. Various theoretical approaches will be employed to test the robustness of the results. In Sec. II these nuclei are analyzed in terms of shell-model calculations and the occupancies of the proton and neutron orbitals are determined. In Sec. III we first address the role of pairing correlations in mean-field approaches and then show results on microscopic nucleon density profiles obtained from (i) non-relativistic Hartree-Fock (HF) and Hartree-Fock-Bogoliubov (HFB) and (ii) relativistic mean-field (RMF) and relativistic Hartree-Bogoliubov (RHB) microscopic calculations. Comparisons to experimental data will be made whenever possible. Conclusions are drawn in Sec. IV.

## II. SHELL-MODEL PREDICTIONS

The occurrence of bubbles in nuclei, as previously defined, is directly linked to the occupancy of  $s_{1/2}$  orbitals. For both bubble candidates under study in this article,  $^{22}\text{O}$  and  $^{34}\text{Si}$ , experimental values for the occupancies are not yet available. Thus, we rely hereafter on shell-model (SM) calculations to estimate the occupation numbers of interest. Calculations have been performed with the ANTOINE code [23,24] using the USD interaction [25]. The full  $sd$  valence space was considered for protons and neutrons to study the ground-state configuration of the nuclei under consideration.

Special care should be taken concerning the contamination of the physical states of interest by spurious states originating from the center-of-mass (CM) translation. The internal structure of a nucleus with  $N$  nucleons is described by  $3N - 3$  coordinates giving the relative positions of its constituents. The three remaining degrees of freedom describe the CM motion of the whole nucleus and give rise to spurious CM

effects that modify the properties of the physical states such as binding energies and occupation numbers, as already shown by Dieperink and de Forest [26]. Following the work presented in Ref. [26], it is possible to obtain CM-corrected occupation numbers, referred to as  $S'$  in the following, from the occupation numbers  $S$  calculated within the SM framework. For the  $2s_{1/2}$  and  $1d_{3/2,5/2}$  orbits, the relation  $S'_{sd} = \left(\frac{A}{A-1}\right)^2 S_{sd}$  holds, where  $A$  is the mass number of the considered nucleus. The corrected occupation numbers for  $1p$  orbits are defined as  $S'_{1p} = \frac{A}{A-1}(S_{1p} - \frac{2S_{sd}}{A-1})$  for the nuclei under consideration in this article. Finally, the sum rule on occupation numbers allows us to deduce the CM-corrected value for the deeply bound  $1s_{1/2}$  orbit as

$$S'_{1s} = M - \sum_{\alpha \neq 1s} S'_{\alpha},$$

where  $M$  is either the neutron or the proton number of the considered nucleus.

The nucleon densities presented in the following have been evaluated by using the wave functions of a Woods-Saxon potential (without spin-orbit term), with parameters  $V_0 = -50$  MeV,  $a = 0.65$  fm, and  $r_0 = 1.25$  fm [27], and the SM occupation numbers corrected for CM effects. One notices that not considering the spin-orbit interaction leads to the same radial dependence for wave functions of nucleons occupying orbits with the same principal quantum number ( $n$ ) and orbital angular momentum ( $\ell$ ), but with different total angular momentum ( $J$ ), as for the  $1p_{3/2}$  and  $1p_{1/2}$  orbitals.

### A. Neutron bubble: $^{24}\text{O}$ and $^{22}\text{O}$

The mean occupation numbers  $S$  and  $S'$  of neutron orbits deduced from SM calculations are reported in Table I. The difference of the neutron  $2s_{1/2}$  occupancy between  $^{24}\text{O}$  to  $^{22}\text{O}$  amounts to 1.69, where a value of 2 was expected without nuclear correlations. The remaining neutron strength is mainly taken from the  $\nu d_{5/2}$  and to a lesser extent from the  $\nu d_{3/2}$  orbital. As a result of the depletion of the  $1s_{1/2}$  and  $1p$  inner shells, the  $S'$  occupation numbers for the  $\nu 1d_{5/2}$  and  $\nu 2s_{1/2}$  orbits in  $^{24}\text{O}$  slightly exceed the standard value of  $(2J + 1)$  (see Table I).

The neutron densities of  $^{22,24}\text{O}$  shown in Fig. 1 include the CM correction just discussed. The effect of the removal of two neutrons between  $^{24}\text{O}$  and  $^{22}\text{O}$  is clearly visible from the comparison of their densities. The effect of the CM correction

TABLE I. Ground-state occupation numbers  $S$  of neutron orbits obtained in the present SM calculations for  $^{24}\text{O}$  and  $^{22}\text{O}$ . The corresponding values  $S'$ , corrected for CM effects, are also reported.

Orbital	$S(^{24}\text{O})$	$S'(^{24}\text{O})$	$S(^{22}\text{O})$	$S'(^{22}\text{O})$
$\nu 1s_{1/2}$	2.00	1.75	2.00	1.73
$\nu 1p_{3/2}$	4.00	3.69	4.00	3.79
$\nu 1p_{1/2}$	2.00	1.85	2.00	1.90
$\nu 1d_{5/2}$	5.75	6.26	5.38	5.91
$\nu 2s_{1/2}$	1.89	2.06	0.34	0.37
$\nu 1d_{3/2}$	0.36	0.39	0.28	0.31

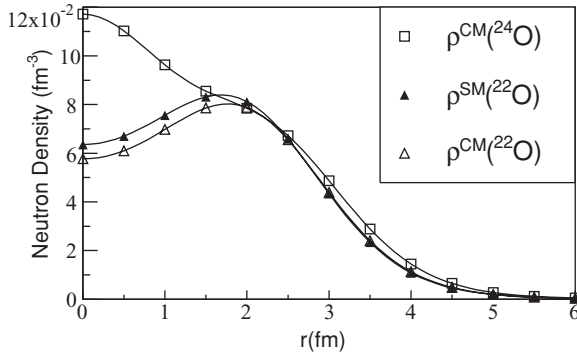


FIG. 1. Neutron densities of  $^{24}\text{O}$  and  $^{22}\text{O}$  (open squares and triangles, respectively) obtained using the occupation numbers corrected for CM motion and Woods-Saxon wave functions. The density of  $^{22}\text{O}$  without CM correction is also shown (black triangles).

is to slightly deepen the density profile at small radial distances ( $r < 2$  fm). Indeed the depletion fraction in  $^{22}\text{O}$ , as defined in Eq. (1), is found to be 28% for the CM-corrected density (open triangles on Fig. 1) and 24% for the uncorrected density (filled triangles).

In lighter oxygen isotopes this central depletion should not persist as the neutron  $1d_{5/2}$  orbital, located at the surface of the nucleus, is depleted in concert with the  $2s_{1/2}$ . It follows that the relative difference of the density in the vicinity of the surface and at the interior of the nucleus is also reduced.

### B. Proton bubble: $^{36}\text{S}$ and $^{34}\text{Si}$

The mean occupation numbers of the proton  $1d_{3/2}$  (0.31),  $2s_{1/2}$  (1.63), and  $1d_{5/2}$  (5.95) orbitals in  $^{36}\text{S}$  have been obtained from the  $^{36}\text{S}(d, ^3\text{He})^{35}\text{P}$  experiment [28]. The small occupancy of the  $1d_{3/2}$  state is due to correlations. The sum of the deduced spectroscopic factors from the proton pickup reaction from the whole  $sd$  states amounts to  $\sum C^2S \approx 7.9$ . Within the 20% uncertainties of the method, this is compatible with  $\sum C^2S = 8$ . The mean calculated occupation numbers  $S$  for the proton orbitals, as well as those corrected for CM motion,  $S'$ , are reported in Table II. The agreement with the experimental values for  $^{36}\text{S}$  is very good, lending confidence to the SM predictions for  $^{34}\text{Si}$ . The mean occupation number in  $^{34}\text{Si}$ , summed over the  $1s$  and  $2s$  orbits, is smaller than in  $^{22}\text{O}$ . Moreover, a larger mean occupation number of the  $d_{5/2}$  orbital is predicted in  $^{34}\text{Si}$  as compared to  $^{22}\text{O}$ . Both effects,

TABLE II. Same as Table I for proton orbits in  $^{36}\text{S}$  and  $^{34}\text{Si}$ . Experimental occupancies obtained in Ref. [28] for  $^{36}\text{S}$  and  $S^{\text{Exp}}(^{36}\text{S})$  are also reported.

Orbital	$S(^{36}\text{S})$	$S'(^{36}\text{S})$	$S^{\text{Exp}}(^{36}\text{S})$	$S(^{34}\text{Si})$	$S'(^{34}\text{Si})$
$\pi 1s_{1/2}$	2.00	1.84		2.00	1.82
$\pi 1p_{3/2}$	4.00	3.80		4.00	3.87
$\pi 1p_{1/2}$	2.00	1.90		2.00	1.94
$\pi 1d_{5/2}$	5.85	6.19	6.0(12)	5.76	6.11
$\pi 2s_{1/2}$	1.88	1.99	1.63(32)	0.08	0.09
$\pi 1d_{3/2}$	0.27	0.29	0.31(6)	0.16	0.17

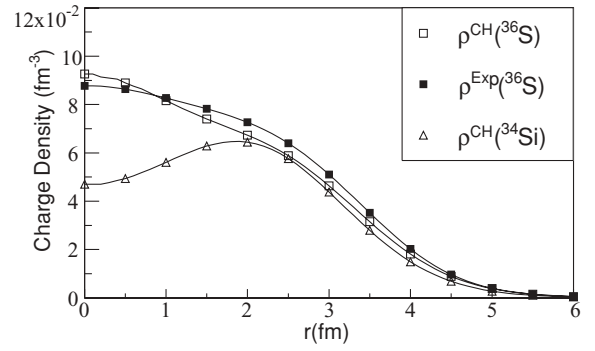


FIG. 2. Same as Fig. 1 but for charge densities in  $^{36}\text{S}$  and  $^{34}\text{Si}$  (see text).

that is, weaker (larger) occupancy at the center (surface), account for the depletion fraction in the proton density of  $^{34}\text{Si}$  found to be  $F = 44\%$  ( $F = 41\%$ ) with (without) the CM corrections. The charge densities displayed on Fig. 2 for  $^{34}\text{Si}$  and  $^{36}\text{S}$  are obtained by including CM and proton finite-size corrections. The resulting value of  $F$  for  $^{34}\text{Si}$  is  $F = 28\%$ . It has been shown in the previous section that the effect of the CM correction is to increase the bubble; this means that the proton finite-size correction acts in the opposite way: When both effects are taken into account in the charge density, the net result is a bubble weakening in  $^{34}\text{Si}$ . In the case of the stable nucleus  $^{36}\text{S}$ , the experimental charge distribution is available [29] and is reported on Fig. 2 as a set of black squares. The agreement with the SM profile is satisfactory.

It is interesting to note that the proton density depletion between the  $N = 20$  isotones  $^{34}\text{Si}$  and  $^{36}\text{S}$  is stronger than the one reported for the  $N = 16$  isotones  $^{30}\text{Si}$  and  $^{32}\text{S}$  derived from Ref. [30]. As seen on Fig. 4 of Ref. [30], the measured charge density for  $^{30}\text{Si}$  does not present a significant dip at the interior of the nucleus and looks similar to that of  $^{32}\text{S}$ . This feature comes from the modest change in occupancy of the  $\pi 2s_{1/2}$  between  $^{32}\text{S}$  (1.35) and  $^{30}\text{Si}$  (0.65), which is ascribed to the large nuclear correlations existing in the  $N = 16$  isotones. These experimental occupation numbers are in excellent agreement with the presently calculated ones, reinforcing the reliability of the SM description to model the nuclei of interest.

The reduction of proton correlations between the  $N = 16$  and  $N = 20$  isotones can be ascribed to the increase of the  $Z = 14$  shell gap formed between the proton  $d_{5/2}$  and  $s_{1/2}$  orbitals. While growing in size, excitations across it are progressively hampered. This results in calculated occupancies of the  $\pi 2s_{1/2}$  orbit of 0.65 in  $^{30}\text{Si}_{16}$  and 0.09 in  $^{34}\text{Si}_{20}$ . The driving mechanism to increase the  $Z = 14$  gap is likely the strongly attractive  $\pi d_{5/2} - \nu d_{3/2}$  proton-neutron interaction. Adding four neutrons from  $N = 16$  to  $N = 20$  into the  $\nu d_{3/2}$  orbit strongly binds the  $\pi d_{5/2}$  orbit in  $^{34}\text{Si}$ , thus increasing the size of the  $Z = 14$  shell gap.

To conclude this section, using SM calculations we have determined occupation numbers of the proton and neutron  $2s_{1/2}$  shells in the ( $^{36}\text{S}$ ,  $^{34}\text{Si}$ ) and ( $^{24}\text{O}$ ,  $^{22}\text{O}$ ) nuclei, respectively. From these values, proton or neutron density distributions have been derived using Woods-Saxon wave functions. The large depletion of the  $2s_{1/2}$  orbit gives rise to a central

density depletion and the appearance of bubble phenomena. We stress the good agreement between experimental and calculated occupation numbers for the known nuclei  $^{36}\text{S}$ ,  $^{32}\text{S}$ , and  $^{30}\text{Si}$ . This gives us confidence in the results obtained for the other nuclei under study. Even though the present method to derive density distributions is approximate, a reasonable agreement is found with experimental results for  $^{36}\text{S}$ . The density profiles will be examined in the following section within a self-consistent microscopic treatment.

### III. MEAN-FIELD CALCULATIONS

Self-consistent mean-field approaches enable us to determine microscopically the density distributions of nuclei. We solve the self-consistent mean-field equations directly in coordinate space. As in the previous section, we consider neutron densities for  $^{22}\text{O}$  and proton densities for  $^{34}\text{Si}$ . These densities should be corrected for CM effects inherent to the mean-field procedure. Since we calculate the point proton and neutron densities directly in coordinate space, we can use the Campi and Sprung procedure (see Eqs. (3.1) and (3.2) of Ref. [31]) to obtain the CM-corrected charge density of  $^{34}\text{Si}$ , the finite proton size being treated by a Gaussian form factor as in Ref. [31]. The Fourier transform of the CM-corrected charge densities could eventually be compared with the form factors measured by electron scattering (not available so far), but accurate predictions for this kind of comparison are beyond the scope of this article. For this reason, we keep using the Gaussian finite-size form factor of Ref. [31] rather than adopting more sophisticated form factors. To obtain the radial profiles of the CM-corrected neutron densities in  $^{22}\text{O}$  we should transform to  $k$ -space the mean-field point neutron densities, correct them with the proper CM factor, and transform back to  $r$ -space. However, the strongly model dependent results that we have obtained for  $^{22}\text{O}$  with our mean-field treatments indicate that further refinements of the mean-field neutron densities will not help us to reach a conclusion on the issue of a possible neutron bubble in this nucleus.

For the calculation of nucleon occupation factors, pairing correlations have to be eventually taken into account. As a first step before describing the density distributions, we discuss whether pairing correlations are expected to play some role in the development of proton and neutron bubbles in  $^{34}\text{Si}$  and  $^{22}\text{O}$  nuclei, respectively.

#### A. Pairing effects

As already alluded to in Sec. I,  $^{22}\text{O}$  is expected to behave almost as a doubly-magic nucleus, being that the  $N = 14$  subshell closure has been experimentally determined. However, as shown in the previous section, SM calculations predict an 18% occupancy of the  $2s$  neutron state, suggesting that pairing correlations are likely to have some effect on this nucleus. Pairing correlations will be then included and their effect on the neutron density profile of  $^{22}\text{O}$  will be shown in the following for both the nonrelativistic and the relativistic mean-field cases.

Let us now consider the case of  $^{34}\text{Si}$ . As an illustration, we discuss the role of pairing in the nonrelativistic case. Pairing correlations can be modeled in the Skyrme-Hartree-Fock-Bogoliubov (Skyrme-HFB) framework by adopting the following zero-range density-dependent pairing interaction:

$$V_{\text{pair}} = V_0 \left[ 1 - \eta \left( \frac{\rho(r)}{\rho_0} \right)^\alpha \right] \delta(\mathbf{r}_1 - \mathbf{r}_2), \quad (2)$$

with  $\eta = 0.5$  (mixed surface-volume interaction),  $\alpha = 1$ , and  $\rho_0 = 0.16 \text{ fm}^{-3}$ . In the particle-hole channel, we employ the SLy4 Skyrme parametrization, which is well suited to describe neutron-rich nuclei. We fix the parameter  $V_0$  in Eq. (2) to reproduce the two-proton separation energy in  $^{34}\text{Si}$ . Note that the two-proton separation energy is defined as

$$S_{2p} = E(N, Z) - E(N, Z - 2), \quad (3)$$

where  $E(N, Z)$  is the total binding energy of the  $(N, Z)$  nucleus. It should be noted that the experimental value of  $S_{2p} = 33.74 \text{ MeV}$  is already reasonably well reproduced without pairing: The HF value is equal to 35.19 MeV. Moreover the HFB calculations—which include the pairing interaction—yield negligible corrections, as  $Z = 14$  is predicted by the HFB approach to be a robust subshell closure in agreement with the shell-model spectroscopic factors (see Table II where the SM occupation of the  $s$  state is only 4.5%). Our conclusion is that we can safely perform the analysis of this nucleus by neglecting pairing since the associated correlations are expected to be practically zero.

#### B. Nonrelativistic mean-field approach

Figure 3 displays neutron density profiles in  $^{22}\text{O}$  (full line) and  $^{24}\text{O}$  (dashed line) calculated self-consistently within the SLy4-HF approach. The depletion of the central density in  $^{22}\text{O}$  relative to  $^{24}\text{O}$  is clearly visible. However, the bubble profile is not obvious: Since the central neutron density in  $^{24}\text{O}$  is strongly enhanced, the depletion in  $^{22}\text{O}$  does not lead to the development of a significant central hole. The central depletion fraction  $F$  is  $\sim 13\%$ , much weaker than the SM result. As one switches on pairing and chooses the same parameters as in Ref. [32] for the pairing interaction, the central hole is seen to be partially washed out (dotted line in Fig. 3;  $F = 3.4\%$ ).

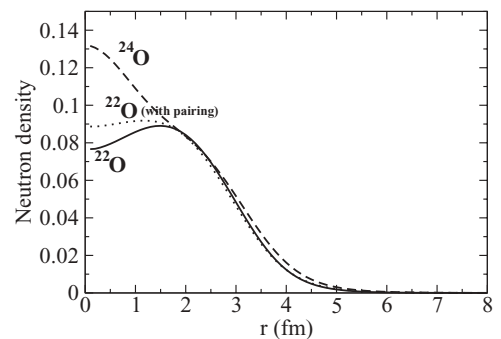


FIG. 3. HF neutron densities (in units of  $\text{fm}^{-3}$ ) of  $^{22}\text{O}$  (full line) and  $^{24}\text{O}$  (dashed line) calculated with the Skyrme interaction SLy4. The dotted line represents the SLy4-HFB neutron density of  $^{22}\text{O}$ .

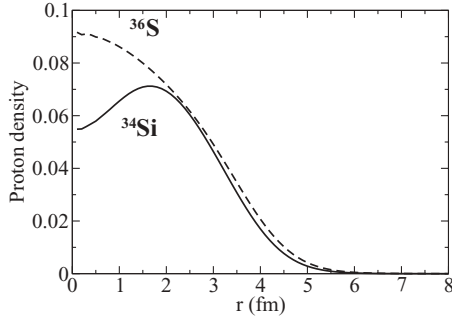


FIG. 4. HF charge densities (in units of  $\text{fm}^{-3}$ ) of  $^{36}\text{S}$  (dashed line) and  $^{34}\text{Si}$  (solid line) calculated with the Skyrme interaction SLy4.

Note that the density profile of  $^{24}\text{O}$  remains unchanged when pairing is switched on.

The SLy4-HF charge density profiles calculated in  $^{34}\text{Si}$  and  $^{36}\text{S}$  (where the  $s$  state is fully occupied) are shown in Fig. 4. One observes that the bubble is more prominent in this case than in  $^{22}\text{O}$ . The depletion fraction  $F$  is  $\sim 23\%$  ( $38\%$  for the proton density without CM and proton finite-size corrections). The confidence in this result is enhanced by the good agreement between the predicted density profile for  $^{36}\text{S}$  and the experimental one shown in Fig. 2. We should mention that pairing is expected to modify the density profile of  $^{36}\text{S}$ . By comparing the HF proton point density in  $^{34}\text{Si}$  ( $F = 38\%$ ) with the HF neutron density in  $^{22}\text{O}$  ( $F = 13\%$ ), one observes that the central value in  $^{34}\text{Si}$  is much lower than in  $^{22}\text{O}$ . The contribution to the central value of the density is entirely due to the first  $s$  wave function (i.e., the  $1s$ ). The difference between the two central values may be related to the presence of a neutron excess at the surface of  $^{34}\text{Si}$ . The effect of this neutron skin on the proton  $1s_{1/2}$  wave function is to attract and push it toward the surface, thereby lowering its value at the center. This effect is obviously absent for the neutron  $1s$  wave function in  $^{22}\text{O}$  because the proton density in this nucleus is well concentrated in the interior. This can be observed in Fig. 5 where the neutron (proton)  $1s$  contribution to the HF density is plotted for  $^{22}\text{O}$  ( $^{34}\text{Si}$ ).

### C. Relativistic mean-field approach

As in the previous section, calculations are performed for the two oxygen isotopes  $^{22}\text{O}$  and  $^{24}\text{O}$  as well as for the two  $N =$

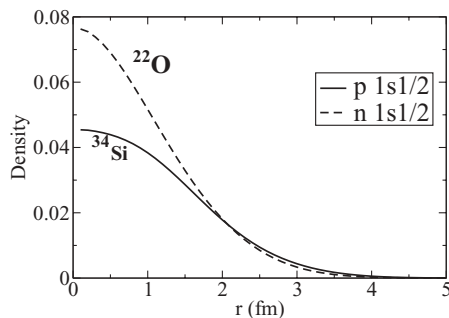


FIG. 5. Neutron (proton)  $1s$  contributions to the density (in units of  $\text{fm}^{-3}$ ) for  $^{22}\text{O}$  ( $^{34}\text{Si}$ ).

TABLE III. Binding energy per nucleon, charge radii, and neutron skin thickness for  $^{34}\text{Si}$  (upper block) and  $^{36}\text{S}$  (lower block) as predicted by the two RMF models used in this work. When available, experimental data are provided for comparison.

Model	$B/A$ (MeV)	$R_{\text{ch}}$ (fm)	$R_n - R_p$ (fm)
NL3	8.36	3.13	0.25
FSUGold	8.28	3.13	0.21
Experiment	8.34	—	—
NL3	8.50	3.26	0.12
FSUGold	8.42	3.26	0.09
Experiment	8.58	3.28	—

20 isotones  $^{34}\text{Si}$  and  $^{36}\text{S}$ , but now using an RMF approach. Pairing effects are evaluated within the RHB model. In one particular realization of the relativistic formalism the dynamics of the system is dictated by an interacting Lagrangian density of the following form:

$$\begin{aligned} \mathcal{L}_{\text{int}} = & \bar{\psi} \left[ g_s \phi - \left( g_v V_\mu + \frac{g_\rho}{2} \tau \cdot \mathbf{b}_\mu + \frac{e}{2} (1 + \tau_3) A_\mu \right) \gamma^\mu \right] \psi \\ & - \frac{\kappa}{3!} (g_s \phi)^3 - \frac{\lambda}{4!} (g_s \phi)^4 + \frac{\zeta}{4!} (g_v^2 V_\mu V^\mu)^2 \\ & + \Lambda_v (g_\rho^2 \mathbf{b}_\mu \cdot \mathbf{b}^\mu) (g_v^2 V_\mu V^\mu), \end{aligned} \quad (4)$$

where  $\psi$  represents an isodoublet nucleon field interacting via the exchange of two isoscalar mesons—a scalar ( $\phi$ ) and a vector ( $V^\mu$ ), one isovector meson ( $b^\mu$ ), and the photon ( $A^\mu$ ) [33,34]. In addition to meson-nucleon interactions, the Lagrangian density is supplemented by nonlinear meson interactions with coupling constants denoted by  $\kappa$ ,  $\lambda$ ,  $\zeta$ , and  $\Lambda_v$  that are responsible for a softening of the nuclear-matter equation of state, both for symmetric and pure-neutron matter. For the RMF case we consider two parametrizations: the very successful NL3 parameter set [35,36] and a more recent set known as FSUGold [37]. The main difference between these two models lies in the prediction of the density dependence of the symmetry energy. This difference manifests itself in significantly larger neutron skins for NL3 than for FSUGold [37]. Neutron skins for the two isotones of interest in the present work, alongside other ground-state properties, have been listed in Table III for  $^{34}\text{Si}$  and  $^{36}\text{S}$ .

RMF neutron densities for the two neutron-rich isotopes  $^{22}\text{O}$  and  $^{24}\text{O}$  are displayed in Fig. 6. Whereas the RMF results show a mild model dependence, differences between the relativistic and nonrelativistic models are significant. Indeed, in contrast to the nonrelativistic case, the relativistic results display no enhancement of the central neutron density in  $^{24}\text{O}$ . Moreover, the removal of both  $2s_{1/2}$  neutrons from  $^{24}\text{O}$  yields a strong depletion of the interior neutron density in  $^{22}\text{O}$ . As a result, central depletion fractions of  $F = 34\%$   $F = 28\%$  are predicted for  $^{22}\text{O}$  by the FSUGold and NL3 models, respectively. These values are significantly larger than the  $13\%$  depletion fraction obtained with the SLy4-HF parametrization.

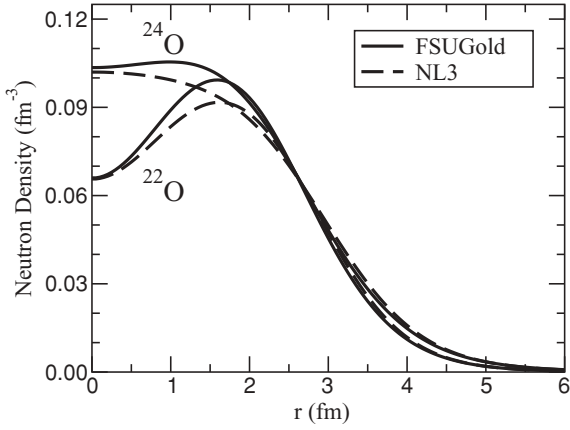


FIG. 6. RMF neutron densities of  $^{22}\text{O}$  and  $^{24}\text{O}$  calculated with the two RMF models described in the text.

In the case of  $^{34}\text{Si}$  and  $^{36}\text{S}$  one observes, now in agreement with the nonrelativistic results, how the charge density of  $^{34}\text{Si}$  is significantly depleted in the nuclear interior and how the proton bubble disappears as soon as the  $2s_{1/2}$  proton orbital is filled in  $^{36}\text{S}$  (see Fig. 7). This behavior results in central depletion factors for  $^{34}\text{Si}$  of  $F = 29\%$  and  $F = 25\%$  for the FSUGold and NL3 parameter sets, respectively. For the proton densities of  $^{34}\text{Si}$  the values of  $F$  are  $42\%$  and  $37\%$  for FSUGold and NL3, respectively.

Let us quantify now the effects of pairing correlations within the RHB model. A medium dependence for a relativistic mean-field interaction can either be introduced by including nonlinear meson self-interaction terms in the Lagrangian, as in the case of NL3 and FSUGold, or by assuming an explicit density dependence for the meson-nucleon couplings. This is the case of the DD-ME2 model [38] that we adopt to perform RHB calculations. The couplings of the  $\sigma$  meson and  $\omega$  meson to the nucleon are assumed to be of the form

$$g_i(\rho) = g_i(\rho_{\text{sat}}) f_i(x) \quad \text{for } i = \sigma, \omega, \quad (5)$$

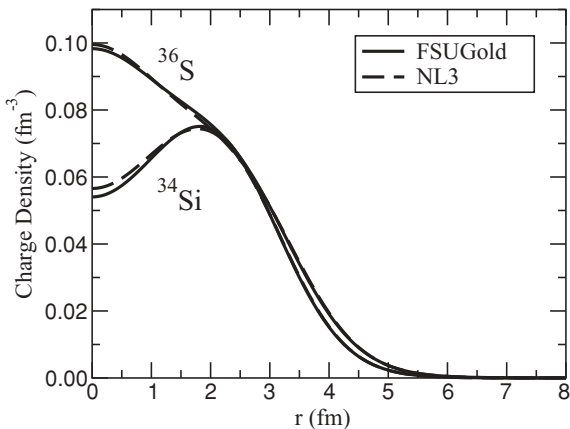


FIG. 7. RMF charge densities of  $^{36}\text{S}$  and  $^{34}\text{Si}$  calculated with the two RMF models described in the text.

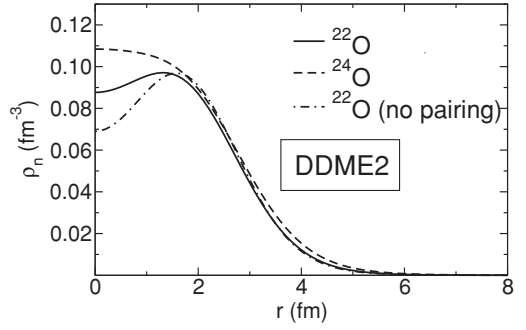


FIG. 8. Neutron density profiles of  $^{22}\text{O}$  and  $^{24}\text{O}$  calculated in the RHB model with the density-dependent interaction DD-ME2 and Gogny pairing.

where

$$f_i(x) = a_i \frac{1 + b_i(x + d_i)^2}{1 + c_i(x + d_i)^2} \quad (6)$$

is a function of  $x = \rho/\rho_{\text{sat}}$ , and  $\rho_{\text{sat}}$  denotes the nucleon density at saturation in symmetric nuclear matter. Constraints at nuclear matter saturation density and at zero density are used to reduce the number of independent parameters in Eq. (6) to three. Three additional parameters in the isoscalar channel are  $g_\sigma(\rho_{\text{sat}})$ ,  $g_\omega(\rho_{\text{sat}})$ , and  $m_\sigma$ —the mass of the phenomenological  $\sigma$  meson. For the  $\rho$  meson coupling the functional form of the density dependence is suggested by Dirac-Brueckner calculations of asymmetric nuclear matter:

$$g_\rho(\rho) = g_\rho(\rho_{\text{sat}}) \exp[-a_\rho(x - 1)], \quad (7)$$

and the isovector channel is parametrized by  $g_\rho(\rho_{\text{sat}})$  and  $a_\rho$ . Bare values are used for the masses of the  $\omega$  and  $\rho$  mesons:  $m_\omega = 783$  MeV and  $m_\rho = 763$  MeV. DD-ME2 is determined by eight independent parameters, adjusted to the properties of symmetric and asymmetric nuclear matter, binding energies, charge radii, and neutron radii of spherical nuclei [38]. The interaction has been tested in the calculation of ground-state properties of a large set of spherical and deformed nuclei. When used in the relativistic RPA, DD-ME2 reproduces with high accuracy data on isoscalar and isovector collective excitations [38].

In Figs. 8 and 9 we display, respectively, the neutron and charge density profiles for  $^{22,24}\text{O}$  ( $^{34}\text{Si}$  and  $^{36}\text{S}$ ) calculated in

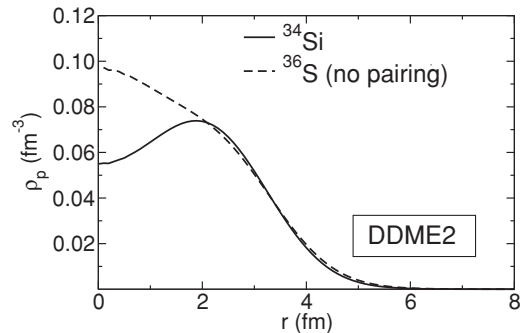


FIG. 9. Charge densities of  $^{36}\text{S}$  and  $^{34}\text{Si}$  calculated in the RHB model with the DD-ME2 interaction plus Gogny D1S pairing. The charge density of  $^{36}\text{S}$  has been calculated by neglecting pairing.

TABLE IV. Central fraction of depletion  $F$  for neutron densities in  $^{22}\text{O}$  (first line) and proton and charge densities in  $^{34}\text{Si}$  (second and third lines, respectively).

Nucleus	SM	SLy4 HF	SLy4 HFB	NL3 RMF	FSUGold RMF	DDME2 RMF	DDME2 RHB
$^{22}\text{O}$	24%	13%	3.4%	28%	34%	29%	10%
$^{34}\text{Si}$	41%	38%	38%	37%	42%	36%	36%
$^{34}\text{Si}$ (ch.)	28%	23%	23%	25%	29%	25%	25%

the RHB model [39] with the DD-ME2 effective interaction in the particle-hole channel, and with the Gogny interaction [40] in the pairing channel,

$$V^{pp}(1, 2) = \sum_{i=1,2} e^{-[(r_1-r_2)/\mu_i]^2} \times (W_i + B_i P^\sigma - H_i P^\tau - M_i P^\sigma P^\tau), \quad (8)$$

with the set D1S [41] for the parameters  $\mu_i$ ,  $W_i$ ,  $B_i$ ,  $H_i$ , and  $M_i$  ( $i = 1, 2$ ).

For  $^{24}\text{O}$  and  $^{34}\text{Si}$  the RHB calculation with the DD-ME2 interaction predicts neutron and charge density profiles similar to those calculated with NL3 and FSUGold. Because of the large gaps between  $\nu s_{1/2}$  and  $\nu d_{3/2}$  in  $^{24}\text{O}$ , and between  $\pi d_{5/2}$  and  $\pi s_{1/2}$  in  $^{34}\text{Si}$ , we find a pairing collapse in these nuclei, in agreement with nonrelativistic predictions. However, the inclusion of pairing correlations has a pronounced effect on the neutron density profile in  $^{22}\text{O}$ . When pairing is set to zero (dash-dot curve in Fig. 8) the  $\nu s_{1/2}$  orbital is empty in  $^{22}\text{O}$ . The resulting DD-ME2 density profile is again very similar to that calculated with the two other RMF interactions. However, the pairing interaction in the RHB model calculation modifies the occupancy of the two  $2s_{1/2}$  orbitals, thus reducing the pronounced bubble in the neutron density of  $^{22}\text{O}$ . For an easier and coherent comparison between Figs. 4 and 9, the charge density of  $^{36}\text{S}$  shown in Fig. 9 has been calculated by neglecting pairing.

In the DD-ME2 model the  $F$  values are found equal to 29%, 10%, and 25% for  $^{22}\text{O}$  (without pairing),  $^{22}\text{O}$  (with pairing), and charge density of  $^{34}\text{Si}$  (giving the same result with and without pairing), respectively. For the proton density of  $^{34}\text{Si}$   $F = 36\%$ .

#### IV. SUMMARY AND CONCLUSIONS

The occurrence of proton and neutron bubbles in  $^{34}\text{Si}$  and  $^{22}\text{O}$ , respectively, has been investigated using three different theoretical approaches: (i) the shell model, (ii) the Skyrme mean-field model, and (iii) the relativistic mean-field model. This occurrence can be quantified by the values of the depletion fraction  $F$ , which we have evaluated in these different approaches and which are summarized in Table IV.

For the  $^{22}\text{O}$  nucleus the CM correction has been performed only in the SM framework. The strongly model dependent results that we have obtained for this nucleus with our

mean-field treatments indicate that further refinements of the mean-field neutron densities will not help us to reach a conclusion on the issue of a possible neutron bubble. To compare in a coherent way all the values of  $F$  for  $^{22}\text{O}$  in Table IV, the SM values without CM correction have been used. Indeed, a very significant model dependence has been found for this nucleus. Moreover, in both nonrelativistic and relativistic cases, pairing correlations have been shown to weaken the bubble phenomenon. It would be worth having experimental confirmation of this prediction. In contrast, for  $^{34}\text{Si}$  an overall agreement exists: A central depletion fraction of  $\sim 40\%$  is predicted by all the models for the proton densities. In the last line of Table IV, the values of  $F$  for the charge density are shown ( $F \sim 25\%–30\%$ ).

The strong model dependence for  $^{22}\text{O}$  and the overall agreement for  $^{34}\text{Si}$  are easy to explain. For both nuclei the single-particle spectra are sensibly model dependent. However, the gap  $N = 14$  is predicted by all the models to be much smaller than the gap  $Z = 14$ . The very large gap  $Z = 14$  prevents pairing and other correlations from being active in  $^{34}\text{Si}$ , providing thus density profiles that are not sensible to the differences of the models. In contrast, for  $^{22}\text{O}$ , pairing plays some role and, consequently, the density profiles show a dependence on the model (based on single-particle spectra and intensity of pairing interaction). This reinforces the conclusion that  $^{34}\text{Si}$  is indeed a good candidate for a bubble density profile. The measurement of the charge density in  $^{34}\text{Si}$  could be undertaken, for instance, by electron scattering in an exotic beam collider, such as EXL in FAIR and RIBF in Riken. The bubble impact on the momentum distribution in these experiment has been investigated in Ref. [8]. The fraction  $F$  for the charge densities is equal to  $\sim 25\%–30\%$ . The effect is reduced with respect to what is found for the proton densities, but it is still important and could be observed experimentally. The study of  $^{34}\text{Si}$ , either by high-energy proton scattering (to focus on the matter distribution) or by direct reactions (to determine whether the occupancy of the  $2s_{1/2}$  proton orbit has dropped to nearly zero, thus confirming the SM predictions shown in Sec. II.), is already feasible [8].

#### ACKNOWLEDGMENTS

The authors thank J. F. Berger, A. E. L. Dieperink, F. Nowacki, A. Poves, and K. Yoshida for valuable discussions. The research of J.P. is supported in part by the United States DOE Grant No. DE-FD05-92ER40750.

- [1] H. A. Wilson, Phys. Rev. **69**, 538 (1946).
- [2] X. Campi and D. W. L. Sprung, Phys. Lett. **B46**, 291 (1973).
- [3] M. Bender, K. Rutz, P.-G. Reinhard, J. A. Maruhn, and W. Greiner, Phys. Rev. C **60**, 034304 (1999).
- [4] J. Dechargé, J.-F. Berger, M. Girod, and K. Dietrich, Nucl. Phys. **A716**, 55 (2003).
- [5] J. M. Cavedon *et al.*, Phys. Rev. Lett. **49**, 978 (1982).
- [6] V. R. Pandharipande, I. Sick, and P. K. A. deWitt Huberts, Rev. Mod. Phys. **69**, 981 (1997).
- [7] B. G. Todd-Rutel, J. Piekarewicz, and P. D. Cottle, Phys. Rev. C **69**, 021301(R) (2004).
- [8] E. Khan, M. Grasso, J. Margueron, and N. Van Giai, Nucl. Phys. **A800**, 37 (2008).
- [9] L. Gaudefroy *et al.*, Phys. Rev. Lett. **99**, 099202 (2007).
- [10] A. Gade *et al.*, Phys. Rev. C **74**, 034322 (2006).
- [11] M. Grasso, Z. Y. Ma, E. Khan, J. Margueron, and N. Van Giai, Phys. Rev. C **76**, 044319 (2007).
- [12] O. Sorlin and M. G. Porquet, Prog. Part. Nucl. Phys. **61**, 602 (2008).
- [13] K. Yoshida (private communication).
- [14] S. Hilaire and M. Girod, [http://www-phynu.cea.fr/science\\_en\\_ligne/carte\\_potentiels\\_microscopiques/carte\\_potentiel\\_nucleaire.htm](http://www-phynu.cea.fr/science_en_ligne/carte_potentiels_microscopiques/carte_potentiel_nucleaire.htm) (2006).
- [15] S. Raman, C. W. Nestor Jr., and P. Tikkanen, At. Data Nucl. Data Tables **78**, 1 (2001).
- [16] B. Bastin *et al.*, Phys. Rev. Lett. **99**, 022503 (2007).
- [17] M. Stanoiu *et al.*, Phys. Rev. C **69**, 034312 (2004).
- [18] A. Schiller *et al.*, Phys. Rev. Lett. **99**, 112501 (2007).
- [19] Z. Elekes *et al.*, Phys. Rev. Lett. **98**, 102502 (2007).
- [20] P. G. Thirolf *et al.*, Phys. Lett. **B485**, 16 (2000).
- [21] E. Becheva *et al.*, Phys. Rev. Lett. **96**, 012501 (2006).
- [22] C. R. Hoffman *et al.*, Phys. Rev. Lett. **100**, 152502 (2008).
- [23] E. Caurier, ANTOINE code, IReS, Strasbourg, 1989–2002.
- [24] E. Caurier and F. Nowacki, Acta Phys. Pol. B **30**, 705 (1999).
- [25] B. A. Brown and B. H. Wildenthal, Annu. Rev. Nucl. Part. Sci. **38**, 29 (1988).
- [26] A. E. L. Dieperink and T. de Forest Jr., Phys. Rev. C **10**, 543 (1974).
- [27] A. Bohr and B. R. Mottelson, *Nuclear Structure* (Benjamin, New York, 1975), Vol. I.
- [28] S. Khan *et al.*, Phys. Lett. **B156**, 155 (1985).
- [29] D. Rychel *et al.*, Phys. Lett. **B130**, 5 (1983).
- [30] J. Wesseling *et al.*, Phys. Rev. C **55**, 2773 (1997).
- [31] X. Campi and D. W. L. Sprung, Nucl. Phys. **A194**, 401 (1972).
- [32] E. Khan, N. Sandulescu, M. Grasso, and N. Van Giai, Phys. Rev. C **66**, 024309 (2002).
- [33] B. D. Serot and J. D. Walecka, Adv. Nucl. Phys. **16**, 1 (1986).
- [34] B. D. Serot and J. D. Walecka, Int. J. Mod. Phys. E **6**, 515 (1997).
- [35] G. A. Lalazissis, J. König, and P. Ring, Phys. Rev. C **55**, 540 (1997).
- [36] G. A. Lalazissis, S. Raman, and P. Ring, At. Data Nucl. Data Tables **71**, 1 (1999).
- [37] B. G. Todd-Rutel and J. Piekarewicz, Phys. Rev. Lett. **95**, 122501 (2005).
- [38] G. A. Lalazissis, T. Nikšić, D. Vretenar, and P. Ring, Phys. Rev. C **71**, 024312 (2005).
- [39] D. Vretenar, A. V. Afanasjev, G. A. Lalazissis, and P. Ring, Phys. Rep. **409**, 101 (2005).
- [40] J. F. Berger, M. Girod, and D. Gogny, Nucl. Phys. **A428**, 23 (1984).
- [41] J. F. Berger, M. Girod, and D. Gogny, Comput. Phys. Commun. **63**, 365 (1991).

**$N = 14$  Shell Closure in  $^{22}\text{O}$  Viewed through a Neutron Sensitive Probe**

E. Becheva,<sup>1</sup> Y. Blumenfeld,<sup>1</sup> E. Khan,<sup>1</sup> D. Beaumel,<sup>1</sup> J. M. Daugas,<sup>2</sup> F. Delaunay,<sup>1</sup> Ch-E. Demonchy,<sup>3</sup> A. Drouart,<sup>4</sup> M. Fallot,<sup>1</sup> A. Gillibert,<sup>4</sup> L. Giot,<sup>3</sup> M. Grasso,<sup>1,5</sup> N. Keeley,<sup>4</sup> K. W. Kemper,<sup>6</sup> D. T. Khoa,<sup>7</sup> V. Lapoux,<sup>4</sup> V. Lima,<sup>1</sup> A. Musumarra,<sup>5</sup> L. Nalpas,<sup>4</sup> E. C. Pollacco,<sup>4</sup> O. Roig,<sup>2</sup> P. Roussel-Chomaz,<sup>3</sup> J. E. Sauvestre,<sup>2</sup> J. A. Scarpaci,<sup>1</sup> F. Skaza,<sup>4</sup> and H. S. Than<sup>7</sup>

<sup>1</sup>*Institut de Physique Nucléaire, IN2P3-CNRS, 91406 Orsay, France*

<sup>2</sup>*DPTA/SPN-CEA Bruyères, 91680 Bruyères-le-Château Cedex 12, France*

<sup>3</sup>*GANIL (CEA/DSM-CNRS/IN2P3), B.P. 5027, 14076 Caen Cedex, France*

<sup>4</sup>*SPhN, DAPNIA, CEA Saclay, 91191 Gif sur Yvette Cedex, France*

<sup>5</sup>*INFN-Laboratorio Nazionale del Sud, Via S. Sofia 44, Catania, Italy*

<sup>6</sup>*Department of Physics, Florida State University, Tallahassee, Florida 32306, USA*

<sup>7</sup>*Institute for Nuclear Science and Technique, VAEC, P.O. Box 5T-160, Nghia Do, Hanoi, Vietnam*

(Received 28 April 2005; published 4 January 2006)

To investigate the behavior of the  $N = 14$  neutron gap far from stability with a neutron-sensitive probe, proton elastic and  $2_1^+$  inelastic scattering angular distributions for the neutron-rich nucleus  $^{22}\text{O}$  were measured using the MUR à STrip detector array at the Grand Accélérateur National d'Ions Lourds facility. A deformation parameter  $\beta_{p,p'} = 0.26 \pm 0.04$  is obtained for the  $2_1^+$  state, much lower than in  $^{20}\text{O}$ , showing a weak neutron contribution to this state. A microscopic analysis was performed using matter and transition densities generated by continuum Skyrme-Hartree-Fock-Bogoliubov and quasiparticle random phase approximation calculations, respectively. The ratio of neutron to proton contributions to the  $2_1^+$  state is found close to the  $N/Z$  ratio, demonstrating a strong  $N = 14$  shell closure in the vicinity of the neutron drip line.

DOI: [10.1103/PhysRevLett.96.012501](https://doi.org/10.1103/PhysRevLett.96.012501)

PACS numbers: 21.10.Re, 25.40.Cm, 25.40.Ep, 27.30.+t

Shell structure is a distinctive feature of many-body fermionic systems, such as metallic clusters, atoms, and nuclei [1–3]. Such structure is characterized by the existence of magic numbers. Nuclei are composed of two types of interacting fermions, giving rise to a specific degree of freedom, isospin. Therefore, there are magic numbers for both neutrons and protons, which are, in principle, the same if charge independence holds. An important question, specific to nuclear physics, is the robustness of the shell closures as a function of neutron to proton asymmetry: An eventual modification of magic numbers far from stability could have major implications on our understanding of nucleosynthesis through the  $r$  and  $rp$  processes, as nuclear structure is an important input to the models of explosive astrophysical scenarios [4]. Theoretical predictions for the disappearance of well-known magic numbers and the appearance of new shell gaps far from stability have recently been given [5,6]. With the advent of radioactive beams during the past decade, experimental indications of such a behavior have emerged (see, e.g., [7]) for neutron magic numbers. However, the neutron gap is usually measured with an exclusively proton sensitive probe, such as Coulomb excitation. Only indirect information on the neutron gap evolution is obtained, through the neutron-proton interaction. Complementary probes are, therefore, necessary to investigate the neutron behavior. The purpose of this Letter is to give, for the first time, experimental evidence for a new neutron magic number using a probe mainly sensitive to neutrons.

In this context, one of the most studied areas is the neutron-rich part of the oxygen isotopic chain which has a well-established proton magic number  $Z = 8$ : Many experimental [8–11] and theoretical [5,12–14] efforts have been devoted to the  $^{18-24}\text{O}$  isotopes, showing possible  $N = 14$  and  $N = 16$  shell closures, which would make both  $^{22}\text{O}$  and  $^{24}\text{O}$  doubly magic nuclei. The energy of the first  $2_1^+$  state of  $^{22}\text{O}$  has been measured at 3199(8) keV [9], compared to 1670 keV in  $^{20}\text{O}$ , and its small  $B(E2)$  value of  $21(8)e^2 \cdot \text{fm}^4$  [10] indicates a strengthening of the  $N = 14$  shell gap. Even though the  $2_1^+$  state of  $^{24}\text{O}$  has not been directly observed, its energy has been shown to lie above 3.8 MeV, indicating an  $N = 16$  shell closure [11]. Conversely,  $^{28}\text{O}$ , which is doubly magic in the standard shell model, was found to be unbound [15], contrary to most theoretical predictions. Theoretically, both quasiparticle random-phase approximation (QRPA) [8] and shell model [16] calculations predict a decrease of  $B(E2)$  from  $^{20}\text{O}$  to  $^{22}\text{O}$ . Moreover, shell model calculations [6] show a strong gap of 4.3 MeV between the  $1d_{5/2}$  and  $2s_{1/2}$  subshells, making  $^{22}\text{O}$  a magic nucleus.

However, all above mentioned experimental indications of the  $N = 14$  magicity in  $^{22}\text{O}$  are partial, since they do not probe separately the proton and the neutron contribution to the  $2_1^+$  excitation. In Ref. [10], the  $B(E2)$  value is obtained from inelastic scattering of  $^{22}\text{O}$  from  $^{197}\text{Au}$  at an energy of 50 MeV/nucleon. The deduced  $B(E2)$  value provides the proton transition matrix element  $M_p$ , but, since both Coulomb and nuclear interactions were important in the

reaction, the authors had to rely on theoretical predictions to isolate the neutron and proton contributions to the excitation. In other words, in the absence of data from a second experimental probe, the  $B(E2)$  value is model-dependent. Moreover, it is somewhat delicate to interpret the neutron gap behavior using the  $B(E2)$  values, which depend only on the proton contribution to the excitation: As stated above, the neutron gap is probed through the neutron-proton interaction, the knowledge of which is subject to debate close to the neutron drip line [5,17].

The neutron and proton transition matrix elements  $M_{n,p} = \langle 2^+ | r^2 Y_{20} | 0^+ \rangle$  of a quadrupole operator are obtained by integrating the corresponding transition densities  $\delta\rho_{n,p}(r)$  over  $r$ . In this case, the proton transition matrix element  $M_p$  is related to the reduced transition probability by  $B(E2) = M_p^2$ .  $B(E2)$  must be measured through an electromagnetic experiment. To disentangle the proton ( $M_p$ ) and the neutron ( $M_n$ ) transition matrix elements of the  $2_1^+$  excitation in  $^{22}\text{O}$ , we make use of a  $(p, p')$  scattering experiment on  $^{22}\text{O}$ . This second experimental probe, complementary to the  $^{197}\text{Au}$  target, should allow us to deduce a model-independent value of  $B(E2)$  and to evaluate the neutron contribution to the excitation. The combined data probe more directly the possible  $N = 14$  shell closure.

Protons at a few tens of MeV are known to interact 3 times more strongly with neutrons than with protons in the nucleus [18], whereas Coulomb excitation or lifetime measurements probe directly only the proton density distributions. The combination of the two types of measurements can, therefore, disentangle proton and neutron contributions to excited states. With the development of radioactive beams, proton scattering data can now be obtained for unstable nuclei. Elastic and inelastic proton scattering experiments on  $^{20}\text{O}$  were recently performed [8,19], indicating a large isovector component in the excitation of the  $2_1^+$  state, which is driven by the excitation of neutrons. This behavior is characteristic for a single closed-shell nucleus with, in this case, a partially filled  $1d_{5/2}$  subshell.

Direct reactions on short-lived unstable nuclei must be performed in inverse kinematics, where a secondary beam of the radioactive nucleus of interest bombards a target containing the light particles [20]. Here the secondary beam was produced by fragmentation of a

77 MeV/nucleon  $^{36}\text{S}$  primary beam delivered by the Accélérateur National d'Ions Lourds (GANIL) facility with a power of 1.5 kW on a  $540 \text{ mg/cm}^2$   $^{12}\text{C}$  target located between the solenoids of the superconducting intense source for secondary ions device. The secondary beam was selected and purified using the beam analysis spectrometer, equipped with a  $150 \text{ mg/cm}^2$  Al achromatic degrader, as a fragment separator. The average intensity on target of the  $46.6 \text{ MeV/nucleon}$   $^{22}\text{O}$  beam was only 1200 pps with a large contamination of  $^{25}\text{Na}$  and  $^{23}\text{F}$ , which made up 88% of the beam. The incident nuclei were tracked event-by-event using two low pressure multi-wire proportional chambers (CATS) [21]. The reconstructed position resolution on the target was approximately 1 mm. The secondary beam impinged on a  $5 \text{ mg/cm}^2$  polypropylene  $(\text{CH}_2)_n$  target. In order to select the elastic and inelastic reaction channels, the scattered heavy nuclei were identified in the focal plane of the Spectromètre à Perte d'Énergie du GANIL (SPEG) spectrometer [22]. To gain access to the excitation energy and the scattering angle characterizing the reaction, the energy and angle of the recoiling protons were measured using the MUR à STrip (MUST) array [23], consisting of eight silicon-strip detectors, backed by Si(Li) diodes and CsI crystals. Protons were unambiguously identified through a combination of energy, energy-loss, and time-of-flight measurements. The coincidence between the SPEG plastic detector and the MUST array effectively reduced the background from the carbon component of the target.

Figure 1(a) shows the scatter plot of the proton laboratory angle vs energy for  $^{22}\text{O}$ , where kinematic lines corresponding to the ground and  $2_1^+$  states are very well separated. Figure 1(b) displays the resulting excitation energy spectrum, where the  $2_1^+$  state is clearly visible at the energy of  $3.2 \pm 0.2 \text{ MeV}$ . No indication for higher lying states is observed. The angular distributions could be obtained directly by selecting the corresponding events in energy. The background is very low, as is shown by the absence of significant background to the left of the elastic peak. The absolute normalization was deduced from the number of incident nuclei measured with the CATS detectors and the target thickness. The error on the normalization is estimated to be 10% including the background effect. Figure 2 displays the measured elastic and  $2_1^+$  angular distributions. The error bars are purely statistical.

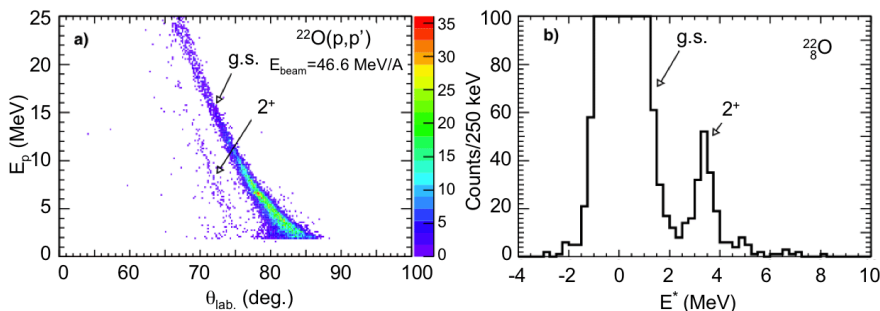


FIG. 1 (color online). (a) Scatter plot of recoiling proton energy versus scattering angle in the laboratory frame for the  $^{22}\text{O}$  beam. (b)  $^{22}\text{O}$  excitation energy spectrum deduced from the proton kinematics.

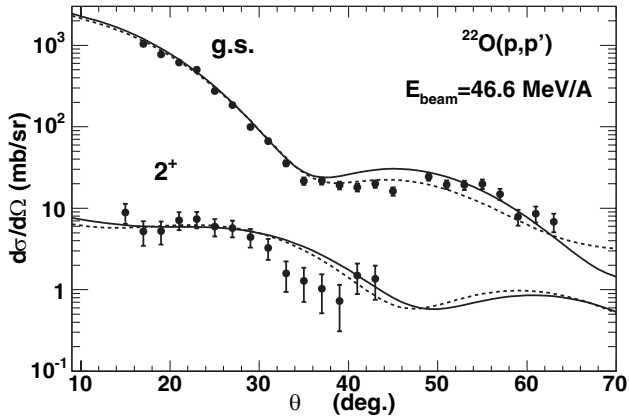


FIG. 2. Elastic and  $2_1^+$  inelastic angular distributions of  $^{22}\text{O}$  at 46.6 A MeV (dots). DWBA using the phenomenological KD global optical potential (solid lines) and folding model (dashed lines) calculations are shown (see text).

A first approach to understand the results is the so-called phenomenological analysis, which makes use of optical potential systematics. The most recent nucleon-nucleus global potential is the parametrization elaborated by Koning and Delaroche (KD) [24] for  $24 \leq A \leq 209$  nuclei with reaction energies ranging from 2 keV to 200 MeV. We have also performed the analysis using the more familiar Becchetti-Greenlees [25] and CH89 [26] potentials, which yield the same conclusions. Coupled channel calculations using standard vibrational form factors were performed with the ECIS97 [27] code to obtain inelastic cross sections. The normalization of the inelastic angular distribution to the data leads to the value of the  $(p, p')$  deformation parameter  $\beta_{(p,p')}$ .

The calculated elastic and inelastic angular distributions are displayed in Fig. 2. An overall good agreement with the data is observed. The extracted deformation parameter is  $\beta_{(p,p')} = 0.26 \pm 0.04$ . We have chosen to normalize on the forward data up to  $30^\circ$ . Normalizing to the entire angular distribution reduces the  $\beta$  value by less than 0.01. The error bars correspond to the minimum and maximum  $\beta_{(p,p')}$  values which allow the measured angular distributions to be reproduced within the error bars. The  $\beta_{(p,p')}$  value of  $^{22}\text{O}$  is much smaller than the one measured for  $^{20}\text{O}$  ( $\beta_{(p,p')} = 0.55 \pm 0.06$ ) and also smaller than for  $^{18}\text{O}$  ( $\beta_{(p,p')} = 0.37 \pm 0.03$ ) [8]. Since proton scattering is much more sensitive to neutron than to proton excitation, this result clearly indicates a weak neutron contribution to the  $2_1^+$  excitation in  $^{22}\text{O}$ , compared to less neutron-rich isotopes.

Such a simple analysis is valuable for comparison purposes between isotopes, but a more detailed understanding of proton scattering calls for a fully microscopic analysis, totally independent of the phenomenological approach. In the microscopic study performed here, neutron and proton ground state densities are calculated using Skyrme Hartree-Fock-Bogoliubov (HFB) in coordinate space,

with the very recently developed exact quasiparticle continuum treatment, the inclusion of which is expected to be important for weakly bound nuclei [28]. The HFB equations are solved in coordinate space assuming spherical symmetry. In the present continuum-HFB calculations, the mean field quantities are evaluated using the Skyrme interaction SLy4 [29], while for the pairing interaction we take a zero-range density-dependent force [12].

To describe nuclear transitions, continuum-QRPA calculations are performed using the HFB single quasiparticle spectra. QRPA equations are derived in coordinate space using the linear response theory. For the first time, the residual interaction is taken from the second derivative of the HFB energy functional with respect to the matter and pairing densities, together with exact continuum treatment (see [12]).

A measurement of the cross section of the first  $2_1^+$  state of  $^{22}\text{O}$  was obtained by Thirof *et al.* [10] using inelastic scattering from  $^{197}\text{Au}$  at 50 MeV/nucleon. However, due to the range of scattering angles covered, both Coulomb and nuclear components are involved in the excitation. We have reanalyzed the data of the  $^{22}\text{O} + ^{197}\text{Au}$  reaction using the same optical potentials as in Ref. [10]. We found that, for a given  $B(E2)$  value, the calculated excitation cross sections vary very little with respect to the nuclear deformation parameter  $\beta_N$ . Destructive interference between nuclear and Coulomb amplitudes implies that, when the rather large error bar on the cross section [10] is taken into account, the  $B(E2)$  value extracted is not sensitive to the nuclear contribution as long as  $\beta_N$  is less than 0.4. The experimental  $B(E2)$  from this study is equal to  $21 \pm 8e^2 \cdot \text{fm}^4$ . The calculated  $B(E2)$  value from QRPA is  $22e^2 \cdot \text{fm}^4$ , which agrees well with the measured value, showing that the magnitude of the proton transition density is faithfully reproduced by the theory.

In order to directly compare the model with the proton scattering data, microscopic optical potentials are generated from the HFB and QRPA densities using two different methods: the folding model [30] and a microscopic optical model potential (OMP) parametrization using the Jeukenne, Lejeune, and Mahaux (JLM) interaction [31]. The folding model analysis uses the CDM3Y6 interaction folded with the HFB densities to generate the isoscalar and isovector parts of the OMP. The spin-orbit potential as well as the transition potentials are obtained from the folding of the QRPA transition densities with the nucleon-nucleon interaction. The imaginary part of the OMP is generated with the Koning and Delaroche [24] phenomenological parametrization, already used in our phenomenological analysis above. Cross sections are calculated using distorted-waves Born approximation (DWBA) with the ECIS97 [27] code.

The  $^{22}\text{O}(p, p')$  angular distributions are displayed in Fig. 2. The elastic angular distribution is well described, even at large angles. Since the  $B(E2)$  is well reproduced by the proton transition density, we renormalize the neutron

transition density in order to fit the data. This procedure assumes that QRPA reliably describes the shape of the transition density for collective states [32]. It provides an experimental value of the  $M_n/M_p$  ratio for the  $2_1^+$  state, deduced from the combination of the electromagnetic and the  $(p, p')$  measurements [8]. We obtain  $M_n/M_p = 2.5 \pm 1.0$ , or  $(M_n/M_p)/(N/Z) = 1.4 \pm 0.5$ . This is to be compared to the value for  $^{20}\text{O}$ ,  $(M_n/M_p)/(N/Z) = 2.2 \pm 0.5$ , significantly different from 1 [8]. Incidentally, in the case of  $^{22}\text{O}$ , the error coming from the heavy ion measurement is greater than from our experiment.

In order to check the dependence on the potential used, complex optical and transition potentials were also obtained by injecting the calculated ground state and transition densities into the JLM density-dependent optical potential [31], which was derived from Brückner-Hartree-Fock nuclear matter calculations. Cross sections were then calculated in a DWBA approach with the TAMURA code [33]. We have tested that coupling to  $(p, d)$  pickup, which can have a significant effect on  $(p, p')$  scattering of very weakly bound nuclei [34], can be neglected in the present case. Renormalizing the neutron transition density in order to reproduce the inelastic data leads to the same value of the  $M_n/M_p$  ratio as when the folding potential is used. Two optical potentials which are known to be reliable yield the same result, which gives confidence that the matter and transition densities are being critically tested here.

The phenomenological analysis points to a small neutron deformation in  $^{22}\text{O}$ . The microscopic analysis indicates that protons ( $Z = 8$  closed shell) and neutrons contribute in a balanced way to the first  $2^+$  excitation. This is different from the case of  $^{20}\text{O}$ , where the excitation is driven by the neutrons, as expected due to the  $Z = 8$  shell closure. The result here, combined with the high energy of the  $2^+$  state, points to a strong  $N = 14$  (sub)shell closure in neutron-rich nuclei. Shell model calculations reported by [10] predict strong  $N = 14$  and  $N = 16$  gaps in oxygen isotopes. This calculation predicts  $M_n/M_p = 2.6$ , in agreement with the experimental result.

In summary, the angular distributions for elastic and inelastic scattering to the  $2_1^+$  state of  $^{22}\text{O}$  have been measured using a secondary radioactive beam of only 1200 pps coupled to a highly efficient particle detection system. Proton and neutron contributions to the excitation are disentangled through the comparison of the present results with a heavy ion scattering experiment dominated by electromagnetic excitation. This method is shown to be a general tool to search for neutron shell closures which are only indirectly observed through Coulomb excitation. In the present case, evidence for a strong  $N = 14$  shell closure is obtained from several independent analyzes. This effect has been predicted by recent shell model calculations. Attention should now turn to  $^{24}\text{O}$  and the  $N = 16$  subshell closure. A successful  $^{24}\text{O}(p, p')$  experiment will have to wait for the next generation radioactive beam

facilities, but the generality of the present method should allow us to enhance our knowledge of neutron shell closure far from stability in regions of heavy nuclei.

We thank P. Gangnant, J.F. Libin, and L. Petizon for their expert technical help. The work of K.W.K. was supported by the U.S. National Science Foundation. D.T.K. and H.S.T. have been supported by Natural Science Council of Vietnam.

- 
- [1] P. Leboeuf and A. Monastra, *Ann. Phys. (N.Y.)* **297**, 127 (2002).
  - [2] Y. Imry, *Introduction to Mesoscopic Physics* (Oxford University, New York, 1997).
  - [3] M. Brack, *Rev. Mod. Phys.* **65**, 677 (1993).
  - [4] C. Freiburghaus *et al.*, *Astron. J.* **516**, 381 (1999).
  - [5] T. Otsuka *et al.*, *Phys. Rev. Lett.* **87**, 082502 (2001).
  - [6] B.A. Brown, *Prog. Part. Nucl. Phys.* **47**, 517 (2001).
  - [7] A. Ozawa, T. Kobayashi, T. Suzuki, K. Yoshida, and I. Tanihata, *Phys. Rev. Lett.* **84**, 5493 (2000).
  - [8] E. Khan *et al.*, *Phys. Lett. B* **490**, 45 (2000).
  - [9] M. Bellegric *et al.*, *Nucl. Phys. A* **682**, 136c (2001).
  - [10] P.G. Thirolf *et al.*, *Phys. Lett. B* **485**, 16 (2000).
  - [11] M. Stanoiu *et al.*, *Phys. Rev. C* **69**, 034312 (2004).
  - [12] E. Khan, N. Sandulescu, M. Grasso, and Nguyen Van Giai, *Phys. Rev. C* **66**, 024309 (2002).
  - [13] M. Tohyama and A. S. Umar, *Phys. Lett. B* **549**, 72 (2002).
  - [14] P. Ring *et al.*, *Nucl. Phys. A* **722**, C372 (2003).
  - [15] O. Tarasov *et al.*, *Phys. Lett. B* **409**, 64 (1997).
  - [16] Y. Utsuno, T. Otsuka, T. Mizusaki, and M. Honma, *Phys. Rev. C* **60**, 054315 (1999).
  - [17] T. Otsuka *et al.*, *Phys. Rev. Lett.* **95**, 232502 (2005).
  - [18] A.M. Bernstein *et al.*, *Comments Nucl. Part. Phys.* **11**, 203 (1983).
  - [19] J.K. Jewell *et al.*, *Phys. Lett. B* **454**, 181 (1999).
  - [20] G. Kraus *et al.*, *Phys. Rev. Lett.* **73**, 1773 (1994).
  - [21] S. Ottini-Hustache *et al.*, *Nucl. Instrum. Methods Phys. Res., Sect. A* **431**, 476 (1999).
  - [22] L. Bianchi *et al.*, *Nucl. Instrum. Methods Phys. Res., Sect. A* **276**, 509 (1989).
  - [23] Y. Blumenfeld *et al.*, *Nucl. Instrum. Methods Phys. Res., Sect. A* **421**, 471 (1999).
  - [24] A.J. Koning and J.P. Delaroche, *Nucl. Phys. A* **713**, 231 (2003).
  - [25] F.D. Becchetti and G.W. Greenlees, *Phys. Rev.* **182**, 1190 (1969).
  - [26] R.L. Varner *et al.*, *Phys. Rep.* **201**, 57 (1991).
  - [27] J. Raynal, *Phys. Rev. C* **23**, 2571 (1981).
  - [28] M. Grasso, N. Sandulescu, Nguyen Van Giai, and R.J. Liotta, *Phys. Rev. C* **64**, 064321 (2001).
  - [29] E. Chabanat, P. Bonche, P. Haensel, J. Meyer, and R. Schaeffer, *Nucl. Phys. A* **635**, 231 (1998).
  - [30] D.T. Khoa *et al.*, *Nucl. Phys. A* **706**, 61 (2002).
  - [31] J.P. Jeukenne, A. Lejeune, and C. Mahaux, *Phys. Rev. C* **16**, 80 (1977).
  - [32] P. Ring and P. Schuck, *The Nuclear Many-Body Problem* (Springer-Verlag, Berlin, 1980).
  - [33] T. Tamura, W.R. Coker, and F. Rybicki, *Comput. Phys. Commun.* **2**, 94 (1971).
  - [34] R.S. Mackintosh, *Nucl. Phys. A* **209**, 91 (1973).

## 2.6 Halos dans les noyaux de masse intermédiaire

Si les halos pour les noyaux légers et les peaux pour les noyaux plus lourds sont des phénomènes exotiques désormais bien connus pour les systèmes riches en neutrons, certains modèles indiqueraient l'existence d'autres types de profils de densités très étendus : des halos appelés géants sont prédits dans quelques noyaux de masse intermédiaire ou lourds. Dans ces systèmes très riches en neutrons, l'extension de la surface est bien plus importante que dans une peau. Les premiers travaux qui ont mis en évidence ce phénomène ont été réalisés dans le cadre des modèles relativistes Relativistic-Hartree-Bogoliubov (voir, par exemple, [MR98, Me02]).

Nous avons abordé ce problème pour les isotopes de Ca et Zr avec le modèle Skyrme-HFB [Gr06,Gr07b]. Nous avons montré que les résultats dépendent assez fortement du modèle : la présence des halos dépend essentiellement de la position de la drip line, qui est à son tour liée au spectre d'états individuels que chaque modèle fournit. À cause de la position de la drip line prédite avec les modèles choisis dans notre travail (SLy4-HFB et SkI4-HFB), nous n'avons pas prévu de halos pour les isotopes de Ca. Pour les isotopes de Zr, nous prévoyons des halos avec le modèle SkI4-HFB parce que la drip line est placée au-delà du noyau  $^{122}\text{Zr}$ . C'est la présence d'orbitales de petit  $l$  faiblement liés ( $3p1/2$  et  $3p3/2$  pour les isotopes de Zr au-delà du  $^{122}\text{Zr}$ ) qui génère ces densités très étendues.

Je montre dans la Figure 2.4 les rayons neutroniques des isotopes de Ca et Zr obtenus avec SLy4-HFB (triangles noirs) et SkI4-HFB (cercles rouges). Les résultats obtenus avec les modèles relativistes présentés dans les articles [Me02, MR98] sont aussi montrés pour comparaison. Les points correspondent aux rayons calculés avec  $r_0 A^{1/3}$  ( $r_0 = 1$  fm).

Le changement de pente à  $N=82$  pour les rayons neutroniques des isotopes de Zr est clairement visible dans la figure.

L'article qui suit [Gr06] décrit en détail les résultats de cette analyse.

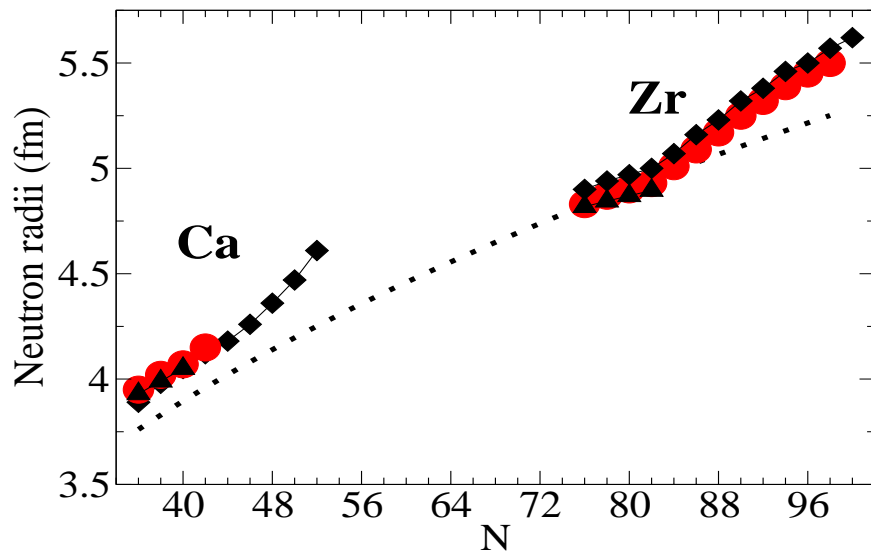


**Fig. 2.4.** Rayons neutroniques calculés avec *SLy4-HFB* (triangles noirs) et *SkI4-HFB* (cercles rouges). Les résultats relativistes présentés dans les articles [Me02, MR98] sont aussi montrés pour comparaison. Les points correspondent aux rayons calculés avec  $r_0 A^{1/3}$  ( $r_0 = 1$  fm).

**Giant neutron halos in the non-relativistic mean field approach**M. Grasso,<sup>1,2,3</sup> S. Yoshida,<sup>1,4</sup> N. Sandulescu,<sup>5,6</sup> and N. Van Giai<sup>1</sup><sup>1</sup>*Institut de Physique Nucléaire, 15 rue Georges Clémenceau, F-91406 Orsay Cedex, France*<sup>2</sup>*Dipartimento di Fisica e Astronomia, Via Santa Sofia 64, I-95123 Catania, Italy*<sup>3</sup>*INFN, Sezione di Catania, Via Santa Sofia 64, I-95123 Catania, Italy*<sup>4</sup>*Science Research Center, Hosei University, 2-17-1 Fujimi, Chiyoda, Tokyo 102-8160, Japan*<sup>5</sup>*Service de Physique Nucléaire, CEA-DAM Ile-de-France, BP 12, F-91680 Bruyères-le-Châtel, France*<sup>6</sup>*Institute for Physics and Nuclear Engineering, P.O. Box MG-6, RO-76900 Bucharest, Romania*

(Received 23 March 2006; published 26 December 2006)

Giant neutron halos in medium-heavy nuclei are studied in the framework of the Hartree-Fock-Bogoliubov (HFB) approach with Skyrme interactions. The appearance of such structures depends sensitively on the effective interaction adopted. This is illustrated by comparing the predictions of SLy4 and SkI4 in the Ca and Zr isotopic chains. The latter force predicts a neutron halo in the Zr chain with  $A > 122$  due to the weakly bound orbitals  $3p_{1/2}$  and  $3p_{3/2}$ . It is found that the energies of states near the separation threshold depend sensitively on effective mass values. The structure of the halo is analyzed in terms of the occupation probabilities of these orbitals and their partial contributions to the neutron density. The antihalo effect is also discussed in the case of  $^{124}\text{Zr}$  by comparing the occupation probabilities and wave functions of the Hartree-Fock neutron single-particle states near the Fermi energy with the corresponding HFB quasiparticle states.

DOI: [10.1103/PhysRevC.74.064317](https://doi.org/10.1103/PhysRevC.74.064317)

PACS number(s): 21.10.Gv, 21.10.Pc, 21.60.Jz, 27.40.+z

**I. INTRODUCTION**

Currently, several projects for the construction of a new generation of radioactive beam facilities are in progress (see, e.g., Ref. [1]). Such facilities will permit researchers to investigate the properties of unstable nuclei situated close to drip-line regions. From the theoretical side, many efforts are devoted to performing accurate predictions to locate the proton and neutron drip lines as well as to describe the behavior of unstable nuclei. Unfortunately, theoretical predictions in exotic regions of the nuclear chart can be rather model dependent.

Self-consistent mean field methods are well-suited theoretical tools for describing medium and heavy nuclei. There are two main lines of investigation based on the mean field approach, namely, the relativistic mean field (RMF) method, which treats effective Lagrangians in the Hartree approximation, and the nonrelativistic Hartree-Fock (HF) method, which uses effective interactions such as the Gogny and Skyrme forces. Recent reviews can be found in Refs. [2,3]. When approaching the drip lines, one deals with open-shell nuclei for which the effects of pairing correlations become quite important, especially for such properties as the tails of matter distributions. The pairing correlations can be described by the nonrelativistic Hartree-Fock-Bogoliubov (HFB) theory [4,5] or by the relativistic Hartree-Bogoliubov (RHB) theory. The most widely used choice is to add a phenomenological pairing interaction acting in the particle-particle channel [6]. Alternatively, one can use the same meson-nucleon Lagrangian to generate the particle-particle interaction, then make a zero-range approximation, and finally readjust the particle-particle interaction by an overall factor [7].

Furthermore, the chemical potential  $\lambda$  becomes close to zero in the vicinity of drip lines, and it is necessary to treat properly the contributions of the quasiparticle continuum when evaluating the pairing correlations [5]. Thus, the most

appropriate approach for such cases is to solve the self-consistent mean field equations in coordinate space, and this is the method we use to obtain the results of this work.

A very interesting phenomenon has been recently predicted within the RHB approach: the formation of a neutron giant halo (with up to six neutrons involved) in some very neutron-rich isotopes. The radius of the neutron distribution as a function of  $A$  shows a kink at the nucleus where the halo structure starts to be formed. This effect has been found to be particularly strong in Ca (with  $A > 60$ ) [8] and Zr (with  $A > 122$ ) [9] isotopes. These predictions are based on the NLSH parametrization, and similar results are obtained with the TM1 parametrization [10]. The giant halo phenomenon is also found in the near-drip-line Zr isotopes if one uses the NL3 parametrization in an RMF plus resonant continuum BCS [11]. The giant halo effect in medium-heavy nuclei has been much less investigated within the nonrelativistic mean field approach, apart from Ref. [12], where the halo phenomenon is studied in Ni and Sn, and Ref. [13] for Ca isotopes. The purpose of the present work is to investigate the giant halo effect in Ca and Zr isotopes within the nonrelativistic Skyrme-Hartree-Fock-Bogoliubov mean field approach. This effect may appear in the vicinity of drip lines, if at all, and therefore it is probably still out of reach of the next generation facilities.

Important discrepancies are often found in the position of the neutron drip line predicted by different models. For instance, these differences clearly appear in the neutron drip line of Ni isotopes calculated in relativistic [14] and nonrelativistic [5] approaches. Even among parametrizations of the Skyrme force used in HFB calculations, one can obtain different drip-line predictions. It is found in Ref. [13] that drip lines in Ca isotopes occur for heavier systems if one uses SkM\* rather than the widely used SLy4. In this work, we find that the parametrization SkI4 [15] also leads to bound Ca and

Zr isotopes with a larger neutron excess than SLy4. Thus, it is foreseen that giant halo predictions based on the Skyrme-HFB approach will suffer from some model dependences. While waiting for new experimental data that will help discriminate among the available models, it would be interesting to analyze the reasons for some of these discrepancies.

For our analysis, we choose two Skyrme parametrizations, namely, SLy4, which is commonly adopted to treat neutron-rich systems since it includes constraints coming from the neutron matter equation of state, and the SkI4 energy functional of Reinhard and Flocard [15]. The reason for the latter choice is simply that it leads to bound Zr isotopes having more neutrons than the SLy4 force, and, hence, the giant halo phenomenon can take place. As for the Ca isotopes, neither SLy4 nor SkI4 can produce bound Ca isotopes that are neutron rich enough to lead to a halo effect.

The present calculations include pairing correlation effects, and these correlations can induce an antihalo effect, as pointed out in Ref. [16]. We discuss this effect in the case of the  $^{124}\text{Zr}$  nucleus by comparing the HFB results with the corresponding HF ones.

The article is organized as follows. In Sec. II, we briefly describe the theoretical framework. In Sec. III A, we present the two-neutron separation energies, neutron radii, and HF single-particle spectra for neutron-rich Ca and Zr isotopes, and we compare our nonrelativistic results with the corresponding RHB results obtained with the NLSH parametrization [8,9]. We discuss the differences found in the HF spectra with the adopted Skyrme parametrizations by analyzing, in some cases, the mean field and spin-orbit contributions to the total potential. In Sec. III B, we consider in more detail the case of Zr isotopes and investigate giant halo and antihalo effects by analyzing occupation probabilities, neutron density profiles, and wave function tails. In Sec. IV, our conclusions are drawn.

## II. THEORETICAL FRAMEWORK

The theoretical framework used in this paper is the HFB approach. For zero-range two-body forces, the HFB equations have the form

$$\begin{aligned} [h(\mathbf{r}) - \lambda]u(E, \mathbf{r}) + \Delta(\mathbf{r})v(E, \mathbf{r}) &= Eu(E, \mathbf{r}), \\ \Delta(\mathbf{r})u(E, \mathbf{r}) - [h(\mathbf{r}) - \lambda]v(E, \mathbf{r}) &= Ev(E, \mathbf{r}), \end{aligned} \quad (1)$$

where  $\lambda$  is the Fermi energy,  $h$  is the sum of the kinetic energy and the HF mean field potential, and  $\Delta$  is the pairing potential;  $u$  and  $v$  are the upper and lower components of the quasiparticle wave function associated with the quasiparticle energy  $E$ , which we choose to be positive. In this work, we assume spherical symmetry as in the RHB approach, so that the HFB equations depend only on the radial coordinate  $r$  and they can be solved directly in  $r$  space.

We shall only consider bound systems, i.e., cases in which  $\lambda$  is negative. The reason is that, if  $\lambda$  becomes positive, there are states with  $0 \leq E \leq \lambda$  whose wave functions  $u, v$  do not decrease exponentially at large distances [4]. Then, the matter density built with  $v^2$  does not vanish asymptotically, and the nucleus is unbound. For negative  $\lambda$ , the spectrum consists

of a discrete part for  $E$  less than  $-\lambda$  and a continuous part for  $E$  above  $-\lambda$ . To calculate the continuum spectrum, the HFB equations should be solved with scattering type boundary conditions for the upper components of the HFB wave functions [5]. Since the continuum-HFB calculations are rather heavy, the continuum spectrum is usually discretized by imposing box boundary conditions, i.e., the condition that the HFB wave functions vanish at a given distance from the nucleus. This is sufficient for our present purpose provided that the box radius is properly chosen. We have checked that our results obtained with a box radius of 20 fm are very close to those of a full continuum calculation. Thus, most of the results presented here have been obtained by imposing box boundary conditions. Only the results discussed in Sec. III B are obtained with scattering-type boundary conditions.

In the present HFB calculations, the mean field is calculated with a Skyrme-type force, while for the pairing channel, we use a zero-range interaction with the following density dependence:

$$V(\mathbf{r}_1 - \mathbf{r}_2) = V_0 \left[ 1 - x \left( \frac{\rho(r)}{\rho_0} \right)^\gamma \right] \delta(\mathbf{r}_1 - \mathbf{r}_2). \quad (2)$$

The value of  $\rho_0$  is  $0.16 \text{ fm}^{-3}$ , corresponding approximately to the nuclear matter saturation density given by SLy4 and SkI4. We choose  $x = 0.5$  to represent a pairing force half-way between a pure volume and pure surface interaction. As for  $\gamma$ , we simply take  $\gamma = 1$ , a choice compatible with the conclusions of the study made in Ref. [17] about the influence of  $\gamma$  on the asymptotics of nucleon distributions. The quasiparticle energy cutoff is equal to 70 MeV, and the maximum value of  $j$  is  $15/2$ . The strength  $V_0$  is chosen so as to reproduce the gaps extracted from the odd-even mass differences (in the regions where such experimental data are available), i.e.,  $V_0$  is adjusted to be  $-365$  and  $-290 \text{ MeV fm}^3$  ( $-350$  and  $-300 \text{ MeV fm}^3$ ) for the Ca and Zr isotopes calculated with SLy4 (SkI4).

## III. RESULTS OF HFB CALCULATIONS

### A. Separation energies, neutron radii, and HF results

The two-neutron separation energy is defined as

$$S_{2n}(N, Z) = E(N, Z) - E(N - 2, Z), \quad (3)$$

where  $E(N, Z)$  is the total energy of the isotope with  $N$  neutrons and  $Z$  protons. The two-neutron separation energies for Ca and Zr isotopes are shown in Figs. 1 and 2. We display in these figures only the separation energies for the bound nuclei, i.e., those having a negative chemical potential in the HFB calculations. For instance, the separation energy is still positive in  $^{64}\text{Ca}$  with SkI4-HFB ( $S_{2n} = 0.2 \text{ MeV}$ ) but the chemical potential is already positive and equal to  $0.24 \text{ MeV}$ . We thus define as the drip-line nucleus the last isotope having both positive separation energy and negative chemical potential. The shown results correspond to box-HFB calculations, which give practically the same  $S_{2n}$  values as continuum-HFB calculations.

The most important fact we can observe in Fig. 1 is the large difference between the drip-line location predicted by

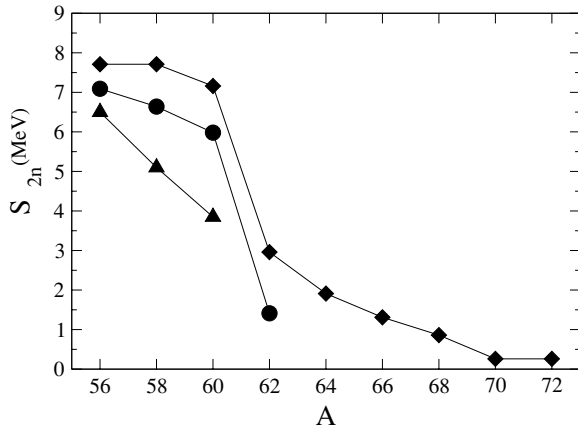


FIG. 1. Two-neutron separation energies for Ca isotopes calculated with SLy4-HFB (triangles), SkI4-HFB (circles), and RHB (diamonds). The RHB results correspond to Ref. [8].

the Skyrme-HFB with SLy4 and SkI4 and that predicted by the RHB calculations of Ref. [8] for the Ca isotopes. It can be seen that for Skyrme forces, the drip line is located at  $^{62}\text{Ca}$  ( $^{60}\text{Ca}$ ) with SkI4 (SLy4), while for RHB calculations, the drip line extends up to  $^{72}\text{Ca}$ . It must be noted that in Ref. [13], the two-neutron separation energy was found to be still positive in  $^{78}\text{Ca}$  with the interaction SkM\*. In any case, with the two Skyrme parametrizations adopted here, the region in which a giant halo could exist in Ca isotopes cannot be explored, since the last bound nucleus is reached before.

In the Zr isotopes, differences also occur among the model predictions. As seen in Fig. 2, for the force SLy4, the drip line is located at  $^{122}\text{Zr}$ , whereas for SkI4, it is at  $^{138}\text{Zr}$ . The latter result is similar to the RHB prediction in which the drip line is located at  $^{140}\text{Zr}$ .

We check now whether our nonrelativistic model can predict a giant neutron halo structure by analyzing the neutron radii, which are shown in Fig. 3. As mentioned before, for Ca isotopes, the neutron drip line is reached before the halo structure starts to be formed for both the adopted Skyrme parametrizations. The same is happening for Zr isotopes if one

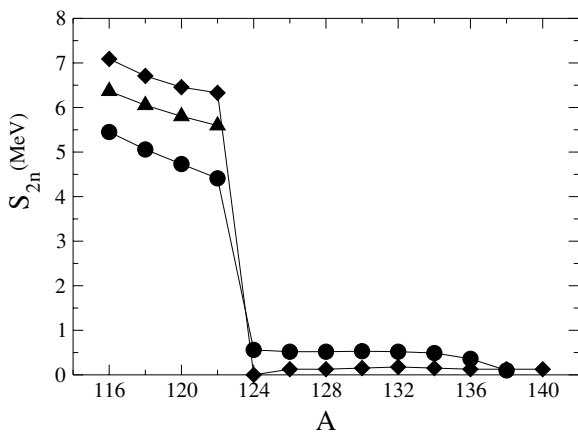


FIG. 2. Same as Fig. 1, but for Zr isotopes. RHB results correspond to Ref. [9].

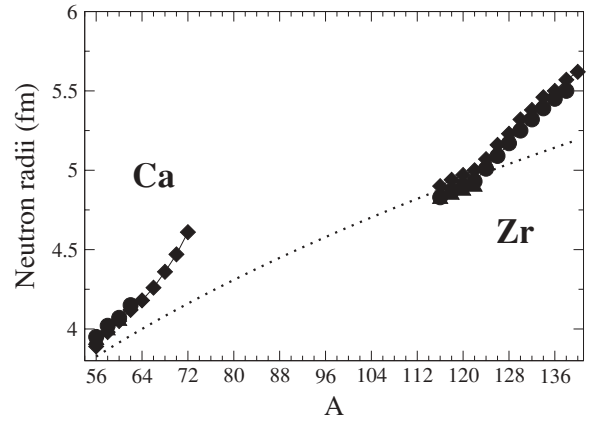


FIG. 3. Neutron radii for Ca and Zr isotopes. Symbols same as in Fig. 1; RHB results correspond to Refs. [8,9]. Radii calculated as  $r_0 A^{1/3}$  ( $r_0 = 1$  fm) are shown by a dotted line.

uses the SLy4 force. However, in the case of SkI4, the situation is very different, with a change in the slope of neutron radii around  $A = 122$  and values close to those of RHB.

To understand better why the drip line is so model dependent, Figs. 4 and 5 show the HF energies of the bound states close to the Fermi level in Ca and Zr isotopes, respectively. For Ca isotopes, we can see that apart from a different splitting of the  $1f$  and  $2p$  states, the two Skyrme forces give a rather similar pattern for the bound spectrum. The HF drip-line nucleus is  $^{60}\text{Ca}$  with both SLy4 and SkI4;  $^{62}\text{Ca}$  is not bound since the state  $1g_{9/2}$  remains slightly unbound with the two forces, at variance with the RMF calculations in which this state becomes weakly bound at  $A = 62$  [8]. Because of this fact, the drip line in the RHB calculations is extended up to the region where the giant halo can be formed, in contrast with the HFB calculations of Ca isotopes based on SLy4 or SkI4. It must be noted, however, that this tendency is not obeyed by the Skyrme SkM\* parametrization, which gives a bound  $1g_{9/2}$  orbital in the Ca isotopes with  $A \geq 60$  resulting in a drip line located at higher  $A$  [13].

For Zr isotopes, the structure of the HF bound spectrum is not the same for the two adopted Skyrme parametrizations. We

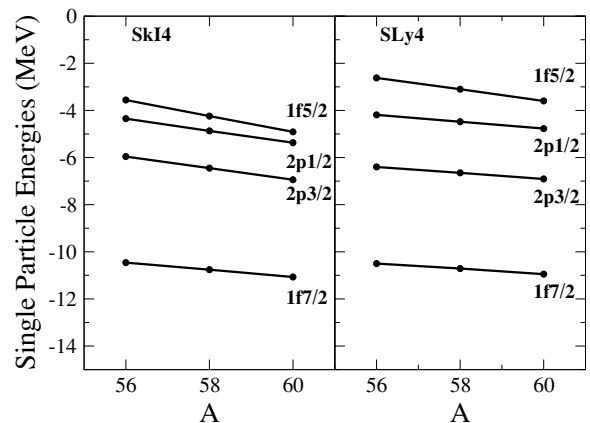


FIG. 4. SkI4-HF (left) and SLy4-HF (right) neutron single-particle energies for bound states in Ca isotopes.

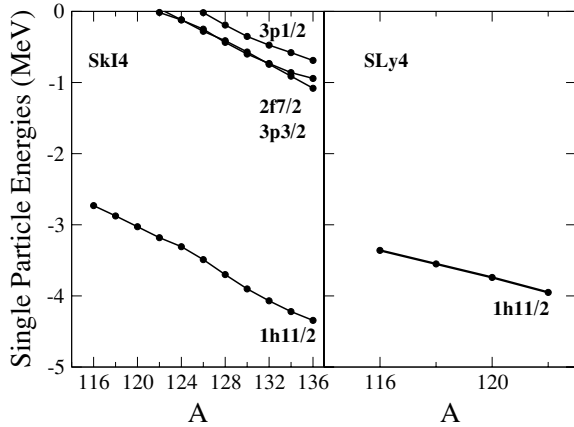


FIG. 5. Same as Fig. 4, but for Zr isotopes.

can observe that at  $A = 122$ , the state  $3p3/2$  becomes weakly bound with SkI4, while it remains slightly unbound with SLy4. This allows one to shift the drip line with SkI4, the states  $2f7/2$  and  $3p1/2$  becoming then weakly bound at  $A = 124$  and  $126$ , respectively. This is similar to what happens in the RMF calculations and explains why both the SkI4-HFB and the RHB calculations provide a halo structure in Zr isotopes. How these weakly bound HF states contribute to the halo structure in the presence of pairing correlations is discussed in the next subsection.

Let us now analyze the elements responsible for the differences found in the single-particle spectra and in the drip-line predictions. We can write the HF equation as

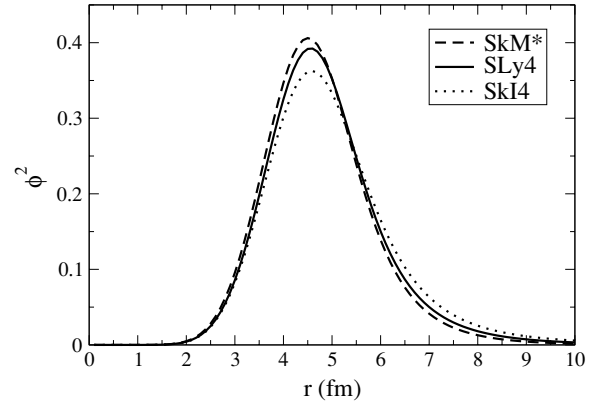
$$\frac{\hbar^2}{2m} \left[ -\frac{d^2}{dr^2} \psi(r) + \frac{l(l+1)}{r^2} \psi(r) \right] + V_{\text{eq}}(r, \epsilon) \psi(r) = \epsilon \psi(r), \quad (4)$$

where the equivalent potential  $V_{\text{eq}}$  reads

$$V_{\text{eq}}(r, \epsilon) = \frac{m^*(r)}{m} U_0(r) + \frac{m^*(r)}{m} U_{\text{so},lj}(r) - \frac{m^{*2}(r)}{2m\hbar^2} \left( \frac{\hbar^2}{2m^*(r)} \right)^2 + \frac{m^*(r)}{2m} \left( \frac{\hbar^2}{2m^*(r)} \right)'' + \left[ 1 - \frac{m^*(r)}{m} \right] \epsilon. \quad (5)$$

with  $U_{\text{so},lj}(r) = U_{\text{so}}(r) \times [j(j+1) - l(l+1) - 3/4]$ . The local equivalent potential  $V_{\text{eq}}$  takes into account the effects of the Skyrme-HF effective mass, and the exact HF wave function  $\phi(lj)$  of energy  $\epsilon$  is related (up to a normalization factor) to the solution  $\psi$  of Eq. (4) by the relation  $\psi = (m^*/m)^{1/2} \phi$ . The functions  $U_0(r)$  and  $U_{\text{so}}(r)$  are the central and spin-orbit HF potentials, whereas  $m^*(r)$  is the effective mass [18]. The first two terms of Eq. (5) are the main contributions, the next two terms are small corrections, and the last term has a small contribution for states in the vicinity of zero energy.

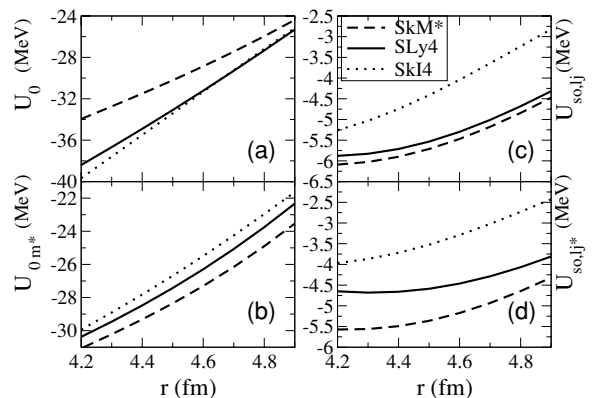
We first consider the Ca isotopes, as illustrated by the nucleus  $^{60}\text{Ca}$  and the single-particle state  $1g9/2$ . For this nucleus, the state  $1g9/2$  is bound with the force SkM\* ( $\epsilon \sim -1.3$  MeV) [13], whereas it is a single-particle resonance with SLy4 ( $\epsilon \sim 0.3$  MeV) and with SkI4 ( $\epsilon \sim 1$  MeV). We


FIG. 6. Square of the  $1g9/2$  wave function with the forces SkM\*, SLy4, and SkI4 in  $^{60}\text{Ca}$ .

display in Fig. 6 the square of the HF  $1g9/2$  wave functions in  $^{60}\text{Ca}$  calculated with SkM\*, SLy4, and SkI4. Their general behaviors are quite similar up to more than twice the nuclear radius.

The four functions (a) the mean field  $U_0(r)$ , (b) the mean field multiplied by the effective mass,  $U_{0m^*}(r) = U_0(r)[m^*(r)/m]$ , (c) the spin-orbit term  $U_{\text{so},lj}(r)$ , and (d) the spin-orbit term multiplied by the effective mass,  $U_{\text{so},lj^*}(r)$ , are calculated with the three parametrizations and displayed in Fig. 7. They are shown in the radial region around 4.5 fm where the square of the single-particle wave function  $1g9/2$  has its maximum. In this region, one sees that the potentials  $U_{0m^*}(r)$  and  $U_{\text{so},lj^*}(r)$  of SkM\* are deeper than those of SkI4 and SLy4. One can observe that the effective mass  $m^*(r)$  plays an important role in shifting down the  $1g9/2$  single-particle energy of SkM\* to below the values of SkI4 and SLy4. In the nucleus  $^{60}\text{Ca}$ , the values of the neutron effective mass  $m_n^*/m$  at  $r = 0$  are 0.788, 0.680, and 0.606 for SkM\*, SLy4, and SkI4, respectively; whereas at  $r = 4.6$  fm, they are 0.946, 0.842, and 0.814. This explains why  $U_{0m^*}$  is deepest for SkM\*, although  $U_0(\text{SkM}^*)$  itself is the least attractive.

We perform a similar analysis for Zr isotopes. We consider the case of  $^{122}\text{Zr}$  and the HF wave function of the state  $3p3/2$  calculated with the two parametrizations SLy4 and SkI4. This state is bound in the HF spectrum with SkI4 ( $\epsilon \sim -0.02$  MeV),


FIG. 7. Four functions defined in text calculated with the three parametrizations in  $^{60}\text{Ca}$  for  $l = 4$  and  $j = 9/2$ .

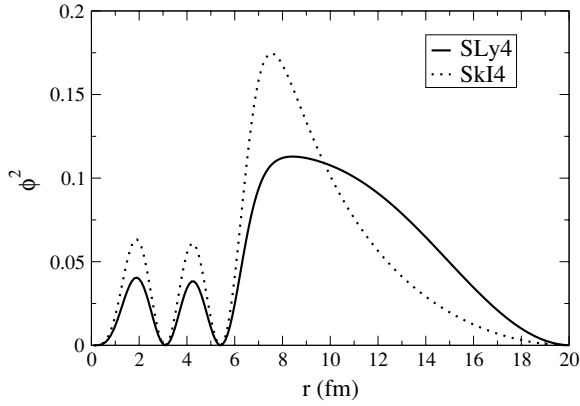


FIG. 8. Square of the  $3p3/2$  wave function with forces SLy4 and SkI4 in  $^{122}\text{Zr}$ .

but it is unbound with SLy4 ( $\epsilon \sim 0.6$  MeV). We show in Fig. 8 the square of the wave function  $3p3/2$  calculated with the two forces.

Figure 9 shows the four functions  $U_0(r)$ ,  $U_{0m^*}(r)$ ,  $U_{so,lj}(r)$ , and  $U_{so,lj^*}(r)$  calculated with SLy4 and SkI4. They are plotted in the radial region around 8 fm where the square of the single-particle wave function has its highest maximum. The differences between the top and bottom panels are negligible, reflecting the fact that around  $r = 8$  fm, the effective mass  $m_n^*/m$  in  $^{122}\text{Zr}$  is 0.994 and 0.990 for SLy4 and SkI4, respectively. Furthermore, one can see that the mean field potential is sizably deeper with SkI4, while the differences in the spin-orbit potentials are much less important.

From this study, we can see the decisive role of the effective mass upon the energy of single-particle states when their wave functions are around the surface region. In the example of the  $1g9/2$  state in  $^{60}\text{Ca}$ , the relative positions of the central and spin-orbit potentials are much affected by the  $m^*/m$  factor. When the states are outside the surface region and the  $m^*/m$  factor becomes close to unity, the single-particle energies are directly governed by the mean field  $U_0(r)$ , which in turn depends on neutron-proton symmetry properties such as the symmetry energy coefficient.

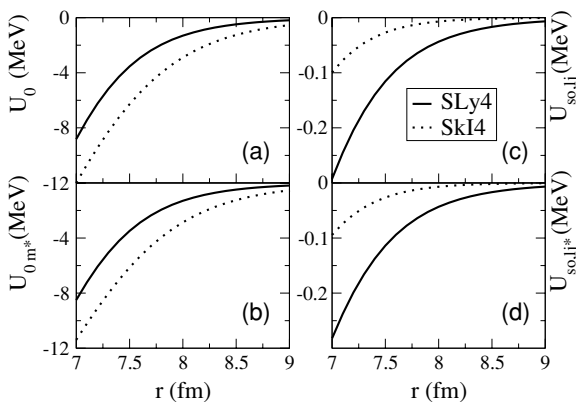


FIG. 9. Four functions calculated with the forces SLy4 and SkI4 in  $^{122}\text{Zr}$  for  $l = 1$  and  $j = 3/2$ .

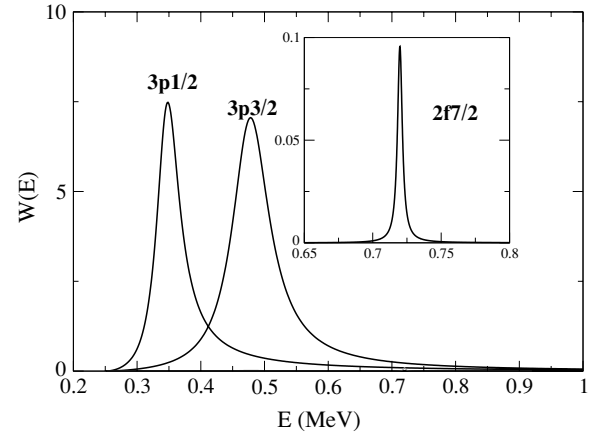


FIG. 10. Occupation profiles  $W(E)$  (in  $\text{MeV}^{-1}$ ) for three states in  $^{132}\text{Zr}$ , calculated with SkI4-HFB.

### B. Structure of the giant halo in Zr isotopes

In the presence of pairing correlations, the bound single-particle states shown in Fig. 5 are becoming quasiparticle resonances. To describe them properly, we solved the HFB equations with scattering-type boundary conditions. To reduce the numerical effort, we employed scattering boundary conditions only for the quasiparticle states with the energy  $-\lambda < E < 15$  MeV because they are the most affected by pairing correlations, while for the other states we used box boundary conditions.

With the continuum HFB solutions, we can calculate how the occupation probability changes in the region around a resonance. This information is provided by the quantity

$$W(E) = \int_0^R dr r^2 v_E^2(r), \quad (6)$$

where  $v$  is the lower component of the HFB wave function, and  $R$  is taken equal to 20 fm. As an example, we show in Fig. 10 the values of  $W(E)$  corresponding to the states  $3p1/2$ ,  $3p3/2$ , and  $2f7/2$  in the nucleus  $^{132}\text{Zr}$ . In this nucleus, the quasiparticle continuum starts at the energy  $E = -\lambda = 0.251$  MeV.

By integrating the function  $W(E)$  over an energy interval in which it has a significant value, we can associate to each resonance an occupation probability  $n$ , i.e.,

$$n = \int_{E_1}^{E_2} W(E) dE. \quad (7)$$

The occupation probabilities of the relevant resonant states in Zr isotopes are shown in Fig. 11. It can be seen that the occupation probabilities corresponding to the weakly bound states increase progressively when going from  $^{124}\text{Zr}$  to  $^{138}\text{Zr}$ . Thus, these states contribute significantly to the pairing correlations.

To analyze the structure of the halo, we plot in Fig. 12 the quantity

$$R_{lj}(r) = \frac{\rho_{lj}(r)}{\rho(r)}, \quad (8)$$

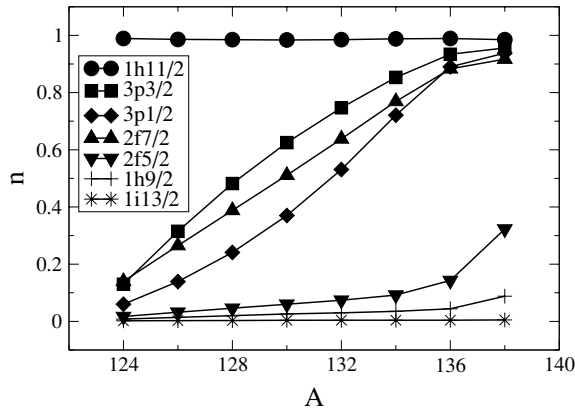


FIG. 11. Occupation probabilities for Zr isotopes, calculated with SkI4-HFB.

where  $\rho$  and  $\rho_{lj}$  are the total neutron density and the density corresponding to the channel  $(l, j)$ , respectively. From Fig. 12, we can clearly see that at large distances, the dominant contribution to the neutron density is given by the  $p$  states, which are less confined by the centrifugal barrier than are the other states with higher  $(l, j)$  values. This structure of the giant halo obtained by using the SkI4-HFB model is very similar to that given by the relativistic calculations [9,11].

By comparing the neutron densities of  $^{124,138}\text{Zr}$  with that of the reference nucleus  $^{122}\text{Zr}$  we can estimate the number of neutrons involved in the outer skin and halo regions. We thus find that this number is 1.15 neutrons (14.27 neutrons) in the region beyond 6.8 fm (5.4 fm) in  $^{124}\text{Zr}$  ( $^{138}\text{Zr}$ ). Alternatively, one can evaluate the number of neutrons in the weakly bound orbitals and the resonant continuum as suggested in Ref. [13], which gives 1.97 and 15.92 neutrons in  $^{124}\text{Zr}$  and  $^{138}\text{Zr}$ , respectively.

### C. Antihalo effect

We turn now to the analysis of the so-called antihalo effect, which was mainly discussed in light nuclei close to the neutron

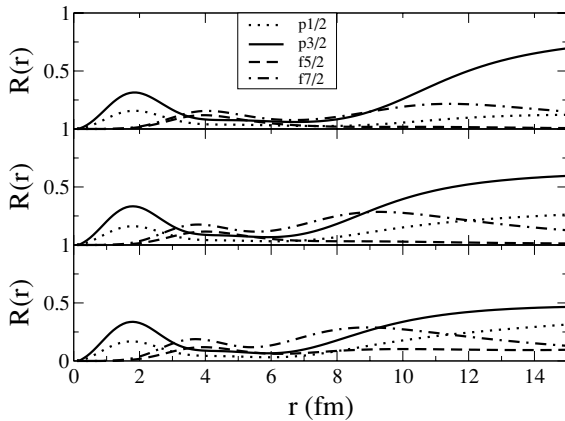


FIG. 12. Contributions of different  $(l, j)$  channels to the total neutron density for  $^{124}\text{Zr}$  (top),  $^{132}\text{Zr}$  (middle), and  $^{138}\text{Zr}$  (bottom). The interaction is SkI4.

drip line [16]. This effect is associated with a reduction of the neutron radii by the pairing correlations.

In Zr isotopes, the pairing correlations affect the neutron halo through the  $p$  and  $f$  states. We take as an illustration the case of  $^{124}\text{Zr}$  for which the neutron radius is equal to 5.08 (5.01) fm in HF (HFB). We adopt a spherical symmetry scheme for the present discussion since it is found in RMF calculations that Zr isotopes are predicted to be spherical beyond  $A = 122$  [9]. In  $^{124}\text{Zr}$ , the  $3p3/2$  state is half occupied, while  $2f7/2$  (weakly bound) is empty in HF. When pairing correlations are switched on within HFB, the occupancy of the  $3p3/2$  state is much reduced and that of the  $2f7/2$  is enhanced, as one can observe in Fig. 11.

Bennaceur *et al.* [16] analyzed the antihalo effect in terms of the asymptotic behavior of the neutron densities calculated in HF and in HFB. In the latter case, the existence of a finite pairing gap due to pairing correlations gave a faster decaying tail in the neutron density. The states responsible for this effect were those close to the Fermi energy, i.e., those with single-particle energies  $\epsilon \sim \lambda$ . We plot in Fig. 13 the neutron wave function tails of the states  $3p3/2$  (top) and  $2f7/2$  (bottom) calculated in HF and HFB for  $^{124}\text{Zr}$ . To compare the HF and HFB wave functions, we plotted in the HFB case the lower component of the quasiparticle wave functions, normalized to unity. In the two insets of the figure, we display the tails of the wave functions in logarithmic scale. One can observe that at large distances, the HFB wave functions decay faster than the corresponding HF ones in both cases. This confirms the argument given by Bennaceur *et al.* [16] and explains in part why the HFB neutron radius is smaller than the HF one. However, it should be noted that the antihalo effect is not only due to the slope of the wave functions at large distances. Another contribution to this effect is related to the occupancies of the states in HF and HFB. As mentioned before, when pairing correlations are taken into account, the occupancy of the  $3p3/2$  state is reduced while that of  $2f7/2$  is enhanced. Since  $2f7/2$  has a smaller radial extension than  $3p3/2$  due to the centrifugal barrier, the HFB radius is less than the HF one. We can thus say that a stronger effect of the pairing correlations

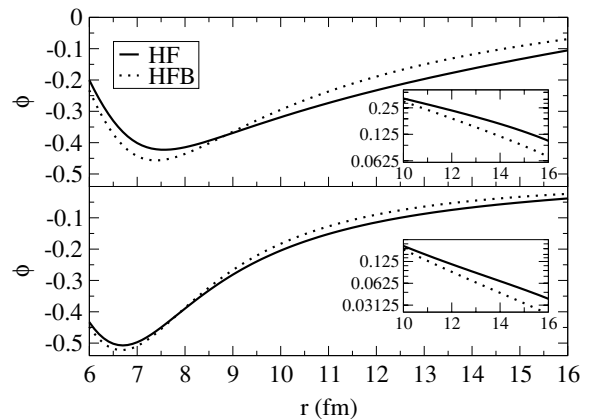


FIG. 13. HF (full lines) and HFB (dotted lines) neutron wave functions for the states  $3p3/2$  (top) and  $2f7/2$  (bottom) in  $^{124}\text{Zr}$ . Insets show the tails of the wave functions plotted in logarithmic scale. The interaction is SkI4.

upon the reduction of the neutron radius is expected when close to the Fermi level one finds a weakly bound low- $l$  state ( $3p_{3/2}$  in our case) together with states with higher angular momenta ( $2f_{7/2}$  in our case).

We conclude, however, by stressing that the antihalo effect caused by pairing is not strong enough to prevent the formation of a neutron giant halo close to the drip line for Zr isotopes, as we have shown in the previous sections.

#### IV. CONCLUSIONS

In this work, we have examined the evolution of the nuclear structure of Zr isotopes at large neutron excess, giving special attention to the far out region of neutron densities. This is motivated by the predictions of the RHB approach which indicate the presence of a giant neutron halo in these nuclei. We have used a different approach, namely, the Skyrme-HFB model. We find that in this isotopic chain, the presence or absence of giant halos depends essentially on the location of the predicted neutron drip line. Thus, there is a strong model dependence in this type of study, as illustrated by the results obtained with the Skyrme forces SLy4 and SkI4.

For the drip line to be displaced toward heavier isotopes, a necessary condition is that some HF orbitals become bound when  $A$  increases. In this case, additional bound neutrons can

be accommodated, and bound nuclei of heavier mass can be formed. An illustration of this situation is provided by the Zr isotopes, for which this necessary condition is fulfilled by some model like SkI4 but not by SLy4. Once the necessary condition is realized, a neutron halo may exist if some of the weakly bound HF orbitals correspond to low angular momenta ( $3p_{3/2}$  and  $3p_{1/2}$  in the case of Zr) so that the centrifugal barrier is weak enough to let the wave functions extend far out.

Thus, the decisive factor is the HF mean field which governs the HF single-particle spectrum, while the pairing correlations play a lesser role. For states that are relatively outside the nuclear surface, the single-particle energies depend mostly on the HF mean field, i.e., on the neutron-proton symmetry properties of the energy functional. On the other hand, the states located near the nuclear surface have their single-particle energies influenced by the value of the effective mass in that region. Actually, experimental determination of neutron drip lines in some nuclei would help place bounds on the values of effective masses.

We have also seen that the pairing correlations can lead to the antihalo effect. This can be understood by analyzing the occupation probabilities and the wave function tails of the least bound ( $lj$ ) orbitals. Finally, we note that this antihalo effect is not strong enough to prevent the formation of a neutron giant halo structure in neutron-rich Zr isotopes.

- 
- [1] Proceedings of the 17th International Conference on Cyclotrons and Their Applications, October 2004, Tokyo.
  - [2] M. Bender, P.-H. Heenen, and P.-G. Reinhard, *Rev. Mod. Phys.* **75**, 121 (2003).
  - [3] J. Meng, H. Toki, S. G. Zhou, S. Q. Zhang, W. H. Long, and L. S. Geng, *Prog. Part. Nucl. Phys.* **57**, 470 (2006).
  - [4] J. Dobaczewski, H. Flocard, and J. Treiner, *Nucl. Phys.* **A422**, 103 (1984); J. Dobaczewski, W. Nazarewicz, T. R. Werner, J.-F. Berger, C. R. Chinn, and J. Dechargé, *Phys. Rev. C* **53**, 2809 (1996).
  - [5] M. Grasso, N. Sandulescu, Nguyen Van Giai, and R. J. Liotta, *Phys. Rev. C* **64**, 064321 (2001).
  - [6] J. Meng and P. Ring, *Phys. Rev. Lett.* **77**, 3963 (1996); J. Meng, *Nucl. Phys.* **A635**, 3 (1998).
  - [7] B. V. Carlson and D. Hirata, *Phys. Rev. C* **62**, 054310 (2000).
  - [8] J. Meng, H. Toki, J. Y. Zeng, S. Q. Zhang, and S.-G. Zhou, *Phys. Rev. C* **65**, 041302 (2002).
  - [9] J. Meng and P. Ring, *Phys. Rev. Lett.* **80**, 460 (1998).
  - [10] S. Q. Zhang, J. Meng, H. Toki, I. Tanihata, and S.-G. Zhou, *Science China Ser. G* **46**, 632 (2003).
  - [11] N. Sandulescu, L. S. Geng, H. Toki, and G. C. Hillhouse, *Phys. Rev. C* **68**, 054323 (2003).
  - [12] S. Mizutori, J. Dobaczewski, G. A. Lalazissis, W. Nazarewicz, and P.-G. Reinhard, *Phys. Rev. C* **61**, 044326 (2000).
  - [13] J. Terasaki, S. Q. Zhang, S. G. Zhou, and J. Meng, *Phys. Rev. C* **74**, 054318 (2006).
  - [14] J. Meng, *Phys. Rev. C* **57**, 1229 (1998); M. Del Estal, M. Centelles, X. Viñas, and S. K. Patra, *Phys. Rev. C* **63**, 044321 (2001).
  - [15] P.-G. Reinhard and H. Flocard, *Nucl. Phys.* **A584**, 467 (1995).
  - [16] S. A. Fayans, S. V. Tolokonnikov, and D. Zawischa, *Phys. Lett.* **B491**, 245 (2000); K. Bennaceur, J. Dobaczewski, and M. Ploszajczak, *ibid.* **B496**, 154 (2000).
  - [17] J. Dobaczewski, W. Nazarewicz, and P.-G. Reinhard, *Nucl. Phys.* **A693**, 361 (2001).
  - [18] E. Chabanat, P. Bonche, P. Haensel, J. Meyer, and R. Schaeffer, *Nucl. Phys.* **A635**, 231 (1998); **A643**, 441(E) (1998).

## 2.7 Interaction d'appariement et vibrations d'appariement

Après la formulation du modèle HFB avec continuum [Gr01], les travaux sur le traitement du continuum ont été poursuivis dans notre groupe avec la formulation de la méthode QRPA avec continuum qui a été appliquée à l'étude des excitations dans les Oxygènes riches en neutrons pour le canal particule-trou [Kh02] et le canal particule-particule [Kh04]. Cette dernière analyse, en particulier, nous a permis d'aborder l'étude des vibrations d'appariement que nous poursuivons actuellement. Ces dernières années, d'autres équipes ont effectué des études microscopiques de ces vibrations [Av08, Ma05, Ma09]. Les sections efficaces qui sont calculées pour les réactions de transfert de paires dépendent de l'interaction d'appariement choisie dans le modèle théorique [Br73, DV87, OV01]. Nous avons donc décidé de regarder de manière systématique les liens entre les prédictions microscopiques sur les vibrations d'appariement et les propriétés et le choix de l'interaction d'appariement.

Un certain nombre de travaux visant à analyser les propriétés de l'interaction d'appariement ont été réalisés récemment. Dans le cadre du modèle de champ moyen Skyrme-HFB, différentes stratégies peuvent être suivies pour contraindre les fonctionnelles qui décrivent l'appariement. Mentionnons quelques exemples :

- (i) fonctionnelles non empiriques ;
  - (i.a) dérivées des interactions réalistes avec des techniques issues de la théorie des perturbations à  $N$  corps (Many-Body perturbation theory) [He09, Le09] ;
  - (i.b) en ajustant les paramètres de manière à reproduire les gaps d'appariement obtenus avec une interaction réaliste dans la matière symétrique et neutronique. Dans cette procédure, la validité de l'approximation de densité locale (LDA) a été supposée [Ma08] ;
- (ii) fonctionnelles phénoménologiques ajustées sur quelques propriétés des noyaux (gaps et/ou énergies de séparation). Des fonctionnelles d'appariement dépendant de la densité isoscalaire et de portée nulle sont souvent utilisées. La possibilité d'enrichir la fonctionnelle avec une dépendance linéaire et quadratique en la densité isovectorielle a été aussi analysée [Ya08].

Nous choisissons une fonctionnelle phénoménologique et voulons vérifier si le fit des paramètres peut être amélioré en considérant les vibrations d'appariement comme observables additionnelles dans la procédure d'ajustement. L'interaction d'appariement adoptée dans notre travail est celle usuelle de portée nulle et dépendante de la densité isoscalaire :

$$V_{\text{pair}} = V_0 \left[ 1 - \eta \left( \frac{\rho(r)}{\rho_0} \right)^\alpha \right] \delta(\vec{r}_1 - \vec{r}_2). \quad (2.9)$$

Les isotopes de Sn ont été considérés et les paramètres de l'interaction d'appariement ont été fixés pour reproduire les valeurs expérimentales disponibles pour les énergies de séparation de deux neutrons dans ces isotopes. Différentes valeurs de  $\eta$  ont été considérées pour modifier le caractère volume/surface de l'interaction et l'effet de ces choix sur les fonctions de réponse et les densités de transition associées aux vibrations d'appariement a été montré [Gr09a, Kh09]. Je fais suivre l'article [Kh09] où nous montrons que des différences existent, surtout pour les noyaux plus riches en neutrons, dans les fonctions de réponse et les densités de transition.

Ce travail va être poursuivi en collaboration avec des collègues expérimentateurs (D. Beaumel, IPN-Orsay) pour calculer, avec les différentes interactions d'appariement, les sections efficaces associées aux réactions de transfert de paires de neutrons. Nous voulons établir si des mesures de sections efficaces pourraient éventuellement nous aider à mieux comprendre les propriétés de l'interaction d'appariement et indiquer quel est le meilleur choix pour cette interaction.

# Constraining the nuclear pairing gap with pairing vibrations

E. Khan,<sup>1</sup> M. Grasso,<sup>1</sup> and J. Margueron<sup>1</sup>

<sup>1</sup> *Institut de Physique Nucléaire, Université Paris-Sud, IN2P3-CNRS, F-91406 Orsay Cedex, France*

Pairing interactions with various density dependencies (surface/volume mixing) are constrained with the two-neutron separation energy in the Tin isotopic chain. The response associated with pairing vibrations in very neutron-rich nuclei is sensitive to the density dependence of the pairing interaction. Using the same pairing interaction in nuclear matter and in Tin nuclei, the optimal range of densities relevant for the pairing channel is also studied.

PACS numbers: 21.60.Jz, 21.65.Cd, 25.40.Hs, 25.60.Je

## I. INTRODUCTION

Studies on pairing effects in both nuclear matter and finite nuclei have known intensified interests in the recent years [1]. There are two main approaches for pairing, depending whether the mean field is based on Gogny finite range interaction or on Skyrme interaction. In the first approach, a similar functional is used in both the particle-hole channel and the pairing channel, although interactions are not exactly the same due to the density dependence of the pairing interaction: the density-dependent term of the Gogny interaction is omitted in the pairing channel due to its spin-isospin structure not contributing to the T=1, S=0 pairing. In the Skyrme approach, the functionals are meant to be different in the two channels, as witnessed for instance by their density dependence. The use of a different interaction in the particle-hole channel and in the pairing channel has been justified a decade ago [2]; this is for instance the case of employing the Skyrme interaction in the particle-hole channel and a zero range density dependent interaction in the pairing channel. We shall focus on the Skyrme approach: in this case the pairing density functional is difficult to constrain and it has not been possible to derive an universal pairing interaction during past decades, using for instance the odd-even mass staggering on finite nuclei (see e.g. [3, 4]). This may indicate the need for another approach, using additional constraints: should the pairing density functional be extended, and are there additional relevant observables to constrain it ?

Nuclear matter could help in constraining the pairing functional. This requires however to bridge nuclei and nuclear matter through LDA in the pairing channel: its condition of validity should be more systematically analysed. It has been recently shown that the two paired neutrons are spatially localised in low density medium which corresponds to the surface of the nucleus [5]. The same conclusion is drawn by analysing the di-neutron configuration in the excited states [6, 7], and also performing calculations in low density matter in [8, 9], mainly renewing the possibility to link in some cases the nuclear matter and nuclei in the pairing channel through the LDA.

Concomitantly the pairing functional has been extended in order to study the condensation of the Cooper pairs (BEC-BCS crossover) in both symmetric and neu-

tron matter. In nuclear matter the medium polarization increases the pairing gap at low densities in symmetric matter, whereas it reduces the gap in neutron matter, indicating an isospin dependence of the pairing functional [10]. The application to finite nuclei of extended pairing density functional have shown the relevance of the LDA in the pairing channel [11].

The pairing functional studies may thus enter in a new era, renewing the method to design the pairing interaction: i) using an isospin dependence of the pairing interaction ii) using eventually the nuclear matter as an additional constrain for the pairing interaction iii) looking for additional observables in nuclei than the odd-even mass staggering to constrain the pairing interaction. Point i) has been investigated in [10, 11]. Point ii) requires the validity of the LDA in the pairing channel.

In the case of point iii) an interesting observable is pairing vibrations, measured through two-particle transfer. It is well known that the transfer cross section crucially depends on the pairing interaction at work in the transferred pair [12, 13]. However in the 70-80's the form factor of the transition has never been calculated fully microscopically. The first microscopic calculations has been performed only recently [14], allowing for a strong link between the pairing interaction and pairing vibrations. Several calculations followed [6, 15], showing the renewed interest for such studies.

It is therefore meaningful to use pairing vibrations as a complementary observable to the masses, in order to constrain the pairing interaction, and study the implications to the nuclear matter. One purpose of this work is to evaluate if pairing vibrations could play this role (Section III).

The method is to analyse the sensitivity of pairing vibrations to various pairing interactions which provide the same two-neutron separation energy in Tin isotopes, and evaluate the consequences on the pairing gap in symmetric and neutron matter. On this purpose it is necessary to determine the range of density where pairing gaps are strongly sensitive to the pairing interaction (Section II).

## II. DENSITY DEPENDENCE OF THE PAIRING OBSERVABLES

After many years of study, there is still no unambiguous universal pairing functional ranging on the whole nuclear chart, and current efforts are aiming in that direction. The problem may be due to the method used to constrain it, namely comparing the pairing gap with odd-even mass differences, or evaluating the separation energies along a given isotopic chain. It therefore may be useful to consider a more general context: the evaluation of several pairing interactions constrained by odd-even mass difference, on nuclear matter on one side, and on additional observables on the other side, should shed a renewed light on the problem. To achieve this goal it is first necessary to determine the range of density which is relevant for pairing studies.

### A. Method to determine the functional

The method is the following: we first consider surface and various mixed pairing interactions. The parameters are determined so as to describe the two neutron separation energy. Then pairing vibrations are used in order to disentangle between the various pairing interactions (Section III). We choose  $^{124}\text{Sn}$  and  $^{136}\text{Sn}$  nuclei: these are spherical nuclei where pairing vibrations are likely to occur [13]. One is stable and the second has a large neutron excess.

The microscopic calculations for the ground state are based on the Hartree-Fock-Bogoliubov (HFB) model. The Skyrme interaction SLy4 [16] is chosen for the particle-hole channel of the HFB equations. The adopted pairing interaction is the usual zero-range density-dependent interaction

$$V_{pair} = V_0 \left[ 1 - \eta \left( \frac{\rho(r)}{\rho_0} \right)^\alpha \right] \delta(\mathbf{r}_1 - \mathbf{r}_2) \quad (1)$$

where  $\eta$  provides the surface/volume character of the interaction. We set  $\alpha = 1$  and  $\rho_0 = 0.16 \text{ fm}^{-3}$ . The numerical cutoff for the microscopic calculations is given by  $E_{max} = 60 \text{ MeV}$  (in quasiparticle energies) and  $j_{max} = 15/2$ . For each value of  $\eta$ ,  $V_0$  is chosen to fit the known experimental two-neutron separation energies for even-even  $^{114}\text{--}^{134}\text{Sn}$  isotopes. The typical r.m.s. value obtained on this observable, compared to the experimental data is several hundreds of keV. Surface and mixed interactions have been considered in this work and the used values of  $(\eta, V_0)$  are listed in Table I. It should be noted that there is no ideal method to adjust this strength. Using the pairing gap could also be considered. However only even-even nuclei are calculated, and one cannot directly compare the pairing gap to the experimental odd-even mass difference. Therefore only the trend of the experimental pairing gaps has to be reproduced, as well as their overall magnitude. Using  $S_{2n}$  is just an alternative method and we have checked that the corresponding

TABLE I: Values of  $\eta$  and  $V_0$  of the pairing interaction.

$\eta$	$V_0 \text{ (MeV fm}^{-1}\text{)}$
0.35	-285
0.65	-390
1	-670

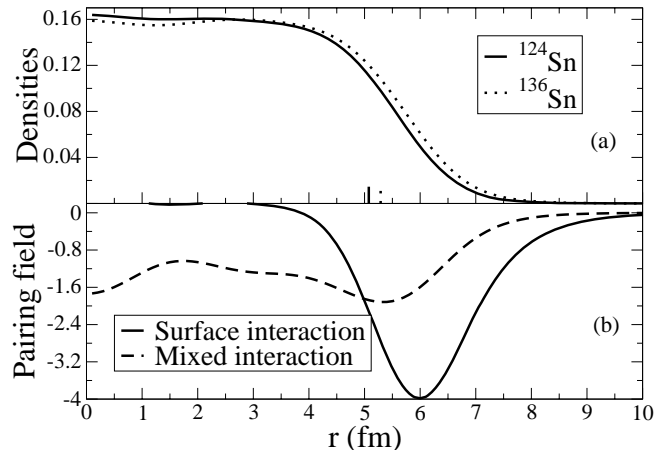


FIG. 1: (a) Matter densities calculated with the HFB model for  $^{124}\text{Sn}$  and  $^{136}\text{Sn}$ . The vertical lines indicate the radius corresponding the density at which all the pairing interactions converge in uniform matter (see text). (b) Pairing field of  $^{124}\text{Sn}$  calculated with a surface  $\eta = 1$  (top) and a mixed  $\eta = 0.35$  (bottom) pairing interaction.

average pairing gaps are of the expected magnitude, typically between 1 and 2 MeV in the Sn isotopes.

As an illustration to visualize the features of the calculated pairing effects, we display in Fig. 1 the neutron pairing field for  $^{124}\text{Sn}$  corresponding to the surface  $\eta = 1$  and the mixed  $\eta = 0.35$  interactions.

### B. Pairing gap in uniform matter

The relation between the pairing gap in uniform matter at a given density and the pairing field at a given radius in nuclei has been explored in Ref. [11]. It has been found that in the case of mixed interactions, the LDA is in good agreement with the full microscopic HFB calculation (differences less than 15% on the pairing field). This might be related to the extension of the Cooper pair which is getting smaller at the surface of nuclei (about 2 fm) compared to that in the interior (about 5-6 fm) [5]. Close to the surface, pairing properties shall not be very different from that of a uniform piece of matter at the same density. It is then interesting to explore the low density properties of the different pairing interactions listed in Table I.

Fig. 2 displays the pairing gap in uniform matter for various pairing interactions. It is observed that the differ-

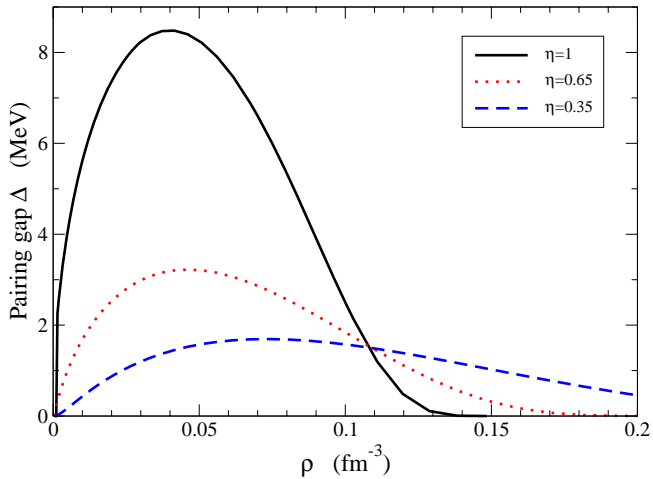


FIG. 2: (Color online) Pairing gap versus the density for uniform matter for different pairing interactions.

ent interactions leads to very different pairing gap at low density while around saturation density, there is a density ( $\rho=0.11 \text{ fm}^{-3}$ ) at which the pairing gap and pairing strength coincide for the three pairing interactions.

From Fig. 2, two conclusions can be drawn: i) the two-neutron separation energy used to adjust the parameters of the pairing interaction is an observable which provides a strong constrain on the pairing gap localized at the surface of the nuclei: the pairing gap in nuclear matter has been constrained for  $\rho=0.11 \text{ fm}^{-3}$ , which corresponds to  $R \simeq 5 \text{ fm}$  in Tin nuclei, as shown by the  $^{124}\text{Sn}$  densities displayed on Fig. 1 ii) to better constrain the value of the parameter  $\eta$ , one shall find another observable sensitive to the pairing strength at low density (large radius, experimentally easier to probe). Indeed, in the very external part of the nuclei the pairing strength is very different from one interaction to another. The pure surface pairing interaction predicts a pairing gap as high as 8 MeV at low density while the various mixed pairing interactions are grouped below 3 MeV (see Fig. 2).

Therefore, one might expect that properties of collective modes sensitive to the external part of the nuclei could be changed by the properties of the pairing interaction at low density. Pair transfer reaction mechanisms like (p,t) or ( $\alpha$ ,  $^6\text{He}$ ) which are very surface peaked shall also help in extracting the value of the pairing gap in the external part of nuclei or equivalently at low density.

### III. PAIRING VIBRATIONS

As stated above, it may be useful to consider an additional observable than the separation energy, in order to constrain the pairing interaction, namely its density dependence. There are only few observables which could be relevant to constrain pairing effects. It has been shown that the first  $2^+$  state in nuclei is sensitive to the pairing

interaction [17]: both its position and strength depend of the pairing interaction. However this is mainly related to the pairing gap value, which is the same observable extracted from odd-even mass difference. It should be noted that none of these two observables (the first  $2^+$  state and the odd-even mass staggering) can be directly linked to predictions. On one side there is the difficulty to modelize excited states. On the other side, the difficulty is to describe odd nuclei.

Pairing vibrations may be a more adequate observable. They can be probed for instance with two neutrons transfer in nuclei close to shell closure. We refer to [12, 13] for details on pairing vibrations. Basically, these modes correspond to the (collective) filling of subshells, in a transition from an  $A$  to  $A+2$  nuclei.

With pairing vibrations, pairing effects are probed by 3 ways. The first one is the magnitude of the pairing gap  $\Delta$  (average of the pairing field): a large pairing gap implies strength at larger energies, following the formula  $E^2 \simeq (\epsilon - \lambda)^2 + \Delta^2$ . This component is also present in the first  $2^+$  state in the ph response as well as in the odd-even mass staggering. But in the case of the pairing vibrations, there are two additional contributions: first, the transition densities generating the strength are the pairing one, which means that the unperturbed response as well as the perturbed response are sensitive to the impact of the pairing on the wave functions. Finally, the residual interaction, generating the Quasiparticle Random Phase Approximation (QRPA) response, is also sensitive to pairing. Therefore using both the unperturbed and the QRPA response functions, the relative pairing dependence of the wave functions and the residual interaction can be probed.

Pairing vibrations are therefore expected to be very sensitive to the pairing interaction. On the other hand, it may also be difficult to disentangle between the three above mentioned effects. However, the first one can be evaluated using the energies of the unperturbed response, the second one by studying the pairing transition densities, and the last one by comparing the unperturbed and the QRPA responses. It should be noted that a related study will also be performed in [18].

#### A. Method: QRPA in the pp channel

The method is described in [14, 17]. Namely the QRPA equations are solved in coordinate space, using the Green's functions formalism. The variation of the generalized density  $\mathcal{R}'$  is expressed in term of 3 quantities, namely  $\rho'$ ,  $\kappa'$  and  $\bar{\kappa}'$ , which are written as a column vector:

$$\rho' = \begin{pmatrix} \rho' \\ \kappa' \\ \bar{\kappa}' \end{pmatrix}, \quad (2)$$

where  $\rho'_{ij} = \langle 0 | c_j^\dagger c_i | \rho' \rangle$  is the variation of the particle density,  $\kappa'_{ij} = \langle 0 | c_j c_i | \rho' \rangle$  and  $\bar{\kappa}'_{ij} = \langle 0 | c_j^\dagger c_i^\dagger | \rho' \rangle$  are the fluctuations of the pairing tensor associated to the pairing vibrations and  $|\rho'\rangle$  denotes the change of the ground state wavefunction  $|0\rangle$  due to the external field. In contrast with the RPA where one needs to know only the change of the ph density ( $\rho'$ ), the variation of the three quantities (2) have to be calculated in the QRPA. In the three dimensional space introduced in Eq. (2), the first dimension represents the particle-hole (ph) subspace, the second the particle-particle (pp) one, and the third the hole-hole (hh) one. The response matrix has therefore 9 coupled elements in QRPA, compared to one in the RPA formalism.

The variation of the HFB Hamiltonian is given by:

$$H' = \mathbf{V}\rho', \quad (3)$$

where  $\mathbf{V}$  is the matrix of the residual interaction expressed in terms of the second derivatives of the HFB energy functional, namely:

$$\mathbf{V}^{\alpha\beta}(\mathbf{r}\sigma, \mathbf{r}'\sigma') = \frac{\partial^2 \mathcal{E}}{\partial \rho_\beta(\mathbf{r}'\sigma') \partial \rho_\alpha(\mathbf{r}\sigma)}, \quad \alpha, \beta = 1, 2, 3. \quad (4)$$

In the above equation the notation  $\bar{\alpha}$  means that whenever  $\alpha$  is 2 or 3 then  $\bar{\alpha}$  is 3 or 2.

The QRPA Green's function  $G$  can be used for calculating the strength function associated with the two-particle transfer from the ground state of a nucleus with  $A$  nucleons to the excited states of a nucleus with  $A+2$  nucleons. This strength function is :

$$S(\omega) = -\frac{1}{\pi} Im \int F^*(\mathbf{r}) \mathbf{G}^{22}(\mathbf{r}, \mathbf{r}'; \omega) F(\mathbf{r}') d\mathbf{r} d\mathbf{r}' \quad (5)$$

where  $\mathbf{G}^{22}$  denotes the (pp,pp) component of the Green's function and  $F$  is the external perturbing field associated with the addition of two particles.

The residual interaction in the pp,pp channel is the pairing interaction. However, when solving the Bethe-Salpeter (BS) equation, the Green's functions  $G$  and the residual interaction are 3x3 matrices, with ph, pp and hh dimensions (Eq. (4)). Solving the BS equation couples these dimensions. Therefore, there is for instance an effect of the ph,pp component of the residual interaction on the pp,pp channel.

In the QRPA calculations the full HFB quasiparticle spectrum up to 60 MeV is included. These states are used to construct the unperturbed Green's function  $\mathbf{G}_0$ . The residual interaction is derived from the two-body force used in HFB according to Eq. (4). The contribution given by the velocity-dependent terms of the Skyrme force to the residual interaction is calculated in the Landau-Migdal approximation, which is shown to be accurate [19]. The strength function for the two-neutron

transfer is calculated using Eq. (5). The unperturbed Green's function is calculated with an averaging interval equal to 0.15 MeV. All details can be found in Ref. [14].

The response function is calculated for the pp channel. All the calculations are performed in a box of size 22.5 fm. It should be noted that exact continuum treatment is heavy, especially for nuclei such as Sn isotopes. Moreover the aim is not to study the impact of the continuum treatment (see [14] for such a study). Finally the Sn isotopes under study are far from the drip line, and continuum effects are expected to play a negligible role.

## B. Unperturbed response results

The HFB solutions are used in the QRPA scheme to analyze self-consistently the excitation modes associated to the pair transfer reactions. Since we study here two-neutron transfers, we focus on the neutron HFB quasiparticle states that are used to construct the elementary configurations of the excited modes. We work with positive-energy quasiparticle states. Once calculated the quasiparticle spectrum, it is possible to deduce some properties of the unperturbed response function.

The quasiparticle states with energy less than 6 MeV and an occupation probability  $\leq 80\%$  are presented in Tables II and III for  $^{124}\text{Sn}$  and  $^{136}\text{Sn}$ , respectively. Let us discuss the two cases  $\eta = 0.35$  and  $\eta = 1$  (for  $\eta = 0.65$ , results are similar to those obtained with  $\eta = 0.35$ ). For  $^{124}\text{Sn}$ , in the case of a mixed pairing interaction,  $\eta = 0.35$ , all the quasiparticle states with energy lower than 5 MeV are totally occupied with the exception of a  $h_{11/2}$  state at 1.5 MeV which is 42% occupied. This is the only low-energy state that can contribute to some extent to the excitation mode. The states that are completely empty and can thus contribute more to the excitation are located at higher energies. The first is an  $f_{7/2}$  state at 5.8 MeV. The others have larger energies (at least 1 MeV more). One can thus expect that the unperturbed response profile starts with a peak at twice 5.8 MeV, i.e. at  $\sim 11.6$  MeV (with some small contribution at 3 MeV). In the case of a surface interaction,  $\eta = 1$ , again, all the states between 0 and 5 MeV are occupied with the exception of a  $h_{11/2}$  state at 2.2 MeV (42% of occupation). This time there are several unoccupied states just above 5 MeV, the lowest energy being at 5.4 MeV ( $p_{3/2}$  state). Hence, the unperturbed response is expected to have some structure starting from  $\sim 10.8$  MeV with a small contribution at  $\sim 4.4$  MeV.

For the nucleus  $^{136}\text{Sn}$  the situation is different: there are several low-lying unoccupied states. For  $\eta = 0.35$  the lowest energy for a completely unoccupied state is 1.9 MeV ( $p_{3/2}$  state). At 0.8 MeV one also finds a  $f_{7/2}$  state with 45% of occupation. In the case  $\eta = 1$  the lowest energy for a totally unoccupied state is 1.7 MeV ( $p_{3/2}$  state) and a  $f_{7/2}$  state is found at 1.6 MeV with 32% of occupation. The unperturbed response is expected to start at  $\sim 3.8$  and 3.2 MeV for  $\eta = 0.35$  and 1, respec-

TABLE II: Neutron quasiparticle states with  $E \leq 6$  MeV and occupation less than 80%. The nucleus is  $^{124}\text{Sn}$ .

$\eta$	State	$E$ (MeV)	occ
0.35	h11/2	1.5	0.42
	f7/2	5.8	0.01
0.65	h11/2	1.7	0.42
	f7/2	5.7	0.01
1	h11/2	2.2	0.42
	p3/2	5.4	0.003
	f7/2	5.5	0.02
	p1/2	5.6	0.002
	s1/2	5.7	0.002

TABLE III: Same as in Table II but for  $^{136}\text{Sn}$ .

$\eta$	State	$E$ (MeV)	occ
0.35	f7/2	0.8	0.45
	p3/2	1.9	0.01
	p1/2	2.4	0.006
	f5/2	2.9	0.01
	s1/2	3.3	0.0005
	d5/2	4.0	0.0002
	d3/2	4.1	0.0005
	g9/2	5.6	0.0001
	g7/2	5.6	0.0001
0.65	f7/2	0.9	0.43
	p3/2	1.9	0.02
	p1/2	2.4	0.008
	f5/2	2.9	0.02
	s1/2	3.2	0.0004
	d5/2	3.9	0.0001
	d3/2	3.9	0.0003
	g9/2	5.4	0.0001
	g7/2	5.5	0.00003
1	f7/2	1.6	0.32
	p3/2	1.7	0.02
	p1/2	1.9	0.01
	s1/2	1.9	0.0004
	d5/2	2.6	0.0003
	d3/2	2.6	0.0002
	f5/2	3.0	0.01
	g9/2	4.1	0.0002
	g7/2	4.1	0.0001

tively. In the former case a small contribution at  $\sim 1.6$  MeV is also expected.

In order to disentangle between the various pairing effects, the unperturbed response in the two neutrons addition mode is first shown on Fig. 3 for  $^{124}\text{Sn}$ . The unperturbed response is built on the HFB single quasipar-

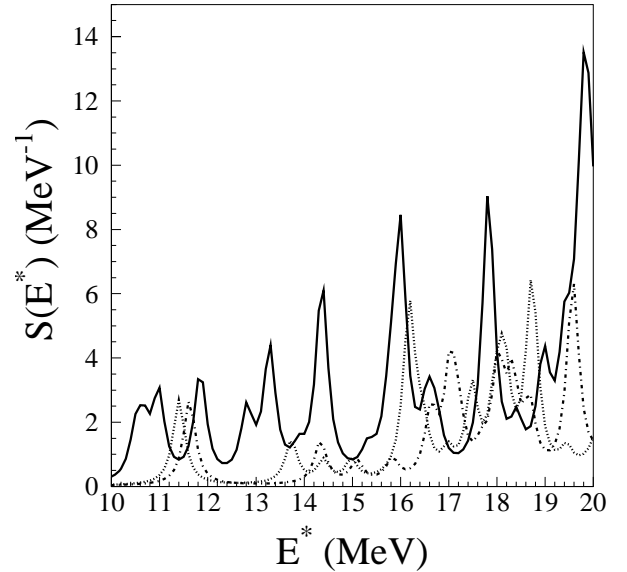


FIG. 3: Unperturbed response function for  $^{124}\text{Sn}$  in the two neutrons  $0^+$  addition mode. The pure surface mode is in solid line, the  $\eta=0.65$  mode is in dotted line, and the  $\eta=0.35$  mode is in dashed-dotted lines

ticle (QP) spectrum, for the three pairing interactions. It should be noted that the spectrum is shown above 10 MeV, because there is only the  $h_{11/2}$  subshell which can welcome two neutrons to make a low energy state: all the other configurations belong to the next major shell (see Table II), explaining this high energy feature of the spectrum, as stated above. For all the mixed pairing interaction, the unperturbed spectrum is similar, showing that both the single quasiparticle energy and wave functions are close to each other in that case. However, in the case of the pure surface pairing, the spectrum is changed. The energies are shifted to lower values, and the overall strength is increased. The lower energy shift can be understood by more single QP states located at low energy. This can be explained by a lower pairing gap and a different energy spectrum found in the HFB self-consistent procedure. The larger magnitude comes from the wave functions, and will be studied with the QRPA response. It can already be stated that the QRPA response will also have more strength at lower energy, due to this peculiar feature of the unperturbed spectrum for the pure surface pairing force.

Fig. 4 shows the unperturbed response for the two neutron addition mode in  $^{136}\text{Sn}$ . In this case, at the beginning of an open neutron shell several low energies configurations can welcome the two neutrons (see Table III). As in the case of  $^{124}\text{Sn}$ , the response exhibits larger strength at low energy in the specific case of the pure surface pairing interaction, compared to others pairing interaction. This is related to the pairing field profile as

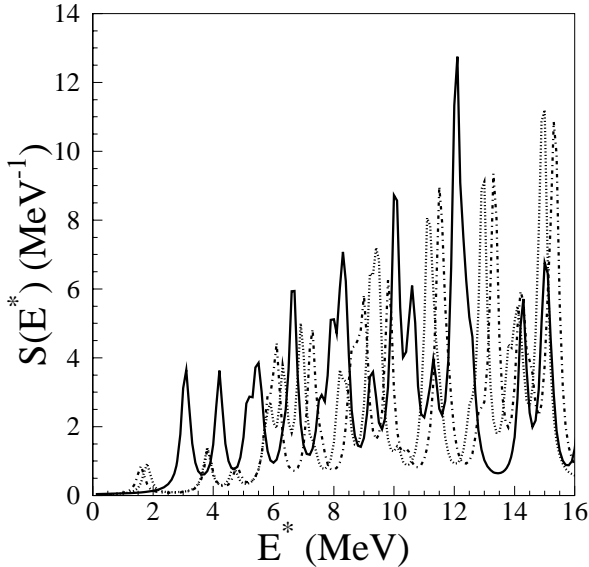


FIG. 4: Unperturbed response function for  $^{136}\text{Sn}$  in the two neutrons  $0^+$  addition mode. The pure surface mode is in solid line, the  $\eta=0.65$  mode is in dotted line, and the  $\eta=0.35$  mode is in dashed-dotted lines.

shown on Fig. 1. It should be noted that in order to clearly see the effect due to the surface pairing, not only the first  $0^+$  state, but also the energy area of a few MeV above should be explored since the results are different from 0 to 4 MeV on Fig. 4.

### C. Perturbed response results

Fig. 5 shows the QRPA response for  $^{124}\text{Sn}$ , with a pure surface and the two mixed interactions. As expected the residual interaction plays a similar role in all the cases, gathering strength and shifting it to lower energy. In the case of  $^{124}\text{Sn}$ , a peak around 9 MeV is the strongest for the surface pairing interaction, to be compared with the one around 10 MeV for the other interactions. Hence it is expected that the pairing vibration transition strength should be larger in the case of a pure surface force. However it is known that it is difficult to accurately describe the magnitude of these transitions, especially for absolute cross section calculations [20]: one-step or sequential two-step process, triton wave function, zero-range or finite-range DWBA have to be considered. The main elements of such a calculation are the optical potentials in both the entrance and the exit channel: they can be either phenomenological such as the Becchetti and Greenlees optical potential [21], or microscopic by using a double folding approach. The other relevant element is the form factor related to the reaction, which includes the information on nuclear structure: it is expected that the relative

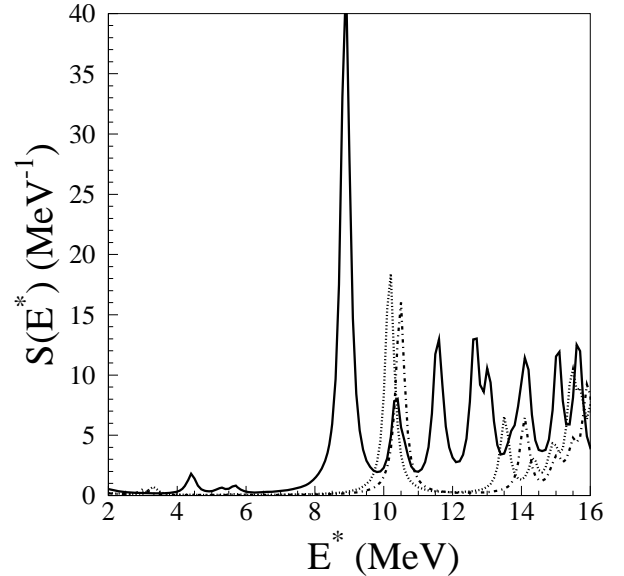


FIG. 5: QRPA response function for  $^{124}\text{Sn}$  in the two neutrons  $0^+$  addition mode. The pure surface mode is in solid line, the  $\eta=0.65$  mode is in dotted line, and the  $\eta=0.35$  mode is in dashed-dotted lines.

magnitude of the angular distributions of two  $0^+$  states remains mainly sensitive to the form factor, related itself to the pairing transition density (Eq. (41) of [13]). It should be noted that in the case of zero-range DWBA, the pairing transition density directly provides the form factor.

The pairing transition density is defined as:

$$\kappa^\nu(\mathbf{r}, \sigma) = \langle 0 | c(\mathbf{r}, \bar{\sigma}) c(\mathbf{r}, \sigma) | \nu \rangle \quad (6)$$

where  $c^\dagger(\mathbf{r}, \bar{\sigma}) = -2\sigma c^\dagger(\mathbf{r}, -\sigma)$  is its time reversed counterpart.

It allows to calculate the form factor in the zero-range DWBA approximation. The pairing transition densities of Fig. 6 show, in the case of  $^{124}\text{Sn}$ , a difference, going from surface to other modes: the transition density decreases at the surface. However the difference is not dramatic and may be overruled by the experimental uncertainties. The larger strength of the 9 MeV peak in the pure surface pairing interaction is due to a larger transition density at the surface.

For the  $^{136}\text{Sn}$  neutron-rich nucleus, the low energy spectrum displayed on Fig. 7 is dramatically changed from using surface to other interactions, on a several MeV area. A three peaks structure appears in the surface case, compared to the two peaks structure of the other cases. The integrated strength is also larger in the surface case.

Fig. 8 and 9 show the corresponding transition densities. They exhibit very different shapes, comparing results with the pure surface pairing interaction and the mixed pairing interaction. Hence  $^{136}\text{Sn}$  is a good test

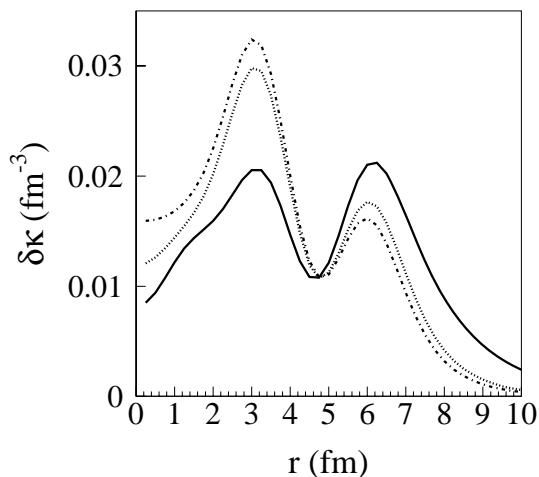


FIG. 6: Neutron transition density in the two neutrons addition mode for  $^{124}\text{Sn}$  for the first peak located at 9-10 MeV. The pure surface mode is in solid line, the  $\eta=0.65$  mode is in dotted line, and the  $\eta=0.35$  mode in dashed-dotted lines.

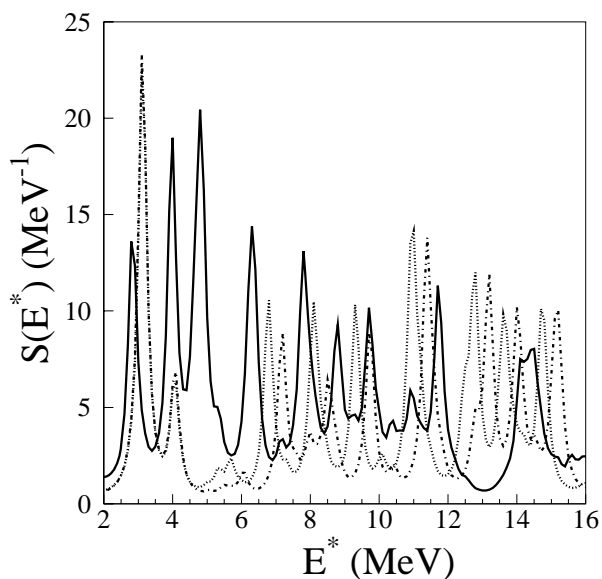


FIG. 7: QRPA response function for  $^{136}\text{Sn}$  in the two neutrons  $0^+$  addition mode. The pure surface mode is in solid line, the  $\eta=0.65$  mode is in dotted line, and the  $\eta=0.35$  mode in dashed-dotted lines.

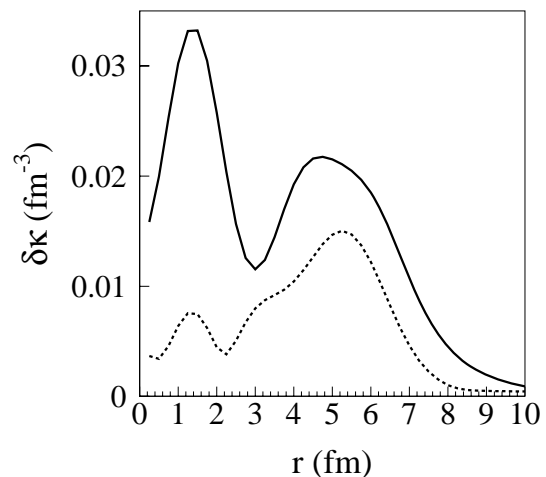


FIG. 8: Neutron transition density in the two neutrons addition mode for  $^{136}\text{Sn}$  for the first two peaks of the strength, in the case of the mixed  $\eta=0.65$  interaction

case to probe the pairing interaction through pairing vibrations. For instance in the case of the most intense peak, the central part is dominant in the transition density for the mixed case, whereas the surface part of the transition density dominates in the pure surface interaction. Hence a measurement of the angular distributions associated with the pairing vibration strength in very neutron rich-nuclei such as  $^{136}\text{Sn}$  seems more decisive to disentangle between the pairing interactions than with  $^{124}\text{Sn}$ . This may be due to the larger neutron skin in  $^{136}\text{Sn}$ , consisting of low density neutron-rich matter.

It has been shown in a previous work how the pairing transition densities allow to calculate the two neutron form factor in order to predict angular distributions for pairing vibrations [14]. Work along these lines should be undertaken in order to bring additional constraints on the pairing interaction. Recently dynamical approaches related to pairing have been developed, such as time-dependent HFB model [15]. They can also be tested using pairing vibrations, through their calculated transition densities, in a similar way than the present method.

#### IV. CONCLUSIONS

The impact of various pairing interactions on pairing vibrations predictions has been analysed for the first time using a HFB+QRPA approach. They should provide a good sensitivity from a pure surface interaction compared to mixed interactions, especially in the case of very

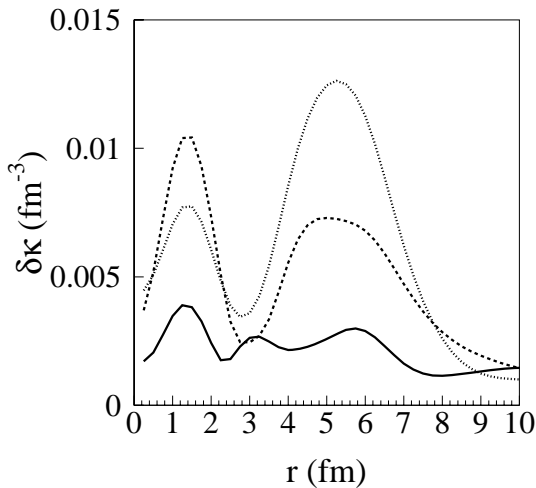


FIG. 9: Neutron transition density in the two neutrons addition mode for  $^{136}\text{Sn}$  for the first 3 peaks of the strength, in the case of the pure surface interaction

neutron-rich nuclei such as  $^{136}\text{Sn}$ . Moreover nuclear matter gap calculations show that the low density range is sensitive to the surface/volume character of the pairing interaction. In the case of exotic nuclei, pairing vibrations are also found more sensitive to the surface/volume type of the pairing interaction, than in the case of stable nuclei. This may be due to the larger extension of the neutron density in very neutron-rich nuclei.

The same study using an isospin dependent pairing interaction will be undertaken. The hope is to come one step closer to a more global pairing interaction, using odd even mass staggering, pairing vibrations, and nuclear matter as constraints. Experimentally, the pairing transition densities can be tested through the form factor used to calculate the two neutrons transfer cross section. This implies to use an adequate reaction model. Work along these lines will be undertaken in an near future.

**Acknowledgements** The authors thank D. Beaumel, M. Matsuo and A. Vitturi for fruitful discussions

- 
- [1] D. J. Dean and M. Hjorth-Jensen, *Rev. Mod. Phys.* **75**, 607 (2003)
  - [2] E. Garrido, P. Sarriguren, E. Moya de Guerra, P. Schuck, *Phys. Rev.* **C60** (1999) 064312.
  - [3] J. Dobaczewski, H. Flocard, and J. Treiner, *Nucl. Phys.* **A 422**, 103 (1984)
  - [4] S. Goriely, M. Samyn, and J. M. Pearson, *Phys. Rev.* **C75**, 064312 (2007)
  - [5] N. Pillet, N. Sandulescu, P. Schuck, *Phys. Rev.* **C76** 024310 (2007).
  - [6] M. Matsuo, K. Mizuyama, Y. Serizawa, *Phys. Rev.* **C71** 064326 (2005).
  - [7] K. Hagino and H. Sagawa, *Phys. Rev.* **C76**, 047302 (2007)
  - [8] M. Matsuo, *Phys. Rev.* **C73** 044309 (2006).
  - [9] K. Hagino, H. Sagawa, J. Carbonell, and P. Schuck *Phys. Rev. Lett.* **99**, 022506 (2007)
  - [10] J. Margueron, H. Sagawa, K. Hagino, *Phys. Rev.* **C76** 064316 (2007).
  - [11] J. Margueron, H. Sagawa, K. Hagino, *Phys. Rev.* **C77** 054309 (2008).
  - [12] R. A. Broglia, O. Hansen and C. Riedel, *Advances in Nuclear Physics, NY Plenum* **6**(1973) 287.
  - [13] W. von Oertzen, A. Vitturi, *Rep. Prog. Phys.* **64**(2001) 1247.
  - [14] E. Khan, N. Sandulescu, Nguyen Van Giai, M. Grasso, *Phys. Rev.* **C69** 014314 (2004).
  - [15] B. Avez, C. Simenel, Ph. Chomaz, *Phys. Rev.* **C78** 044318 (2008).
  - [16] E. Chabanat, P. Bonche, P. Haensel, J. Meyer, R. Schaeffer, *Nucl. Phys.* **A635** (1998) 231.
  - [17] E. Khan, N. Sandulescu, M. Grasso, N. V. Giai, *Phys. Rev.* **C66** (2002) 024309.
  - [18] M. Matsuo, *Proc. of COMEX 3 Conference* (2009)
  - [19] K. Mizuyama, M. Matsuo and Y. Serizawa *Phys. Rev.* **C79** (2009) 024313.
  - [20] M. Igarashi, K. Kubo and K. Yagi, *Phys. Rep.* **199**(1991) 1.
  - [21] F.D. Becchetti and G.W. Greenlees, *Phys. Rev.* **182** (1969) 1190.

## 2.8 Termes non standard dans l'interaction de Skyrme : termes dépendant de la densité de spin.

Les canaux de spin et de spin-isospin de l'interaction nucléaire sont difficiles à explorer dans l'état fondamental des noyaux parce que les noyaux pairs ne sont pas polarisés en spin et les noyaux impairs sont polarisés au plus par les derniers nucléons impairs. Les modes d'excitation de spin et de spin-isospin comme le dipôle magnétique M1 et le mode de Gamow-Teller (GT) permettent de sonder ces canaux de l'interaction nucléaire. Le paramètre de Landau  $G'_0$  a été déduit par l'étude de ces modes [Bo84, Os92, Su99, Wa05, Bo06, Ic06, Fr07]. Les composantes de spin et de spin-isospin se manifestent aussi dans les termes du champ moyen impairs par renversement du temps (time-odd). Ces termes sont très mal connus parce que les ajustements phénoménologiques de la plupart des interactions effectives se font sur des noyaux pairs qui contraignent seulement les termes pairs par rapport au temps (time-even). L'étude des bandes superdéformées des noyaux en rotation rapide pourrait apporter des informations sur les termes impairs [Do95, Do97].

Margueron et collaborateurs [Ma09a] ont introduit dans l'interaction de Skyrme de nouveaux termes dépendant de la densité de spin pour traiter les instabilités ferromagnétiques présentes dans toutes les paramétrisations de Skyrme [Ma02]. En définissant les densités de spin  $\rho_s$  et de spin-isospin  $\rho_{st}$  comme  $\rho_s \equiv \rho_{\uparrow} - \rho_{\downarrow}$  et  $\rho_{st} \equiv \rho_{n\uparrow} - \rho_{n\downarrow} - \rho_{p\uparrow} + \rho_{p\downarrow}$ , les nouveaux termes introduits dans l'interaction de Skyrme sont égaux à :

$$\begin{aligned} V^{\text{add}}(\vec{r}_1, \vec{r}_2) = & \frac{1}{6} t_3^s \left( 1 + x_3^s P_{\sigma} \right) \left[ \rho_s(\vec{R}) \right]^{\gamma_s} \delta(\vec{r}) \\ & + \frac{1}{6} t_3^{\text{st}} \left( 1 + x_3^{\text{st}} P_{\sigma} \right) \left[ \rho_{st}(\vec{R}) \right]^{\gamma_{\text{st}}} \delta(\vec{r}). \end{aligned} \quad (2.10)$$

Dans l'article [Ma09a], les effets de ces termes sont étudiés dans la matière nucléaire et les six nouveaux paramètres sont ajustés pour reproduire dans la matière les paramètres de Landau réalistes extraits d'une matrice G. Comme les densités de spin sont égales à zéro dans les noyaux pairs-pairs, les nouveaux termes peuvent être ajoutés de manière perturbative dans la plupart des interactions de Skyrme qui sont ajustées pour reproduire les propriétés de noyaux pairs.

Nous avons voulu estimer combien ces nouveaux termes affectent les propriétés des états fondamentaux des noyaux impairs et notamment les masses. Pour traiter les noyaux impairs et calculer les densités de spin sans briser la symétrie par renversement du temps, deux approximations sont faites :

- 1) le noyau impair est calculé dans l'approximation de remplissage égal (equal filling) ;
- 2) dans ce cadre, les densités de spin seraient identiquement égales à zéro. Donc, quand les densités de spin sont construites avec les fonctions d'onde des nucléons impairs, nous supposons que, entre les deux états de spin possibles  $\uparrow$  et  $\downarrow$ , l'état  $\uparrow$  est complètement rempli et l'état  $\downarrow$  est vide (ou le contraire). Cette approximation, que nous appelons 'one-spin polarized approximation', fournit une estimation de l'effet maximal de ces nouveaux termes.

Dans le travail [Ma09b] que je fais suivre :

- (i) nous avons analysé en détail l'effet de ces nouveaux termes sur les énergies de liaison des noyaux impairs ;
- (ii) nous avons aussi introduit ces termes dans la formule de masse HFB [Go09], réajusté les paramètres et estimé la qualité du fit de masse.
- (iii) Nous avons enfin analysé les propriétés de l'état fondamental de la matière nucléaire.

# Extended Skyrme interaction (II): ground state of nuclei and of nuclear matter

J. Margueron<sup>1</sup>, S. Goriely<sup>2</sup>, M. Grasso<sup>1</sup>, G. Colò<sup>3</sup> and H. Sagawa<sup>4</sup>

<sup>1</sup>Institut de Physique Nucléaire, Université Paris-Sud, IN2P3-CNRS, F-91406 Orsay Cedex, France

<sup>2</sup>Institut d'Astronomie et d'Astrophysique, CP-226, Université Libre de Bruxelles, 1050 Brussels, Belgium

<sup>3</sup>Dipartimento di Fisica, Università degli Studi and INFN Sez. di Milano, Via Celoria 16, 20133 Milano, Italy

<sup>4</sup>Center for Mathematics and Physics, University of Aizu, Aizu-Wakamatsu, 965-8580 Fukushima, Japan

**Abstract.** We study the effect of time-odd components of the Skyrme energy density functionals on the ground state of finite nuclei and in nuclear matter. The spin-density dependent terms, which have been recently proposed as an extension of the standard Skyrme interaction, are shown to change the total binding energy of odd-nuclei by only few tenths of keV, while the time-odd components of standard Skyrme interactions give an effect that is larger by one order of magnitude. The HFB-17 mass formula based on a Skyrme parametrization is adjusted including the new spin-density dependent terms. A comprehensive study of binding energies in the whole mass table of 2149 nuclei gives a root mean square (rms) deviation of 0.575 MeV between experimental data and the calculated results, which is as good as the original HFB-17 mass formula. From the analysis of the spin instabilities of nuclear matter, restrictions on the parameters governing the spin-density dependent terms are evaluated. We conclude that with the extended Skyrme interaction, the Landau parameters  $G_0$  and  $G'_0$  could be tuned with a large flexibility without changing the ground-state properties in nuclei and in nuclear matter.

PACS numbers: 21.30.Fe, 21.10.Dr, 21.65.-f , 26.60.-c

Submitted to: *J. Phys. G: Nucl. Phys.*

## 1. Introduction

Despite many theoretical and experimental investigations, the spin and the spin-isospin channels in either the ground and the excited states of nuclei are still widely open for future study [1, 2, 3, 4, 5, 6]. It is indeed difficult to probe the spin and the spin-isospin channels of nuclear interaction since the ground states of nuclei are non-spin polarized

in the case of even-even nuclei and at most polarized by the last unpaired nucleons in odd nuclei.

The analysis of spin and spin-isospin collective modes such as magnetic dipole (M1) and Gamow-Teller (GT) states gives access to the nuclear interaction in these channels. The Landau parameter  $G'_0$  has been deduced from the analysis of the GT mode: a model based on Woods-Saxon single-particle states plus one-pion and rho meson exchange interactions gives  $G'_0 = 1.3 \pm 0.2$  (see Ref. [2, 3] and references therein). A slightly different value  $G'_0 = 1.0 \pm 0.1$  was derived from observed GT and M1 strength distributions using the phenomenological energy density functionals DF3 [1, 7]. Anyway, in both cases empirical single-particle energies are used (that is, for states close to the Fermi energy the effective mass  $m^*/m$  is  $\approx 1$ ).

Self-consistent Hartree-Fock (HF) plus Random Phase Approximation (RPA) calculations constitute a somewhat different framework, in which the density of states around the Fermi energy is lower (or, equivalently, the effective mass is about 30% smaller). As compared with the empirical case, the unperturbed particle-hole transitions have larger energies and as a consequence one needs a smaller residual repulsive effect to fit the observed GT peak. It is not surprising, therefore, that self-consistent calculations of the GT resonance, performed using different Skyrme interactions in Ref. [6], point to  $G'_0 \sim 0.6$ . Skyrme interactions are characterized by a spin-isospin  $G'_1$  parameter as well, and specific terms of the effective mean field, like the spin-orbit potential, may also break the simple correlation between the GT properties and the parameter  $G'_0$ . However, as widely used interaction like SLy5 have unrealistic (negative) values of  $G'_0$ , it is undeniable that adding more flexibility to the spin-isospin part of Skyrme forces is useful.

The spin and spin-isospin component of the nuclear interaction is also reflected into the time-odd component of the mean field. The properties of even nuclei give constraints to the time-even component of the mean field while very little is known about properties of the time-odd mean fields. Time-odd components of the mean field compete with pairing correlations in determining the odd-even mass staggering [8]. Fast rotation induces time-odd components in the mean field [9] which could be probed from the measurement of the dynamical moments of superdeformed bands.

In Ref. [10], new spin-density dependent terms have been introduced on top of standard Skyrme forces in order to remove the ferromagnetic instability associated with all Skyrme parameterizations [5]. The new terms retain the simplicity and the good properties of Skyrme interactions for nuclear matter and the ground states of even-even nuclei. However, these new terms slightly change the properties of odd systems. This work aims at studying quantitatively the effects of these new terms on the ground state properties of odd nuclei, in particular the total binding energy and the density distribution. Since these terms contribute only in odd nuclei, both odd-even and odd-odd nuclei are considered in the present study. To provide an approximate maximal estimate of the effects while keeping our model simple, we perform HF calculations with the following approximation to treat odd nuclei. We use the equal filling approximation,

so that the time-reversal symmetry is not broken, but with an additional ansatz. As within this scheme the spin-densities would be by definition equal to zero, when constructing the spin-densities with the wave function of the odd nucleon, we assume that the spin-up state is completely filled while the spin-down state is empty between the two possible spin orientations (or, equivalently, the opposite). We call this procedure for the construction of spin-densities the *one-spin polarized approximation* (OSPA). The OSPA gives an upper value of the contribution of the new terms.

The article is organized as follows: in Sec. II we remind the newly proposed spin-density dependent terms as in Ref. [10]. In Sec. III, we estimate how much these new spin-density dependent terms affect the total binding energy of odd nuclei. In Sec. IV, it will be shown that, introducing these terms in the most predictive HF-Bogoliubov (HFB) mass formula [11], the quality of the mass fit can be recovered with an optimal renormalization of the Skyrme parameters. In Sec. V we will analyze the ground state properties of infinite nuclear matter with respect to spin-polarization and give a range for the parameter of newly introduced spin-density  $x_3^s$ . Finally, conclusions and outlook are given in Sec. VI.

## 2. Extended Skyrme interactions

As described in Ref. [10], the new spin-density dependent terms added to the conventional Skyrme force are of the following form:

$$V^{s,st}(\mathbf{r}_1, \mathbf{r}_2) = \frac{1}{6}t_3^s(1 + x_3^s P_\sigma)[\rho_s(\mathbf{R})]^{\gamma_s} \delta(\mathbf{r}) + \frac{1}{6}t_3^{st}(1 + x_3^{st} P_\sigma)[\rho_{st}(\mathbf{R})]^{\gamma_{st}} \delta(\mathbf{r}) \quad (1)$$

where  $P_\sigma = (1 + \sigma_1 \cdot \sigma_2)/2$  is the spin-exchange operator,  $\mathbf{r} = \mathbf{r}_1 - \mathbf{r}_2$  and  $\mathbf{R} = (\mathbf{r}_1 + \mathbf{r}_2)/2$ . In Eq. (1), we have introduced the spin-density  $\rho_s \equiv \rho_\uparrow - \rho_\downarrow$  and the spin-isospin-density  $\rho_{st} \equiv \rho_{n\uparrow} - \rho_{n\downarrow} - \rho_{p\uparrow} + \rho_{p\downarrow}$ . Spin symmetry is satisfied if the power of the density-dependent terms  $\gamma_s$  and  $\gamma_{st}$  is even.

The total energy  $E_{\text{TOT}}$  in finite nuclei is related to the (local) energy density  $\mathcal{H}(r)$  through

$$E_{\text{TOT}} \equiv \int d^3r \mathcal{H}(r). \quad (2)$$

In the following, we adopt the notation of Ref. [12] where  $\mathcal{H}$  is expressed as the sum of a kinetic term  $\mathcal{K}$ , a zero-range term  $\mathcal{H}_0$ , a density-dependent term  $\mathcal{H}_3$ , an effective-mass term  $\mathcal{H}_{\text{eff}}$ , a finite-range term  $\mathcal{H}_{\text{fin}}$ , spin-orbit and spin-gradient terms ( $\mathcal{H}_{\text{so}}$  and  $\mathcal{H}_{\text{sg}}$ ), and eventually the Coulomb term  $\mathcal{H}_{\text{Coul}}$ . However, the expression for the energy density provided in [12] holds in the case of time-reversal symmetry; in odd nuclei, the energy density  $\mathcal{H}$  acquires also a dependence on the spin-densities  $\rho_s$  and  $\rho_{st}$ , hereafter named  $\mathcal{H}^{\text{odd}}$ , even without additional terms in the force depending on these densities. Expressions for  $\mathcal{H}^{\text{odd}}$  have been derived for instance in Refs. [9, 13] or in Appendix I of Ref. [14]. For the reader's convenience we repeat here, in Appendix A, the expression for  $\mathcal{H}^{\text{odd}}$ .

The additional terms (1) modify the standard  $\mathcal{H}_3$  contribution to be  $\mathcal{H}_3 + \mathcal{H}_3^s + \mathcal{H}_3^{st}$ , where the last two terms read

$$\mathcal{H}_3^s = \frac{t_3^s}{12} \rho_s^{\gamma_s} \left[ \left(1 + \frac{x_3^s}{2}\right) \rho^2 + \frac{x_3^s}{2} \rho_s^2 - \left(x_3^s + \frac{1}{2}\right) (\rho_n^2 + \rho_p^2) - \frac{1}{2} (\rho_{sn}^2 + \rho_{sp}^2) \right], \quad (3)$$

$$\mathcal{H}_3^{st} = \frac{t_3^{st}}{12} \rho_{st}^{\gamma_{st}} \left[ \left(1 + \frac{x_3^{st}}{2}\right) \rho^2 + \frac{x_3^{st}}{2} \rho_s^2 - \left(x_3^{st} + \frac{1}{2}\right) (\rho_n^2 + \rho_p^2) - \frac{1}{2} (\rho_{sn}^2 + \rho_{sp}^2) \right] \quad (4)$$

with  $\rho_{sn} = \rho_{n\uparrow} - \rho_{n\downarrow}$  and  $\rho_{sp} = \rho_{p\uparrow} - \rho_{p\downarrow}$ .

The additional terms to the mean field coming from  $\mathcal{H}_3^s$  and  $\mathcal{H}_3^{st}$  are ( $q = n, p$ )

$$U_q^{s,st} = \frac{t_3^s}{12} \rho_s^{\gamma_s} \left[ (2 + x_3^s) \rho - (1 + 2x_3^s) \rho_q \right] + \frac{t_3^{st}}{12} \rho_{st}^{\gamma_{st}} \left[ (2 + x_3^{st}) \rho - (1 + 2x_3^{st}) \rho_q \right]. \quad (5)$$

where the small contribution of the time-odd component has not been considered.

As already mentioned, the additional contributions to the mean field are zero in even-even nuclei. Since most of the Skyrme interactions are adjusted on (few) even-even nuclei, it is thus possible to add for these interactions the new terms (1) in a perturbative manner. The new four parameters  $t_3^s$ ,  $x_3^s$ ,  $t_3^{st}$  and  $x_3^{st}$  in Eq. (1) have been adjusted in Ref. [10] in order to reproduce the Landau parameters extracted from a G-matrix calculation in uniform matter, while  $\gamma_s = \gamma_{st} = 2$  is imposed by spin symmetry.

Some other interactions, in particular those produced by the Brussels-Montréal group, are globally adjusted by fitting the properties (essentially the nuclear masses) of both even and odd nuclei. In this case, when including the new spin-density terms, a global re-adjustment of the interaction might be necessary.

In the following, we first analyze the effect of the new spin-density dependent terms for a few selected nuclei using the SLy5 Skyrme interaction for which the new spin-density dependent terms are added perturbatively. Later, on the basis of the latest BSk17 Skyrme parameter set, we study the global impact of our new terms on nuclear masses and show that the Skyrme parameters can be refitted to provide almost equivalent properties.

### 3. Ground states of Ca nuclei

According to the OSPA, we define the densities  $\rho_s(r)$  and  $\rho_{st}(r)$  in odd nuclei as

$$\rho_s(r) = \frac{1}{4\pi r^2} \sum_i \varphi_i^2(r) m_s(i), \quad (6)$$

$$\rho_{st}(r) = \frac{1}{4\pi r^2} \sum_i \varphi_i^2(r) m_s(i) m_t(i), \quad (7)$$

where  $m_s(i)$  and  $m_t(i)$  are the spin and isospin z-component for each single nucleon having the wave function  $\varphi_i(r)$ . The last occupied state fully contributes to the spin-density. It is then clear that the OSPA corresponds to maximizing the spin-density and its effects.

Note that if the time-reversal symmetry is not broken (in the filling approximation, for instance) both spin-up and spin-down states must be degenerate and the densities

$\rho_s$  and  $\rho_{st}$  are zero. Since in this work we aim at an approximate and maximal estimate and not at a precise prediction of the effects, we use the HF method with the OSPA to treat odd nuclei.

All calculations in this Section are performed with the SLy5 parameterization for the conventional Skyrme force and the additional parameters for the spin-density terms given in Table 2 of [10]. We choose two systems:  $^{41}\text{Ca}$  and  $^{49}\text{Ca}$ . Being built on top of double magic nuclei, pairing is neglected for these nuclei in this section. Both nuclei are odd-even, then the proton spin-density is zero and the spin-isospin-density is equal to the spin-density for neutrons. For the nucleus  $^{41}\text{Ca}$  the spin-density is built with the neutron  $1f_{7/2}$  wave function while in  $^{49}\text{Ca}$  it is constructed with the neutron  $2p_{3/2}$  wave function. The choice of these nuclei has been driven by the fact that one of the nuclei,  $^{41}\text{Ca}$ , has a spin-density which probes the external region of the nucleus, while for the other nucleus,  $^{49}\text{Ca}$ , the spin-density may probe more the central part. We could not use the OSPA if the single-particle wave functions changed when adding one or two nucleons. Therefore, as a necessary step to proceed with the evaluation of the impact of spin-density dependent terms within the OSPA, we have first checked that the wave function of the neutron state  $1f_{7/2}$  does not change appreciably when passing from the even nucleus  $^{40}\text{Ca}$  to the next even isotope with  $N + 2$  neutrons,  $^{42}\text{Ca}$ . An analogous check has been made for the wave function of the proton state  $1f_{7/2}$  in  $^{40}\text{Ca}$  and in the  $Z + 2$  isotone  $^{42}\text{Ti}$ . Also, the spin-density calculated with the OSPA for  $^{41}\text{Ca}$  has been compared with half the difference of the neutron densities of  $^{42}\text{Ca}$  and  $^{40}\text{Ca}$ , where effects coming from the rearrangement of the deeper state are also included. Very small differences are found, mainly in the central region. Analogous results are obtained for  $^{48}\text{Ca}$ ,  $^{49}\text{Ca}$  and  $^{50}\text{Ca}$ .

The spin-densities in  $^{41}\text{Ca}$  and  $^{49}\text{Ca}$  are plotted in the two panels of Fig. 1 together with the neutron densities of both nuclei. For comparison, the neutron densities of the nearest even-even nuclei  $^{42}\text{Ca}$  and  $^{50}\text{Ca}$  are also displayed. The spin-densities and the neutron densities have been calculated in the two odd-even systems. Two independent calculations have been actually performed with and without the new spin-density dependent terms (1) and only negligible differences have been found so that they are not appreciable in the figures.

Since the contributions to the total energy  $E_{\text{TOT}}$  coming from the spin-density dependent terms (3) and (4) are proportional to the square of the spin densities represented in Fig. 1, these contributions are expected to be negligible as compared to the usual density dependent term  $\mathcal{H}_3$ . To be more quantitative, we have made several calculations for the ground-state energies that are summarized in Tables 1 and 2. The partial contributions to the ground-state energy (2) are written  $E_{\text{MF}} \equiv \int d^3r (\mathcal{H}_0 + \mathcal{H}_3 + \mathcal{H}_{\text{eff}} + \mathcal{H}_{\text{fin}} + \mathcal{H}_{\text{sg}})$ ,  $E_{\text{so}} \equiv \int d^3r \mathcal{H}_{\text{so}}$ ,  $E_{\text{Coul}} \equiv \int d^3r \mathcal{H}_{\text{Coul}}$  and  $E_{\text{kin}} \equiv \int d^3r \mathcal{H}_{\text{kin}}$ , using the notations of Ref. [12]. In Table 1 the total energy, the mean field, the spin-orbit, the Coulomb and the kinetic contributions to the total energy and the single-particle energy (for the neutron states  $1f_{7/2}$  or  $2p_{3/2}$ ) are provided for the odd nuclei  $^{41}\text{Ca}$  and  $^{49}\text{Ca}$  and for the nearest even-even nuclei  $^{42}\text{Ca}$  and  $^{50}\text{Ca}$ . The calculation

for the odd nuclei are performed either with or without the spin-density dependent interaction (1). The difference between the total energy, and its contributions, without and with the corrections  $\Delta E$  is shown to be less than 50 keV in both odd nuclei  $^{41}\text{Ca}$  and  $^{49}\text{Ca}$ . It is interesting to notice that the kinetic energy contributes to reduce the impact of the spin-dependent interaction (1). The spin-orbit and the Coulomb energies are very weakly affected by the spin-density terms.

In Table 2 the total and separate contributions coming from the time-odd terms of the Skyrme interaction (see Eqs. (A.2)-(A.5) in Appendix A) are provided, in the case of the odd nuclei  $^{41}\text{Ca}$  and  $^{49}\text{Ca}$ : these contributions are calculated perturbatively within the OSPA. These terms are classified according to the standard notations and labeled as  $E_0^{\text{odd}}$ ,  $E_{\text{eff+fin+sg}}^{\text{odd}}$  and  $E_3^{\text{odd}}$  which are the contributions from the central, the momentum dependent and the density dependent terms, respectively. The corrections  $E_0^{\text{odd}}$  and  $E_3^{\text{odd}}$  give a dominant and repulsive contribution which increases the total energy while the correction  $E_{\text{eff+fin+sg}}^{\text{odd}}$  is smaller and attractive. The total correction remains quite small, that is, of the order of 0.15-0.3 MeV for both nuclei. Note that the sign of these corrections could change from one Skyrme interaction to another, but such corrections in Table 2 remain larger than  $\Delta E_{\text{TOT}}$  in Table 1. From the quantitative comparison shown in Tables 1 and 2, we can infer, as expected, that the new spin-density dependent terms (1) modify the ground state energies of odd nuclei much smaller than those coming from the time-odd terms of the standard Skyrme interaction.

#### 4. Global adjustment on the nuclear chart

Some Skyrme interactions have been determined by fitting the parameters to essentially all of the available mass data and therefore are constrained to even as well as odd systems. In this case, the new spin-density dependent terms (1) added to the standard Skyrme interaction may modify the quality of the fit. To study the impact of the new terms on the prediction of nuclear masses, we consider now the latest and most accurate HFB-17 mass formula (with a rms deviation of 0.581 MeV on the 2149 measured masses of [17]) obtained with the BSk17 Skyrme force [11].

If we consider the parameters of the additional spin-density dependent interaction (1) determined in Ref. [10], namely  $t_3^s = 2 \times 10^4 \text{ MeV fm}^4$ ,  $t_3^{st} = 1.5 \times 10^4 \text{ MeV fm}^4$ ,  $x_3^s = -2$ ,  $x_3^{st} = 0$  and  $\gamma_s = \gamma_{st} = 2$ , we find that the impact of the new terms on nuclear masses are relatively small, as already discussed in Sect. III. Fig. 2 shows the mass difference obtained by a spherical HFB calculation when the spin terms are added or not. The nuclear masses of odd- $A$  and odd-odd nuclei are globally increased by a value of the order of 100 keV. For light nuclei this correction is the largest and can reach at most 350 keV. As already shown in Ref. [10], the spin-density terms are repulsive and leads to an increase of the rms deviation with respect to all the 2149 measured masses from 0.581 MeV to 0.591 MeV, keeping the good quality of the mass fit. Deterioration can potentially be avoided if the force parameters are re-adjusted to the nuclear mass data.

We have determined a new BSk17st Skyrme force which essentially corresponds to the BSk17 force, but for which the Skyrme as well as the pairing parameters have been slightly renormalized by a new fit on the whole set of mass data. The new parameter set has been built with the idea of evaluating a maximum effect of the new spin-density dependent term (in the same spirit of the OSPA discussed above). The values adopted for the parameters are  $t_3^s = 4 \times 10^4 \text{ MeV fm}^4$ ,  $t_3^{st} = 3 \times 10^4 \text{ MeV fm}^4$ ,  $x_3^s = -0.5$ ,  $x_3^{st} = 0$  and  $\gamma_s = \gamma_{st} = 2$ .  $t_3^s$  and  $t_3^{st}$  are twice larger than in Ref. [10] and this leads to Landau parameters  $G_0 = -0.03$  and  $G'_0 = 0.99$  in symmetric matter at saturation density, whereas the parameter set of Ref. [10] is associated with lower values, namely  $G_0 = -0.36$  and  $G'_0 = 0.75$ . As explained in the Introduction, the value of  $G'_0$  may be considered large in keeping with the effective mass 0.8 of BSk17, yet still quite acceptable for the purpose of the present study. With a value of  $t_3^s$  twice larger than BSk16st, the value of  $x_3^s = -2$  in Ref. [10] has been modified consistently to be  $-0.5$  to keep the contribution to the Landau parameter  $G_0$  in spin-saturated infinite neutron matter identical to the one determined in Ref. [10] [see Eq. (11) of Ref. [10]]. As far as the parameter  $x_3^{st}$  is concerned, there is so far no constraint that could guide us in fixing its value. For this reason the zero value was assumed in Ref. [10]. However, as shown in Sec V, the value of  $x_3^{st}$  influences the stability of the partially polarized neutron matter, i.e., the lower its value, the higher the barrier between the  $S = 0$  and  $S = 1$  configuration. For this reason, as discussed in Sec. V, the value of  $x_3^{st}$  is set to  $-3$ .

The strategy of the mass fit is the same as the one described in Ref. [11, 16]. In particular, the mass model is given from deformed HFB and the pairing force is constructed from the microscopic pairing gaps of symmetric nuclear matter and neutron matter calculated from realistic two- and three-body forces, with medium-polarization effects included. To accelerate the fit, a first estimation of the energy gained by deformation is performed and subtracted to the experimental masses. A first series of parameters are then obtained from the comparison of spherical HFB mass model with the corrected experimental masses. The corrections due to deformation are then reevaluated and a new fit is performed. This fast procedure is repeated until convergence. The isoscalar effective mass  $m_s^*/m$  is constrained to 0.80 and the symmetry energy at saturation  $J$  to be 30 MeV in order to reproduce at best the energy-density curve of neutron matter [15] from realistic two- and three-nucleon forces. Note that the parameters of the additional spin-density interaction are not fitted in this procedure.

The final force parameters labeled BSk17st and resulting from a fit to essentially all mass data are given in Table 3. It can be seen that there is little difference between the parameters of the BSk17 and BSk17st forces; note that the parameters of the rotational and vibrational corrections [16], are identical for both forces. The same holds for the parameters of infinite matter with the incompressibility coefficient  $K_v = 241.7 \text{ MeV}$ , the volume energy coefficient  $a_v = -16.053 \text{ MeV}$  and the isovector effective mass of  $m_v^*/m = 0.784$ , as in Ref. [11].

The rms residuals for the BSk17 and BSk17st sets are compared in Table 4. The inclusion of the new spin-density dependent terms (1) which slightly deteriorated the

accuracy of the BSk17 force leads now even to a small improvement of the predictions by about 6 keV, with the BSk17st force parameters. Both forces have been used to estimate the mass of the 8508 nuclei with  $8 \leq Z \leq 110$  and lying between the proton and neutron drip lines. Differences of no more than roughly  $\pm 0.5$  MeV are found on the entire set. The new spin-density dependent interaction does not destroy the good fit obtained by the original interaction BSk17, and the effect on the masses is rather small.

Finally note that the nuclear binding energies remain extremely insensitive to the value adopted for the parameters  $x_3^s$  and  $x_3^{st}$ . In particular, setting  $x_3^s = -2$  instead of  $-0.5$  decreases the binding energy by no more than 10 keV. Similarly, a change of  $x_3^{st}$  from zero to  $-3$  impact the masses by maximum 8 keV. Therefore, these two parameters should be constrained rather by stability conditions of polarized or non-polarized infinite nuclear matter, as shown in the next Section.

## 5. Ground state of infinite nuclear matter

In Ref. [10], it has been shown that the new spin-density dependent interaction (1) stabilize non-polarized matter with respect to spin-fluctuations. As shown in Fig. 3, with the new terms, the Landau parameters  $G_0$  and  $G'_0$  remains larger than  $-1$  at all densities for SLy5st, LNSst [19] (which include the new terms as parametrized in Ref. [10]) and the BSk17st forces

However, it has not been checked if the true ground state is really that of non-polarized matter. To do so, the energy for different spin-polarizations should be compared with that of non-polarized matter. This is done in the next two subsections for both symmetric nuclear matter and neutron matter

### 5.1. Symmetric nuclear matter

The difference of the binding energy of spin-polarized matter to that of spin-symmetric matter,  $E/A(\delta_S, \rho) - E/A(\delta_S = 0, \rho)$ , is represented in Fig. 4 as a function of the polarization  $\delta_S = (\rho_\uparrow - \rho_\downarrow)/\rho$ . In the left panel, we have represented the binding energy of the BSk17 Skyrme interaction without the new spin-density dependent terms (1). The instability occurs between  $\rho=0.18$  and  $0.2 \text{ fm}^{-3}$ . At  $\rho=0.2 \text{ fm}^{-3}$  the minimum energy is obtained for a polarization  $\delta_S=0.76$ .

The binding energy of BSk17st which includes the spin-density dependent terms is represented in the right panel of Fig. 4. As expected, the energy of non-polarized matter is convex around  $\delta_S = 0$ , but there is a change of convexity for large values of  $\delta_S \sim 0.8$ . We have indeed observed a large influence of the parameter  $x_3^s$  on the binding energy of fully polarized matter. In Fig. 5 are represented the binding energies  $E/A(\delta_S, \rho) - E/A(\delta_S = 0, \rho)$  for the three modified Skyrme interactions BSk17st, LNSst and SLy5st for which we changed the values of the parameter  $x_3^s$ . Its values are indicated in the legend of Fig. 5. We fixed the density  $\rho=0.6 \text{ fm}^{-3}$  to be the highest value where the nuclear Skyrme interaction is applied. For values of the parameter  $x_3^s=-3$  the ground

state of nuclear matter is fully polarized ( $\delta_S = 1$ ) for the interactions BSk17st and LNSst. Increasing the value of the parameter  $x_3^s$  from -3 to 0, the binding energy of fully polarized matter is going up in Fig. 5. There is then a critical value above which non-polarized matter is the ground-state of nuclear matter.

One could obtain an estimate of this critical value by analyzing the contribution of the new spin-density terms (1) in spin-polarized symmetric matter. It reads

$$\mathcal{H}_3^s(sym.) = \frac{t_3^s}{16} \rho^2 \rho_s^{\gamma_s} \left[ 1 + \frac{2x_3^s - 1}{3} \delta_S^2 \right], \quad (8)$$

and  $\mathcal{H}_3^{st}(sym.) = 0$  since  $\rho_{st} = 0$ . The term (8) is zero for the spin-symmetric matter with  $\rho_s = 0$  and is always positive for  $\delta_S = 1$  if one chooses  $x_3^s > -1$ . It is thus clear that one necessary condition for the spin-symmetric matter to be the absolute ground state at all densities is  $x_3^s > -1$ . This is the case for the adopted value of  $x_3^s = -0.5$  for BSk17st. Nevertheless, as shown in Fig. 5 for instance for SLy5st, the stability of spin-symmetric matter could be obtained even if  $x_3^s < -1$  at the density  $\rho = 0.6 \text{ fm}^{-3}$ . At lower density, SLy5st is also stable, but not at higher density.

We remind that from the analysis of the Landau parameters the stability around spin-symmetric matter requires that  $x_3^s < 1$  (see Eq. (11) of Ref. [10]). As a conclusion, one could adjust the parameter  $x_3^s$  inside the range  $-1 \lesssim x_3^s < 1$ .

## 5.2. Neutron matter

The case of pure neutron matter is somehow very peculiar. The correction due to the spin-density dependent terms reads

$$\mathcal{H}_3^s(neut.) = \frac{t_3^s}{24} \rho^2 \rho_s^{\gamma_s} (1 - x_3^s) \left[ 1 - \delta_S^2 \right]. \quad (9)$$

It is then clear that the correction is zero for  $\delta_S = 0$  and also for  $\delta_S = 1$ . This property is related to the anti-symmetrization of the interacting nucleons. Indeed, in fully polarized neutron matter, the quantum numbers for spin and isospin are  $S = 1$  and  $T = 1$  while the new spin-density dependent interaction (1) act in the  $L = 0$  channel. The new spin-density dependent interaction (1) have thus no effect at all in the purely spin-polarized neutron matter. Only odd  $L$  terms could play a role in the fully polarized neutron matter. This property has been used to provide a necessary condition to remove the spin instabilities and lead to the condition  $-5/4 < x_2 < -1$  [20]. This condition has been used in the fitting procedure of SLy5 [12] and it explains the robustness of the spin-symmetric ground state for this interaction. However if more flexibility in the Skyrme parameters is necessary, it might be interesting to introduce an interaction of the following form

$$t_5^s (1 + x_5^s P_\sigma) \mathbf{k}' \rho_s(\mathbf{R}) \cdot \delta(\mathbf{r}) \mathbf{k}. \quad (10)$$

This  $L = 1$  term will not contribute to spin-symmetric matter and could be adjusted to fit the energy of fully polarized matter.

In Fig. 6, it is shown that the new spin-density terms (1) contribute to the binding energy for partially polarized matter and tend to stabilize the state  $\delta_S = 0$ . After the

ferromagnetic transition, the state  $\delta_S = 0$  is not any more the absolute ground state in pure neutron matter. However, the new spin-density terms generate a potential barrier between the non-polarized and fully polarized states. The height of the barrier depends on the chosen parameters of the new spin terms (1) as well as on the neutron matter density. In the right panel of Fig. 6, the top of the barrier at the ferromagnetic transition is located around the polarization  $\delta_S = 1/\sqrt{2}$  with a height (in MeV per nucleon) of

$$\frac{1}{96} (t_3^s(1 - x_3^s) + t_3^{st}(1 - x_3^{st})) \rho^3. \quad (11)$$

So, the higher the density, the higher the barrier. This barrier height is always positive since the curvature of the binding energy around  $\delta_S = 0$  is related to the Landau parameter  $G_{0,NM}$  in neutron matter which is larger than -1 at all densities (see Fig. 3). For the BSk17st force, at  $\rho \simeq \rho_f = 0.19 \text{ fm}^{-3}$  this barrier amounts to about 10 MeV per nucleon.

From Eq. (11), it can also be seen that the parameter  $x_3^{st}$  influences the height of the barrier. The lower  $x_3^{st}$ , the larger the barrier. For BSk17st, we set  $x_3^{st} = -3$  to get a barrier above the non-polarized ground state of the order of 10 MeV per nucleon. This condition is chosen with respect to the theoretical predictions [21, 22, 23, 24] that nuclear matter is spin-symmetric up to reasonable high densities (see for instance discussion in the introduction of Ref. [10]). With a barrier height of the order of 10 MeV per nucleon, newly born neutron stars with typical temperature going from 1 to 5 MeV might not be the site of a ferromagnetic phase transition. The transition towards a non-polarized cold neutron star shall then be stable and the remaining neutron star spin-symmetric. Notice however that despite the theoretical predictions that dense matter is not spin-polarized [21, 22, 23, 24], there are no strong evidences against the occurrence of ferromagnetic phase transition from observation of neutron stars. Indeed, a spin-polarized phase in the core of neutron stars might induce the very huge magnetic fields  $10^{15-16} \text{ G}$  yet unexplained that have been proposed as the driving force for the braking of magnetars [25].

## 6. Conclusions

The occurrence of the spin instability beyond the saturation density is a common feature shared by different effective mean-field approaches such as Skyrme HF, Gogny HF [26] or relativistic HF [27]. The analysis of the spin component of the Skyrme interaction as well as its extensions might thus guide us to a wider understanding of the spin channel in general for nuclear interaction. There are many reason for looking at this channel. For instance for its competition with pairing correlations in the odd-even-mass staggering [8], for rotating superdeformed nuclei [9], for a better description of GT response, and for all applications in astrophysics such as for instance predictions of  $\beta$ -decay half-lives of very neutron rich nuclei produced during the  $r$ -process nucleosynthesis [7], reliable calculation of neutron star crust properties such as ground-states and collective motion [28], for  $0\nu$ -

and  $2\nu$  double beta decay processes, for URCA fast cooling, and also for neutrino mean free path in proto-neutron stars.

In this paper we have carefully analyzed the ground state properties of finite nuclei and infinite matter obtained by the extended Skyrme interactions with the spin-density terms proposed in Ref. [10]. In finite even nuclei, the new spin-density interaction (1) are simply zero and from the OSPA we have shown that these terms has only negligible contributions to the ground-state of odd nuclei. These results has been obtained either by introducing the new spin-density dependent terms in a perturbative way to existing Skyrme interactions such as SLy5st or performing a global adjustment of the parameter set on the nuclear chart. A new mass formula HFB-17st adjusted in the whole isotope chart (2149 nuclei) is obtained with the rms deviation of about 575 keV. From the analysis of the ground state of nuclear matter, a range for the parameter  $x_3^s$  is restricted to  $-1 \lesssim x_3^s < 1$  in order to stabilize the spin-symmetric matter. The case of neutron matter is also discussed and it is shown that the new terms (1) with the relative angular momentum  $L = 0$  have no contribution to fully polarized neutron matter. Thus, it has been shown that by using the extended Skyrme interactions [10], the Landau parameters  $G_0$  and  $G'_0$  could be tuned to realistic values without altering the ground-state properties in odd nuclei as well as of nuclear matter.

## Acknowledgments

S.G. acknowledges financial support from FNRS. The work is partially supported by COMPSTAR, an ESF Research Networking Programme and the Japanese Ministry of Education, Culture, Sports, Science and Technology by Grant-in-Aid for Scientific Research under the program numbers (C) 20540277.

## Appendix A. Time-odd components in the mean field of the Skyrme interaction

In odd nuclei, the energy density  $\mathcal{H}$  acquires a dependence on the spin-densities  $\rho_s$  and  $\rho_{st}$  [9, 13]. Respecting the decomposition of the Skyrme energy functional proposed in Ref. [12], the components of  $\mathcal{H}^{\text{odd}}$  are

$$\mathcal{H}_0^{\text{odd}} = \frac{1}{4}t_0 \left[ (x_0 - \frac{1}{2})\rho_s^2 - \frac{1}{2}\rho_{st}^2 \right], \quad (\text{A.1})$$

$$\mathcal{H}_3^{\text{odd}} = \frac{1}{24}t_3\rho^\gamma \left[ (x_3 - \frac{1}{2})\rho_s^2 - \frac{1}{2}\rho_{st}^2 \right], \quad (\text{A.2})$$

$$\begin{aligned} \mathcal{H}_{\text{fin}}^{\text{odd}} = & \frac{1}{32}[3t_1(1 - x_1) + t_2(1 + x_2)] \left( \rho_{sn} \nabla^2 \rho_{sn} + \rho_{sp} \nabla^2 \rho_{sp} \right) \\ & + \frac{1}{32}[t_2x_2 - 3t_1x_1] \left( \rho_{sn} \nabla^2 \rho_{sp} + \rho_{sp} \nabla^2 \rho_{sn} \right), \end{aligned} \quad (\text{A.3})$$

$$\mathcal{H}_{\text{eff}}^{\text{odd}} = \frac{1}{16}[-t_1(1 - 2x_1) + t_2(1 + 2x_2)]\rho_s\tau_s + \frac{1}{16}[t_2 - t_1]\rho_{st}\tau_{st}, \quad (\text{A.4})$$

$$\mathcal{H}_{\text{sg}}^{\text{odd}} = \frac{1}{16}[t_1(1 - 2x_1) - t_2(1 + 2x_2)]\mathbf{j}_s^2 + \frac{1}{16}[t_1 - t_2]\mathbf{j}_{st}^2, \quad (\text{A.5})$$

where  $\tau_s$  ( $\tau_{st}$ ) is the spin (spin-isospin) kinetic density energy defined as  $\tau_s = \tau_\uparrow - \tau_\downarrow$  ( $\tau_{st} = \tau_{n\uparrow} - \tau_{n\downarrow} - \tau_{p\uparrow} + \tau_{p\downarrow}$ ) and  $\mathbf{j}_s^2$  ( $\mathbf{j}_{st}^2$ ) is the spin (spin-isospin) current.

## References

- [1] I.N. Borzov, S.V. Tolokonnikov, and S.A. Fayans 1984 *Sov. J. Nucl. Phys.* **40**, 732
- [2] F. Osterfeld 1992 *Rev. Mod. Phys.* **64**, 491
- [3] E. T. Suzuki and H. Sakai 1999 *Phys. Lett.* **B455**, 25; M. Ichimura, H. Sakai and T. Wakasa 2006 *Prog. Part. Nucl. Phys.* **56**, 446; T. Wakasa, M. Ichimura and H. Sakai 2005 *Phys. Rev. C* **72**, 067303
- [4] J. Engel, M. Bender, J. Dobaczewski, W. Nazarewicz, and R. Surman 1999 *Phys. Rev. C* **60**, 014302; M. Bender, J. Dobaczewski, J. Engel, and W. Nazarewicz 2002 *Phys. Rev. C* **65**, 054322
- [5] J. Margueron, J. Navarro, and N.V. Giai 2002 *Phys. Rev. C* **66**, 014303
- [6] S. Fracasso and G. Colò 2007 *Phys. Rev. C* **76**, 044307
- [7] I.N. Borzov 2006 *Nucl. Phys.* **A777**, 645
- [8] T. Duguet, P. Bonche, P.-H. Heenen, and J. Meyer 2001 *Phys. Rev. C* **65**, 014310
- [9] J. Dobaczewski and J. Dudek 1995 *Phys. Rev. C* **52**, 1827; *ibid.* 1997 **55**, 3177(E)
- [10] J. Margueron and H. Sagawa, submitted to *J. Phys. G: Nucl. Phys.*
- [11] S. Goriely, N. Chamel, and J.M. Pearson 2009 *Phys. Rev. Lett.* **102**, 152503
- [12] E. Chabanat et al. 1997 *Nucl. Phys.* **A 627**, 710; *ibid.* 1998 **A 635**, 231; *ibid.* 1998 **A 643**, 441
- [13] M. Bender, J. Dobaczewski, J. Engel, and W. Nazarewicz 2002 *Phys. Rev. C* **65**, 054322
- [14] H. Flocard PhD Thesis, unpublished
- [15] B. Friedman and V. R. Pandharipande 1981 *Nucl. Phys.* **A361**, 502
- [16] N. Chamel, S. Goriely and J. M. Pearson 2008 *Nucl. Phys.* **A812**, 72
- [17] G. Audi, A.H. Wapstra, and C. Thibault 2003 *Nucl. Phys.* **A729**, 337
- [18] I. Angeli 2004 *At. Data and Nucl. Data Tables* **87**, 185
- [19] L. G. Cao, U. Lombardo, C. W. Shen and N.V. Giai 2006 *Phys. Rev. C* **73**, 014313
- [20] M. Kutschera and W. Wójcik 1994 *Phys. Lett.* **B 325**, 271
- [21] S. Fantoni, A. Sarsa, and K.E. Schmidt 2001 *Phys. Rev. Lett.* **87**, 181101
- [22] I. Vidaña, A. Polls and A. Ramos 2002 *Phys. Rev. C* **65**, 035804
- [23] I. Vidaña and I. Bombaci 2002 *Phys. Rev. C* **66**, 045801
- [24] I. Bombaci, A. Polls, A. Ramos, A. Rios, and I. Vidaña 2006 *Phys. Lett.* **B 632**, 638
- [25] P. Haensel and S. Bonazzola 1996 *Astron. Astrophys.* **314**, 1017
- [26] J. Margueron PhD thesis 2001, unpublished.
- [27] R. Niembro, P. Bernardos, M. López-Quelle, and S. Marcos 2001 *Phys. Rev. C* **64**, 055802
- [28] M. Grasso, E. Khan, J. Margueron, and N. Van Giai 2008 *Nucl. Phys.* **A 807**, 1

**Table 1.** Total energy, mean field, spin-orbit, Coulomb and kinetic contributions to the total energy (third column) and single-particle energy of the neutron state  $1f_{7/2}$  for  $^{41-42}\text{Ca}$  and  $2p_{3/2}$  for  $^{49-50}\text{Ca}$  calculated, for the nearest even nuclei and for the odd nuclei, without/with the spin-dependent terms (1) in the mean field.  $\Delta E$  is the difference of energy with and without the spin-dependent terms (1).

Nucleus	$E_{\text{TOT}}$ (MeV)	$E_{\text{MF}}$ (MeV)	$E_{\text{so}}$ (MeV)	$E_{\text{Coul}}$ (MeV)	$E_{\text{kin}}$ (MeV)	s.p. energy (MeV)
$^{42}\text{Ca}$	-362.591	-1111.434	-9.173	72.023	685.993	-9.66
$^{41}\text{Ca}$	-352.942	-1081.395	-5.259	72.116	661.596	-9.64
$^{41}\text{Ca}$ with (1)	-352.918	-1081.359	-5.259	72.115	661.584	-9.64
$\Delta E$	0.024	0.036	0.000	-0.001	-0.012	
$^{50}\text{Ca}$	-429.654	-1326.381	-33.958	70.905	859.779	-5.84
$^{49}\text{Ca}$	-423.876	-1305.865	-33.639	71.105	844.523	-5.70
$^{49}\text{Ca}$ with (1)	-423.825	-1305.754	-33.634	71.102	844.461	-5.70
$\Delta E$	0.051	0.111	0.005	-0.003	-0.062	

**Table 2.** Total and separate contributions to the energy from the time-odd (spin symmetry breaking) terms of the SLy5 Skyrme interaction [14, 13].

Nucleus	$E_{\text{TOT}}^{\text{odd}}$ (MeV)	$E_0^{\text{odd}}$ (MeV)	$E_{\text{eff+fin+sg}}^{\text{odd}}$ (MeV)	$E_3^{\text{odd}}$ (MeV)
$^{41}\text{Ca}$	0.329	0.196	-0.007	0.140
$^{49}\text{Ca}$	0.151	0.187	-0.176	0.140

**Table 3.** Parameter sets for BSk17 and BSk17st: the first 15 lines give the Skyrme and additional spin parameters, the 16th the spin-orbit term, the 17th to 20th lines the pairing parameters and the last 4 lines the Wigner correction [16]. See the text and Ref. [11] for more details

	BSk17	BSk17st
$t_0$	-1837.33	-1837.19
$t_1$	389.102	388.916
$t_2$	-3.1742	-5.3076
$t_3$	11523.8	11522.7
$t_3^s$	0	40000
$t_3^{st}$	0	30000
$x_0$	0.411377	0.410279
$x_1$	-0.832102	-0.834832
$x_2$	49.4875	29.0669
$x_3$	0.654962	0.655322
$x_3^s$	0	-0.5
$x_3^{st}$	0	-3
$\gamma$	0.3	0.3
$\gamma^s$	-	2
$\gamma^{st}$	-	2
$W_0$	145.885	146.048
$f_n^+$	1.000	1.000
$f_n^-$	1.044	1.045
$f_p^+$	1.055	1.059
$f_p^-$	1.050	1.059
$V_W$	-2.00	-2.06
$\lambda$	320	410
$V'_W$	0.86	084
$A_0$	28	28

**Table 4.** Rms ( $\sigma$ ) deviations between experimental data [17] and HFB-17 or HFB17st predictions. The first line refers to all the 2149 measured masses  $M$ , the second to the masses  $M_{nr}$  of the subset of 185 neutron-rich nuclei with  $S_n \leq 5.0$  MeV, the third to the 1988 measured neutron separation energies  $S_n$  and the fourth to 1868 measured beta-decay energies  $Q_\beta$ . The fifth line shows the comparison with the 782 measured charge radii [18]. Note that units for energy and radius are MeV and fm, respectively.

	HFB-17	HFB-17st
$\sigma(2149 M)$	0.581	0.575
$\sigma(M_{nr})$	0.729	0.738
$\sigma(S_n)$	0.506	0.495
$\sigma(Q_\beta)$	0.583	0.585
$\sigma(R_c)$	0.0300	0.0302

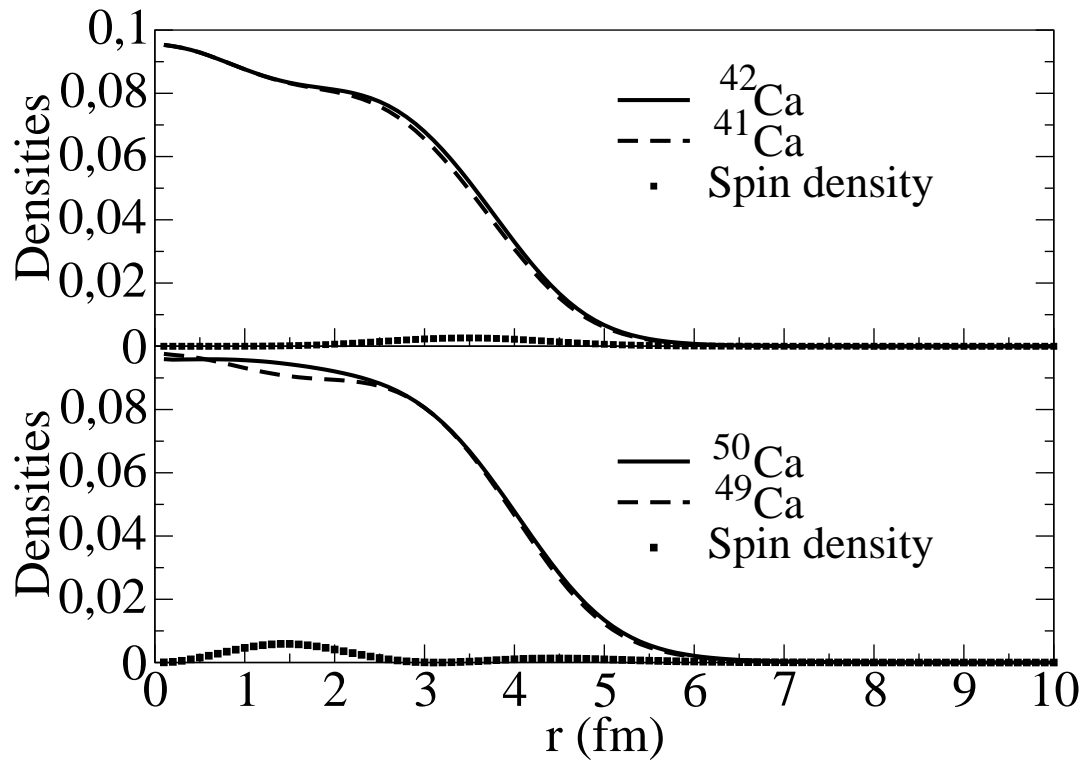


**Figure 1.** Top panel: neutron density of  $^{42}\text{Ca}$  (solid line) and  $^{41}\text{Ca}$  (dashed line) and spin-density in  $^{41}\text{Ca}$  (squares). The densities are given in units of  $\text{fm}^{-3}$ . Bottom panel: the same as top panel, but for  $^{50}\text{Ca}$  and  $^{49}\text{Ca}$ .

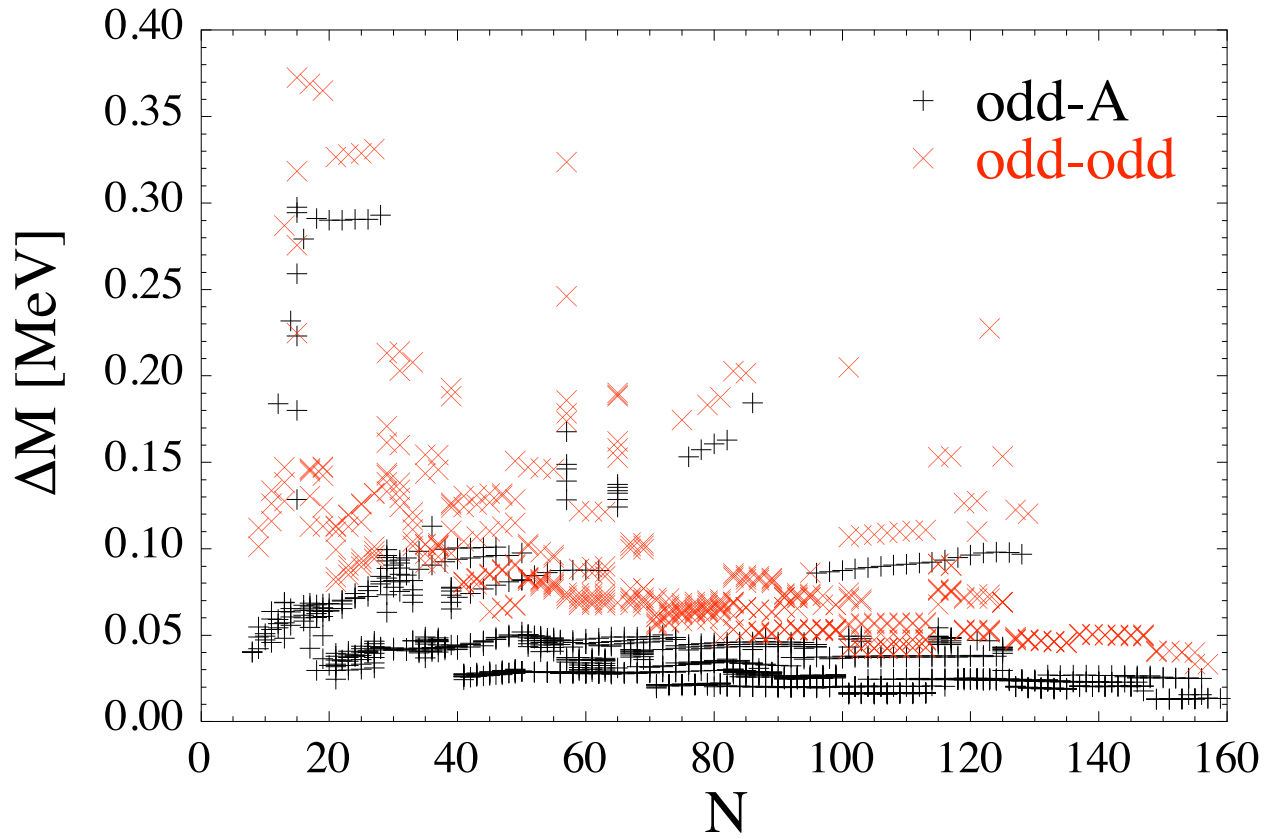


**Figure 2.** Difference between the nuclear mass of odd-A and odd-odd nuclei obtained with the BSk17 force with and without the additional spin-density dependent terms. The calculation is made here assuming spherical symmetry.

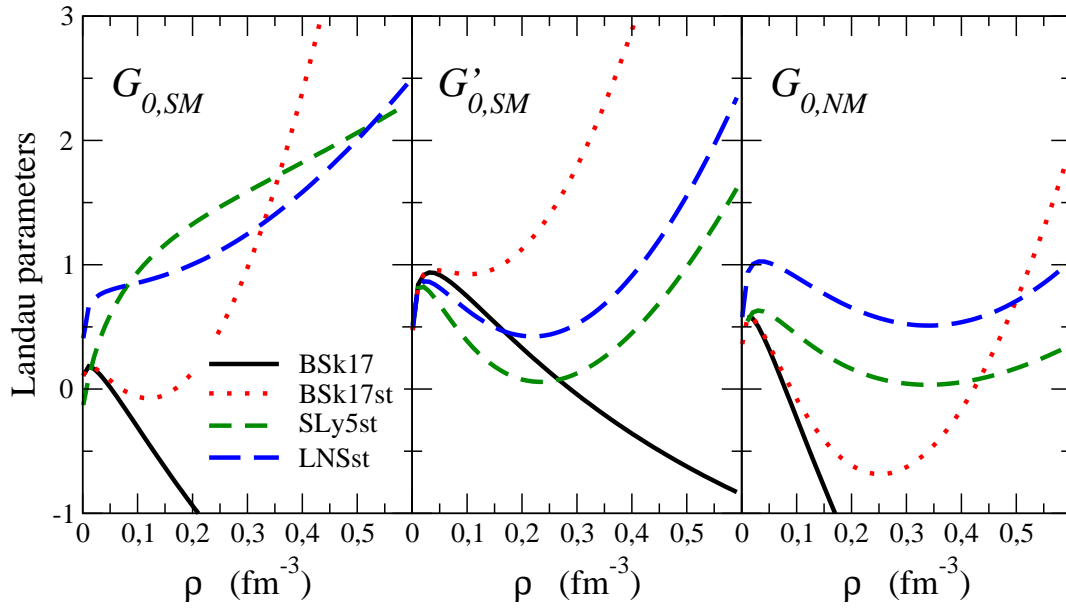


**Figure 3.** Landau parameters for spin and spin-isospin channels as a function of density. The left panel and middle panels show  $G_0$  and  $G'_0$ , respectively, in symmetric nuclear matter and the right panel  $G_0$  in neutron matter. The SLy5st and LNSst curves correspond to SLy5 and LNS standard Skyrme forces with the additional spin-density dependent terms, respectively [10]. The interactions BSk17 and BSk17st are described in Sect. IV.

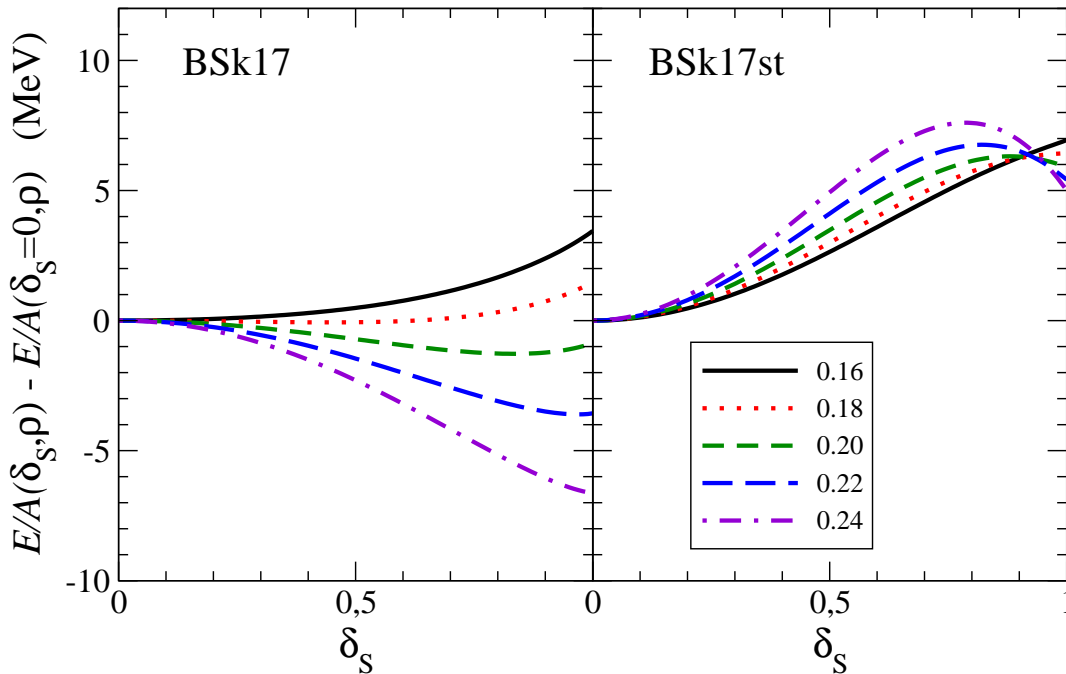


**Figure 4.** Difference between the binding energies  $E/A(\delta_S, \rho) - E/A(\delta_S = 0, \rho)$  in symmetric matter for BSk17 and BSk17st Skyrme interaction as a function of the spin polarization  $\delta_S = (\rho_\uparrow - \rho_\downarrow)/\rho$  for the different densities, as indicated in the legend (in units of  $\text{fm}^{-3}$ ).

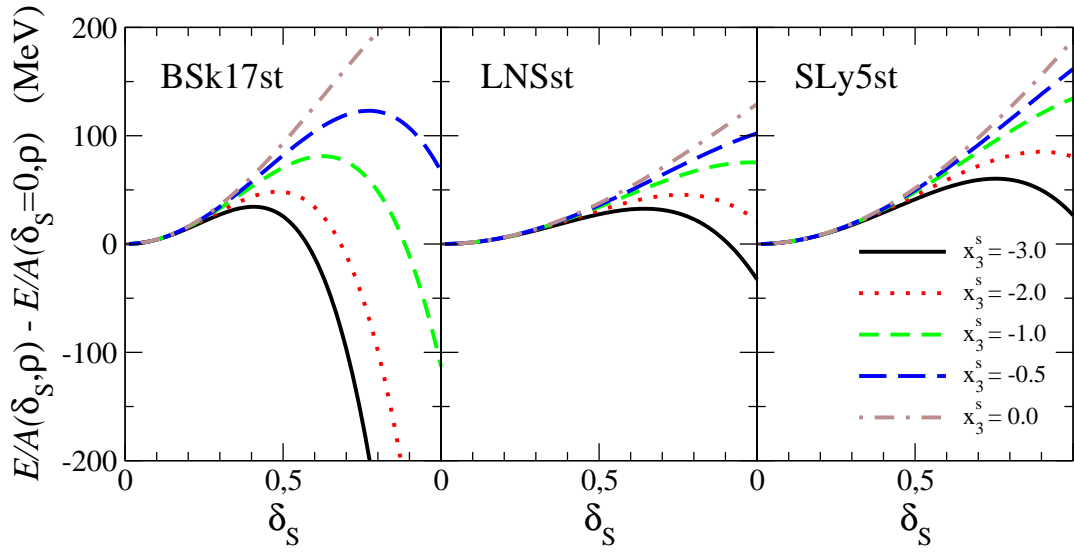


**Figure 5.** Difference between the binding energies  $E/A(\delta_S, \rho) - E/A(\delta_S = 0, \rho)$  in symmetric matter for BSk17st, LNSst and SLy5st Skyrme interactions as a function of the spin polarizations and for  $\rho = 0.6 \text{ fm}^{-3}$ . A different value from 0.0 to  $-3.0$  for the parameter  $x_3^s$  is adopted for each line.

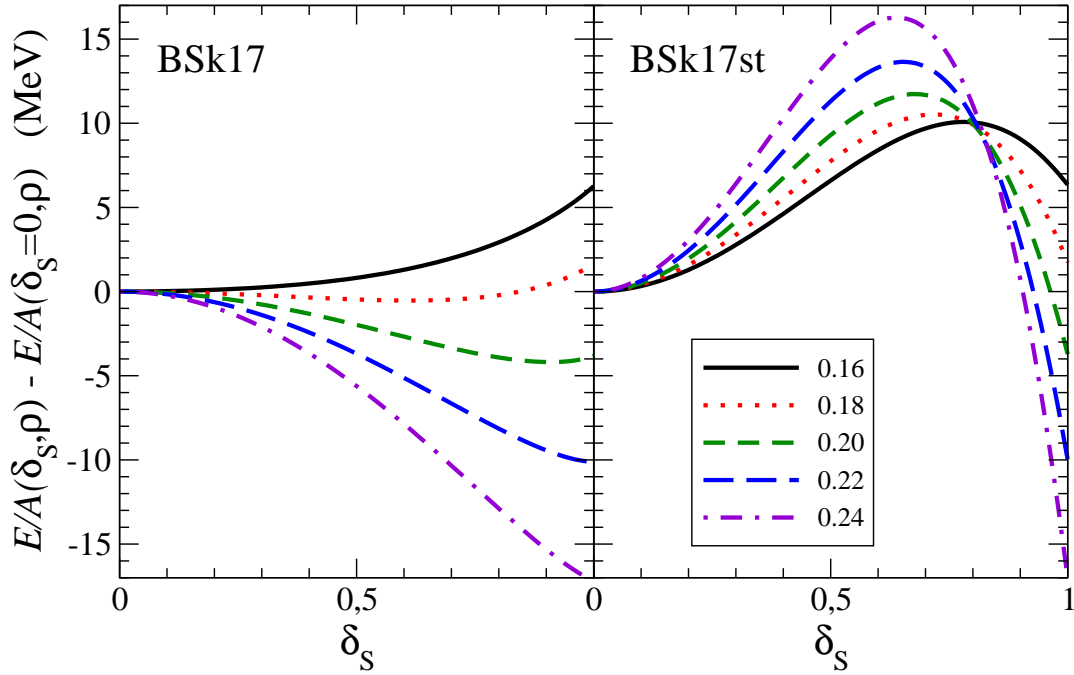


**Figure 6.** Same as Fig. 4, but for neutron matter.

## 2.9 Les résultats microscopiques de champ moyen : ingrédients importants dans les études de réactions

Une manière différente d'utiliser et de tester les résultats microscopiques de champ moyen est de faire des applications dans le domaine des réactions nucléaires, notamment, par exemple, pour l'évaluation des sections efficaces.

Les densités neutroniques et protoniques sont des ingrédients nécessaires dans les modèles de folding pour la construction des potentiels optiques. Dans un des articles reportés dans la Section 2.4 [Be06], un modèle de folding utilisant un potentiel optique microscopique (avec une interaction nucléon-nucléon dépendante de la densité et basée sur l'interaction M3Y) a été adopté. L'expérience effectuée à Ganil pour tester le rapport des contributions neutronique et protonique au premier état  $2^+$  de  $^{22}\text{O}$  a été analysée avec ce potentiel microscopique. J'ai souligné que ce travail a montré l'existence de la fermeture de couche  $N=14$  dans  $^{22}\text{O}$ .

Dans la Section 2.6, j'ai présenté une analyse des modes de transfert de paires et j'ai mentionné un travail en cours dans lequel nous sommes en train de calculer les sections efficaces associées aux transferts de paires pour analyser l'effet du choix de l'interaction d'appariement sur les distributions angulaires.

Je mentionne ici un autre travail où un modèle de folding avec un potentiel optique microscopique a été utilisé [Kho03, Kho04]. Les densités des isotopes de O et de C calculées avec HFB (avec inclusion des états du continuum comme états de diffusion) ont été les ingrédients microscopiques provenant du champ moyen. Dans l'article [Kho04], dans le cadre de la DWIA (distorted wave impulse approximation), les sections efficaces d'interaction  $\sigma_I$  et totales de réaction  $\sigma_R$  ont été calculées en utilisant des potentiels optiques microscopiques obtenus avec un modèle de folding. Une cible de  $^{12}\text{C}$  et des projectiles stables et instables de He, Li, C et O ont été considérés. Dans le modèle de folding, les densités nucléoniques obtenues microscopiquement pour la cible et les projectiles de C et O ont été utilisées. Dans le même modèle, la matrice T de Franey et Love [Fr85] (paramétrisation de l'interaction nucléon-nucléon libre) a été choisie. Ce choix est justifié par l'énergie très élevée en jeu ( $E_{\text{lab}} \sim 0.8$  et  $1$  GeV). Les sections efficaces  $\sigma_I$ , calculées pour les noyaux stables, reproduisent bien les résultats expérimentaux correspondants (différences de 1-2 %). Je fais suivre l'article [Kho04].

# Microscopic calculation of the interaction cross section for stable and unstable nuclei based on the nonrelativistic nucleon-nucleon $t$ matrix

Dao T. Khoa\* and Hoang Sy Than

*Institute for Nuclear Science & Technique, VAEC, P. O. Box 5T-160, Nghia Do, Hanoi, Vietnam*

Tran Hoai Nam

*Department of Physics, Hanoi University of Natural Sciences, 334 Nguyen Trai Street, Thanh Xuan, Hanoi, Vietnam*

Marcella Grasso and Nguyen Van Giai

*Institut de Physique Nucléaire, IN2P3-CNRS, 91406 Orsay Cedex, France*

(Received 1 August 2003; published 19 April 2004)

Fully quantal calculations of the total reaction cross sections  $\sigma_R$  and interaction cross sections  $\sigma_I$ , induced by stable and unstable He, Li, C, and O isotopes on  $^{12}\text{C}$  target at  $E_{\text{lab}} \approx 0.8$  and 1 GeV/nucleon have been performed, for the first time, in the distorted wave impulse approximation (DWIA) using the microscopic *complex* optical potential and inelastic form factors given by the folding model. Realistic nuclear densities for the projectiles and  $^{12}\text{C}$  target as well as the complex  $t$ -matrix parametrization of free nucleon-nucleon interaction by Franey and Love were used as inputs of the folding calculation. Our *parameter-free* folding + DWIA approach has been shown to give a very good account (within 1–2%) of the experimental  $\sigma_I$  measured at these energies for the stable, strongly bound isotopes. With the antisymmetrization of the dinuclear system properly taken into account, this microscopic approach is shown to be more accurate than the simple optical limit of Glauber model that was widely used to infer the nuclear radii from the measured  $\sigma_I$ . Therefore, the results obtained for the nuclear radii of neutron-rich isotopes under study can be of interest for further nuclear structure studies.

DOI: 10.1103/PhysRevC.69.044605

PACS number(s): 24.10.Eq, 24.10.Ht, 24.50.+g, 25.60.Bx

## I. INTRODUCTION

Since 1980s the radioactive ion beams have been used intensively to measure the total reaction cross sections and interaction cross sections induced by unstable nuclei on stable targets (see a recent review in Ref. [1]) which serve as an important data bank for the determination of nuclear sizes. The discovery of exotic structures of unstable nuclei, such as neutron halos or neutron skins, are among the most fascinating results of this study.

The theoretical tool used dominantly by now to analyze the interaction cross sections measured at energies of several hundred MeV/nucleon is the Glauber model [2,3] which is based on the eikonal approximation. This approach provides a simple connection between the ground state densities of the two colliding nuclei and the total reaction cross section of the nucleus-nucleus system, and has been used, in particular, to deduce the nuclear density parameters for the neutron-rich halo nuclei [4].

In general, the total reaction cross section  $\sigma_R$ , which measures the loss of flux from the elastic channel, must be calculated from the transmission coefficient  $T_l$  as

$$\sigma_R = \frac{\pi}{k^2} \sum_l (2l+1) T_l, \quad (1)$$

where  $k$  is the relative momentum (or wave number). The summation is carried over all partial waves  $l$  with  $T_l$  determined from the elastic  $S$  matrix as

$$T_l = 1 - |S_l|^2. \quad (2)$$

In the standard optical model (OM), the quantal  $S$ -matrix elements  $S_l$  are obtained from the solution of the Schrödinger equation for elastic nucleus-nucleus scattering using a *complex* optical potential. At low energies, the eikonal approximation is less accurate and, instead of Glauber model, the OM should be used to calculate  $\sigma_R$  for a reliable comparison with the data. At energies approaching 1 GeV/nucleon region, there are very few elastic scattering data available and the choice of a realistic optical potential becomes technically difficult, especially for unstable nuclei. Perhaps, this is the reason why different versions of Glauber model are widely used to calculate  $\sigma_R$  at high energies. Depending on the structure model for the nuclear wave functions used in the calculation, those Glauber model calculations can be divided into two groups: the calculations using a simple optical limit of Glauber model (see Ref. [1] and references therein) and the more advanced approaches where the few-body correlation and/or breakup of a loosely bound projectile into a core and valence (halo) nucleons are treated explicitly [3,5,6].

In the present work, we explore the applicability of the standard OM to calculate the total reaction cross section (1) induced by stable and unstable beams at high energies using the microscopic optical potential predicted by the folding model. The basic inputs of a folding calculation are the densities of the two colliding nuclei and the effective nucleon-nucleon ( $NN$ ) interaction [7]. At low energies, a realistic density-dependent  $NN$  interaction [8] based on the M3Y in-

\*Electronic address: khoa@vaec.gov.vn

teraction [9] has been successfully used to calculate the  $\alpha$ -nucleus and nucleus-nucleus optical potential [10]. This interaction fails, however, to predict the shape of the  $\alpha$ -nucleus optical potential as the bombarding energy increases to about 340 MeV/nucleon [11]. On the other hand, at incident energies approaching a few hundred MeV/nucleon the  $t$ -matrix parametrization of free  $NN$  interaction was often used in the folding analysis of proton-nucleus scattering [12,13]. The use of the  $t$ -matrix interaction corresponds to the so-called *impulse approximation* (IA), where the medium modifications of the  $NN$  interaction are neglected [14].

In the present folding calculation we adopt a local representation of the free  $NN$   $t$  matrix developed by Franey and Love [13] based on the experimental  $NN$  phase shifts. The folded optical potentials and inelastic form factors are used further in the distorted wave impulse approximation (DWIA) to calculate  $\sigma_R$  and interaction cross section  $\sigma_I$ , induced by stable and unstable He, Li, C, and O isotopes on  $^{12}\text{C}$  target at bombarding energies around 0.8 and 1 GeV/nucleon. Since relativistic effects are significant at high energies, the relativistic kinematics are taken into account properly in both the folding and DWIA calculations. To clarify the adequacy and possible limitation of the present folding model, we also discuss the main approximations made in our approach and compare them with those usually assumed in the Glauber model.

Given the realistic nuclear densities and validity of IA, the folding approach presented below in Sec. II is actually parameter-free and it is necessary to test first the reliability of the model by studying the known stable nuclei before going to study unstable nuclei. Such a procedure is discussed briefly in Sec. III. Then,  $\sigma_I$  measured for the neutron-rich He, Li, C, and O isotopes are compared with the results of calculation and the sensitivity of nuclear radii to the calculated  $\sigma_I$  is discussed. The discrepancy between  $\sigma_I^{\text{calc}}$  and  $\sigma_I^{\text{expt}}$  found for some light halo nuclei is discussed in detail to indicate possible effects caused by the dynamic few-body correlation. Conclusions are drawn in Sec. IV.

## II. FOLDING MODEL FOR THE COMPLEX NUCLEUS-NUCLEUS OPTICAL POTENTIAL

The details of the latest double-folding formalism are given in Ref. [10] and we only recall briefly its main features. In general, the projectile-target interaction potential can be evaluated as an energy-dependent Hartree-Fock-type potential of the dinuclear system:

$$U = \sum_{i \in a, j \in A} [\langle ij | v_D | ij \rangle + \langle ij | v_{\text{EX}} | ji \rangle] = V_D + V_{\text{EX}}, \quad (3)$$

where the nuclear interaction  $V$  is a sum of effective  $NN$  interactions  $v_{ij}$  between nucleon  $i$  in the projectile  $a$  and nucleon  $j$  in the target  $A$ . The antisymmetrization of the dinuclear system is done by taking into account the single-nucleon knock-on exchanges.

The direct part of the potential is local (provided that the  $NN$  interaction itself is local), and can be written in terms of the one-body densities,

$$V_D(E, \mathbf{R}) = \int \rho_a(\mathbf{r}_a) \rho_A(\mathbf{r}_A) v_D(E, \rho, s) d^3 r_a d^3 r_A, \quad (4)$$

where  $s = \mathbf{r}_A - \mathbf{r}_a + \mathbf{R}$ .

The exchange part is, in general, nonlocal. However, an accurate local approximation can be obtained by treating the relative motion locally as a plane wave [15]:

$$V_{\text{EX}}(E, \mathbf{R}) = \int \rho_a(\mathbf{r}_a, \mathbf{r}_a + s) \rho_A(\mathbf{r}_A, \mathbf{r}_A - s) \times v_{\text{EX}}(E, \rho, s) \exp\left(\frac{i\mathbf{K}(E, \mathbf{R}) \cdot s}{M}\right) d^3 r_a d^3 r_A. \quad (5)$$

Here  $\rho_a(\mathbf{r}_a) \equiv \rho_a(\mathbf{r}_a, \mathbf{r}_a)$  and  $\rho_a(\mathbf{r}_a, \mathbf{r}_a + s)$  are the diagonal and nondiagonal parts of the one-body density matrix for the projectile, and similarly for the target.  $\mathbf{K}(E, \mathbf{R})$  is the local momentum of relative motion determined as

$$K^2(E, \mathbf{R}) = \frac{2\mu}{\hbar^2} [E_{\text{c.m.}} - \text{Re } U(E, \mathbf{R}) - V_C(\mathbf{R})], \quad (6)$$

$\mu$  is the reduced mass,  $M = aA/(a+A)$  with  $a$  and  $A$  the mass numbers of the projectile and target, respectively. Here,  $U(E, \mathbf{R}) = V_D(E, \mathbf{R}) + V_{\text{EX}}(E, \mathbf{R})$  and  $V_C(\mathbf{R})$  are the total nuclear and Coulomb potentials, respectively. More details on the calculation of the direct and exchange potentials (4) and (5) can be found in Refs. [10,16]. The folding inputs for mass numbers and incident energies were taken as given by the relativistically corrected kinematics [17].

To calculate consistently both the optical potential and inelastic form factor one needs to take into account explicitly the multipole decomposition of the nuclear density that enters the folding calculation [10]:

$$\rho_{JM \rightarrow J'M'}(\mathbf{r}) = \sum_{\lambda\mu} \langle JM \lambda\mu | J'M' \rangle C_{\lambda} \rho_{\lambda}(r) [i^{\lambda} Y_{\lambda\mu}(\hat{\mathbf{r}})]^*, \quad (7)$$

where  $JM$  and  $J'M'$  are the nuclear spin and its projection in the initial and final states, respectively, and  $\rho_{\lambda}(r)$  is the nuclear transition density for the corresponding  $2^{\lambda}$ -pole excitation. In the present work, we adopt the collective-model Bohr-Mottelson prescription [18] to construct the nuclear transition density for a given excitation in the  $^{12}\text{C}$  target as

$$\rho_{\lambda}(r) = -\delta_{\lambda} \frac{d\rho_0(r)}{dr}. \quad (8)$$

Here  $\rho_0(r)$  is the total ground state (g.s.) density and  $\delta_{\lambda}$  is the deformation length of the  $2^{\lambda}$ -pole excitation in the  $^{12}\text{C}$  target.

### A. Impulse approximation and the $t$ -matrix interaction

If the total spin and isospin are zero for one of the two colliding nuclei ( $^{12}\text{C}$  in our case) only the spin- and isospin-independent components of the central  $NN$  forces are necessary for the folding calculation. We discuss now the choice of  $v_{D(\text{EX})}(E, \rho, s)$  for the two bombarding energies of 0.8 and 1 GeV/nucleon. At these high energies, one can adopt the IA

which reduces the effective  $NN$  interaction approximately to that between the two nucleons in vacuum [14]. Consequently, the microscopic optical potential and inelastic form factors can be obtained by folding the g.s. and transition densities of the two colliding nuclei with an appropriate  $t$ -matrix parametrization of the free  $NN$  interaction.

In the present work, we have chosen the nonrelativistic  $t$ -matrix interaction which was developed by Franey and Love [13] based on experimental  $NN$  phase shifts at bombarding energies of 0.8 and 1 GeV. The spin- and isospin-independent direct ( $v_D$ ) and exchange ( $v_{EX}$ ) parts of the central  $NN$  interaction are then determined from the singlet- and triplet-even (SE and TE) and singlet- and triplet-odd (SO and TO) components of the local  $t$ -matrix interaction (see Table I of Ref. [13]) as

$$v_{D(EX)}(s) = \frac{k_a k_A}{16} [3t_{TE}(s) + 3t_{SE}(s) \pm 9t_{TO}(s) \pm 3t_{SO}(s)]. \quad (9)$$

Here  $k_a$  and  $k_A$  are the energy-dependent kinematic modification factors of the  $t$ -matrix transformation [19] from the  $NN$  frame to the  $Na$  and  $NA$  frames, respectively.  $k_a$  and  $k_A$  were evaluated using Eq. (19) of Ref. [12]. The explicit, complex strength of the *finite-range* central  $t$ -matrix interaction (9) is given in terms of four Yukawas [13]. Since the medium modifications of the  $NN$  interaction are neglected in the IA [14], the  $t$ -matrix interaction (9) does not depend on the nuclear density.

### B. Main steps in the calculation of $\sigma_I$

With properly chosen g.s. densities for the two colliding nuclei, the elastic scattering cross section and  $\sigma_R$  are obtained straightforwardly in the OM calculation using the microscopic optical potential (4)–(6). We recall that the interaction cross section  $\sigma_I$  is actually the sum of all particle removal cross sections from the projectile [1] and accounts, therefore, for all processes when the neutron and/or proton number in the *projectile* is changed. As a result,  $\sigma_I$  must be smaller than the total reaction cross section  $\sigma_R$  which includes also the cross section of inelastic scattering to excited states in both the target and projectile as well as cross section of nucleon removal from the target. At energies of several hundred MeV/nucleon, the difference between  $\sigma_R$  and  $\sigma_I$  was found to be a few percent [3,20,21] and was usually neglected to allow a direct comparison of the calculated  $\sigma_R$  with the measured  $\sigma_I$ . Since the experimental uncertainty in the measured  $\sigma_I$  is very small at the considered energies (around 1% for stable projectiles such as  $^4\text{He}$ ,  $^{12}\text{C}$ , and  $^{16}\text{O}$  [1]) neglecting the difference between  $\sigma_R$  and  $\sigma_I$  might be too rough an approximation in comparing the calculated  $\sigma_R$  with the measured  $\sigma_I$  and testing nuclear radius at the accuracy level of  $\pm 0.05$  fm or less [1,22]. In the present work, we try to estimate  $\sigma_I$  as accurately as possible by subtracting from the calculated  $\sigma_R$  the total cross section of the main inelastic scattering channels; namely, we have calculated in DWIA, using the complex folded optical potential and inelastic form factors, the integrated cross sections  $\sigma_{2^+}$  and  $\sigma_{3^-}$  of inelastic scattering to the first excited  $2^+$  and  $3^-$  states of

$^{12}\text{C}$  target at 4.44 and 9.64 MeV, respectively. These states are known to have the largest cross sections in the inelastic proton and heavy ion scattering on  $^{12}\text{C}$  at different energies. The deformation lengths used to construct transition densities (8) for the folding calculation were chosen so that the electric transition rates measured for these states are reproduced with the proton transition density as

$$B(E\lambda\uparrow) = e^2 \left| \int_0^\infty \rho_\lambda^p(r) r^{\lambda+2} dr \right|^2. \quad (10)$$

Using a realistic Fermi distribution for the g.s. density of  $^{12}\text{C}$  (see the following section) to generate the transition densities, we obtain  $\delta_2 \approx 1.54$  fm and  $\delta_3 \approx 2.11$  fm which reproduce the experimental transition rates  $B(E2\uparrow) \approx 41 e^2 \text{ fm}^4$  [23] and  $B(E3\uparrow) \approx 750 e^2 \text{ fm}^6$  [24], respectively, via Eq. (10). Since inelastic scattering to excited states of the unstable projectile is suppressed by a much faster breakup process,  $\sigma_I$  can be approximately obtained as

$$\sigma_I = \sigma_R - \sigma_{\text{Inel}} \approx \sigma_R - \sigma_{2^+} - \sigma_{3^-}. \quad (11)$$

All the OM and DWIA calculations were made using the code ECIS97 [25] with the relativistic kinematics properly taken into account. At the energies around 1 GeV/nucleon the summation (1) is usually carried over up to 800–1000 partial waves to reach the full convergence of the  $S$ -matrix series for the considered nucleus-nucleus systems.

### C. Adequacy and limitation of the folding approach

Since the measured  $\sigma_I$  have been analyzed extensively by different versions of Glauber model and its optical limit (OL) is sometimes referred to as the folding model [6,26], we find it necessary to highlight the distinctive features of the present folding approach in comparison with the OL of Glauber model before going to discuss the results of calculation.

On the level of the nucleus-nucleus optical potential (OP), the present double-folding approach evaluates OP using fully *finite-range*  $NN$  interaction and taking into account the exchange effects accurately via the Fock term in Eq. (3). Therefore, individual nucleons are allowed to scatter after the collision into unoccupied single-particle states only. Sometimes, one discusses these effects as the exchange  $NN$  correlation. An appropriate treatment of the exchange  $NN$  correlation is indispensable not only in the folding calculation of OP and inelastic form factor, but also in the Hartree-Fock (HF) calculations of nuclear matter [27] and of the finite nuclei [28].

To obtain from the double-folding model presented above the simple expression of nucleus-nucleus OP used in the OL of Glauber model one needs to make a “double-zero” approximation which reduces the complex finite-range  $t$ -matrix interaction (9) to a *zero-range* (purely imaginary)  $NN$  scattering amplitude at *zero NN angle*  $t_{NN}(\theta=0^\circ)\delta(s)$  that can be further expressed through the total  $NN$  cross section  $\sigma_{NN}$ , using the optical theorem. As a result, one needs to evaluate in the OL of Glauber model only a simple folding integral over local densities of the two colliding nuclei [6]:

$$U(\mathbf{R}) \rightarrow V_{OL}(\mathbf{R}) = \frac{i\sigma_{NN}}{2} \int \rho_a(\mathbf{R})\rho_A(\mathbf{R}-\mathbf{r}_A)d^3r_A. \quad (12)$$

The prescription (12) is also known as the *tpp* approximation [29] which neglects the off-shell part of the *t* matrix. Besides the inaccuracy caused by the use of zero-range approximation [30], the zero-angle approximation takes into account only the on-shell *t*-matrix at zero momentum transfer [see Eq. (3) in Ref. [12]]. Since the antisymmetrization of  $t_{NN}$  requires an accurate estimation of the *NN* knock-on exchange term which is strongest at *large* momentum transfers ( $q > 6 \text{ fm}^{-1}$  at energies around 0.8 GeV [12,13]), the zero-angle approximation could strongly reduce the strength of the exchange term. A question remains, therefore, whether the *NN* antisymmetry is properly taken into account when one uses the empirical  $\sigma_{NN}$  in the Glauber folding integral (12). A similar aspect has been raised by Brandan *et al.* [31] who found that an *overestimated* absorption in the nucleus-nucleus system (by the *tpp* model) is due to the effects of Pauli principle. To illustrate the importance of the knock-on exchange term, we have plotted in Fig. 1 the *direct* and *exchange* components of the microscopic OP for  ${}^6\text{He}+{}^{12}\text{C}$  system at 790 MeV/nucleon predicted by our double-folding approach using realistic g.s. densities (see the following section) of the two colliding nuclei. One can see that the exchange term of the real OP is repulsive and much stronger than the (attractive) direct term, which makes the total real OP repulsive at all internuclear distances [see panel (a) of Fig. 1]. The exchange term of the imaginary OP is also repulsive but its relative strength is much weaker compared to that of the real OP, and the total imaginary OP remains attractive or *absorptive* at all distances. As a result, the direct part of the imaginary OP is about 10% more absorptive than the total imaginary OP [see panel (b) of Fig. 1]. The total reaction cross section predicted by the complex OP shown in Fig. 1 is  $\sigma_R \approx 727 \text{ mb}$ . This value increases to  $\sigma_R \approx 750 \text{ mb}$  when the exchange potential  $V_{EX}$  is omitted in the OM calculation. Consequently, the relative contribution by the exchange term in  $\sigma_R$  is about 3%. This difference is not small because it can lead to a difference of up to 7% in the extracted nuclear rms radii. Due to an overwhelming contribution by the exchange part of the real OP, the exchange potential affects the calculated elastic scattering cross section (see Fig. 2) much more substantially compared to  $\sigma_R$ , which is determined mainly by the *imaginary* OP.

We will show below a slight (but rather systematic) difference in  $\sigma_R$  values obtained in our approach and the OL of Glauber model that might be due to the exchange effect. We note further that the elastic *S* matrix is obtained in our approach rigorously from the quantal solution of the Schrödinger equation for elastic scattering wave, while the elastic *S* matrix used in the Glauber model is given by the eikonal approximation which neglects the second-derivative term of the same Schrödinger equation.

A common feature of the present folding approach and the OL of Glauber model is the use of single-particle nuclear densities of the projectile and target as input for the calculation, leaving out all few-body correlations to the structure model used to construct the density. This simple ansatz has been referred to as “static density approximation” [5,6]

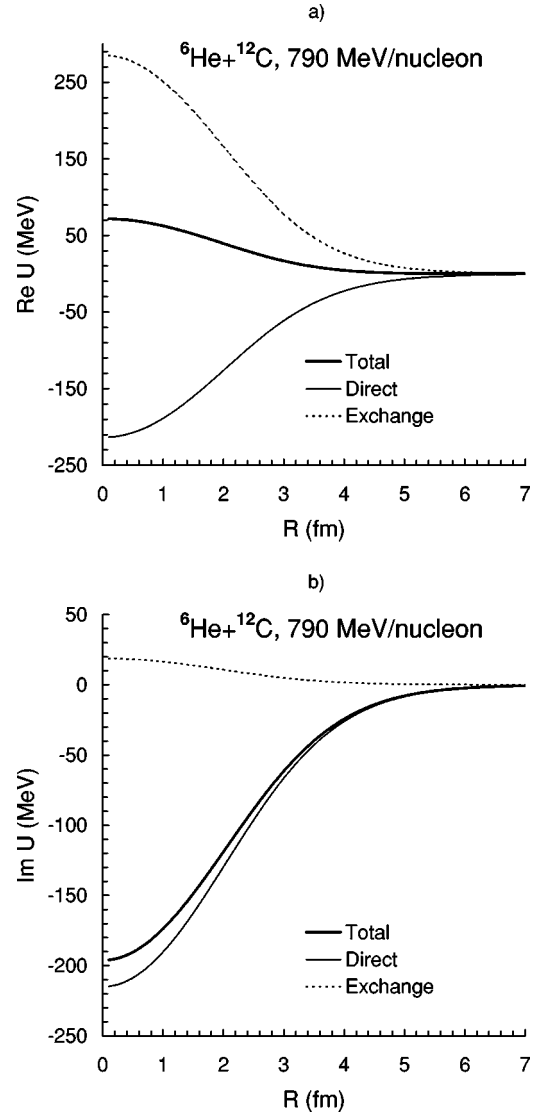


FIG. 1. Radial shape of the *direct*  $V_D$  and *exchange*  $V_{EX}$  parts of the *total* optical potential  $U$  for  ${}^6\text{He}+{}^{12}\text{C}$  system at 790 MeV/nucleon. The real and imaginary part of  $U$  are shown in panels (a) and (b), respectively.

which does not take into account explicitly the dynamic few-body correlation between the core and valence nucleons in a loosely bound projectile while it collides with the target. In the Glauber model, this type of few-body correlation can be treated explicitly [3,5,6] using simple assumptions for the wave functions of the core and valence nucleons as well as that of their relative motion. For unstable nuclei with a well-extended halo structure, such as  ${}^{11}\text{Li}$  or  ${}^6\text{He}$ , such an explicit treatment of the dynamic few-body correlation leads consistently to a smaller  $\sigma_R$ , i.e., to a larger nuclear radius compared to that given by the OL of Glauber model [3,5,6]. On the level of the HF-type folding calculation (3), an explicit treatment of the core and valence nucleons would result in a much more complicated triple-folding formalism which involves the antisymmetrization not only between the projectile nucleons and those of the target, but also between the nucleons of the core and the valence nucleons. Such an ap-

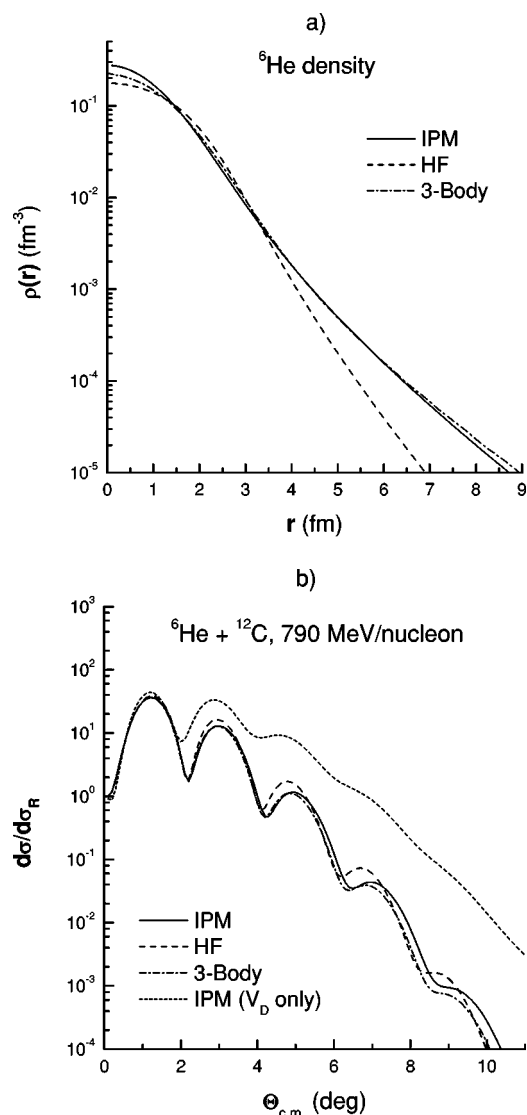


FIG. 2. Three versions of  ${}^6\text{He}$  g.s. density used in the folding calculation [panel (a)] and elastic  ${}^6\text{He} + {}^{12}\text{C}$  scattering cross sections at 790 MeV/nucleon obtained with the corresponding complex folded optical potentials [panel (b)]. The dotted curve in panel (b) is obtained without the exchange part of the OP.

proach would clearly end up with a *nonlocal* OP which will not be easily used with the existing direct reaction codes. The lack of an appropriate treatment of the dynamic few-body correlations remains, therefore, the main limitation of the present folding approach in the calculation of the OP for systems involving unstable nuclei with halo-type structure.

Note that an effective way of taking into account the loose binding between the core and valence nucleons is to add a higher-order contribution from breakup (dynamic polarization potential) to the first-order folded potential [21,32] or simply to renormalize the folded potential to fit the data. However, validity of the IA implies that higher-order multiple scattering or contribution from the dynamic polarization potential is negligible, and the folded OP and inelastic form factor based on the  $t$ -matrix interaction (9) should be used in the calculations without any further renormalization. Therefore, we will discuss below only results obtained with the

unrenormalized folded potentials, keeping in mind possible effects due to the few-body correlation.

### III. RESULTS AND DISCUSSION

#### A. Results for stable ( $N=Z$ ) isotopes

An important step in any experimental or theoretical reaction study with unstable beams is to gauge the method or model by the results obtained with stable beams. Therefore, we have considered first the available data of  $\sigma_1$  induced by stable  ${}^4\text{He}$ ,  ${}^6\text{Li}$ ,  ${}^{12}\text{C}$ , and  ${}^{16}\text{O}$  beams on  ${}^{12}\text{C}$  target [1]. These ( $N=Z$ ) nuclei are strongly bound, and the rms radius of the (point) proton distribution inferred from the elastic electron scattering data [33] can be adopted as the “experimental” nuclear radius if the proton and neutron densities are assumed to be the same. To show the sensitivity of the calculated  $\sigma_1$  to the nuclear radius, we present in Table I results obtained with different choices for the projectile density in each case. We use for the g.s. density of  ${}^{12}\text{C}$  target a realistic Fermi (FM) distribution [16]

$$\rho_0(r) = \rho_0 \{1 + \exp[(r - c)/a]\}, \quad (13)$$

where  $\rho_0 = 0.194 \text{ fm}^{-3}$ ,  $c = 2.214$ , and  $a = 0.425 \text{ fm}$  were chosen to reproduce the shape of shell model density and experimental radius of 2.33 fm for  ${}^{12}\text{C}$ .

${}^4\text{He}$  is a unique case where a simple harmonic oscillator (HO) model can reproduce quite well its ground state density. If one chooses the HO parameter to give  $\langle r^2 \rangle^{1/2} = 1.461 \text{ fm}$  (close to the experimental radius of  $1.47 \pm 0.02 \text{ fm}$ ), then one obtains the Gaussian form adopted in Ref. [7] for  $\alpha$  density. This choice of  ${}^4\text{He}$  density has been shown in the folding analysis of elastic  $\alpha$ -nucleus scattering [16] to be the most realistic. By comparing the calculated  $\sigma_1$  with the data, we find that this same choice of  ${}^4\text{He}$  density gives the best agreement between  $\sigma_1^{\text{calc}}$  and  $\sigma_1^{\text{expt}}$ . Similar situation was found for  ${}^{12}\text{C}$  and  ${}^{16}\text{O}$  isotopes, where the best agreement with the data is given by the densities which reproduce the experimental nuclear radii. Besides a simple Fermi distribution [16], microscopic g.s. densities given by the Hartree-Fock-Bogoliubov (HFB) calculation that takes into account the continuum [34] were also used. The agreement with the data for  ${}^{12}\text{C}$  and  ${}^{16}\text{O}$  given by the HFB densities is around 2%, quite satisfactory for a fully microscopic structure model. We have further used  $sp$ -shell HO wave functions to construct the g.s. densities of  ${}^6\text{Li}$ ,  ${}^{12}\text{C}$ , and  ${}^{16}\text{O}$ . For  ${}^{12}\text{C}$  and  ${}^{16}\text{O}$ , the best agreement with the  $\sigma_1$  data is again reached when the HO parameter is tuned to reproduce the experimental radii.

The agreement is slightly worse for  ${}^6\text{Li}$  compared to  ${}^4\text{He}$ ,  ${}^{12}\text{C}$ , and  ${}^{16}\text{O}$  cases if  ${}^6\text{Li}$  density distribution reproduces the experimental radius. We have first used  ${}^6\text{Li}$  density given by the independent particle model (IPM) developed by Satchler [7,35] which generates realistic wave function for each single-particle orbital using a Woods-Saxon (WS) potential for the bound state problem. The IPM density gives  $\langle r^2 \rangle^{1/2} \approx 2.40 \text{ fm}$  for  ${}^6\text{Li}$ , rather close to the experimental radius of  $2.43 \pm 0.02 \text{ fm}$  inferred from  $(e, e)$  data [33]. The HO density gives the same  $\sigma_1$  as that given by the IPM density if the HO

TABLE I. The total reaction cross section  $\sigma_R$  and interaction cross section  $\sigma_I$  calculated for stable  ${}^4\text{He}$ ,  ${}^6,7\text{Li}$ ,  ${}^{12}\text{C}$ , and  ${}^{16}\text{O}$  nuclei in comparison with  $\sigma_I^{\text{expt}}$  taken from the data compilation in Ref. [1].  $\Delta\sigma_I = |\sigma_I^{\text{calc}} - \sigma_I^{\text{expt}}|/\sigma_I^{\text{expt}}$ .

Nucleus	Energy (MeV/nucleon)	Density model	$\langle r^2 \rangle_{\text{calc}}^{1/2}$ (fm)	Reference	$\langle r^2 \rangle_{\text{expt}}^{1/2}$ (fm)	$\sigma_R^{\text{calc}}$ (mb)	$\sigma_I^{\text{calc}}$ (mb)	$\sigma_I^{\text{expt}}$ (mb)	$\Delta\sigma_I$ (%)
${}^4\text{He}$	790	HO	1.461	[7]	$1.47 \pm 0.02^{\text{a}}$	513	504	$503 \pm 5$	0.2
		HO	1.550	[16]		523	515		2.4
		HO	1.720	[36]		543	536		6.6
${}^6\text{Li}$	790	IPM	2.401	[35]	$2.43 \pm 0.02^{\text{a}}$	722	717	$688 \pm 10$	4.2
		HO	2.401	This work		723	718		4.4
		HO	2.320	This work		709	703		2.2
${}^7\text{Li}$	790	IPM	2.367	[35]	$2.33 \pm 0.02^{\text{b}}$	746	741	$736 \pm 6$	0.7
		HO	2.334	This work		744	739		0.4
${}^{12}\text{C}$	950	FM	2.332	[16]	$2.33 \pm 0.02^{\text{a}}$	854	844	$853 \pm 6$	1.1
		HO	2.332	[16]		853	843		1.1
		HFB	2.446	This work		881	872		2.2
${}^{16}\text{O}$	970	FM	2.618	[16]	$2.61 \pm 0.01^{\text{a}}$	992	981	$982 \pm 6$	0.1
		HO	2.612	[16]		988	978		0.4
		HFB	2.674	This work		1006	997		1.4

<sup>a</sup>rms radius of the proton density given by the experimental charge density [33] unfolded with the finite size of proton.

<sup>b</sup>Nuclear rms radius deduced from the Glauber model analysis of the same  $\sigma_I$  data in the OL approximation [1].

parameter is chosen to give the same radius of 2.40 fm. These two versions of  ${}^6\text{Li}$  density overestimate the  $\sigma_I$  data by about 4%. If the HO parameter is chosen to give  $\langle r^2 \rangle^{1/2} \approx 2.32$  fm, then the agreement with the  $\sigma_I$  data improves to around 2%. This result indicates that our folding + DWIA analysis slightly overestimates the absorption in  ${}^6\text{Li}+{}^{12}\text{C}$  system. Since  ${}^6\text{Li}$  is a loosely bound  $\alpha+d$  system, this few percent discrepancy with the  $\sigma_I$  data might well be due to the dynamic correlation between the  $\alpha$  core and deuteron cluster in  ${}^6\text{Li}$  during the collision which is not taken into account by our approach. Note that a few-body Glauber calculation [6] (which takes into account explicitly the dynamic correlation between  $\alpha$  and  $d$ ) ends up, however, with about the same discrepancy (see Fig. 4 in Ref. [6]).  ${}^6\text{Li}$  remains, therefore, an interesting case for the reaction models to improve their ingredients. For  ${}^7\text{Li}$ , the IPM density [7] gives  $\langle r^2 \rangle_p^{1/2} \approx 2.28$  fm (close to the experimental value of  $2.27 \pm 0.01$  fm [33]) and  $\langle r^2 \rangle_n^{1/2} \approx 2.43$  fm which make the matter radius  $\langle r^2 \rangle^{1/2} \approx 2.37$  fm. As a result,  $\sigma_I$  calculated with the IPM density for  ${}^7\text{Li}$  agrees with the data within less than 1%. In the HO model for  ${}^7\text{Li}$  density, we have chosen the HO parameter for protons to reproduce the experimental radius of 2.27 fm and that for neutrons adjusted by the best agreement with the  $\sigma_I$  data. The best-fit  $\langle r^2 \rangle^{1/2}$  radius then becomes around 2.33 fm.

We conclude from these results that the present folding + DWIA approach and local  $t$ -matrix interaction by Franey and Love [13] are quite suitable for the description of the nucleus-nucleus interaction cross section at energies around 1 GeV/nucleon, with the prediction accuracy as fine as 1–2% for the stable and strongly bound nuclei.

### B. Results for neutron-rich isotopes

Our results for neutron-rich He, Li, C, and O isotopes are presented in Table II. Since  ${}^6\text{He}$  beams are now available

with quite a good resolution, this nucleus is among the most studied unstable nuclei. In the present work we have tested three different choices for  ${}^6\text{He}$  density in the calculation of  $\sigma_I$ . The microscopic  ${}^6\text{He}$  density obtained in a HF calculation [30] has a rather small radius  $\langle r^2 \rangle^{1/2} \approx 2.20$  fm and the calculated  $\sigma_I$  underestimates the data by about 5%. A larger radius of 2.53 fm is given by the density obtained in a consistent three-body formalism [5] and the corresponding  $\sigma_I$  agrees better with the data. Given an accurate  ${}^7\text{Li}$  density obtained in the IPM [7] as shown above and the fact that  ${}^6\text{He}$  can be produced by a proton-pickup reaction on  ${}^7\text{Li}$ , we have constructed the g.s. density of  ${}^6\text{He}$  in the IPM (with the recoil effect properly taken into account [35]) using the following WS parameters for the single-particle states:  $r_0 = 1.25$  fm,  $a = 0.65$  fm for the  $s_{1/2}$  neutrons and protons which are bound by  $S_n = 25$  MeV and  $S_p = 23$  MeV, respectively;  $r_0 = 1.35$  fm,  $a = 0.65$  fm for the  $p_{3/2}$  halo neutrons which are bound by  $S_n = 1.86$  MeV. The WS depth is adjusted in each case to reproduce the binding energy. The obtained IPM density gives the proton, neutron, and total nuclear radii of  ${}^6\text{He}$  as 1.755, 2.746, and 2.460 fm, respectively. This choice of  ${}^6\text{He}$  density also gives the best agreement with the  $\sigma_I$  data. We note that a Glauber model analysis of the elastic  ${}^6\text{He}+p$  scattering at 0.7 GeV/nucleon [37], which takes into account higher-order multiple-scattering effects, gives a best-fit  $\langle r^2 \rangle^{1/2} \approx 2.45$  fm for  ${}^6\text{He}$ , very close to our result. Since elastic  ${}^6\text{He}+{}^{12}\text{C}$  scattering has recently been measured at lower energies [38], we found it interesting to plot the three densities and elastic  ${}^6\text{He}+{}^{12}\text{C}$  scattering cross sections at 790 MeV/nucleon predicted by the corresponding complex folded OP (the radial shape of the OP obtained with the IPM density for  ${}^6\text{He}$  is shown in Fig. 1). As can be seen from Fig. 2, the IPM density has the neutron-halo tail very close to that of the density calculated in the three-body model [5] and they both give a good description of  $\sigma_I$ . The

TABLE II. The same as Table I but for neutron-rich He, Li, C, and O isotopes. Note that  $\langle r^2 \rangle_{\text{calc}}^{1/2}$  given by the HO densities should have about the same uncertainties as those deduced for  $\langle r^2 \rangle_{\text{expt}}^{1/2}$  by the OL of Glauber model.

Nucleus	Energy (MeV/nucleon)	Density model	$\langle r^2 \rangle_{\text{calc}}^{1/2}$ (fm)	Reference	$\langle r^2 \rangle_{\text{expt}}^{1/2}$ (fm)	$\sigma_R^{\text{calc}}$ (mb)	$\sigma_I^{\text{calc}}$ (mb)	$\sigma_I^{\text{expt}}$ (mb)	$\Delta\sigma_I$ (%)
$^6\text{He}$	790	HF	2.220	[30]	$2.48 \pm 0.03^{\text{a}}$	691	686	$722 \pm 6$	5.0
		3-BODY	2.530	[5]		738	733		1.5
		IPM	2.460	This work	$2.45 \pm 0.10^{\text{b}}$	727	722		0.0
$^8\text{He}$	790	COSMA	2.526	[39]	$2.52 \pm 0.03^{\text{a}}$	816	812	$817 \pm 6$	0.6
$^8\text{Li}$	790	HO	2.371	This work	$2.37 \pm 0.02^{\text{a}}$	782	775	$768 \pm 9$	0.9
$^9\text{Li}$	790	HO	2.374	This work	$2.32 \pm 0.02^{\text{a}}$	809	802	$796 \pm 6$	0.7
$^{11}\text{Li}$	790	HO+halo	3.227	This work	$3.12 \pm 0.16^{\text{a}}$	1066	1061	$1060 \pm 10^{\text{c}}$	0.1
		HF	2.868	[30]		971	967		8.8
$^{13}\text{C}$	960	IPM	2.389	[35]	$2.28 \pm 0.04^{\text{a}}$	887	877	$862 \pm 12$	1.7
		HO	2.355	This work		875	866		0.5
$^{14}\text{C}$	965	HFB	2.585	This work	$2.30 \pm 0.07^{\text{a}}$	951	941	$880 \pm 19$	6.9
		IPM	2.417	[35]		910	900		2.3
		HO	2.386	This work		899	888		0.9
$^{15}\text{C}$	740	HO	2.481	This work	$2.40 \pm 0.05^{\text{a}}$	961	952	$945 \pm 10$	0.7
$^{16}\text{C}$	960	HFB	2.724	This work	$2.70 \pm 0.03^{\text{a}}$	1026	1018	$1036 \pm 11$	1.7
		HO	2.782	This work		1039	1030		0.6
$^{17}\text{C}$	965	HO	2.831	This work	$2.72 \pm 0.03^{\text{a}}$	1069	1060	$1056 \pm 10$	0.4
$^{18}\text{C}$	955	HFB	2.860	This work	$2.82 \pm 0.04^{\text{a}}$	1102	1094	$1104 \pm 15$	0.9
		HO	2.900	This work		1107	1098		0.5
$^{19}\text{C}$	960	HO	3.238	This work	$3.13 \pm 0.07^{\text{a}}$	1234	1227	$1231 \pm 28$	0.3
$^{20}\text{C}$	905	HFB	2.991	This work	$2.98 \pm 0.05^{\text{a}}$	1186	1179	$1187 \pm 20$	0.7
		HO	3.061	This work		1196	1187		0.0
$^{17}\text{O}$	970	IPM	2.766	[35]	$2.59 \pm 0.05^{\text{a}}$	1026	1016	$1010 \pm 10$	0.6
		HO	2.672	This work		1021	1011		0.1
$^{18}\text{O}$	1050	HFB	2.763	This work	$2.61 \pm 0.08^{\text{a}}$	1053	1042	$1032 \pm 26$	1.0
		IPM	2.768	[35]		1057	1048		1.6
		HO	2.742	This work		1046	1036		0.4
$^{19}\text{O}$	970	HO	2.774	This work	$2.68 \pm 0.03^{\text{a}}$	1076	1066	$1066 \pm 9$	0.0
$^{20}\text{O}$	950	HFB	2.849	This work	$2.69 \pm 0.03^{\text{a}}$	1122	1112	$1078 \pm 10$	3.1
		HO	2.786	This work		1100	1089		1.0
$^{21}\text{O}$	980	HO	2.811	This work	$2.71 \pm 0.03^{\text{a}}$	1116	1105	$1098 \pm 11$	0.6
$^{22}\text{O}$	965	HFB	2.919	This work	$2.88 \pm 0.06^{\text{a}}$	1170	1159	$1172 \pm 22$	1.1
		HO	2.956	This work		1178	1168		0.3
$^{23}\text{O}$	960	HO	3.286	This work	$3.20 \pm 0.04^{\text{a}}$	1310	1302	$1308 \pm 16$	0.5
$^{24}\text{O}$	965	HFB	3.050	This work	$3.19 \pm 0.13^{\text{a}}$	1248	1238	$1318 \pm 52$	6.1
		HO	3.280	This work		1319	1311		0.5

<sup>a</sup>Nuclear rms radius deduced from the Glauber model analysis of the  $\sigma_I$  data in the OL approximation [1].

<sup>b</sup>Nuclear rms radius deduced from the Glauber model analysis of elastic  $^6\text{He}+p$  scattering data at 0.7 GeV/nucleon [37].

<sup>c</sup> $\sigma_I$  data taken from Ref. [41].

predicted elastic cross section is strongly forward peaked and the difference in densities begins to show up after the first diffractive maximum. Such a measurement should be feasible at the facilities used for elastic  $^6\text{He}+p$  scattering at 0.7 GeV/nucleon [37] and would be very helpful in testing finer details of  $^6\text{He}$  density. As already discussed in the preceding section, the exchange part of the microscopic OP affects the elastic cross section very strongly [see dotted curve in panel (b) of Fig. 2] and the elastic  $^6\text{He}+^{12}\text{C}$  scattering

measurement would be also a very suitable probe of the exchange effects in this system.

Since  $^6\text{He}$  is a loosely bound halo nucleus with a well established three-body  $\alpha+n+n$  structure, the dynamic correlation between the  $\alpha$  core and dineutron is expected to be important during the collision. Our folding + DWIA approach using three-body density for  $^6\text{He}$  (version FC [5]) gives  $\sigma_I \approx 733$  mb compared to about 720 mb given by the few-body calculation by Tostevin *et al.* (see Fig. 4 in Ref.

TABLE III. The HO-density parameters (14) for neutron-rich Li, C, and O isotopes.

Nucleus	$P_n$	$P_p$	$D_n$	$D_p$	$b_n$ (fm)	$b_p$ (fm)	$\langle r^2 \rangle_n^{1/2}$ (fm)	$\langle r^2 \rangle_p^{1/2}$ (fm)	$\langle r^2 \rangle^{1/2}$ (fm)
${}^7\text{Li}$	2/3	1/3	0.0	0.0	1.684	1.6766	2.382	2.270	2.334
${}^8\text{Li}$	1.0	1/3	0.0	0.0	1.6770	1.6776	2.430	2.270	2.371
${}^9\text{Li}$	4/3	1/3	0.0	0.0	1.6470	1.6766	2.424	2.270	2.374
${}^{13}\text{C}$	5/3	4/3	0.0	0.0	1.6058	1.5722	2.389	2.314	2.355
${}^{14}\text{C}$	2.0	4/3	0.0	0.0	1.6226	1.5762	2.434	2.320	2.386
${}^{15}\text{C}$	2.0	4/3	2/15	0.0	1.6630	1.5898	2.570	2.340	2.481
${}^{16}\text{C}$	2.0	4/3	4/15	0.0	1.8512	1.7128	2.927	2.521	2.782
${}^{17}\text{C}$	2.0	4/3	2/5	0.0	1.8552	1.7128	2.986	2.521	2.831
${}^{18}\text{C}$	2.0	4/3	8/15	0.0	1.8752	1.7297	3.062	2.546	2.900
${}^{19}\text{C}$	2.0	4/3	2/3	0.0	2.1252	1.7297	3.512	2.546	3.238
${}^{20}\text{C}$	2.0	4/3	4/5	0.0	1.9462	1.7467	3.248	2.571	3.061
${}^{17}\text{O}$	2.0	2.0	2/15	0.0	1.7775	1.7232	2.747	2.585	2.672
${}^{18}\text{O}$	2.0	2.0	4/15	0.0	1.7601	1.7935	2.783	2.690	2.742
${}^{19}\text{O}$	2.0	2.0	2/5	0.0	1.7601	1.7935	2.833	2.690	2.774
${}^{20}\text{O}$	2.0	2.0	8/15	0.0	1.7401	1.8005	2.842	2.701	2.786
${}^{21}\text{O}$	2.0	2.0	2/3	0.0	1.7401	1.8005	2.876	2.701	2.811
${}^{22}\text{O}$	2.0	2.0	4/5	0.0	1.8498	1.8081	3.087	2.712	2.956
${}^{23}\text{O}$	2.0	2.0	14/15	0.0	2.1118	1.8081	3.555	2.712	3.286
${}^{24}\text{O}$	2.0	2.0	16/15	0.0	2.0758	1.8261	3.520	2.739	3.280

[6]) based on the same three-body wave function for  ${}^6\text{He}$ . The difference in the calculated  $\sigma_1$  leads to an increase of about 2–3% in the  $\langle r^2 \rangle^{1/2}$  value. It is likely that such a difference is, in part, due to the dynamic correlation between the  $\alpha$  core and dineutron which was not considered in our folding + DWIA approach. For  ${}^8\text{He}$  nucleus, the OL of Glauber analysis of  $\sigma_1$  data [1], and the multiple-scattering Glauber analysis of elastic  ${}^8\text{He}+p$  data at 0.7 GeV/nucleon [38] give  $\langle r^2 \rangle^{1/2}$  around 2.52 and 2.53 fm, respectively. By using the microscopic  ${}^8\text{He}$  density obtained in a four-body (COSMA) model [39], which gives  $\langle r^2 \rangle^{1/2}=2.526$  fm, our folding + DWIA approach reproduces the measured  $\sigma_1$  data within less than 1%. Note that a (multiple scattering) Glauber model analysis of the elastic  ${}^6,8\text{He}+p$  scattering at 0.7 GeV/nucleon which takes into account the dynamic few-body correlation explicitly was done by Al-Khalili and Tostevin [40], and they have obtained the best-fit nuclear radii of about 2.5 and 2.6 fm for  ${}^6\text{He}$  and  ${}^8\text{He}$ , respectively, around 2% larger than our results.

### 1. Parameters of HO densities deduced from $\sigma_1$ data

Although the HO model is a very simple approach, the HO densities were shown above to be useful in testing the nuclear radii for stable ( $N=Z$ ) nuclei. Moreover, the HO-type densities (with the appropriately chosen HO lengths) for the  $sd$ -shell nuclei have been successfully used in the analysis of ( $e, e$ ) data, measurements of isotope shift, and muonic atoms [1]. Therefore, it is not unreasonable to use simple HO parametrization for the g.s. densities of neutron-rich nuclei to estimate the nuclear radii, based on our folding + DWIA

analysis of  $\sigma_1$  data. For a  $N \neq Z$  nucleus, one needs to generate proton and neutron densities separately as

$$\rho_\tau(r) = \frac{2}{\pi^{3/2} b_\tau^3} \left( 1 + P_\tau \frac{r^2}{b_\tau^2} + D_\tau \frac{r^4}{b_\tau^4} \right) \exp\left(-\frac{r^2}{b_\tau^2}\right), \quad (14)$$

where  $\tau=n$  or  $p$ , parameters  $P_\tau$  and  $D_\tau$  are determined from the nucleon occupation of the  $p$  and  $d$  harmonic oscillator shells, respectively.

To generate the g.s. densities of  ${}^8,9\text{Li}$  isotopes, we have assumed the proton density of these nuclei to be approximately that of  ${}^7\text{Li}$  and the neutron HO length  $b_n$  is adjusted in each case to reproduce the measured  $\sigma_1$  (see Tables II and III). While the obtained  $\langle r^2 \rangle^{1/2}$  for  ${}^8\text{Li}$  is rather close to that given by the OL of Glauber model [1], results obtained for  ${}^9\text{Li}$  are different and we could reproduce the  $\sigma_1$  data only if the neutron HO length is chosen to give  $\langle r^2 \rangle_{\text{calc}}^{1/2} \approx 2.37$  fm or about 2% larger than that given by the OL of Glauber model. For the halo nucleus  ${}^{11}\text{Li}$ , a  ${}^9\text{Li}$  core + two-neutron halo model was used to generate its density; namely, we have used HO density of  ${}^9\text{Li}$  that reproduces the measured  $\sigma_1$  for  ${}^9\text{Li}$  and a Gaussian tail for the two-neutron halo density. To reach the best agreement between  $\sigma_1^{\text{expt}}$  taken from Ref. [41] and  $\sigma_1^{\text{calc}}$ , the Gaussian range was chosen to give  $\langle r^2 \rangle_{\text{calc}}^{1/2} \approx 3.23$  fm which is about 0.1 fm larger than that given by the OL of Glauber model [1]. A microscopic density for  ${}^{11}\text{Li}$  obtained in the HF calculation [30] (which gives  $\langle r^2 \rangle^{1/2} = 2.868$  fm) has also been used in our folding analysis. The agreement with the data becomes much worse in this case (see Table II) and we conclude that the radius given by the HF density is somewhat too small. To show the sensitivity of

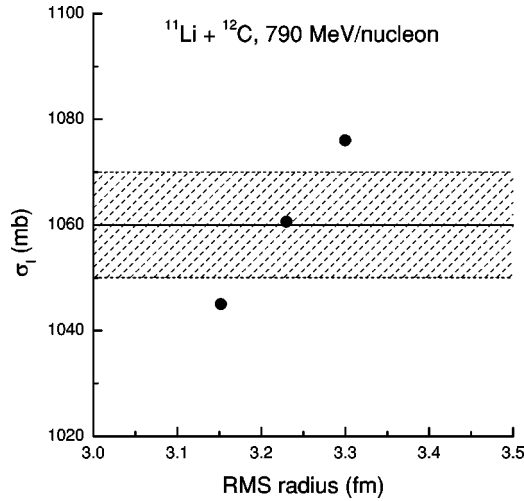


FIG. 3.  $\sigma_1^{\text{calc}}$  obtained with three versions of  $^{11}\text{Li}$  g.s. density, where Gaussian range of the  $2n$ -halo was adjusted to give  $\langle r^2 \rangle^{1/2} = 3.15, 3.23,$  and  $3.30$  fm for  $^{11}\text{Li}$ , in comparison with  $\sigma_1^{\text{expt}} = 1060 \pm 10$  mb [41].

our analysis to the nuclear radius, we have plotted in Fig. 3  $\sigma_1$  predicted by three versions of  $^{11}\text{Li}$  density with the Gaussian range of the  $2n$ -halo adjusted to give  $\langle r^2 \rangle^{1/2} = 3.15, 3.23,$  and  $3.30$  fm, respectively, compared to  $\sigma_1^{\text{expt}} = 1060 \pm 10$  mb [41]. It is easily to infer from Fig. 3 an empirical rms radius of  $3.23 \pm 0.05$  fm for  $^{11}\text{Li}$ . Note that  $\sigma_1$  measurement for  $^{11}\text{Li} + ^{12}\text{C}$  system at 790 MeV/nucleon has been reported in several works with  $\sigma_1^{\text{expt}} = 1040 \pm 60$  [42],  $1047 \pm 40$  [43], and  $1060 \pm 10$  mb [41]. If we adjust Gaussian range of the  $2n$ -halo in  $^{11}\text{Li}$  density to reproduce these  $\sigma_1^{\text{expt}}$  values, the corresponding  $\langle r^2 \rangle^{1/2}$  radii of  $^{11}\text{Li}$  are 3.13, 3.15, and 3.23 fm, respectively. Since  $\sigma_1$  data obtained in Ref. [41] have a much better statistics and less uncertainty, we have adopted  $\langle r^2 \rangle^{1/2} = 3.23 \pm 0.05$  fm as the most realistic rms radius of  $^{11}\text{Li}$  given by our folding + DWIA analysis.

The total reaction cross section for  $^{11}\text{Li} + ^{12}\text{C}$  system at 790 MeV/nucleon has been studied earlier in the few-body Glauber formalism by Al-Khalili *et al.* [5], where  $\langle r^2 \rangle^{1/2}$  radius for  $^{11}\text{Li}$  was shown to increase from 3.05 fm (in the OL) to around 3.53 fm when the dynamic correlation between  $^9\text{Li}$ -core and  $2n$ -halo during the collision is treated explicitly. This is about 9% larger than  $\langle r^2 \rangle^{1/2}$  radius obtained in our folding + DWIA approach based on the same  $\sigma_1$  data. Although various structure calculations for  $^{11}\text{Li}$  give its rms radius around 3.1–3.2 fm (see Refs. [1,4] and references therein), a very recent coupled-channel three-body model for  $^{11}\text{Li}$  by Ikeda *et al.* [44,45] shows that its rms radius is ranging from 3.33 to 3.85 fm if the  $2n$ -halo wave function consists of 21–39% mixture from  $(s_{1/2})^2$  state, respectively. A comparison of the calculated Coulomb breakup cross section with the data [45] suggests that this  $s$ -wave mixture is around 20–30%. Thus, the nuclear radius of  $^{11}\text{Li}$  must be larger than that accepted so far [1,4] and be around 3.3–3.5 fm, closer to the result of the few-body calculation [5] and the upper limit of rms radius given by our folding + DWIA analysis.

For most of neutron-rich C and O isotopes considered here, we have first fixed the proton HO lengths  $b_p$  to repro-

duce the proton  $\langle r^2 \rangle_p^{1/2}$  radii predicted by the microscopic IPM and HFB densities (as described below). The neutron HO lengths  $b_n$  are then adjusted to the best agreement with  $\sigma_1$  data, and the obtained HO parameters are summarized in Table III.

## 2. Microscopic HFB densities

Before discussing the results obtained for the neutron-rich C and O isotopes, we give here a brief description of the microscopic HFB approach used to calculate the g.s. densities of even C and O isotopes. More details about this approach can be found in Ref. [34].

We solve the HFB equations in coordinate representation and in spherical symmetry with the inclusion of continuum states for neutron-rich nuclei. As the neutron Fermi energies of these nuclei are typically quite close to zero, pairing correlations can easily scatter pairs of neutrons from the bound states towards continuum states. For this reason, the inclusion and the treatment of continuum states in the calculation are very important. In our calculation the continuum is treated exactly, i.e., with the correct boundary conditions for continuum wave functions and by taking into account the widths of the resonances. Resonant states are localized by studying the behavior of the phase shifts with respect to the quasiparticle energy for each partial wave  $(l, j)$ .

The calculations were done with the Skyrme interaction SLy4 for the mean field channel and with the following zero-range density-dependent interaction

$$V = V_0 \left[ 1 - \left( \frac{\rho(r)}{\rho_0} \right)^\gamma \right] \delta(\mathbf{r}_1 - \mathbf{r}_2) \quad (15)$$

for the pairing channel. In Eq. (15),  $\rho_0$  is the saturation density and  $\gamma$  is chosen equal to 1. We have adapted the prescription of Refs. [46,47] to finite nuclei in order to fix  $V_0$  together with the quasiparticle energy cutoff. This prescription, requiring that the free neutron-neutron scattering length has to be reproduced in the truncated space, allows us to deduce a relation between the parameter  $V_0$  and the quasiparticle energy cutoff.

## 3. Nuclear radii of carbon and oxygen isotopes

The  $\sigma_1$  data for neutron-rich C and O isotopes are compared in Table II with  $\sigma_1$  predicted by different choices of nuclear densities. We have tested first the IPM density for  $^{13}\text{C}$  [35] based on the single-particle spectroscopic factors obtained in the shell model by Cohen and Kurath [48]. This IPM density gives  $\langle r^2 \rangle^{1/2} \approx 2.39$  fm for  $^{13}\text{C}$  and the predicted  $\sigma_1$  agrees with the data within less than 2%. We have further made IPM calculation for  $^{14}\text{C}$  based on the same single-particle configurations, with the WS parameters for  $sp$  shells appropriately corrected for the recoil effects and experimental nucleon separation energies  $S_{n,p}$  of  $^{14}\text{C}$ . This IPM density gives  $\langle r^2 \rangle^{1/2} \approx 2.42$  fm for  $^{14}\text{C}$  and the predicted  $\sigma_1$  also agrees with the data within 2%. The HO densities were also parametrized for  $^{13,14}\text{C}$  with the proton HO lengths  $b_p$  chosen to reproduce  $\langle r^2 \rangle_p^{1/2}$  values predicted by the IPM. The best-fit neutron HO lengths  $b_n$  result in  $\langle r^2 \rangle^{1/2} = 2.36$  and 2.39 fm for

$^{13}\text{C}$  and  $^{14}\text{C}$ , respectively. These values agree fairly with those given by the IPM densities. The microscopic HFB density gives for  $^{14}\text{C}$  a significantly larger  $\langle r^2 \rangle^{1/2}$  radius of 2.59 fm and the calculated  $\sigma_1$  overestimates the data by nearly 7%. Note that the OL of Glauber model gives smaller radius of 2.28 and 2.30 fm for  $^{13}\text{C}$  and  $^{14}\text{C}$ , respectively, based on the same  $\sigma_1$  data [1]. This means that the absorption given by the OL of Glauber model is indeed stronger than that given by our approach, as expected from discussion in Sec. II.

For the neutron-rich even  $^{16-20}\text{C}$  isotopes, the HFB densities give a remarkably better agreement with the data and it is, therefore, reasonable to fix the proton HO lengths of the HO densities for each of  $^{15-20}\text{C}$  isotopes to reproduce  $\langle r^2 \rangle_p^{1/2}$  radius predicted by the HFB calculation for the nearest even neighbor. The best-fit neutron HO lengths result in the nuclear radii quite close to those given by the HFB densities (see Tables II and III). We emphasize that the nuclear radii given by our analysis, using the HO densities for C isotopes, are about 0.1 fm larger than those deduced from the OL of Glauber model [1]. Given a high sensitivity of  $\sigma_1$  data to the nuclear size, a difference of 0.1 fm is not negligible.

To illustrate the mass dependence of the nuclear radius, we have plotted in Fig. 4(a) the rms radii given by the two sets (HFB and HO) of the g.s. densities for C isotopes together with those deduced from the OL of Glauber model based on the same  $\sigma_1$  data [1]. One can see that our result follows closely the trend established by the OL of Glauber model, although the absolute  $\langle r^2 \rangle^{1/2}$  radii obtained with the HO densities are in most cases larger than those deduced from the OL of Glauber model. With the exception of the  $^{14}\text{C}$  case, the radii of even C isotopes given by the microscopic HFB densities agree reasonably well with the empirical HO results. We have also plotted in Fig. 4 the lines representing  $r_0 A^{1/3}$  dependence with  $r_0$  deduced from the experimental radii of  $^{12}\text{C}$  and  $^{16}\text{O}$  given in Table I. One can see that the behavior of nuclear radius in C isotopes is quite different from the  $r_0 A^{1/3}$  law. While  $\langle r^2 \rangle^{1/2}$  radii found for  $^{12-15}\text{C}$  agree fairly with the  $r_0 A^{1/3}$  law, those obtained for  $^{16-20}\text{C}$  are significantly higher. In particular, a jump in the  $\langle r^2 \rangle^{1/2}$  value was found in  $^{16}\text{C}$  compared to those found for  $^{12-15}\text{C}$ . This result seems to support the existence of a neutron halo in  $^{16}\text{C}$  as suggested from the  $\sigma_R$  measurement for this isotope at 85 MeV/nucleon [49]. We have further obtained a nuclear radius of 3.24 fm for  $^{19}\text{C}$  which is significantly larger than that found for  $^{20}\text{C}$ . This result might also indicate to a neutron halo in this odd C isotope.

Situation is a bit different for O isotopes, where the best-fit  $\langle r^2 \rangle^{1/2}$  radii follow roughly the  $r_0 A^{1/3}$  law up to  $^{22}\text{O}$ . For the stable  $^{17,18}\text{O}$  isotopes, the IPM densities [35] provide a very good description of the  $\sigma_1$  data (within 1–2%). The best-fit HO densities give  $\langle r^2 \rangle^{1/2}$  radii of 2.67 and 2.74 fm for  $^{17}\text{O}$  and  $^{18}\text{O}$ , respectively, which are rather close to those given by the IPM densities. Predictions given by the microscopic HFB densities are also in a good agreement with the data for even O isotopes excepting the  $^{24}\text{O}$  case, where the HFB density gives obviously a too small  $\langle r^2 \rangle^{1/2}$  radius. Since the HFB calculation already takes into account the continuum effects [34], such a deficiency might be due to the

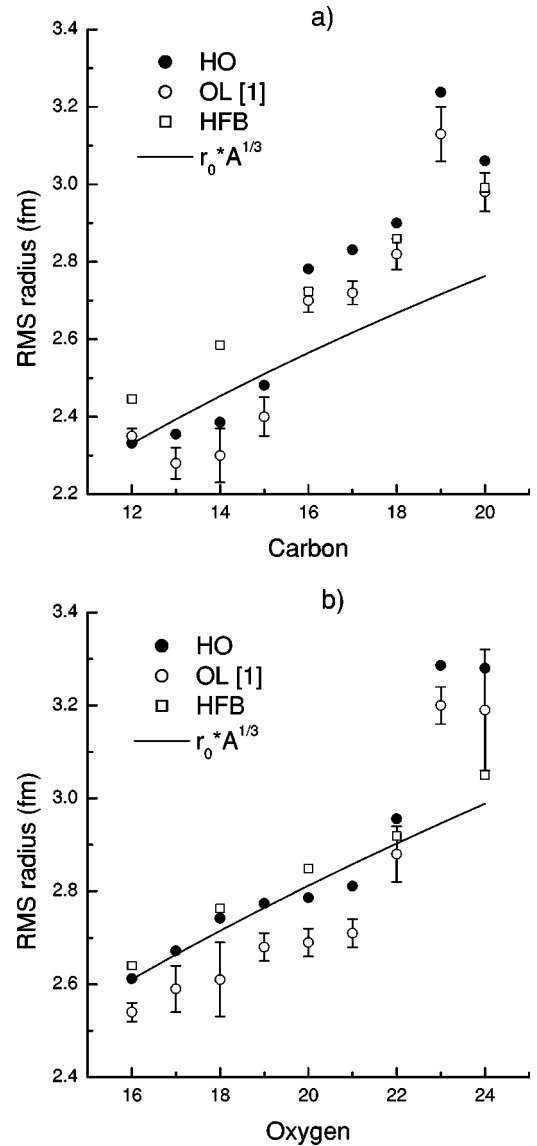


FIG. 4. Mass dependence of the nuclear rms radius for carbon [panel (a)] and oxygen [panel (b)] isotopes given by the two choices (HFB and HO) of the g.s. densities compared to that deduced from the Glauber model analysis in the OL approximation [1]. The lines represent  $r_0 A^{1/3}$  dependence with  $r_0$  deduced from the experimental radii of  $^{12}\text{C}$  and  $^{16}\text{O}$  given in Table I.

static deformation of  $^{24}\text{O}$ . A jump in the  $\langle r^2 \rangle^{1/2}$  value was found for  $^{23}\text{O}$  which could indicate to a neutron halo in this isotope. Behavior of  $\langle r^2 \rangle^{1/2}$  radii given by the best-fit HO densities agrees with the trend established by the OL of Glauber model [1] but, like the case of C isotopes, they are about 0.1 fm larger than those deduced from the OL of Glauber model. Thus, the OL of Glauber model seems to consistently overestimate  $\sigma_R$  for the neutron-rich C and O isotopes under study in comparison with our approach.

One clear reason for the difference between our results and those given by the OL of Glauber model analysis is that one has matched directly the calculated  $\sigma_R$  with the measured  $\sigma_1$  in the Glauber model analysis [1] to deduce the nuclear radius. If we proceed the same way with the HO

densities for the considered nuclei, the best-fit  $\langle r^2 \rangle^{1/2}$  radii decrease slightly but are still larger than those given by the OL of Glauber model. As already discussed in Sec. II, the zero-angle approximation for the  $NN$  scattering amplitude used in the Glauber model might reduce significantly the strength of the exchange part of the imaginary OP given by Eq. (12) and could overestimate, therefore, the absorption in the dinuclear system. This effect should be much stronger if one uses a realistic finite-range representation of the  $NN$  scattering amplitude. Bertsch *et al.* have shown [30] that the zero-range approximation for the  $NN$  scattering amplitude leads to a reduction of the calculated  $\sigma_R$  or an enhancement of the nuclear radius by a few percent (see Figs. 2 and 3 in Ref. [30]). Owing to such a cancellation of the exchange effects by the zero-range approximation for  $NN$  scattering amplitude, the simple OL of Glauber model was able to deliver reasonable estimates of nuclear radii for many stable and unstable isotopes [1]. It should be noted that the eikonal approximation for the scattering wave function used in the Glauber model was introduced in the past to avoid large numerical calculations. With the computing power available today, there is no problem to perform the OM and DWIA calculations for different nucleus-nucleus systems involving large numbers of partial waves, and the folding + DWIA method presented here can be recommended as a reliable microscopic approach to predict the elastic scattering cross section and to deduce the nuclear radius from the measured  $\sigma_1$ .

#### IV. CONCLUSION

In this work we have explored the reliability of the optical model + DWIA approach as a tool for extracting important information on nuclear sizes from interaction cross section measurements. We concentrate on the energy region of 0.8–1 GeV/nucleon where interaction cross section data exist for various combinations of stable as well as unstable projectiles on different targets. At these bombarding energies our knowledge of the empirical optical potential is scarce, especially for unstable systems, and we have used, therefore, the folding model to calculate the microscopic (complex) optical potential and inelastic form factors necessary for our analysis.

We have chosen for the folding input the fully finite-range  $t$ -matrix interaction developed by Franey and Love [13]. The folded optical potentials and inelastic form factors are used further as inputs for the standard optical model and DWIA calculations of total reaction cross sections and interaction cross sections induced by stable and unstable He, Li, C, and O isotopes on  $^{12}\text{C}$  target. By using the well tested nuclear g.s. densities for the stable  $^4\text{He}$ ,  $^{12}\text{C}$ , and  $^{16}\text{O}$  isotopes, we found that the Franey and Love  $t$  matrix gives extremely good account of the measured  $\sigma_1$  for these nuclei.

We have further used the nuclear g.s. densities obtained in various structure models to calculate  $\sigma_1$  and have made realistic estimate for the nuclear radii of (still poorly known) neutron-rich isotopes based on the comparison between  $\sigma_1^{\text{calc}}$  and  $\sigma_1^{\text{expt}}$ . For the chains of C and O isotopes, our results agree reasonably well with the empirical trend established by the OL of Glauber model [1], but give consistently larger  $\langle r^2 \rangle^{1/2}$  radii for these nuclei. Such an effect could be due to the unsatisfactory treatment of the exchange part of the nucleus-nucleus OP in the Glauber model calculation.

Although the nuclear radii deduced by our approach for some light halo nuclei might be a few percent smaller than realistic values because the dynamic few-body correlation was not considered explicitly in the present folding + DWIA formalism, this fully microscopic approach was shown to be more accurate than the OL of Glauber model. Given realistic nuclear densities, it can give a reliable (parameter-free) prediction of the nucleus-nucleus optical potential at energies around 1 GeV/nucleon. Therefore, it provides the necessary link to relate the calculated  $\sigma_1$  to the nuclear density and rms radius.

#### ACKNOWLEDGMENTS

The authors thank G. R. Satchler for making the DOLFIN code available to them for the IPM calculation of nuclear g.s. densities, W. von Oertzen for helpful discussion, and W. G. Love for critical remarks to the manuscript. We also thank A. Ozawa, H. Sagawa, and I. J. Thompson for their correspondence on the nuclear densities. The research has been supported, in part, by the Natural Science Council of Vietnam.

- 
- [1] A. Ozawa, T. Suzuki, and I. Tanihata, Nucl. Phys. **A693**, 32 (2001).  
 [2] R. J. Glauber and G. Matthiae, Nucl. Phys. **B21**, 135 (1970).  
 [3] Y. Ogawa, K. Yabana, and Y. Suzuki, Nucl. Phys. **A543**, 722 (1992).  
 [4] I. Tanihata, J. Phys. G **22**, 157 (1996).  
 [5] J. S. Al-Khalili, J. A. Tostevin, and I. J. Thompson, Phys. Rev. C **54**, 1843 (1996).  
 [6] J. A. Tostevin, R. C. Johnson, and J. S. Al-Khalili, Nucl. Phys. **A630**, 340c (1998).  
 [7] G. R. Satchler and W. G. Love, Phys. Rep. **55**, 183 (1979).  
 [8] Dao T. Khoa, G. R. Satchler, and W. von Oertzen, Phys. Rev.

- C **56**, 954 (1997).  
 [9] G. Bertsch, J. Borysowicz, H. McManus, and W. G. Love, Nucl. Phys. **A284**, 399 (1977); N. Anantaraman, H. Toki, and G. F. Bertsch, *ibid.* **A398**, 269 (1983).  
 [10] Dao T. Khoa and G. R. Satchler, Nucl. Phys. **A668**, 3 (2000).  
 [11] Dao T. Khoa, G. R. Satchler, and N. D. Thuy, Phys. Rev. C **65**, 024611 (2002).  
 [12] W. G. Love and M. A. Franey, Phys. Rev. C **24**, 1073 (1981).  
 [13] M. A. Franey and W. G. Love, Phys. Rev. C **31**, 488 (1985).  
 [14] G. R. Satchler, *Direct Nuclear Reactions* (Clarendon, Oxford, 1983).  
 [15] B. Sinha, Phys. Rep. **20**, 1 (1975); B. Sinha and S. A. Mosz-

- kowski, Phys. Lett. **81B**, 289 (1979).
- [16] Dao T. Khoa, Phys. Rev. C **63**, 034007 (2001).
- [17] M. E. Farid and G. R. Satchler, Phys. Lett. **146B**, 389 (1984).
- [18] A. Bohr and B. R. Mottelson, *Nuclear Structure* (Benjamin, New York, 1975), Vol. 2.
- [19] A. K. Kerman, H. McManus, and R. M. Thaler, Ann. Phys. (N.Y.) **8**, 551 (1959).
- [20] J. Jaros *et al.*, Phys. Rev. C **18**, 2273 (1978).
- [21] Dao T. Khoa, G. R. Satchler, and W. von Oertzen, Phys. Lett. B **358**, 14 (1995).
- [22] A. Ozawa *et al.*, Nucl. Phys. **A691**, 599 (2001).
- [23] S. Raman, C. W. Nestor, Jr., and P. Tikkanen, At. Data Nucl. Data Tables **78**, 1 (2001).
- [24] R. H. Spear, At. Data Nucl. Data Tables **42**, 55 (1989).
- [25] J. Raynal, *Computing as a Language of Physics* (IAEA, Vienna, 1972), p. 75; computer code ECIS97 (unpublished).
- [26] H. Esbensen and G. F. Bertsch, Phys. Rev. C **59**, 3240 (1999).
- [27] Dao T. Khoa and W. von Oertzen, Phys. Lett. B **304**, 8 (1993); **342**, 6 (1995).
- [28] H. Nakada, Phys. Rev. C **68**, 014316 (2003).
- [29] M. S. Hussein, R. A. Rego, and C. A. Bertulani, Phys. Rep. **201**, 279 (1991).
- [30] G. F. Bertsch, B. A. Brown, and H. Sagawa, Phys. Rev. C **39**, 1154 (1989); H. Sagawa (private communication).
- [31] M. E. Brandan, H. Chehime, and K. W. McVoy, Phys. Rev. C **55**, 1353 (1997).
- [32] Dao T. Khoa, G. R. Satchler, and W. von Oertzen, Phys. Rev. C **51**, 2069 (1995).
- [33] H. De Vries, C. W. De Jager, and C. De Vries, At. Data Nucl. Data Tables **36**, 503 (1987).
- [34] M. Grasso, N. Sandulescu, N. Van Giai, and R. J. Liotta, Phys. Rev. C **64**, 064321 (2001).
- [35] G. R. Satchler, Nucl. Phys. **A329**, 233 (1979).
- [36] V. B. Soubbotin and X. Viñas, J. Phys. G **25**, 2087 (1999); Nucl. Phys. **A665**, 291 (2000).
- [37] G. D. Alkhozov *et al.*, Nucl. Phys. **A712**, 269 (2002).
- [38] V. Lapoux *et al.*, Phys. Rev. C **66**, 034608 (2002).
- [39] M. V. Zhukov, A. A. Korshennikov, and M. H. Smedberg, Phys. Rev. C **50**, R1 (1994).
- [40] J. S. Al-Khalili and J. A. Tostevin, Phys. Rev. C **57**, 1846 (1998).
- [41] T. Kobayashi *et al.*, Phys. Lett. B **232**, 51 (1989).
- [42] I. Tanihata *et al.*, Phys. Rev. Lett. **55**, 2676 (1985).
- [43] I. Tanihata *et al.*, Phys. Lett. B **206**, 592 (1988).
- [44] K. Ikeda, T. Myo, and K. Kato, Nucl. Phys. **A722**, 335c (2003).
- [45] T. Myo, S. Aoyama, K. Kato, and K. Ikeda, Phys. Lett. B **576**, 281 (2003).
- [46] E. Garrido, P. Sarriguren, E. Moya de Guerra, and P. Schuck, Phys. Rev. C **60**, 064312 (1999).
- [47] G. F. Bertsch and H. Esbensen, Ann. Phys. (N.Y.) **209**, 327 (1991).
- [48] S. Cohen and D. Kurath, Nucl. Phys. **A101**, 1 (1967).
- [49] T. Zheng *et al.*, Nucl. Phys. **A709**, 103 (2002).

## 2.10 Applications d'intérêt astrophysique. Les étoiles à neutrons

Les étoiles à neutrons sont des objets qui se forment à la suite des explosions (supernovae) des étoiles très massives ayant typiquement au moins 10 fois la masse solaire. À la fin de ces processus d'explosion extrêmement violents, qui fixent la fin de la vie de l'étoile, l'objet qui se forme est très compact avec un rayon d'environ 10 km et une masse autour de 1.4 masses solaires. Cette étoile a une asymétrie d'isospin particulièrement élevée et, sous cet aspect, elle peut être vue comme l'objet nucléaire le plus exotique qui existe dans l'Univers.

L'impact de la physique nucléaire dans le domaine de l'astrophysique est très profond et la physique des étoiles à neutrons représente un des exemples typiques d'application où les données et les prédictions provenant de la physique nucléaire sont indispensables pour réaliser des modélisations et interpréter les propriétés de ces astres.

Nous nous sommes intéressés aux liens que l'on peut établir entre la physique nucléaire et la physique des étoiles à neutrons. Dans l'article qui suit, [Fa07], après une introduction où les propriétés générales des étoiles à neutrons sont décrites, nous mentionnons et décrivons quelques-uns de ces liens.

La réflexion autour des étoiles à neutrons et notamment autour des propriétés de leurs écorces (densité baryonique inférieure à la densité de saturation) nous a motivés à réaliser des modélisations dans ces systèmes en employant les outils théoriques de champ moyen dont nous disposons pour les noyaux. Les modèles théoriques prédisent l'existence de noyaux exotiques dans l'écorce externe des étoiles à neutrons, immergés dans une mer d'électrons relativistes et organisés dans une structure cristalline. La densité baryonique augmente en allant vers l'intérieur de l'étoile et, à la densité dite de 'drip', des neutrons commencent à s'échapper et à former un gaz qui remplit l'espace entre les sites du réseau cristallin. C'est à cette densité que commence l'écorce interne qui est donc formée par un réseau coulombien de systèmes nucléaires riches en neutrons immergés dans une mer d'électrons et un gaz de neutrons superfluides. Si on modélise le réseau par des cellules de Wigner-Seitz (WS), on peut imaginer de traiter le système à  $N$  corps fini contenu dans une cellule de WS en faisant l'approximation que ces cellules ne sont pas en relation les unes avec les autres. Le système à  $N$  corps défini ainsi aura une densité, un rayon et un nombre de protons et de neutrons donnés. Le modèle peut être ultérieurement simplifié en assumant une forme sphérique pour les cellules de WS.

En utilisant cette modélisation, nous avons effectué des calculs HFB et QRPA pour certaines cellules de WS dans l'écorce interne [Kh07, Gr08]. Le spectre d'excitation a été analysé. La chaleur spécifique dans l'écorce et donc le temps de refroidissement de l'étoile sont deux quantités étroitement liées au spectre des états excités et à la présence de corrélations d'appariement (la superfluidité modifie le spectre d'excitation). Je fais

donc suivre un travail sur l'étude des états excités dans certaines cellules de WS de l'écorce [**Gr08**].

# Neutron Stars and Nuclei: Two Dense Systems

M. FALLOT,<sup>1</sup> M. GRASSO,<sup>2,3</sup> E. KHAN,<sup>2</sup> AND J. MARGUERON<sup>2</sup>

<sup>1</sup>*Subatech, 4 rue Alfred Kastler BP 20722, F-44307 Nantes Cedex 3, France*

<sup>2</sup>*Institut de Physique Nucléaire, Université Paris-Sud, IN2P3-CNRS, F-91406 Orsay, France*

<sup>3</sup>*Dipartimento di Fisica e Astronomia and INFN, Via Santa Sofia 64, I-95123 Catania, Italy*

## Introduction: Neutron Stars, Nuclei, and Nuclear Matter

Neutron stars are the remnants of core collapse supernovae [1,2]. They are the most compact stellar objects after black holes. Some of their properties, such as masses, rotation frequencies, and emission of radiations are measurable, whereas other signals like gravitational wave emission are planned to be in the next years. The properties that are not directly linked to observations, such as the internal composition or temperature, require the development of theoretical models. Fortunately, some of the missing information can be obtained from the study of the other dense nuclear systems, atomic nuclei, which are accessible to experimental facilities. Traditionally, the link between neutron stars and bulk nuclei is made via the nuclear matter: an ideal infinite system equally composed of interacting neutrons and protons where Coulomb interaction has been switched off. For instance, the central density of heavy nuclei is very close to the equilibrium density of nuclear matter, called the saturation density  $\rho_0$ . Moreover, the nuclear matter concept can be extended to isospin asymmetries. Asymmetric nuclear matter is rather similar to the nuclear matter found in neutron stars. Coulomb potential energy at those densities is usually small compared to kinetic energy and the main interaction between particles is driven by the nuclear force. Recently, more direct relations between neutron-rich nuclei and neutron star matter have been proposed. Indeed, some of the exotic neutron-rich nuclei produced in nuclear facilities are also located in the outer crust of neutron stars, while the inner crust is composed by drip-line nuclei immersed in a neutron gas. Before entering into this discussion, we should present in more detail the physics of neutron stars.

## Discovery and Observation of a Large Variety of Neutron Star Systems

Landau as well as Baade and Zwicky suggested the existence of neutron stars in the early 1930s. Their existence remained conjectural until 1968 when Jocelyn Bell

and her thesis advisor Anthony Hewish discovered radio pulsars, characterized by radio emission with a periodicity that lies between a few seconds and few tens of milliseconds. Radio pulsars are interpreted as spinning neutron stars with an intense magnetic field misaligned with the rotation axis. Radio waves are thought to be emitted by the electrons accelerated along the polar magnetic fields. Hence, the radio waves are not isotropically emitted but focussed and the rotating neutron star is emitting a pulsed signal like the lighthouses that guide the boats along the coasts (Figure 1). The vast majority of radio pulsars are isolated neutron stars because in binary systems the accretion disk tends to screen the signal. In addition to radio emission, neutron stars are also found in interacting binary systems that emit intense X-rays. In such binaries, a neutron star closely orbits a normal optically visible star and draws gas away from it. The infalling accreted gas is heated to millions of degrees and emits X-rays. Rapidly rotating and relatively young radio pulsars are also found in the visible spectrum (Crab pulsar, Vela pulsar). Some neutron stars are also strong high-energy (greater than tens of MeV) gamma-ray sources. Besides, the strongest known magnetic fields of the present Universe have been found in neutron stars where surface magnetic fields are of the order of  $10^7$  T. In few young neutron stars, much more intense magnetic fields have been observed and may exceed  $10^{11}$  T. The usual dynamo effect is here unable to produce such intense

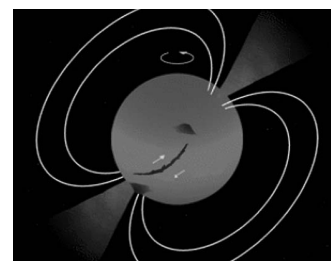


**Figure 1.** Rotating pulsar with its magnetic fields and the focussed radio beams.

magnetic fields. A possible phase transition to strongly spin polarised matter could be responsible, but this is still a speculation in dense matter. From time to time, probably due to the twist of its magnetic field, magnetars emit a giant flare like the one that reached the Earth on December 27, 2004 and has interrupted all radio broadcasts for a few seconds.

Measurements of masses and radii of neutron stars still represent an observational challenge. The most accurate measurements of masses are obtained in binaries of neutron stars applying the Kepler laws. Observed values are typically around 1.4 solar masses. The time derivative of the rotation velocity, associated to the luminosity, provides an estimate of the moment of inertia that, combined with the value of the mass, gives a measure of the radius. This leads to a typical radius of a tenth of kilometers. These measurements cannot reach the accuracy required to disentangle between the models used to describe neutron stars. Other methods are then proposed, like the one based on black body radiation but it has been found that neutron stars may have a non-uniformly distributed surface temperature. This complicates the interpretation of the black body emission.

Up to now, about 1,500 neutron stars have been identified so far and, as shown, they participate to a large variety of observed systems that are characterized by their electromagnetic emission going from visible spectrum to gamma rays. Could those emission processes provide information about the internal composition of neutron stars?

## The Equation of State of Dense Stellar Matter

On the theoretical side, the mass and the radius are determined by solving the hydrostatic equilibrium equation. In the framework of the general relativity the equilibrium of a spherical object is described by the Tolman-Oppenheimer-Volkov equations, and for completeness, the equation of state (EoS) is required. The density increases from  $10^6 \text{ g/cm}^3$  at the surface (starting point of the crust), to several times the saturation density ( $\rho_0$  is  $3 \cdot 10^{14} \text{ g/cm}^3$ ) in the core. The number of neutrons in neutron stars exceeds by far that of protons. The net isospin asymmetry  $\delta = (N - Z)/(N + Z)$  can reach 0.95 in the interior of the stars. The equation of state relies on the composition of dense matter in the star for which very scarce information are available: Where are localized the phase transitions between matter composed of neutrons, protons, and electrons, and more massive hadrons such as hyperons? There is a global consensus that nuclear matter will convert to quark matter, but at which density? Does mesons (pions, kaons)

condensation occur? Several equations of state have been derived in order to investigate the observational consequences of the composition of dense matter. The maximum masses and the radii predicted by those models can be quite different (Figure 2).

On the experimental side, investigations on the atomic nuclei like the measurement of giant monopole resonances, masses, and central densities allow one to probe the equation of state around the saturation density. Heavy ion collisions, hot giant resonances, and exotic nuclei properties, attempt to explore more extreme regions of the phase diagram. However, the improvement of EoS's at lower and higher densities than  $\rho_0$  and for strong isospin asymmetries is still required (Figure 3). In the latter case, the density dependence of the symmetry energy is convenient to explore the relation between isospin symmetric and asymmetric equation of state: it can be shown that the density dependence of the symmetry energy is equivalent to the isospin dependence of the incompressibility modulus. The symmetry energy therefore plays a central role in determining the structure and the evolution (cooling) of the stars. The future facilities producing exotic nuclei will allow one to test this isospin dependency for values of the asymmetry parameter,  $\delta$ , larger than 0.2. This asymmetry is smaller than the asymmetry in neutron star, but may provide at least additional constraints for the theoretical models.

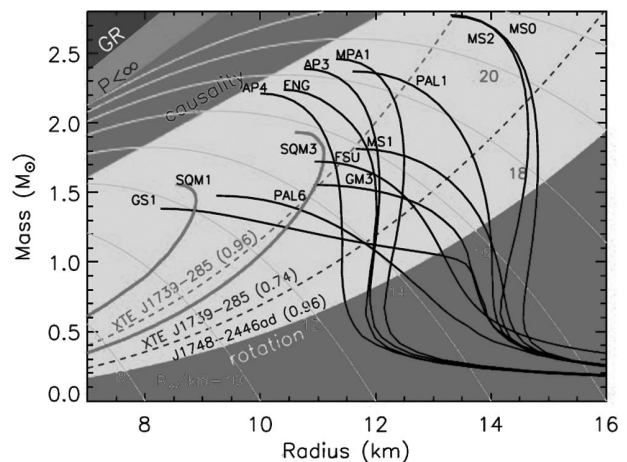


**Figure 2.** Mass-radius diagram for typical EoS, depicted with observational constraints (see J. M. Lattimer and M. Prakash, *Ap. J.* 550 (2001) 426 for notations and further explanations).

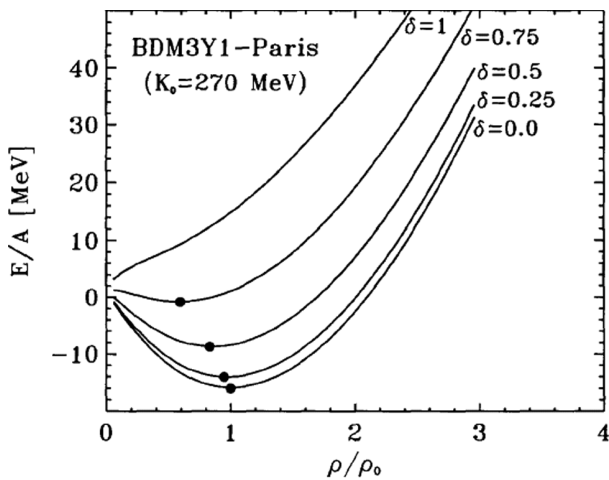


**Figure 3.** Equation of state for various values of the isospin  $\delta$  (from D. T. Khoa et al. Nucl. Phys. A602 (1996) 98).

**Anatomy of the Star**

Neutron stars are quasi-spherical objects composed of six major regions: the inner and outer cores (~99% of the mass) where nuclear matter is homogeneous and that are usually sufficient to understand the main properties of neutron stars; the inner and outer crust (1–2 km width) composed of inhomogeneous nuclear matter (nuclei or nuclear clusters), which screens the core from observations (even from neutrinos), the envelope (few meters), which influences the transport and the release of thermal energy from the surface, and finally the atmosphere (few centimeters), which plays an important role in shaping the emergent photon spectrum (Figure 4).

At the surface defined by the interface between the outer crust and the envelope,  $^{56}\text{Fe}$  atoms are arranged as in a solid. Going toward the interior, the atoms are ionized and in the outer part of the crust one can find nuclei with numbers of nucleons up to  $A=200$  arranged in a Coulomb lattice in the presence of an electron gas. Due to electron capture processes, these nuclei become richer in neutrons with increasing density ( $10^9$  to  $10^{11}$  g/cm $^3$ ). Neutrons start to leak out of nuclei at densities above the neutron drip density—the equivalent of the neutron drip line in a stellar environment (finite pressure, beta-equilibrium):  $4 \cdot 10^{11}$  g/cm $^3$  in the inner crust. Nuclei are located at the sites of a crystal immersed in a super-fluid of neutrons and relativistic leptons. The lattice can be modeled by its elementary constituents, the Wigner-Seitz (WS) cells, each of them

containing the most probable nuclear cluster, the neutron and the electron gases. For densities higher than  $10^{13}$  g/cm $^3$ , the nuclear clusters are close enough to begin a dissolution process and deformed structures appear. They are commonly called the pasta phases because the matter is arranged in noodle shapes like lasagne or spaghetti, or Swiss cheese. At this stage, the proton fraction has decreased down to 0.1. This process results in the formation of homogeneous nuclear matter.

In the inner core, where the density is greater than the saturation density, exotic particles such as strange hyperons and/or Bose condensates (pions or kaons) may become abundant. It is possible that a transition to a mixed phase of hadronic and deconfined quark matter develops.

**Cooling, Glitches, and Vortices: The Life of a Neutron Star**

With time neutron stars evolve and new phenomena occur. In the following we report on some of those phenomena that are directly related to the properties of nuclear matter and in particular to the pairing properties of nuclear matter.

Being at the end point of stellar evolution, neutron stars do not produce energy but lose the gravitational energy gained during the core collapse by neutrino emission.

**Neutron Star**

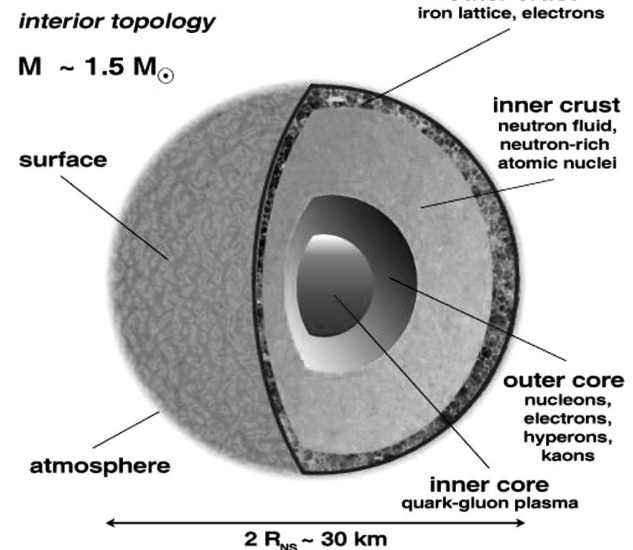


**Figure 4.** The basic structure of a neutron star (from G. Röpke, Univ. Rostock).

Indeed, because of their very weak coupling with matter, neutrinos and anti-neutrinos mainly produced by beta decay and inverse beta decay could carry out the energy of the core and cool down the temperature. This is called the URCA process [3], by reference to the name of a casino existing in the mid 1950s in Rio de Janeiro, known by the promoter of this process, G. Gamow. According to him, the efficiency of this casino in spoiling the money of the gamblers was comparable to the URCA process in cooling down the star. Later on, it was discovered that the URCA process is strongly suppressed by energy and momentum conservation unless a minimum amount of proton, around 11% of the baryonic density, is present [4]. This minimal amount is strongly correlated with the symmetry energy  $a_s$ . Relativistic models, having large values of  $a_s$ , satisfy this criterion around the saturation density while most non-relativistic models, with a lower  $a_s$  value, do not. The difference between non-relativistic and relativistic models predictions should then be investigated. Anyhow, the URCA process is too efficient to explain the slowing down of the surface temperature with time that is observed for a dozen of stars: neutron stars are visible by thermal emission during a few millions of years. Several improvements have been proposed: superfluidity leading to the presence of a neutron gap may quench cooling from the URCA process. A modified URCA process is also considered where adding an additional nucleon as a spectator of the process allows momentum and energy conservation. Other processes are also considered like neutrino bremsstrahlung, pair breaking emission, and so on. It should be noted that the specific heat in the crust is also important in cooling modelization. It depends on the excitation spectrum, which is different in the super-fluid phase than in the normal phase [5].

Neutron stars are also fast rotating stellar objects and we know, from Earth laboratory experiments on Helium 4 for instance, that a rotating super-fluid produces vortices. In the case of finite nuclei, surface effects forbid the formation of vortices. In other words the rotational energy needed is too high and nuclei vaporize at lower energies. In the case of neutron stars, gravitational pressure maintains the nucleons together and vortices can be formed in the core as well as in the inner crust. Those vortices link together two layers of the star (core and crust) and impose a rigid rotation. As the neutron star releases energy, the vortex must be destroyed from time to time and this is the possible origin of observed “giant glitches.” A “giant glitch” is a brutal variation of the rotation period of the star. One possible scenario that explains the existence of the glitches is that

the neutron fluid forms vortices that can pin on the nuclear clusters in the crust. The unpinning would generate the angular momentum transfer from the core to the crust, which is at the origin of the glitches. The pinning force depends on the neutron pairing gap in the crust.

Hence, cooling and giant glitches require accurate modelization of the pairing gap in the crust of neutron stars made of non-homogeneous matter. Most of the actual models are based on the Wigner-Seitz approximation since the seminal work of Negele and Vautherin [6]. This allows straightforward application of the Hartree-Fock BCS or Hartree-Fock-Bogoliubov models built for the description of atomic nuclei. It has recently been shown that those models are valid if the density of states around the Fermi surface is averaged over a few 100 keV by temperature effects or energy exchanged during reaction processes [7]. For temperature below a few 100 keV, it is necessary to improve the modelization of the continuum states. For that, based on the ideas developed in condensed matter, first band theory type approaches have been built [8] and represent certainly the new generation of models. Nevertheless, experimental probes of the pairing gap in nuclei are necessary but still very difficult. With respect to the importance of such knowledge, nuclear physics investigations should be pushed in this direction.

### **Nuclei: A Possible Laboratory for Neutron Stars**

Recently, several empirical relationships have been found that are directly correlated to some properties of nuclei to neutron star physics. For instance, the neutron skin thickness nuclei has been linked to the pressure of pure neutron matter at sub-nuclear densities [9] and consequently to the neutron star radius [10]. Indeed, the pressure is related to the derivative of the symmetry energy [11] and the neutron skin thickness of nuclei is an observable that yields some information about low-density neutron-rich matter and, in particular, about the density dependence of the symmetry energy. In neutron stars, this question is essential: the density dependence of the symmetry energy determines the proton fraction and the threshold density at which direct URCA process occurs, as discussed in the previous section. Moreover, it governs the threshold densities of other particles such as hyperons, pions, kaons, quark, and so on, which trigger phase transitions and cooling processes.

This example illustrates that articulations can be drawn in which nuclear physics experiments could bring useful

constraints. The perspectives offered by the next generation of radioactive beam facilities are in this sense very attractive. Identifying the experimental methods and choosing the relevant observables for the future exotic beam facilities is a strong challenge and requires an important interplay between experimental and theoretical fields. This is the motivation of a series of workshops called Exotic Nuclei and Neutron Stars [12]. These workshops associate nuclear experimentalists, theoreticians, and astrophysicists in five working groups. The aim is to draw physics cases for the experiments relevant to neutron star properties. After the second meeting, held in May 2007 at the Institut de Physique Nucléaire d'Orsay, some tasks have already been defined. We briefly mention some of them.

- Working group 1: *collective excitations in exotic nuclei*. Among the different ways to measure neutron skins, collective vibrational modes furnish very efficient constraints on the models used to compute the neutron skins. Some of them are even more directly related to the neutron skin thickness such as the spin dipole mode. In GSI a pioneering work has been recently performed relating the neutron skin thickness to soft dipole modes [13]. The study of collective modes in exotic nuclei is also relevant because the excitation spectra of neutron-rich nuclei in the crust of the stars can influence the cooling of the star. Furthermore, the incompressibility modulus of nuclear matter can be deduced from Isoscalar Giant Monopole Resonance and Giant Dipole Resonance properties; their study in exotic nuclei will constitute essential piece of information to constraint the symmetry energy and its isospin dependence. As a complementary constraint on the models, charge radius measurements using laser spectroscopy in very neutron rich nuclei will be performed accurately.
- Working group 2: *pairing in exotic nuclei*. The main question lies on the pairing interaction itself [14]. How is pairing generated? What is the contribution of phonon coupling to the pairing? How do medium effects such as isoscalar or isovector densities influence the pairing field? The answer may come from a global and unique description of pairing effects going from halo nuclei to heavy nuclei via low density neutron matter in the crust of neutron stars. The experimental study of two-neutron transfer would constitute an interesting tool, but theoretical developments are required to analyze such data. For instance, to check the dependence of the results (energies and cross-sections for the rotation and vibration pairing modes) on the properties of the chosen pairing interaction.
- Working group 3: *EoS dependence* on density and temperature. Probing the phase diagram away from standard nuclei constitute the Graal of experimental investigations such as fusion-evaporation and multi-fragmentation experiments. Those are also privileged tools to access to level densities at finite temperature. Experiments are already conducted in this aim, but future facilities will allow to probe the nuclear EoS in more asymmetric matter, together with  $4\pi$  arrays such as FAZIA [15]. Nuclear models predict different isospin dependence and further theoretical investigations are required in the coming year(s).
- Working group 4: *nucleosynthesis in neutron star mergers*. Both type II supernovae and neutron star mergers are candidates to be the location of nucleosynthesis through rapid neutron capture process [16]. The paths are known to be dependent on nuclear inputs such as the symmetry energy. Again, the density dependence of symmetry energy is fundamental to furnish precise and reliable predictions. A lot of measurements and theoretical calculations are required for r-process study. Optical potential determinations should be performed at very low energy. From the theoretical point of view many topics are of relevant importance, such as the determination of neutron capture and beta-decay rates and the study of fission processes.
- Working group 5: *hyper-nuclei*. The presence of hyperons in dense matter softens the EoS. Hyperons contribute more to the energy density than to the pressure because they have larger masses and smaller Fermi momenta. Their presence also enhances the neutrino cooling of the core because they can participate in rapid URCA reactions such as  $\lambda \Rightarrow p + e + \bar{\nu}_e$ . Furthermore, they increase proton to neutron ratio and trigger the URCA process involving nucleons. Unfortunately, very few experimental data exist in this field to discriminate the different theoretical predictions. Many data are expected in the future thanks to experiments such as HyPhi in GSI or J-PARC in Japan. Among those data is expected the production of a large variety of  $\sigma$  hyper-nuclei as well as hyper-nuclei having several hyperons. Together with mean-field models, those data should help in understanding the difference between  $\sigma$ -N and  $\lambda$ -N interaction as well as the  $\lambda$ - $\lambda$  interaction.

The next stage of the working groups is to propose concrete experiments on present or future facilities, which will be discussed during the next workshop. In order to prepare these proposals, predictions are needed to investigate the relevance of future measurements. For instance, the sensitivity of two neutron transfer cross-sections on the pairing functional has to be established. Both experimental and theoretical contributions are necessary. Any interested physicist is encouraged to contact the authors of this article, in order to join the next workshop.

We would like to stress that the activity of these workshops and working groups relies on the important contributions of our speakers and group coordinators: Didier Beaumel (IPN, Orsay, France), Brandon Carter (LUTH, Meudon, France), François De Oliveira (Ganil, France), Hans Emling (GSI, Germany), Lydie Giot (Subatech, France), Stephane Goriely (IAA ULB, Brussels, Belgium), Francesca Gulminelli (LPC, France), François Le Blanc (IPN, Orsay, France), Nicolas Le Neindre (IPN, Orsay, France), Marek Lewitowicz (Ganil, France), Patricia Roussel-Chomaz (Ganil, France), Alan Shotter (TRIUMF, Vancouver, Canada), Take Saito (GSI, Germany), and Heinrich Johannes Wörtche (KVI, The Netherlands).

## References

1. N. K. Glendenning, *Compact Stars*, Springer-Verlag, New York (1997).
2. H. Bethe, *Rev. Modern Phys.* 62 (1990) 801.
3. G. Gamow and M. Schoenberg, *Phys. Rev.* 59 (1941) 539.
4. J. M. Lattimer, C. J. Pethick, M. Prakash, and P. Haensel, *Phys. Rev. Lett.* 66 (1991) 2701.
5. P. M. Pizzochero et al., *Astro. J.* 569 (2002) 381; C. Monrozeau, J. Margueron, and N. Sandulescu, *Phys. Rev. C* (2007), in press.
6. J. W. Negele and D. Vautherin, *Nucl. Phys.* A207 (1973) 298.
7. N. Chamel, S. Naimi, E. Khan, and J. Margueron, *Phys. Rev. C* (2007).
8. B. Carter, N. Chamel, and P. Haensel, *Nucl. Phys.* A748 (2005) 675.
9. S. Typel and B. A. Brown, *Phys. Rev. C* 64 (2007) 027301.
10. C. J. Horowitz and J. Piekarewicz, *Phys. Rev. C* 64 (2001) 062802.
11. J. M. Lattimer and M. Prakash, *Phys. Rep.* 333 (2000) 121.
12. <http://snns.in2p3.fr/>
13. A. Klimkiewicz et al., submitted to *Phys. Rev. Lett.*
14. H.-J. Schulze et al., *Phys. Rev. C* 63 (2001) 044310.
15. [http://fazia.in2p3.fr/documents/LoI\\_SPIRAL2\\_ThermoDyn\\_v7.pdf](http://fazia.in2p3.fr/documents/LoI_SPIRAL2_ThermoDyn_v7.pdf)
16. S. Goriely et al., *Nucl. Phys.* A758 (2004) 587.

# Low-energy excitations in nuclear systems: From exotic nuclei to the crust of neutron stars

M. Grasso <sup>\*</sup>, E. Khan, J. Margueron, N. Van Giai

*Institut de Physique Nucléaire, Université Paris-Sud, IN2P3-CNRS, F-91406 Orsay cedex, France*

Received 24 January 2008; received in revised form 14 March 2008; accepted 1 April 2008

Available online 10 April 2008

---

## Abstract

We study the evolution of low-lying quadrupole modes as a function of the neutron excess, from neutron-rich nuclei to the nuclear systems located in the crust of a neutron star. The microscopic analysis is performed within the Hartree–Fock–Bogoliubov + quasiparticle random-phase approximation framework. The Wigner–Seitz approximation is adopted to describe the lattice of nuclear clusters embedded in neutron star crusts. A systematic analysis of  $Z = 50$  nuclear systems, performed by increasing the isospin asymmetry, reveals that a low-energy  $2^+$  mode is found in all the systems. However, the nature of the relevant configurations that construct this mode drastically changes when the drip line is crossed. This result is confirmed by the study of the transition density associated to the mode in the inner crust system with  $Z = 40$  and  $N = 1460$ . It is shown that the transition density profile is different with respect to typical profiles found for  $2^+$  low-lying modes in nuclei: the excitation is mostly constructed with neutrons belonging to the cluster surface and the external free gas.

© 2008 Elsevier B.V. All rights reserved.

PACS: 21.10.Re; 21.60.Jz; 26.60.Gj

---

## 1. Introduction

Neutron stars provide a unique and fascinating stage where the evolution from finite to infinite systems can be analyzed [1,2]. If semiclassical models permit a qualitative picture and work well to describe some general features, the proper treatment of quantum effects is still required to analyze in a more accurate way, for instance, the properties of the inner crust where nuclear clus-

---

<sup>\*</sup> Corresponding author.

*E-mail address:* [grasso@ipno.in2p3.fr](mailto:grasso@ipno.in2p3.fr) (M. Grasso).

ters are present together with a neutron gas. The modern modelization of neutron star crusts has been proposed in the 1970s in the pioneering works of Baym et al. [3] and Negele and Vautherin (NV) [4]; the two analysis have been performed, respectively, within a semiclassical Thomas–Fermi and a microscopic Hartree–Fock framework. To briefly summarize, an outer and an inner part can be distinguished in the crust of a neutron star. In the outer crust exotic nuclei form a Coulomb lattice in the presence of an electron gas. More deeply in the interior of the crust, density increases and nuclei are more and more neutron-rich up to the drip point  $\rho \sim 4 \times 10^{11} \text{ g/cm}^3$ . Beyond, neutrons drip out and exotic structures of clusters surrounded by relativistic electrons and superfluid neutrons form a Coulomb lattice (inner crust). These structures can be regarded as a bridge between a finite nucleus and an infinite nuclear gas. The properties of the crystal of nuclei or clusters have a strong impact on the behavior of the star. For instance, superfluidity of neutrons affects the specific heat of the crust as it has been shown in Ref. [5]. Also dynamic properties, such as the excitation modes, influence the cooling time [6] by modifying the specific heat of the crust [7,8] and the neutrino propagation [9]. The role of the low-lying collective modes, the so-called supergiant resonances, has been underlined in Ref. [7] in connection with the evaluation of the specific heat and the cooling time: by modelizing the Coulomb lattice with spherical Wigner–Seitz (WS) cells [10] of radius  $R_{WS}$ , each cell has been studied as independent of all the others within the Hartree–Fock–Bogoliubov [11,12] + quasiparticle random-phase approximation [13] (HFB + QRPA) approach. The analysis has been limited to the innermost layers of the crust. A detailed analysis, performed within the HFB framework and extended also to the external lower-density regions, has shown that the cooling time depends strongly on the pairing gap [8], and that the largest contribution comes from the intermediate and low-density parts of the inner crust [8,14] where the central cluster is most probably spherical.

All the studies mentioned above have been done within the WS modelization of NV, i.e., by adopting their  $(Z, R_{WS})$  values determined for each baryonic density in the different layers of the crust, where  $Z$  is the number of protons. Baldo and collaborators have recently performed a work analogous to that of NV, but including also pairing correlations within a semi-microscopic approach [15]. Differences with respect to NV have been found and the most important discrepancies are obtained for the charge  $Z$  of the cells (lower values of  $Z$  are typically preferred). These differences appear both in the innermost layers of the crust, where pairing is indeed expected to play a crucial role, as well as in the outermost layers, where pairing is negligible. This means that the result of the minimization procedure employed to evaluate the most stable configurations depends on the density functional that is adopted in the model. A recent work has pointed out that the minimization is also influenced by spurious shell effects coming from the discretization procedure introduced to treat the free neutron gas [16].

The inner crust is formed of nuclear systems with very high isospin asymmetries at densities lower than the saturation density  $\rho_0 = 0.16 \text{ fm}^{-3}$  (the maximum density in the innermost layers of the crust is  $\sim 0.5\rho_0$ ). The challenge to properly treat these systems is thus the formulation of microscopic models that have to be well adapted: (i) for very neutron-rich systems, (ii) at densities  $\rho \leq \rho_0$ . It is however worthwhile to perform some systematic analysis with the presently available models to understand at least qualitatively which phenomena should be expected by increasing the isospin asymmetry: the aim of this work is to study the evolution of low-lying quadrupole excitations with respect to neutron excess, passing from exotic nuclei to the nuclear systems located in the inner crust. We treat the low-lying modes of neutron-rich isotopes as well as the supergiant resonances of a WS cell with the microscopic and self-consistent approach HFB + QRPA. The Skyrme interaction SLy4 [17] is chosen in the particle–hole channel, whereas a zero-range density-dependent interaction is chosen to describe pairing correlations. For conve-

nience, in what follows we refer to the nuclear systems contained in WS cells with the nuclear symbols corresponding to their number of protons. For each density we adopt the values of  $(Z, R_{\text{WS}})$  determined by NV.

The article is organized as follows: in Section 2 the theoretical model is introduced and details on the numerical calculations are provided. In Section 3 a systematic study with respect to isospin asymmetry is presented for nuclear systems with  $Z = 50$ . In Section 4 the transition density associated to the supergiant mode in  $^{150}\text{Zr}$  is analyzed. Conclusions are drawn in Section 5.

## 2. Theoretical framework

We work at zero temperature and in spherical symmetry. The employed model is the same as described in Ref. [7]. We first solve the HFB equations in coordinate representation,

$$\begin{aligned} H(r)u_{vljq}(r) + \Delta(r)v_{vljq}(r) &= E_{vljq}u_{vljq}(r), \\ \Delta(r)u_{vljq}(r) - H(r)v_{vljq}(r) &= E_{vljq}v_{vljq}(r), \end{aligned} \quad (1)$$

where  $H(r)$  contains the kinetic term and the Hartree–Fock mean field while  $\Delta(r)$  represents the pairing field;  $u$  and  $v$  are the upper and lower components of the wave function and  $E$  the corresponding quasiparticle energy;  $q$  stands for  $n$  (neutrons) or  $p$  (protons) and  $\nu, l, j$  are the quantum numbers associated to the wave function. For the nuclei, the HFB equations are solved by imposing box boundary conditions whereas for the nuclear systems enclosed in a WS cell the usual Dirichlet (Von Neumann) boundary conditions for the even-(odd-) $l$  wave functions are adopted [4]. We solve the HFB equations for positive quasiparticle energies. In this case, the particle and anomalous densities are defined as:

$$\rho_q(r) = \sum_{\nu lj} \frac{2j+1}{4\pi} v_{\nu lj q}^*(r)v_{\nu lj q}(r), \quad (2)$$

$$\tilde{\rho}_q(r) = - \sum_{\nu lj} \frac{2j+1}{4\pi} u_{\nu lj q}^*(r)v_{\nu lj q}(r), \quad (3)$$

where the sum is carried over the bound and the unbound states. For a contact pairing interaction the anomalous density, Eq. (3), is known to diverge. An energy cut-off of 60 MeV is thus adopted.

The QRPA equations are solved in coordinate representation [13]. The Bethe–Salpeter-type equation is integrated for the QRPA Green function  $G$ ,

$$G = (1 - G_0 V)^{-1} G_0, \quad (4)$$

where  $G_0$  is the unperturbed Green function and  $V$  the residual interaction. In this work the response function  $S$ ,

$$S(\omega) = -\frac{1}{\pi} \text{Im} \int d\vec{r} d\vec{r}' F^*(\vec{r}) G(\vec{r}, \vec{r}'; \omega) F(\vec{r}'), \quad (5)$$

is evaluated for a quadrupole excitation operator  $F = r^2 Y_{20}$ . For the graphical representation of the results a Lorentzian smearing parameter  $\eta = 150$  keV is used.

In the particle–hole channel, we adopt the Skyrme interaction SLy4 [17], that is well adapted to treat neutron-rich systems because it has been constructed to reproduce neutron matter properties. For the particle–particle channel, a zero-range density dependent interaction is chosen,

$$V(\vec{r} - \vec{r}') = V_0 \left[ 1 - \eta \left( \frac{\rho(r)}{\rho_0} \right)^\alpha \right] \delta(\vec{r} - \vec{r}'). \quad (6)$$

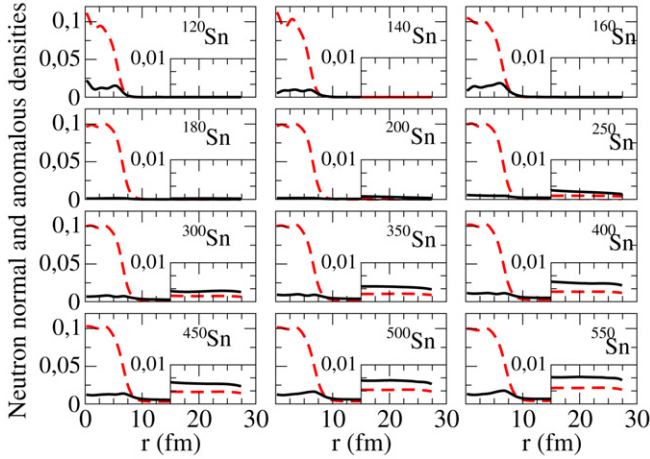


Fig. 1. Normal (dashed line) and anomalous (full line) neutron densities, Eqs. (2) and (3), in units of  $\text{fm}^{-3}$ .

The parameters of the pairing interaction have been set as in Refs. [7] and [8] to reproduce approximately the same results as the bare potentials or the effective Gogny interaction D1S [18] for pure neutron matter, i.e., a maximum gap of  $\sim 3$  MeV at  $k_{Fn} \sim 0.87 \text{ fm}^{-1}$ . It has to be mentioned that, when medium polarization effects are introduced in the BCS gap equations, the maximum gap of neutron matter can be lowered down to about 1.8 MeV (see, e.g., Ref. [19]). The cooling time is strongly sensitive to the pairing gap and important differences are actually found when the parameters of the pairing interaction are fixed to reproduce the gap with or without screening effects [8,20].

### 3. Systematic analysis: Nuclear systems with $Z = 50$

In the work of NV, the nuclear systems with  $Z = 40$  and  $Z = 50$  (with different values of  $R_{WS}$ ) are found several times as the most stable configurations, for all the baryonic densities considered in the inner crust. We thus choose  $Z = 40$  and  $Z = 50$  systems for the analysis discussed in the present and next sections. First, we analyze the systematic evolution of the low-lying  $2^+$  mode in  $Z = 50$  nuclear systems. We start with neutron-rich Sn nuclei. When the drip line ( $^{176}\text{Sn}$  in our model) is crossed we progressively increase the neutron number up to  $N = 1750$ , that represents the innermost  $Z = 50$  configuration predicted in the crust by NV. We use a box radius of 27.4 fm, that is the WS radius associated to the configuration  $Z = 50$ ,  $N = 1750$ . This means that, by increasing the neutron number, the baryonic density of the system grows up and reaches the value of  $\sim 0.02 \text{ fm}^{-3}$  for  $^{1800}\text{Sn}$ .

We plot in Fig. 1 the normal (dashed line) and anomalous (full line) neutron densities, Eqs. (2) and (3), for the nuclei  $^{120}\text{Sn}$ ,  $^{140}\text{Sn}$  and  $^{160}\text{Sn}$  (first row) and for the unbound systems from  $^{180}\text{Sn}$  up to  $^{550}\text{Sn}$ . As expected, one observes the development of a neutron gas when the neutron number is increased. Furthermore, the anomalous density is practically negligible both inside and outside the cluster in  $^{180}\text{Sn}$  and  $^{200}\text{Sn}$ . It starts increasing for  $^{250}\text{Sn}$ . Pairing correlations are actually expected to be small in  $^{180}\text{Sn}$  because this system is located close to the magic nucleus  $^{176}\text{Sn}$ . For the other nuclear systems up to  $^{250}\text{Sn}$ , the weakness of pairing is due to the density dependence of the pairing gap in nuclear matter. The pairing gap obtained from the BCS equations goes to zero [21,22] when the density goes to zero. This explains why pairing correlations

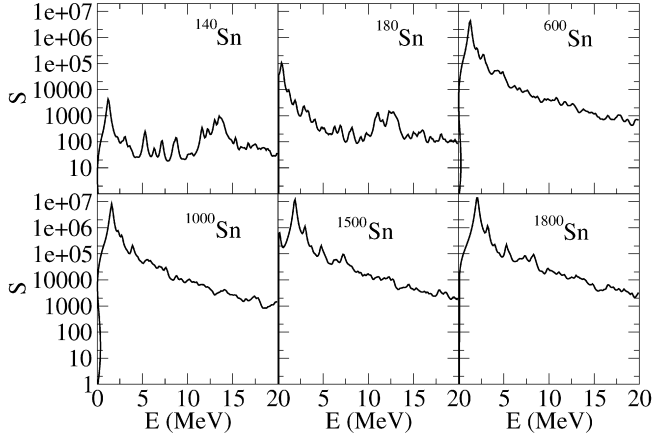


Fig. 2. QRPA strength distributions for the quadrupole mode in units of  $\text{fm}^4 \text{MeV}^{-1}$ .

are so weak in the low-density neutron gas present for instance in  $^{200}\text{Sn}$ . Moreover, the Pipard's coherence length,  $\xi_P = \hbar^2 k_{F_n} / (m_n^* \pi \Delta_n)$ , is very large for a low-density neutron gas (see Ref. [23] for a detailed discussion). As a consequence, the pairing features of the gas affect the whole nuclear system and modify also the pairing inside the nuclear cluster (pairing correlations are weak also inside the cluster). By increasing the density, the pairing gap becomes larger and the coherence length is reduced. The bell-shape dependence of the pairing gap on the density indicates that pairing correlations in the neutron gas are expected to be the strongest approximately at the baryonic density of the crust  $0.02 \text{ fm}^{-3}$  where the system  $^{1800}\text{Sn}$  is predicted, as discussed in Refs. [7,24].

The evolution of the quadrupole response can be observed in Fig. 2, from the nucleus  $^{140}\text{Sn}$  up to  $^{1800}\text{Sn}$ . A low-lying  $2^+$  mode as well as a giant resonance are found in all the systems. The giant resonance is clearly visible in  $^{140}\text{Sn}$  and  $^{180}\text{Sn}$ . For the other systems the giant resonance has a much lower strength with respect to the low-energy supergiant mode and is located in the 5–7 MeV region as expected by the  $65A^{-1/3} \text{ MeV}$  systematics [25]. We concentrate on the low-lying mode that will mainly influence both the specific heat in the crust and the neutrino cross sections. We perform a first analysis of the evolution of the low-lying mode with respect to the neutron excess by checking which are the most important configurations that contribute to the excitation. Since the residual interaction acts in an analogous way in all the systems (pushing downwards the energy and promoting collectivity), we consider the unperturbed spectrum and compare the nucleus  $^{176}\text{Sn}$  and the unbound system  $^{180}\text{Sn}$  that is located just beyond the drip line. Pairing correlations are not present in the nucleus  $^{176}\text{Sn}$  because it is closed-shell; in Fig. 1 it has been shown that pairing correlations are weak also in  $^{180}\text{Sn}$ . We can thus consider just particle-hole configurations constructed with the single-particle states. In  $^{176}\text{Sn}$ , that is the last bound nucleus in our model, all the occupied states are bound;  $2^+$  particle-hole configurations are thus constructed with bound negative energy hole states. Passing to  $^{180}\text{Sn}$  four neutrons are added giving an unbound system. The four additional neutrons are placed in the unbound states  $4p1/2$  and  $4p3/2$ , with an occupation of 54% and 73%, respectively. The occupations are partial (and not strictly 0 and 1) because pairing correlations are not completely absent in the system and the two single-particle states are practically degenerate. We have checked that the low-lying mode is mainly composed of a few single-particle configurations where the hole states are  $4p1/2$  and

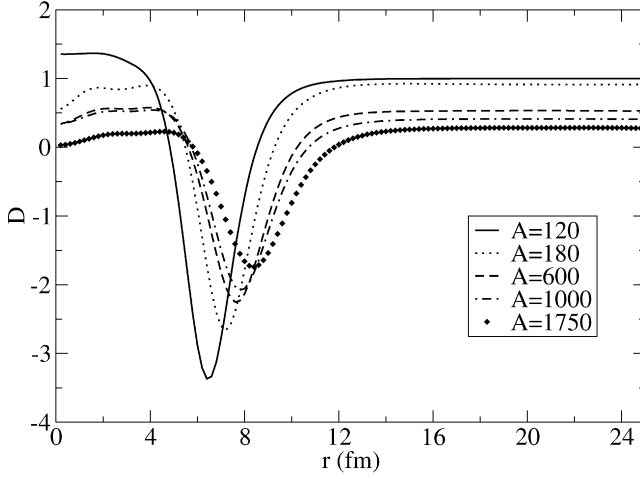


Fig. 3. Determinant  $D$  calculated for the systems  $^{120}\text{Sn}$ ,  $^{180}\text{Sn}$ ,  $^{600}\text{Sn}$ ,  $^{1000}\text{Sn}$  and  $^{1750}\text{Sn}$ .

$4p3/2$  (both single-particle energies are  $\sim 0.2$  MeV) and the particle states are the empty states  $3f5/2$  and  $3f7/2$  (both single-particle energies are  $\sim 0.65$  MeV). By looking at the composition of the low-energy mode at the drip line and just beyond, it thus comes out that the most relevant configurations are completely different in the two cases. In the latter case, in particular, both states of the most important configurations are unbound. It is clear that the transition amplitude of the quadrupole operator  $r^2 Y_{20}$  between two unbound single-particle states is much larger than in the case where one of the single-particle is bound and its wave function is localized in the interior region.

Let us now perform a qualitative test. We calculate the denominator of the RPA response function in asymmetric nuclear matter at the hydrodynamical limit (zero transferred energy and momentum) which is related to the determinant of the polarization in the  $2 \times 2$  isospin space [26],

$$D = \text{Det} \begin{pmatrix} 1 + N_0^n f_0^{nn} & N_0^n f_0^{np} \\ N_0^p f_0^{pn} & 1 + N_0^p f_0^{pp} \end{pmatrix}, \quad (7)$$

where  $N_0^\tau = m_\tau^* k_{F\tau} / \pi^2 \hbar^2$  is the density of states of the Fermi gas and  $f_0^{\tau\tau'}$  is the monopolar Landau parameter in the density-density channel (see, for instance, Ref. [27]). The zeros of the determinant correspond to the poles of the strength and are induced by an attractive residual interaction. We display in Fig. 3 the determinant  $D$ , Eq. (7), calculated within the local density approximation for the systems  $^{120}\text{Sn}$ ,  $^{180}\text{Sn}$ ,  $^{600}\text{Sn}$ ,  $^{1000}\text{Sn}$  and  $^{1750}\text{Sn}$ . The determinant is represented as a function of the radial distance. One observes that, for all the systems situated before and after the drip line, the determinant goes to zero at the surface of the cluster. Moreover, for the systems situated beyond the neutron drip, the determinant is close to zero, on the positive side, in the region of the neutron gas located out of the cluster. When the neutron number increases, the determinant progressively approaches zero (more and more attractive residual interaction in the neutron gas region). One can thus conclude that the nature of the low-lying mode is strongly modified when the drip line is crossed. In nuclei it is constructed with nucleons located at the surface, while in the unbound systems it is built with both nucleons located at the surface and neutrons belonging to the low-density free gas region. This conclusion will be microscopically confirmed in the next section.

#### 4. Transition density in the inner crust system with $Z = 40$ , $N = 1460$

For our analysis of the transition density, we consider the inner crust system with  $Z = 40$  and  $N = 1460$  predicted by NV at the baryonic density  $\rho = 0.041 \text{ fm}^{-3}$  and with the WS radius  $R_{WS} = 19.6 \text{ fm}$ .

In Fig. 4 we show the neutron (full lines) and proton (dotted lines) density profiles for  $^{1500}\text{Zr}$ . A very diffuse surface going from 4.5 to 10 fm can be viewed as analogous to a neutron skin in a nucleus. Outside this region a uniform pure neutron gas fills the volume of the WS cell.

We present in Fig. 5 the QRPA quadrupole strength distribution for  $^{1500}\text{Zr}$ . The strength is concentrated around the very collective low-lying supergiant mode at about 3.5 MeV. In the spectrum the giant resonance region is also present at about 8–10 MeV as shown in the inset. As in the Sn case discussed in the previous section, its associated strength is negligible with respect to the strength of the supergiant mode. This is due to the fact that the giant resonance is built only with the contribution of particles bound to the central cluster while a huge number of particles belonging to both the cluster surface and the free gas participate to the low-energy supergiant

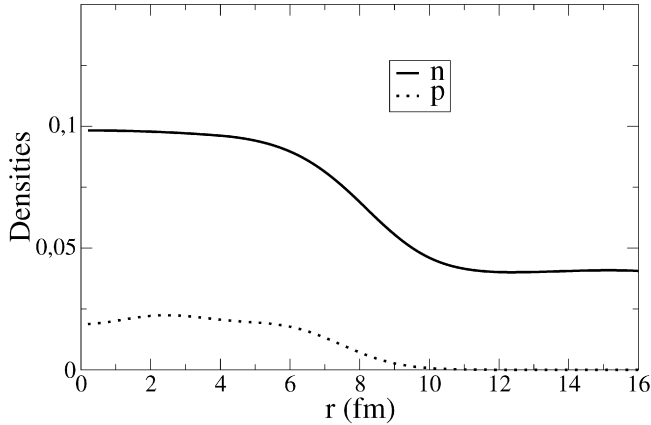


Fig. 4. Neutron (full lines) and proton (dotted lines) density profiles for the inner crust system  $^{1500}\text{Zr}$  in units of  $\text{fm}^{-3}$ .

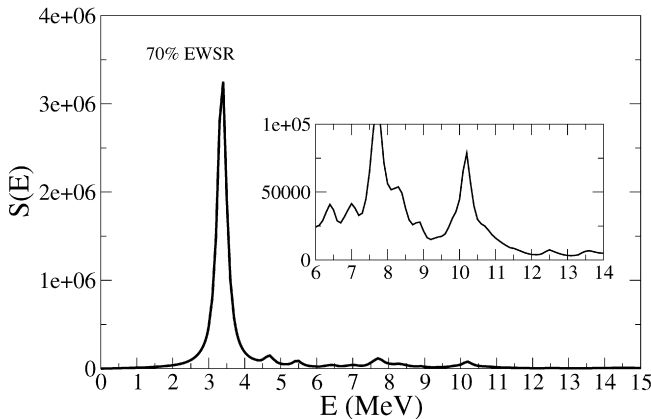


Fig. 5. Neutron quadrupole QRPA strength distributions for  $^{1500}\text{Zr}$  in units of  $\text{fm}^4 \text{ MeV}^{-1}$ .

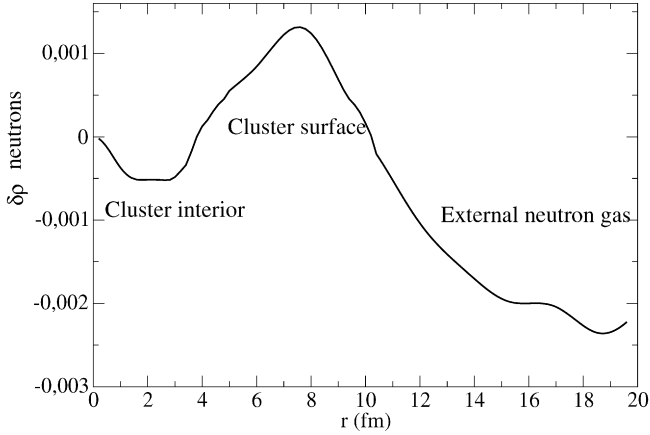


Fig. 6. Neutron transition density in units of  $\text{fm}^{-3}$  for the low-energy mode in  $^{1500}\text{Zr}$ .

mode, as it was argued in the previous section. To confirm this microscopically, we evaluate now the transition density  $\delta\rho(r)$  associated to the supergiant resonance in  $^{1500}\text{Zr}$ . The analysis of the radial profile of the transition density gives indications on the location of the particles which mainly participate to the excitation. The neutron transition density is plotted in Fig. 6 and its profile confirms what expected: a strong contribution is coming from the cluster surface and from the external neutron gas. The internal part of the neutron transition density is weaker and very similar to typical transition densities in nuclei [13]. This is a precise confirmation of the result already found in the previous section: the nature of the  $2^+$  mode in the system  $^{1500}\text{Zr}$  is strongly different with respect to what is typically found in nuclei.

We have verified that the low-lying  $2^+$  state in  $^{1500}\text{Zr}$  is constructed with many configurations, as confirmed by the profile of its transition density that presents only a few nodes: two configurations, with quantum numbers  $l = 17, j = 35/2$  (hole),  $l = 19, j = 39/2$  (particle) and  $l = 17, j = 33/2$  (hole),  $l = 19, j = 37/2$  (particle), are the most important and contribute  $\sim 5\%$  and  $4\%$  to the collectivity, respectively. Each of the other many configurations constructing the mode contributes less than  $4\%$ . This means that, going from just beyond the drip line (see the case of  $^{180}\text{Sn}$  discussed in the previous section) to systems like  $^{1500}\text{Zr}$  or  $^{1800}\text{Sn}$ , the collectivity of the low-lying mode increases.

## 5. Conclusions

We have discussed the evolution of low-lying  $2^+$  modes starting with neutron-rich nuclei and increasing the isospin asymmetry up to the corresponding nuclear systems (having the same number of protons) predicted by NV in the inner crust of neutron stars. We have first performed a systematic study in nuclear systems having  $Z = 50$ , up to  $^{1800}\text{Sn}$ . Low-lying  $2^+$  modes are found in the same energy region both in nuclei and in the unbound nuclear systems. They are characterized by a huge strength in the unbound systems and for this reason they are called supergiant modes. Our analysis reveals that the nature of the most relevant configurations that construct the low-lying modes is very different before and after the drip line. Moreover, the study of the denominator of the RPA response function in asymmetric nuclear matter, evaluated within the local density approximation, shows that the nucleons mostly participating to the excitation, in the systems situated after the drip line, are located at the cluster surface and in the external

gas region. In particular, when increasing the neutron number, the determinant progressively approaches zero from positive values in the radial region  $r$  greater than  $\sim 12$  fm. This is due to the fact that the residual interaction becomes more and more attractive in the low-density pure neutron gas region. It means that the contribution coming from the gas to the collectivity of the low-lying mode becomes more important. This result is confirmed by the analysis of the microscopic transition density associated to the supergiant  $2^+$  mode obtained within the QRPA in the inner crust system  $^{1500}\text{Zr}$ : the transition density has a different radial profile with respect to what is typically found in nuclei. A strong contribution coming from the cluster surface and the external neutron gas is found. As a general conclusion of these results, the nature of the low-lying  $2^+$  mode is strongly modified when the neutron drip line is crossed by increasing the isospin asymmetry. However, a strong link still remains through the theoretical model that is used to describe both nuclei and nuclear systems in the crust of neutron stars. The improvement of the theoretical models is an important challenge; as mentioned in the introduction, the results found for the nuclear systems situated in neutron star crusts are sensitively dependent on the used density functional [15]. First, effective interactions have not yet been validated in very asymmetric systems and the isospin dependence of the interaction is of crucial importance to properly describe neutron star crusts. Also the pairing interaction, which in principle should be derived from the bare potential, is under debate and the role played by medium polarization effects is not yet clarified. Furthermore, a proper theoretical description of the lattice present in the crust should not rely on the Wigner–Seitz approximation but on the band theory [28]. As a consequence, an extensive work is demanded to better set a suitable theoretical model and to constrain a density functional that could reliably describe both types of nuclear systems. The next generation Radioactive Nuclear Beam facilities will allow to explore more systematically regions closer to the nuclear drip lines. In this framework nuclei with diffuse neutron skins, i.e. low-density diffuse surfaces, shall be more easily accessible. The impact of strong neutron excess on low-lying excitations will also be investigated in some cases. These new experimental data will permit to better constrain the effective interactions and, consequently, to improve the theoretical models that are applied to neutron stars.

## References

- [1] N.K. Glendenning, *Compact Stars*, Springer-Verlag, New York, 2000.
- [2] J.M. Lattimer, M. Prakash, *Science* 304 (5670) (2004) 536.
- [3] G. Baym, A. Bethe, C. Pethick, *Nucl. Phys.* 175 (1971) 225.
- [4] J.W. Negele, D. Vautherin, *Nucl. Phys. A* 207 (1973) 298.
- [5] N. Sandulescu, *Phys. Rev. C* 70 (2004) 025801.
- [6] J.M. Lattimer, K.A. Van Riper, M. Prakash, M. Prakash, *Astrophys. J.* 425 (1994) 802.
- [7] E. Khan, N. Sandulescu, N. Van Giai, *Phys. Rev. C* 71 (2005) 042801(R).
- [8] C. Monrozeau, J. Margueron, N. Sandulescu, *Phys. Rev. C* 75 (2007) 065807.
- [9] J. Margueron, J. Navarro, P. Blottiau, *Phys. Rev. C* 70 (2004) 028801.
- [10] E.P. Wigner, F. Seitz, *Phys. Rev.* 43 (1933) 804;  
E.P. Wigner, F. Seitz, *Phys. Rev.* 46 (1934) 509.
- [11] P. Ring, P. Schuck, *The Nuclear Many-Body Problem*, Springer-Verlag, Berlin, 1980.
- [12] J. Dobaczewski, H. Flocard, J. Treiner, *Nucl. Phys. A* 422 (1984) 103;  
M. Grasso, N. Sandulescu, N. Van Giai, R.J. Liotta, *Phys. Rev. C* 64 (2001) 064321.
- [13] E. Khan, N. Sandulescu, M. Grasso, N. Van Giai, *Phys. Rev. C* 66 (2002) 024309.
- [14] P.M. Pizzocchero, F. Barranco, E. Vigezzi, R.A. Broglia, *Astrophys. J.* 569 (2002) 381.
- [15] M. Baldo, E.E. Saperstein, S.V. Tolokonnikov, *Phys. Rev. C* 76 (2007) 025803;  
M. Baldo, U. Lombardo, E.E. Saperstein, S.V. Tolokonnikov, *Nucl. Phys. A* 750 (2005) 409;  
M. Baldo, U. Lombardo, E.E. Saperstein, S.V. Tolokonnikov, *Phys. At. Nucl.* 68 (2005) 1812.

- [16] J. Margueron, N. Van Giai, N. Sandulescu, in: *Proceedings of Exotic States of Nuclear Matter-International Symposium on Exotic States of Nuclear Matter, Italy, 2007*.
- [17] E. Chabanat, et al., *Nucl. Phys. A* 635 (1998) 231.
- [18] J.-F. Berger, M. Girod, D. Gogny, *Nucl. Phys. A* 438 (1984) 236.
- [19] L.G. Cao, U. Lombardo, P. Schuck, *Phys. Rev. C* 74 (2006) 064301.
- [20] J. Margueron, H. Sagawa, K. Hagino, *Phys. Rev. C* 76 (2007) 064316.
- [21] U. Lombardo, in: M. Baldo (Ed.), *Nuclear Methods and the Nuclear Equation of State*, *Int. Rev. Nucl. Physics*, vol. 9, World Scientific, Singapore, 1999.
- [22] E. Garrido, P. Sarriguren, E. Moya de Guerra, P. Schuck, *Phys. Rev. C* 60 (1999) 064312.
- [23] M. Matsuo, *Phys. Rev. C* 73 (2006) 044309.
- [24] N. Sandulescu, N. Van Giai, R.J. Liotta, *Phys. Rev. C* 69 (2004) 045802.
- [25] A. Bohr, B.R. Mottelson, *Nuclear Structure*, vol. II, World Scientific, 1998.
- [26] C. Garcia-Recio, J. Navarro, N. Van Giai, L.L. Salcedo, *Ann. Phys. (N.Y.)* 214 (1992) 293.
- [27] E.S. Hernández, J. Navarro, A. Polls, J. Ventura, *Nucl. Phys. A* 627 (1997) 460.
- [28] B. Carter, N. Chamel, P. Haensel, *Nucl. Phys. A* 748 (2005) 675;  
N. Chamel, S. Naimi, E. Khan, J. Margueron, *Phys. Rev. C* 75 (2007) 055806.



# **Chapitre 3**

**Extensions de la méthode des  
phases aléatoires. Corrélations  
dans l'état fondamental**

### 3.1 Introduction. Nécessité d'aller au-delà de l'approximation de quasiboson (QBA)

Tous les travaux présentés dans le chapitre précédent sont basés sur des approches de champ moyen. Ces dernières années et depuis le développement de la physique des noyaux exotiques, l'évidence s'est imposée de l'importance d'améliorer et d'étendre les outils théoriques actuellement disponibles. La nécessité d'aller au-delà du champ moyen s'impose face à l'existence de phénomènes nouveaux qui caractérisent certains noyaux exotiques. Par exemple, les prédictions sur l'évolution de la structure en couches loin de la stabilité nécessitent une évaluation plus sophistiquée des énergies des états individuels avec l'introduction du couplage particule-vibration dont nous parlerons à la fin de ce mémoire. Par ailleurs, l'existence des modes d'excitation dipolaires pygmées de basse énergie indiquerait que les noyaux exotiques sont des systèmes plus complexes que les noyaux stables et les corrélations y jouent un rôle peut-être plus important. Ce contexte motive nos travaux sur des extensions de la RPA.

La RPA est une approche très couramment utilisée pour la description des états excités d'un système à N corps. Cette approche est plus raffinée que la méthode de Tamm-Dancoff où les états excités sont de simples combinaisons de configurations particule-trou construites sur l'état fondamental de HF. L'état fondamental RPA est défini comme l'état du vide des opérateurs  $Q_v$ ,

$$Q_v |RPA\rangle = 0, \quad (3.1)$$

où les  $Q_v^+$  sont les opérateurs de créations des phonons RPA :

$$Q_v^+ \equiv \sum_{ph} \left( X_v^{ph} a_p^+ a_h - Y_v^{ph} a_h^+ a_p \right). \quad (3.2)$$

Nous utilisons la notation habituelle : p et h désignent les nombres quantiques des états de particule et de trou par rapport à l'état fondamental d'HF. L'opérateur  $Q_v^+$  construit l'état excité  $|v\rangle$  en agissant sur l'état fondamental :

$$Q_v^+ |RPA\rangle = |v\rangle. \quad (3.3)$$

La présence du second terme en Y dans l'expression de  $Q_v^+$  garantit que, en principe, l'état fondamental  $|RPA\rangle$  est corrélé et différent de l'état HF puisque  $a_p |HF\rangle = 0$ . Les amplitudes Y mesurent donc la présence de corrélations dans l'état fondamental.

Une des procédures pour dériver les équations RPA est basée sur la méthode des équations du mouvement [RS80] qui permet d'introduire de manière schématique les équations RPA,

$$\begin{pmatrix} A & B \\ B^* & A^* \end{pmatrix} \begin{pmatrix} X^v \\ Y^v \end{pmatrix} = (E_v - E_0) \begin{pmatrix} 1 & 0 \\ 0 & -1 \end{pmatrix} \begin{pmatrix} X^v \\ Y^v \end{pmatrix}, \quad (3.4)$$

et de définir les matrices A et B :

$$\begin{aligned} A_{ph,p'h'} &\equiv \langle \text{RPA} | [a_h^+ a_p, H, a_p^+ a_{h'}] | \text{RPA} \rangle, \\ B_{ph,p'h'} &\equiv -\langle \text{RPA} | [a_h^+ a_p, H, a_{h'}^+ a_p'] | \text{RPA} \rangle, \end{aligned} \quad (3.5)$$

avec :

$$[A, B, C] \equiv \frac{1}{2} ([A, [B, C]] + [[A, B], C]). \quad (3.6)$$

Les solutions des équations (3.4) sont les énergies d'excitation  $E_v - E_0$  et les amplitudes X et Y. Pour résoudre plus facilement les équations RPA, l'approximation de Quasiboson (QBA) est faite dans le calcul des matrices A et B. Cette approximation peut être écrite comme :

$$\begin{aligned} \langle \text{RPA} | [a_h^+ a_p, a_p^+ a_{h'}] | \text{RPA} \rangle &= \delta_{hh'} \delta_{pp'} - \delta_{pp'} \langle \text{RPA} | a_{h'} a_h^+ | \text{RPA} \rangle \\ - \delta_{hh'} \langle \text{RPA} | a_p^+ a_p | \text{RPA} \rangle &\approx \langle \text{HF} | [a_h^+ a_p, a_p^+ a_{h'}] | \text{HF} \rangle = \delta_{pp'} \delta_{hh'}. \end{aligned} \quad (3.7)$$

L'introduction de cette approximation génère deux problèmes :

(i) le Principe de Pauli est violé puisque des termes sont négligés dans l'évaluation de la valeur moyenne du commutateur ; l'expression (3.7) serait valable exactement si la paire d'opérateurs  $a^+ a$  était un opérateur bosonique (de là dérive le nom de l'approximation).

(ii) Un problème de consistance formelle est introduit : la méthode RPA se propose en principe de tenir compte de la présence de corrélations dans l'état fondamental. D'autre part, en pratique, la violation du Principe de Pauli correspond à calculer les valeurs moyennes qui définissent les matrices A et B en utilisant l'état de HF au lieu de l'état corrélé. Par conséquent, la violation du Principe de Pauli est plus importante dans les systèmes où l'état fondamental est très corrélé : dans ce cas, les amplitudes Y deviennent typiquement très grandes (elles sont normalement petites devant les amplitudes X).

## 3.2 Les règles de somme. Inclusion des configurations particule-particule et trou-trou

Pour résoudre le problème de la violation du Principe de Pauli dans le contexte de la RPA, deux directions ont été explorées :

- (i) développement de techniques basées sur des méthodes d'expansion bosonique [Ca89, Be92, Sa95, Sa97, Sa99, Vo99, Gr02, Ga06a] ;
- (ii) extensions de la RPA dans l'espace fermionique [Du90, Kl91, Ka93, Du96, Ca98, Kr98, Ra98, Ta04, Ga06b, To07].

La plupart de ces approches sont basées sur la RPA renormalisée introduite par Hara et Rowe [Ha64, Ro68]. Dans le cadre de la RPA renormalisée, le Principe de Pauli est satisfait et l'état fondamental est explicitement corrélé avec des nombres d'occupation différents de 0 et 1 qui apparaissent dans des facteurs de renormalisation. Cependant, toutes les méthodes basées sur la RPA renormalisée ont une très forte limitation due au fait qu'elles ne respectent pas les règles de somme pondérées en énergie Energy Weighted Sum Rules (EWSR),

$$\sum_{\nu} (E_{\nu} - E_0) |\langle \nu | F | 0 \rangle|^2 = \frac{1}{2} \langle 0 | [F, [H, F]] | 0 \rangle, \quad (3.8)$$

où  $F$  est un opérateur à un corps hermitique et  $|0\rangle$  l'état fondamental exact. Les violations peuvent atteindre 20-30% dans certains cas [Ca98].

Dans l'article [Gr00], nous avons proposé une manière de résoudre le problème et nous avons montré que, en élargissant l'espace des configurations pour inclure aussi les configurations particule-particule et trou-trou (en plus des configurations particule-trou), les EWSR sont parfaitement satisfaites.

Dans un travail plus récent [Ga09], que je fais suivre, cette extension a été améliorée. Le problème généré par l'introduction des configurations pp et hh est que des états non physiques apparaissent dans le spectre d'excitation, comme il a été montré dans [Gr00] où une application dans un modèle de Lipkin à trois niveaux a été réalisée. Ces états ne correspondent à aucun des états du spectre exact du modèle de Lipkin. En général, leur probabilité de transition est assez faible, mais non nulle, et dans un calcul réaliste il serait difficile de les séparer de manière non ambiguë du spectre exact. Ce problème a été résolu dans [Ga09] où les équations de type RPA ont une matrice de la norme définie par les matrices  $G$  :

$$G_{\alpha\beta, \alpha'\beta'} = \langle 0 | [a_{\beta}^{\dagger} a_{\alpha}, a_{\alpha'}^{\dagger} a_{\beta'}] | 0 \rangle, \quad (3.9)$$

où  $\alpha$  et  $\beta$  indiquent deux états individuels génériques. En diagonalisant la matrice de la norme et en évaluant le recouvrement entre les états excités et l'état fondamental, les états non physiques peuvent être isolés et éliminés du spectre.

Cette extension, présentée plus en détail dans l'article qui suit, ouvre des perspectives intéressantes pour des applications dans des cas réalistes, comme les noyaux atomiques.

# Self-consistent extension of random-phase approximation enlarged beyond particle-hole configurations

Danilo Gambacurta and Francesco Catara

*Dipartimento di Fisica e Astronomia and INFN, Via Santa Sofia 64, I-95123 Catania, Italy*

Marcella Grasso

*Institut de Physique Nucléaire, Université Paris-Sud, IN2P3-CNRS, F-91406 Orsay Cedex, France*

(Received 14 January 2009; revised manuscript received 6 April 2009; published 6 July 2009)

We present a new extension of the random-phase approximation method: the quasiboson approximation is avoided and correlations are included in the ground state without resorting to renormalized operators or renormalized matrix elements; the configuration space is enlarged by considering also elementary excitations corresponding to the annihilation of a particle (hole) and the creation of another particle (hole) on the correlated ground state, together with the particle-hole ones. Two new and relevant advantages of this method with respect to the existing extensions of random-phase approximation are highlighted: (i) the energy weighted sum rules are completely satisfied; (ii) the problem of the existence of nonphysical states in the spectrum, related to the inclusion of particle-particle and hole-hole configurations, is solved: a way to unambiguously disentangle physical from nonphysical states in the excitation spectrum is presented. The method is applied here to a three-level Lipkin model where its quality can be judged by comparing with the exact results. Both advantages (i) and (ii) shall lead to feasible future applications of this extended RPA to several realistic cases.

DOI: [10.1103/PhysRevC.80.014303](https://doi.org/10.1103/PhysRevC.80.014303)

PACS number(s): 21.60.Jz, 21.10.Pc, 21.10.Re

## I. INTRODUCTION

One of the common features characterizing finite-size many-body systems is the existence of collective modes of excitations. Low-lying and giant resonances in nuclei [1], dipole plasmons in clusters [2], and breathing modes in atomic gases [3] are some examples of many-particle coherent motion generating a collective excitation mode. The microscopic approach that is most currently used to analyze collective excitations in many-body systems is the random-phase approximation (RPA) [4], where the modes are described as superpositions of particle-hole and hole-particle individual configurations. This method is extensively used in different domains and, in general, successfully describes the energies and transition probabilities associated to the excitations.

In its standard version, it is a single-reference approach [5], where the reference state is the uncorrelated Hartree-Fock (HF) Slater determinant characterized by 1 and 0 occupation numbers in the single-particle states that construct it (quasiboson approximation (QBA) [4] based approach). The replacement of the correlated ground state with the HF one is justified only if ground state correlations are not too strong, otherwise a better and, if possible self-consistent, treatment of these correlations become important. For example, it has been shown in the context of metal clusters that correlations in the ground state can be quite strong and induce important deviations from 1 and 0 in the occupation numbers of hole and particle states, respectively [6]. On the other side, in nuclear physics, new measurements on weakly bound nuclei start revealing relevant changes in shell structure far from stability [7] and novel properties such as, for example, the existence of pygmy excited modes [8]. The behavior of exotic nuclei presents a more complex scenario with respect to the physics of stable nuclei and the introduction of correlations

beyond standard mean field approaches may be expected to provide an important contribution in this case.

One possible direction is the use of a multireference approach [5]: the generator coordinate method (GCM) [9], for instance, is a multireference approach where the reference state is no longer a single state but a superposition of wave functions associated to some collective coordinates. Another possible way to explicitly introduce correlations in the ground state consists in constructing a RPA-like formalism where the violations of the Pauli principle related to the use of the QBA are cured. Two main lines have been developed in the past decades using either boson expansion methods [10] or extensions in the fermionic space [11]. Many of these approaches are based on the so-called renormalized RPA (RRPA) method starting from the early works of Hara and Rowe in the 1960s [12]. In all these RRPA models: (i) the ground state is explicitly correlated with occupation numbers different from 1 and 0 appearing in some renormalization factors; (ii) the Pauli principle is satisfied because the QBA is not adopted.

A very important feature of standard RPA is that it preserves energy weighted sum rules (EWSR) [9]. This property guarantees that spurious excitations corresponding to broken symmetries (as, for example, the translational invariance) separate out and are orthogonal to the physical states. On the contrary, the common limitation of all the approaches aimed to overcome QBA is that EWSR are not satisfied [13] and can be strongly violated (up to 20–30% in some cases [14]). Such violations are related to the fact that only particle-hole excitations are considered in such approaches.

An attempt to overcome this problem has been discussed in Ref. [15]. A RRPA approach has been introduced where particle-particle and hole-hole configurations have been added to the standard particle-hole configurations. The method has

been applied to a three-level Lipkin model [16] with one hole and two particle levels and it has been shown that the EWSR result exactly satisfied.

However, a new problem arises related to the existence of a so called ‘spurious’ mode that does not correspond to any level in the exact excitation spectrum of the model. In this work, we will call this mode more properly ‘additional’ or ‘nonphysical’ instead of ‘spurious’ because it does not actually correspond to any broken symmetry. Since the transition probability associated to this mode becomes non-negligible at some value of the interaction strength in the Hamiltonian [15], an application of this method to a realistic case would result as unfeasible: various additional modes would be generated and it would be impossible to isolate them from the physical spectrum by simply looking at their transition probabilities.

The appearance of these nonphysical states can be traced back to the use of the enlarged configuration space that, from the other hand, allows to exactly preserve EWSR (see also [17]). Although, in some realistic calculations carried out in extended RPA approaches, it has been discussed that the transition probabilities associated to these modes are quite small (see for example [18]), an approach that allows to identify *a priori* these modes should be very useful.

In this work, we present a new and more general method with respect to that of Ref. [15], where the renormalization scheme is not adopted and, in the range of the existence of RPA and, to some extent, beyond the RPA collapse, the EWSR are satisfied and the separation of the additional modes is unambiguously done.

The proposed approach is a generalization of the self-consistent RPA introduced in Ref. [19] in the context of metal clusters. The generalization with respect to [19] consists in enlarging the space including also particle-particle and hole-hole configurations following the line suggested in Ref. [15]. Similarly to what is done in Ref. [19], the operators  $Q_\nu$  are non-renormalized and the one-body density matrix (OBDM) is not assumed diagonal.

The paper is organized as follows. In Sec. II we discuss the problem of EWSR and the origin of the violation of EWSR when only particle-hole excitations are considered in the phonon operators within generalized RPA approaches aimed to overcome QBA. In Sec. III we discuss how this problem is solved within the present approach. In Sec. IV we apply it to a solvable three-level Lipkin model and we compare the results obtained within this approach with the RPA and exact ones. Finally, in Sec. V, the main conclusions are drawn.

## II. GENERALIZED RPA APPROACHES AND EWSR

Let us briefly recall how the problem of the EWSR raises when generalizations of RPA are considered, still remaining in the space of particle-hole elementary excitations. Within such space, the excited states of the system are written as

$$|\nu\rangle = Q_\nu^\dagger|0\rangle, \quad (1)$$

where

$$Q_\nu^\dagger = \sum_{ph} (X_{ph}^\nu a_p^\dagger a_h - Y_{ph}^\nu a_h^\dagger a_p) \quad (2)$$

with  $a^\dagger$  and  $a$  denoting creation and annihilation operators and  $|0\rangle$  is the correlated ground state, defined as the vacuum of the  $Q_\nu$  operators

$$Q_\nu|0\rangle = 0. \quad (3)$$

The equations of motion method [9] leads to

$$\begin{pmatrix} A & B \\ B^* & A^* \end{pmatrix} \begin{pmatrix} X^{(\nu)} \\ Y^{(\nu)} \end{pmatrix} = \omega_\nu \begin{pmatrix} G & 0 \\ 0 & -G^* \end{pmatrix} \begin{pmatrix} X^{(\nu)} \\ Y^{(\nu)} \end{pmatrix} \quad (4)$$

with

$$A_{ph,p'h'} = \langle 0|[a_h^\dagger a_p, H, a_p^\dagger a_{h'}]|0\rangle, \quad (5)$$

$$B_{ph,p'h'} = -\langle 0|[a_h^\dagger a_p, H, a_h^\dagger a_{p'}]|0\rangle, \quad (6)$$

$$G_{ph,p'h'} = \langle 0|[a_h^\dagger a_p, a_p^\dagger a_{h'}]|0\rangle, \quad (7)$$

where the symmetrized double commutators are defined as

$$[A, B, C] = \frac{1}{2}\{[A, [B, C]] + [[A, B], C]\}. \quad (8)$$

The  $X$  and  $Y$  amplitudes satisfy the orthonormality conditions

$$\sum_{ph,p'h'} (X_{ph}^\nu X_{p'h'}^{\nu'} - Y_{ph}^\nu Y_{p'h'}^{\nu'}) G_{ph,p'h'} = \delta_{\nu\nu'}. \quad (9)$$

The standard RPA equations can be obtained by replacing, in the evaluation of the matrices (5)–(7), the state  $|0\rangle$  with the (uncorrelated) HF one. In particular the norm matrix  $G$  acquires the simpler form

$$G_{ph,p'h'}^{(\text{HF})} = \langle \text{HF} |[a_h^\dagger a_p, a_p^\dagger a_{h'}]| \text{HF} \rangle = \delta_{hh'} \delta_{pp'}, \quad (10)$$

the matrices  $A$  and  $B$  are easily evaluated since

$$a_h^\dagger | \text{HF} \rangle = a_p | \text{HF} \rangle = 0 \quad (11)$$

and the RPA  $X$  and  $Y$  amplitudes satisfy the orthonormality conditions

$$\sum_{ph} (X_{ph}^\nu X_{ph}^{\nu'} - Y_{ph}^\nu Y_{ph}^{\nu'}) = \delta_{\nu\nu'}. \quad (12)$$

A very important feature of standard RPA is that it preserves EWSR [9,20]. It is well known that, if  $|0\rangle$  and  $|\nu\rangle$  are a complete set of exact eigenstates of the Hamiltonian, with eigenvalues  $E_0$  and  $E_\nu$ , the following identity holds:

$$\sum_\nu \omega_\nu |\langle \nu | F | 0 \rangle|^2 = \frac{1}{2} \langle 0 | [F, [H, F]] | 0 \rangle, \quad (13)$$

where  $\omega_\nu = E_\nu - E_0$  and  $F$  is any Hermitian single particle operator. The above equality is in general violated to some extent when  $|0\rangle$ ,  $|\nu\rangle$  and  $\omega_\nu$  are calculated with some approximation. To which extent it is satisfied is a measure of the adequacy of the approximation.

Transition amplitudes  $\langle \nu | F | 0 \rangle$  induced by a one-body operator

$$F = \sum_{\alpha,\beta} \langle \alpha | F | \beta \rangle a_\alpha^\dagger a_\beta \quad (14)$$

between the ground state  $|0\rangle$  and excited states  $|\nu\rangle$  when these are described within RPA and RPA-like approaches

$$\langle \nu | F | 0 \rangle = \langle 0 | [Q_\nu, F] | 0 \rangle, \quad (15)$$

where the definition (1) and the vacuum property (3) have been used. The above expression is general and it is valid independently of the explicit form of the  $Q$  operators. Within standard RPA, where the latter have the form (2), only the p-h components of the transition operator  $F$  are selected, obtaining

$$\langle v|F|0\rangle = \sum_{ph} \{X_{ph}^{v*} \langle p|F|h\rangle + Y_{ph}^{v*} \langle h|F|p\rangle\}. \quad (16)$$

A very important feature of RPA, known as Thouless theorem [20], can be described as follows. When the left hand side of Eq. (13) is evaluated by using the energies and the  $X$  and  $Y$  amplitudes of RPA, one finds the same result as when the right hand side of the same equation is calculated by replacing the exact ground  $|0\rangle$  with the  $|\text{HF}\rangle$  state. This result is very important also because it guarantees that spurious excitations corresponding to broken symmetries (as, for example, the translational invariance) separate out and are orthogonal to the physical states. We remark that, when the r.h.s. is evaluated in the HF state, only the p-h components of the transition operator  $F$  appear in it. The same happens in the l.h.s. but it is essentially related to the p-h nature of the  $Q$  operators. In fact, when the correlated  $|0\rangle$  is maintained, it is still true that only the p-h components of the transition operator  $F$  appear in the l.h.s. and one has

$$\langle v|F|0\rangle = \sum_{php'h'} \{X_{ph}^{v*} \langle p'|F|h'\rangle + Y_{ph}^{v*} \langle h'|F|p'\rangle\} G_{ph,p'h'}, \quad (17)$$

while this is no more the case in the r.h.s., where the whole structure of  $F$  appears. This is the reason why all extension of RPA, with only p-h excitations, violate Eq. (13). On the other hand, the use of the HF state in place of the correlated one, and thus the use of the QBA, is a well known limit of RPA and many efforts have been done in order to overcome this limit by taking into account ground state correlations neglected in standard RPA.

### III. FORMULATION OF THE APPROACH

In the following we present an extension of RPA aimed to overcome the QBA, by taking into account ground state correlations and, at the same time, to obtain a scheme in which EWSR are preserved. As discussed above, the violations of the EWSR in extended RPA approaches are mainly due to the use of phonon operators containing only p-h excitations. In our approach the excited states  $|v\rangle$  of the system are generated by more general operators

$$Q_v^\dagger = \sum_{\alpha>\beta} (X_{\alpha\beta}^v a_\alpha^\dagger a_\beta - Y_{\alpha\beta}^v a_\beta^\dagger a_\alpha), \quad (18)$$

where  $\alpha$  and  $\beta$  are single-particle states and  $\alpha > \beta$  means that  $n_\alpha < n_\beta$  ( $n$  being the occupation number of the state). The equations to solve are similar to RPA equations with a different norm matrix:

$$\begin{pmatrix} A & B \\ B^* & A^* \end{pmatrix} \begin{pmatrix} X^{(v)} \\ Y^{(v)} \end{pmatrix} = \omega_v \begin{pmatrix} G & \bar{G} \\ -\bar{G}^* & -G^* \end{pmatrix} \begin{pmatrix} X^{(v)} \\ Y^{(v)} \end{pmatrix}. \quad (19)$$

The norm matrix is defined by the matrices  $G$  which read

$$\begin{aligned} G_{\alpha\beta,\alpha'\beta'} &= \langle 0|[a_\beta^\dagger a_\alpha, a_{\alpha'}^\dagger a_{\beta'}]|0\rangle \\ &= \delta_{\alpha\alpha'} \rho(\beta,\beta') - \delta_{\beta\beta'} \rho(\alpha',\alpha), \end{aligned} \quad (20)$$

where  $\rho$  is the OBDM

$$\rho(\alpha, \beta) \equiv \langle 0|a_\alpha^\dagger a_\beta|0\rangle \quad (21)$$

and

$$\bar{G}_{\alpha\beta,\alpha'\beta'} = G_{\alpha\beta,\beta'\alpha'}. \quad (22)$$

The new  $A$  and  $B$  matrices have the same expressions defined in Eqs. (5) and (6) but the  $p$ 's and  $h$ 's indices are replaced now by the  $\alpha$ 's and  $\beta$ 's ones, respectively.

All the matrix elements appearing in Eqs. (19) are calculated in the correlated ground state, which is defined as the vacuum of the operators  $Q$ . The explicit expressions of the  $A$  and  $B$  matrices is calculated by using the method of linearization of equations of motion [15,19]. It amounts to contract with respect to the correlated ground state  $|0\rangle$  the two-body terms coming out from the inner commutators appearing in Eqs. (5) and (6). In a loose notations, this means

$$[H, a^\dagger a] \rightarrow a^\dagger a + a^\dagger a^\dagger a a \sim a^\dagger a + \langle 0|a^\dagger a|0\rangle a^\dagger a. \quad (23)$$

In such a way also, the  $A$  and  $B$  matrices are expressed in terms of the OBDM.

By using the number operator method [19,21] the  $\rho$  matrix is expressed in terms of the  $X$  and  $Y$  amplitudes:

$$\rho(p, p') = \sum_{vv'} \sum_h \left( \delta_{vv'} - \frac{1}{2} \sum_{p_1 h_1} R_{h_1 p_1}^{v'} R_{p_1 h_1}^{v*} \right) R_{ph}^v R_{h p'}^{v*}, \quad (24)$$

$$\begin{aligned} \rho(h, h') &= \delta_{hh'} - \sum_{vv'} \sum_p \left( \delta_{vv'} - \frac{1}{2} \sum_{p_1 h_1} R_{h_1 p_1}^{v'} R_{p_1 h_1}^{v*} \right) \\ &\quad \times R_{ph}^v R_{h' p}^{v*}, \end{aligned} \quad (25)$$

$$\rho(p, h) = \sum_{vv'} \sum_{h_2} \left( \delta_{vv'} - \frac{1}{2} \sum_{p_1 h_1} R_{h_1 p_1}^{v'} R_{p_1 h_1}^{v*} \right) R_{ph_2}^v R_{h_2 h}^{v*}, \quad (26)$$

where

$$R_{ij}^v = \sum_{\alpha>\beta} (X_{\alpha\beta}^v G_{ij,\alpha\beta} - Y_{\alpha\beta}^v G_{ij,\beta\alpha}). \quad (27)$$

Therefore Eqs. (19) are nonlinear and in order to solve them we use an iterative procedure. At the  $n$ th iterative step we compute the  $\rho$  matrix, and thus the  $A$ ,  $B$ , and  $G$  matrices, by using the  $X$  and  $Y$  amplitudes of the  $(n-1)$ th step. As starting point, we use the HF OBDM, i.e.,

$$\rho^{(0)}(h, h') = \delta_{h, h'}; \quad \rho^{(0)}(p, p') = 0; \quad \rho^{(0)}(p, h) = 0, \quad (28)$$

obtaining thus the standard RPA solutions, which are used in the next step. The procedure is carried out until convergence is reached, namely, until the maximum relative difference in the excitation energies between two successive iterations is less than a chosen limit ( $10^{-7}$  in the following calculations).

Equations (19) are a generalized eigenvalue problem and can be solved directly by using, for example,  $QR$  or  $QZ$  algorithms [22]. Alternatively, one can extract a set of linear independent states by diagonalizing the norm matrix

$$\begin{pmatrix} G & \bar{G} \\ -\bar{G}^* & -G^* \end{pmatrix}, \quad (29)$$

and make thus a unitary transformation which allows to transform the generalized eigenvalue problem into a standard one [23]. We have used this second way for the following reason. Since, in the enlarged phonon operator (18) the  $\alpha$  and  $\beta$  indices denote generic single particle states, both occupied and unoccupied in the HF ground state, particle-particle, particle-hole, and hole-hole configurations are included. This implies that nonphysical additional states come into play. The strong advantage of this method with respect to that of Ref. [15] is that by diagonalizing the norm matrix and by looking at the overlaps of the excited states with the ground state the nonphysical states can be isolated and eliminated from the spectrum. The implications of the above approach on the description of the collective states in realistic system will be studied in forthcoming works. In the next section we show the advantages of the method within a three-level Lipkin model.

#### IV. AN APPLICATION TO THE LIPKIN MODEL

The three-level Lipkin model consists of three energy levels, each of them is  $2\Omega$ -fold degenerate, in which the total number of fermions  $N = 2\Omega$  is distributed. The Hamiltonian of the model is

$$H = \sum_{i \neq 0} \epsilon_i K_{ii} + V_0 \sum_{i,j \neq 0} K_{i0} K_{0j} + V_1 \sum_{i,j \neq 0} (K_{i0} K_{j0} + h.c.) + V_2 \sum_{i,j,k \neq 0} (K_{i0} K_{jk} + h.c.) + V_3 \sum_{i,j,k,l \neq 0} K_{ij} K_{kl} \quad (30)$$

where  $\epsilon$  are the energies of the levels and the coefficients  $V$  represent the strengths of the various interaction terms. The operators  $K$  have the following form:

$$K_{ij} = \sum_m a_{im}^\dagger a_{jm} \quad (31)$$

and satisfy the commutation relations

$$[K_{ij}, K_{kl}] = \delta_{jk} K_{il} - \delta_{il} K_{kj}. \quad (32)$$

The indices  $i$  and  $j$  indicate the three levels and  $m$  denotes the  $2\Omega$  degenerate states of each level. The operators  $K$  define a  $SU(3)$  algebra. The exact excitation spectrum of the model can be calculated and compared with the obtained results.

We present the results for two choices of the parameters  $\epsilon$  and  $V$  in the Hamiltonian.

As a first set we have

$$\begin{aligned} \epsilon_0 = 0, \quad \epsilon_1 = \epsilon, \quad \epsilon_2 = 2.5\epsilon, \quad V_0 = -\chi, \\ V_1 = \chi, \quad V_2 = -\chi/2, \quad V_3 = \chi/10. \end{aligned} \quad (33)$$

In Fig. 1 the excitation spectrum (a) and the eigenvalues of the norm matrix (b) are displayed as a function of the strength

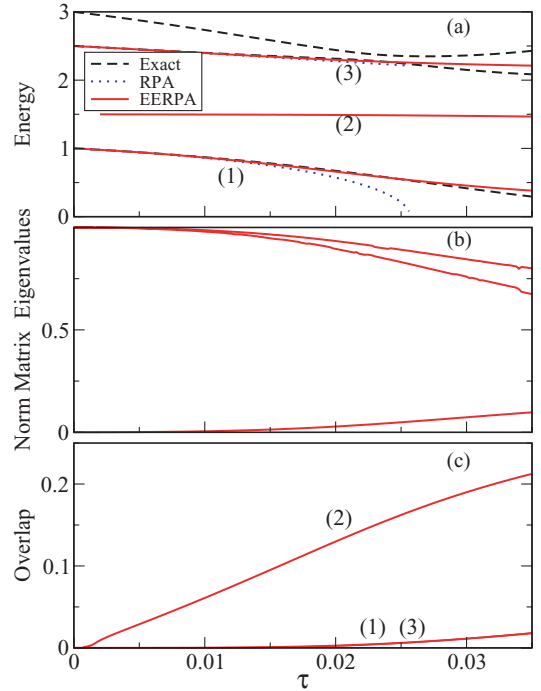


FIG. 1. (Color online) First set of parameters (33). (a): Excitation energies of the states (1), (2), and (3) and the eigenvalues of the norm matrix (b) as a function of the strength parameter  $\tau = \chi/\epsilon$ . The energies in the Y axis are expressed in units of  $\epsilon$ . In (c) the corresponding overlaps [Eq. (34)] of the three states with the ground state are shown. See the text for more details.

parameter  $\tau = \chi/\epsilon$  for the first set of parameters. The present calculation is denoted in the figure with the acronym EERPA (extended and enlarged RPA). EERPA results (solid lines) are compared with the exact corresponding values (dashed lines) and with the standard RPA energies (dotted lines). The first two RPA excited states are indicated with (1) and (3). A much better agreement with the exact results is found for EERPA with respect to RPA. This is mostly evident for the first RPA excited state already before the RPA collapse point,  $\tau = 0.026$ . With EERPA the collapse point is located much further and the good agreement with the exact values is kept in the whole region where the EERPA results exist. The state (2), whose energy is equal to  $\epsilon_2 - \epsilon_1$  when  $\tau$  approaches 0, does not correspond to any exact solution. Thus it is nonphysical. This straightforward identification would not be possible when the EERPA is applied to the study of realistic systems since exact results are not available in that case. Quite in general, however, one can proceed as follows.

The eigenvalues of the norm matrix Eq. (29), are plotted in panel (b) of the figure. One can observe that even beyond the RPA collapse point one eigenvalue is much smaller than the others, its value being equal to 0.03 at the RPA collapse. At  $\tau = 0.035$ , that is far beyond the collapse, the three eigenvalues are still well separated: 0.09, 0.69, and 0.84, respectively. This tells us that one of the three solutions is nonphysical. One condition that the three excited states should satisfy in order to be acceptable as physical states is their orthogonality with

the ground state. In panel (c) of Fig. 1 we show the overlaps

$$\langle 0|v\rangle = \langle 0|Q_v^\dagger|0\rangle = \sum_{\alpha>\beta} X_{\alpha\beta}^v \rho(\alpha,\beta) - Y_{\alpha\beta}^v \rho(\beta,\alpha) \quad (34)$$

between the ground state and the states of panel (a). As it is very clearly visible, such overlap for the state labeled as (2) is strongly different from zero, while for the others it is much smaller. Thus we can conclude that indeed such state is the nonphysical one. Of course, in the case of a schematic, exactly solvable model such identification can be done directly by looking at the exact energy spectrum while this is not possible in realistic cases. On the other hand, the appearance of a (almost) zero eigenvalue of the norm matrix does not allow to identify the nonphysical state. On the contrary, looking at the values of the overlaps Eq. (34) is an unambiguous criterion to single out the states to be eliminated and it is viable also in realistic systems. The fact that the overlaps of the physical states with the ground state are not exactly zero, especially for large values of the strength, is related to the approximations present in the approach. For example, the OBDM is evaluated by using the number operator method truncated at a certain order, which probably is not enough for values of the strength well beyond the RPA collapse point. However, in physical cases we expect to be in situations corresponding to smaller values of the strength or, in worst cases, around the RPA collapse point. We remark that the above discussed criterion, to disentangle physical from nonphysical states, could not be applied in the previous approach [15] where, since the OBDM is assumed diagonal, the overlaps (34) are zero by construction for all the states  $|v\rangle$  and thus the fulfillment of the orthogonality condition is not achievable.

It is worthwhile to underline that even when only particle-hole excitations are included in the phonon operators (18), the self-consistent treatment of the ground state correlations used in our approach leads to a better agreement with the exact results with respect to RPA, as we have checked. However, in this case, violations of EWSR are found. For example, near the RPA collapse point, deviations of the order of 30% are present. When instead the enlarged configuration space is used, EWSR are exactly satisfied, as shown in [15]. This has been numerically verified in the present calculations.

The first set of parameters allows to modelize the case where, in a realistic system, two particle (or hole) states which construct an elementary configuration are quite well separated in energy: the unperturbed energy of the corresponding configuration is then finite and greater than zero. It can happen, however, that a realistic single-particle spectrum presents some very close single-particle states. If a particle-particle or hole-hole configuration can be formed with two of these states, the associated unperturbed energy would be very close to zero. It has been shown in Ref. [18] for a realistic nuclear system that these additional states (that would contribute in the low-energy part of the excitation spectrum) have actually very low transition probabilities and do not contribute in practice to the strength distribution of the excitation mode. The second set of parameters in our Lipkin model has been chosen to mimic such a situation by using the same strength parameters  $V$  of (33)

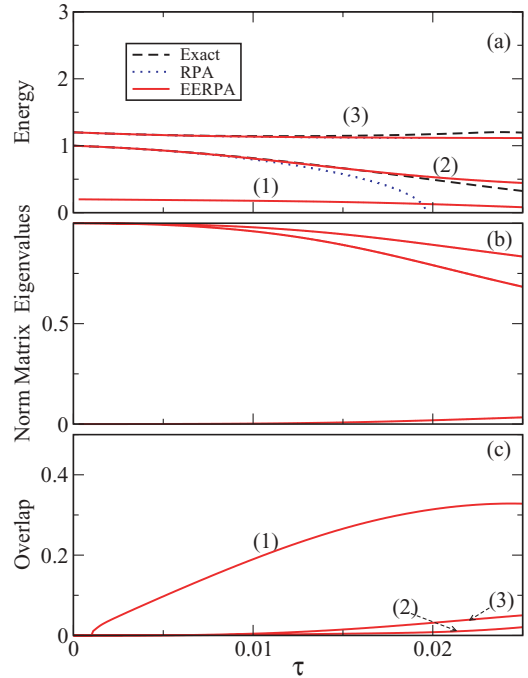


FIG. 2. (Color online) Same parameters of Eq. (33) but with  $\epsilon_1 = \epsilon$ ,  $\epsilon_2 = 1.2\epsilon$ .

and as single particle energies:

$$\epsilon_0 = 0, \quad \epsilon_1 = \epsilon, \quad \epsilon_2 = 1.2\epsilon. \quad (35)$$

In Fig. 2, where we show the same quantities of Fig. 1 for this second choice, we can see that EERPA results are again in better agreement with the exact ones with respect to the RPA, whose collapse point is now at  $\tau = 0.019$ . The energy of the nonphysical state, labeled as (1) in the figure, starts from a value equal to  $\epsilon_2 - \epsilon_1$  when  $\tau$  is near to 0 and then decreases by increasing  $\tau$ . Indeed, the collapse of EERPA ( $\tau = 0.036$ ), that we did not observe in Fig. 1, in this second case happens just because the energy of the nonphysical state approaches 0. However, the EERPA collapse is far beyond the RPA one. In panels (b) and (c) of Fig. 2, we plot the eigenvalues of the norm matrix (29) and the overlaps (34), respectively, which, as in the previous case, allow to disentangle physical from nonphysical states in a very clear way.

## V. CONCLUSIONS

In conclusion, we have presented an extension of RPA in which ground state correlations are treated in a self-consistent way and no use of the quasiboson approximation is made. The method has been applied to a three-level Lipkin model and a better agreement with the exact results than in RPA has been found. By using an enlarged configuration space, with respect to that commonly used (particle-hole excitations), EWSR are exactly preserved. This means that the problem of spurious excitations corresponding to broken symmetries which arises in many, if not all, extensions of RPA is not present in this method. In a previous paper [15], an extension

of RPA with an enlarged basis of elementary excitations within the renormalized RPA framework was introduced and studied in the same three level Lipkin model. A serious problem of that approach is the appearance of a nonphysical state, having no counterpart in the exact spectrum. The strong and innovative advantage of the here presented approach is that by

diagonalizing the norm matrix and by looking at the overlaps of the excited states with the ground state, nonphysical states can be isolated and eliminated from the spectrum. The obtained results strongly encourage the application of the present approach to more realistic systems. Work in this direction is in progress.

- 
- [1] A. Bohr and B. R. Mottelson, *Nuclear Structure* (Benjamin, New York, 1975), Vol. II; M. N. Harakeh and A. van der Woude, *Giant Resonances* (Clarendon, Oxford, 2001).
- [2] W. Ekardt, Phys. Rev. B **31**, 6360 (1985); W. Ekardt, *ibid.* **32**, 1961 (1985); M. Brack, Rev. Mod. Phys. **65**, 677 (1993).
- [3] M. A. Baranov and D. S. Petrov, Phys. Rev. A **62**, 041601(R) (2000); G. M. Bruun and B. R. Mottelson, Phys. Rev. Lett. **87**, 270403 (2001); M. Bartenstein, A. Altmeyer, S. Riedl, S. Jochim, C. Chin, J. H. Denschlag, R. Grimm, *ibid.* **92**, 203201 (2004); J. Kinast, S. L. Hemmer, M. E. Gehm, A. Turlapov, and J. E. Thomas, *ibid.* **92**, 150402 (2004).
- [4] A. Fetter and J. D. Walecka, *Quantum Theory of Many-Particle Systems* (Dover Publications, Inc., Mineola, NY, 1971).
- [5] D. Lacroix, T. Duguet, and M. Bender, Phys. Rev. C **79**, 044318 (2009).
- [6] F. Catara, G. Piccitto, M. Sambataro, and N. Van Giai, Phys. Rev. B **54**, 17536 (1996).
- [7] O. Sorlin and M.-G. Porquet, Prog. Part. Nucl. Phys. **61**, 602 (2008).
- [8] P. Adrich *et al.*, Phys. Rev. Lett. **95**, 132501 (2005).
- [9] P. Ring and P. Schuck, *The Nuclear Many-Body Problem* (Springer-Verlag, Berlin/Heidelberg/New York, 1980).
- [10] F. Catara, Ph. Chomaz, and N. Van Giai, Phys. Lett. **B233**, 6 (1989); D. Beaumel and Ph. Chomaz, Ann. Phys. (NY) **213**, 405 (1992); M. Sambataro and F. Catara, Phys. Rev. C **51**, 3066 (1995); M. Sambataro and J. Suhonen, *ibid.* **56**, 782 (1997); C. Volpe, Ph. Chomaz, M. V. Andres, F. Catara, and E. G. Lanza, Nucl. Phys. **A647**, 246 (1999); M. Sambataro and N. Dinh Dang, Phys. Rev. C **59**, 1422 (1999); M. Grasso, F. Catara, and M. Sambataro, *ibid.* **66**, 064303 (2002); D. Gambacurta, M. Sambataro, and F. Catara, *ibid.* **73**, 014310 (2006).
- [11] J. Dukelsky and P. Schuck, Nucl. Phys. **A512**, 466 (1990); D. Janssen and P. Schuck, Z. Phys. A **339**, 43 (1991); A. Klein, N. R. Walet, and G. Do Dang, Nucl. Phys. **A535**, 1 (1991); D. Karadjov, V. V. Voronov, and F. Catara, Phys. Lett. **B306**, 197 (1993); F. Catara, N. Dinh Dang, and M. Sambataro, Nucl. Phys. **A579**, 1 (1994); J. Dukelsky and P. Schuck, Phys. Lett. **B387**, 233 (1996); F. Catara, M. Grasso, G. Piccitto, and M. Sambataro, Phys. Rev. B **58**, 16070 (1998); A. A. Raduta, C. M. Raduta, A. Faessler, and W. A. Kaminski, Nucl. Phys. **A634**, 497 (1998); F. Krmpotić, E. J. V. de Passos, D. S. Delion, J. Dukelsky, and P. Schuck, *ibid.* **A637**, 295 (1998); F. Šimkovic, A. A. Raduta, M. Veselsky, and A. Faessler, Phys. Rev. C **61**, 044319 (2000); S. Takahara, M. Tohyama, and P. Schuck, *ibid.* **70**, 057307 (2004); D. Gambacurta, M. Grasso, F. Catara, and M. Sambataro, *ibid.* **73**, 024319 (2006); M. Tohyama, *ibid.* **75**, 044310 (2007).
- [12] K. Hara, Prog. Theor. Phys. **32**, 88 (1964); D. J. Rowe, Rev. Mod. Phys. **40**, 153 (1968).
- [13] S. Adachi and E. Lipparini, Nucl. Phys. **A489**, 445 (1988).
- [14] F. Catara, M. Grasso, G. Piccitto, and M. Sambataro, Phys. Rev. B **58**, 16070 (1998).
- [15] M. Grasso and F. Catara, Phys. Rev. C **63**, 014317 (2000).
- [16] S. Y. Li, A. Klein, and R. M. Dreizler, J. Math. Phys. **11**, 975 (1970).
- [17] M. Tohyama and P. Schuck, Eur. Phys. J. A **19**, 203 (2004).
- [18] M. Tohyama, S. Takahara, and P. Schuck, Eur. Phys. J. A **21**, 217 (2004).
- [19] D. Gambacurta and F. Catara, Phys. Rev. B **77**, 205434 (2008).
- [20] D. J. Thouless, Nucl. Phys. **21**, 225 (1960).
- [21] D. J. Rowe, Phys. Rev. **175**, 1283 (1968).
- [22] G. H. Golub and C. Van Loan, *Matrix Computations* (John Hopkins University Press, Baltimore, 1996); J. H. Wilkinson, Linear Algebra Appl. **28**, 285 (1979).
- [23] D. J. Rowe, J. Math. Phys. **10**, 1774 (1969).

### 3.3 Les états à multiphonons

Une des propriétés de la RPA est que les états à multiphonons, obtenus par l'action multiple des opérateurs d'excitation  $Q^+$  sur l'état fondamental, forment un spectre harmonique. Les états à deux ou trois phonons ont donc des énergies égales à deux ou trois fois l'énergie du phonon individuel, respectivement. En physique nucléaire, l'existence d'états à multiphonons (deux et trois phonons) construits sur des états de basse énergie ou sur des résonances géantes a été montrée expérimentalement [Ch95, Fa03, Fa06, Ha01, Bo03]. Des déviations du cadre harmonique ont été observées et différents modèles théoriques qui vont au-delà de la RPA ont été proposés pour expliquer et décrire ces anharmonicités [Ca89, Ha97, La97, Po97, Vo99, Ga00, Pa01, An02, La06].

En ce qui concerne les agrégats métalliques, une première mesure expérimentale publiée en 1998 [Sc98] semblait démontrer l'existence d'excitations multiples du plasmon dipolaire avec des anharmonicités négligeables. Cependant, l'interprétation de ces résultats a été mise en question par la suite et jusqu'à nos jours des conclusions sur ce sujet n'ont toujours pas été établies. Un consensus manque aussi en ce qui concerne les prédictions théoriques sur le spectre de multiphonons dans les agrégats, avec des prédictions assez différentes les unes des autres [Ca93, Ha99, Ge02, Ca06].

Dans la suite, je fais suivre deux articles où nous avons analysé des spectres à multiphonons avec deux approches différentes, une extension de la RPA [Gr02] et un modèle basé sur la seconde RPA (SRPA) [Ga06b]. Les deux approches sont testées dans un modèle de Lipkin à trois niveaux.

Dans le premier article, une procédure de mapping bosonique est effectuée et l'expansion de l'Hamiltonien dans l'espace bosonique est coupée aux termes à quatre bosons. Les équations de la RPA sont écrites et résolues en utilisant cet Hamiltonien. Elles ont la même forme que celles de la RPA standard mais sont non linéaires et sont donc résolues de manière itérative. Pour l'étude des anharmonicités du spectre, l'Hamiltonien bosonique est diagonalisé dans l'espace contenant jusqu'à quatre phonons.

Dans le deuxième article, un schéma de type SRPA [RS80, Ya86] est adopté. Le modèle est ultérieurement enrichi avec une extension qui permet d'éviter d'utiliser la QBA. En effet, la QBA dans le cadre de la SRPA est une approximation encore plus sévère que dans le cas RPA [Ta88, La90, Ma94].

**Boson-mapping-based extension of the random-phase approximation in a three-level Lipkin model**M. Grasso,<sup>1,\*</sup> F. Catara,<sup>2,3,†</sup> and M. Sambataro<sup>3,‡</sup><sup>1</sup>*Institut de Physique Nucléaire, IN2P3-CNRS, Université Paris-Sud, F-91406 Orsay Cedex, France*<sup>2</sup>*Dipartimento di Fisica e Astronomia, Università di Catania Corso Italia 57, I-95129 Catania, Italy*<sup>3</sup>*Istituto Nazionale di Fisica Nucleare, Sezione di Catania Corso Italia 57, I-95129 Catania, Italy*

(Received 13 March 2002; revised manuscript received 16 September 2002; published 4 December 2002)

Working within an exactly solvable three level model a boson Hamiltonian is defined via a mapping procedure and its expansion truncated at four-boson terms. The resulting spectrum is found in good agreement with the exact one. We discuss an extension of the random-phase approximation (RPA) based on this boson formalism. Nonlinear RPA-type equations are constructed and solved iteratively. The new solutions gain in stability with respect to the RPA ones. We perform diagonalizations of the boson Hamiltonian in restricted spaces; approximate spectra exhibit an improved quality with increasing the size of these spaces. Special attention is addressed to the problem of the anharmonicity of the spectrum.

DOI: 10.1103/PhysRevC.66.064303

PACS number(s): 21.60.Jz, 21.10.Pc, 21.10.Re

**I. INTRODUCTION**

The most commonly used microscopic approach for the study of collective vibrational states in many-fermion systems is the random-phase approximation (RPA) [1]. In this theory the lowest collective excitations result from the action of phonon operators  $Q_\nu^\dagger$  on a state  $|RPA\rangle$  which is defined by the condition that  $Q_\nu|RPA\rangle=0$ . This state represents the ground state of the system. It is a distinctive feature of RPA that multiphonon states, i.e., states obtained by repeated actions of phonon operators on the ground state, are eigenstates of the Hamiltonian with energies forming a harmonic spectrum. The existence of states which can be approximately described as corresponding to the multiple excitation of low-lying and/or high-lying phonons is well established in atomic nuclei. However, deviations from the harmonic picture are also observed and their influence on several processes has been analyzed [2].

In a standard derivation of the RPA equations a crucial point is represented by the so called quasiboson approximation (QBA). This is a rather crude approximation which causes the operators  $Q_\nu^\dagger$  to behave as boson operators in spite of their (composite) fermionic structure. Overcoming this approximation has represented the starting point of many attempts aiming at improving RPA [3–22]. One of the line of research in such a context has been based on a reformulation of the whole theory in a boson formalism [16–22]. In other words, the operators  $Q_\nu^\dagger$  have been defined from the beginning in terms of true boson operators and all the fermion operators of interest have been replaced by their boson images via a mapping procedure. The RPA-type equations that one constructs in this formalism depend on the degree of expansion of the boson Hamiltonian. Truncating this expansion at the lowest order, i.e. at two-boson terms only, gives the boson counterpart of RPA. Including higher-order terms

in the boson image of the Hamiltonian provides a natural way to reach a higher level of approximation. In addition to that, the inclusion of these terms has another important effect: it leads to a coupling among multiphonon states. States which result from a diagonalization in a  $m$ -phonon space are therefore superpositions of zero-, one-, . . . ,  $m$ -phonon states. Such a diagonalization is expected to lead to a further improved degree of approximation as well as to cause anharmonicities in the spectrum.

Calculations in this boson formalism have been performed in the recent past for atomic nuclei [19,20] considering a Hamiltonian truncated at four-boson terms and diagonalizing it in the space of one- and two-phonon states. The resulting anharmonicities have not been found large especially in <sup>208</sup>Pb. In particular, the anharmonicity associated with states whose main component is a double giant resonance has been found of the order of a few hundred keV. This is certainly related to the fact that RPA gives a good description of giant resonances especially in heavy closed shell nuclei.

In metallic clusters the dipole plasmon is a strongly collective state which corresponds to the oscillation of the delocalized electrons of the cluster against the positively charged ions. The experimental evidence for states corresponding to the double excitation of the plasmon has not been confirmed [23]. From the theoretical point of view the situation is also quite unclear. On the one hand, in Ref. [24] a purely harmonic spectrum for the multiple excitation of the plasmon has been predicted. On the other hand, by using the same approach as in Refs. [19,20] huge anharmonicities in the two-plasmon states have been found [25]. An important difference with respect to the case of atomic nuclei is that in metallic clusters the two-body interaction is very long ranged. This is probably the main reason why the RPA ground state is very different from the Hartree-Fock one and the RPA backward amplitudes are quite large. Of course, this may cause that the same level of truncation in the boson expansion is not adequate both in the case of nuclei and of metal clusters.

In principle, configuration mixing calculations can give a clear, model independent, indication on the existence of such

\*Email address: grasso@ipno.in2p3.fr

†Email address: catara@ct.infn.it

‡Email address: samba@ct.infn.it

two-phonon states and on their degree of anharmonicity. Unfortunately, since the states one looks for are quite high in energy, the number of configurations required to get stable results is huge. In Ref. [26] such a study has been performed for a very simple case: two interacting electrons moving in a uniform positive charge distribution. This is a kind of precursor of a metal cluster in the jellium approximation and allows for a numerically exact calculation. Important deviations from the harmonic limit have been found. More specifically, in addition to an almost perfectly harmonic vibrational band based on the ground state, other states appear which have a much lower degree of harmonicity.

In this paper we will analyze the anharmonicities present in the low-lying spectrum of a three-level solvable model [27] by providing at the same time an interesting test for a boson-mapping-based extension of RPA. We will shed some light on the limits of the approach adopted in Refs. [20] and [25]. The analysis we are going to present is very similar to that made in Ref. [21] where a two-level model was considered and the parameters were adjusted in such a way to mimic the multiple excitation of giant resonance. Of course, the three-level model is richer. In particular, since there are two single particle states above the Fermi surface (particle states) and one below (hole), two different elementary  $p$ - $h$  configurations and, correspondingly, two different phonons can be excited. Therefore, one can better simulate the situation encountered in nuclei which generally present one high-lying and one low-lying collective modes for each multipolarity. Also, matrix elements of the interaction connecting a particle-hole state with a two-particle one can be included in a natural way as well as those involving four-particle states or four-hole states. These terms are present in a generic two-body interaction and are very important since the former couple states having numbers of phonons differing by one while the latter couple states having the same number of phonons.

The paper is organized as follows. In Sec. II we will describe the model and analyze the anharmonicities of its exact excitation spectrum. In Sec. III we will introduce the boson-mapping technique and construct the image of the fermion Hamiltonian. In Sec. IV we will present an extension of RPA and show the results obtained by diagonalizing the boson hamiltonian. Finally, in Sec. V we will draw some conclusions.

## II. THE MODEL AND THE EXACT SPECTRUM

The model [27] consists of three  $2\Omega$ -fold degenerate single-particle shells which are occupied by  $2\Omega$  particles. Therefore, in the absence of interaction, the lowest level is completely filled while the others are empty. This lowest state represents the ‘‘Hartree-Fock’’ (HF) state of the system and is denoted by  $|0\rangle$ . A single-particle state is specified by a set of quantum numbers  $(j,m)$ , where  $j$  stands for the shell ( $j=0,1,2$ ) and  $m$  specifies the  $2\Omega$  substates within the shell. The creation and annihilation operators of a fermion in a state  $(j,m)$  are defined by  $a_{jm}^\dagger$  and  $a_{jm}$ , respectively.

Let us define the operators

$$K_{ij} \equiv \sum_{m=1}^{2\Omega} a_{im}^\dagger a_{jm} \quad (i,j=0,1,2). \quad (2.1)$$

These operators satisfy the commutation relations

$$[K_{ij}, K_{kl}] = \delta_{jk} K_{il} - \delta_{il} K_{kj} \quad (2.2)$$

thus forming a U(3) algebra. With the additional constraint that fixes the total number of particles, the operators  $K$  become the generators of the algebra SU(3).

The Hamiltonian of the model is written in terms of the generators  $K_{ij}$  only and contains up to two-body interactions. Its most general form is

$$\begin{aligned} H_F = & \sum_{i=1,2} \epsilon(i) K_{ii} + \sum_{i,j=1,2} V_0(i,j) K_{i0} K_{0j} \\ & + \sum_{i,j=1,2} V_1(i,j) (K_{i0} K_{j0} + K_{0j} K_{0i}) \\ & + \sum_{i,j,k=1,2} V_2(i,j,k) (K_{i0} K_{jk} + K_{kj} K_{0i}) \\ & + \sum_{i,j,k,l=1,2} V_3(i,j,k,l) K_{ij} K_{kl} + V_4 K_{00} K_{00}, \quad (2.3) \end{aligned}$$

with real coefficients. The eigenstates and the eigenvalues of  $H_F$  can be constructed either by using the properties of the algebra SU(3) or by diagonalizing  $H_F$  in the following space:

$$F = \left\{ |n_1 n_2\rangle = \frac{1}{\sqrt{\mathcal{N}_{n_1 n_2}}} (K_{10})^{n_1} (K_{20})^{n_2} |0\rangle \right\}_{0 \leq n_1 + n_2 \leq 2\Omega}, \quad (2.4)$$

where  $\mathcal{N}_{n_1 n_2}$  are normalization factors.

We simplify the calculations by assuming the coefficients of the interaction terms independent of the levels, i.e.,  $V_0(i,j) = V_0$ ,  $V_1(i,j) = V_1$ ,  $V_2(i,j,k) = V_2$ ,  $V_3(i,j,k,l) = V_3$ , and proportional to one parameter  $\chi$  which is expressed in units of energy. We have chosen all the coefficients negative, assuming in this way that all the interaction terms are attractive. We set the first two coefficients  $V_0$  and  $V_1$ , which involve only particle-hole excitations, equal to a common value  $-\chi$ . For the remaining coefficients we have considered smaller values: in a first case they have been set all equal to  $-\chi/10$  and in a second case they have been doubled. We have chosen the energies of the three levels equal to 0,  $\epsilon$  and  $2.5\epsilon$  where  $\epsilon$  is expressed in units of energy. Therefore the two sets of parameters used in the calculations are

$$\begin{aligned} \epsilon(0) = 0, \quad \epsilon(1) = \epsilon, \quad \epsilon(2) = 2.5\epsilon, \\ V_0 = -\chi, \quad V_1 = -\chi, \quad V_2 = -\chi/10, \\ V_3 = -\chi/10, \quad V_4 = -\chi/10 \quad (2.5) \end{aligned}$$

and

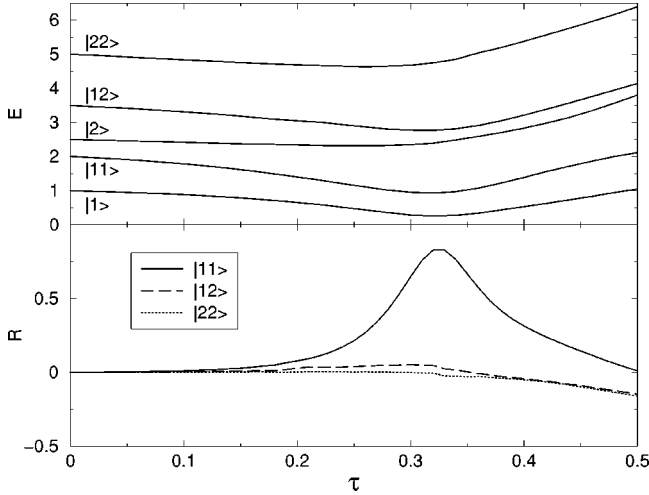


FIG. 1. Top: exact excitation energies in units of  $\epsilon$  for the one-phonon and two-phonon states as function of the strength  $\tau$  for the set of parameters (2.5). Bottom: ratios  $R_{\nu_1\nu_2}$ , Eq. (2.7), for the two-phonon states and the same set of parameters.

$$\begin{aligned} \epsilon(0) &= 0, & \epsilon(1) &= \epsilon, & \epsilon(2) &= 2.5\epsilon, \\ V_0 &= -\chi, & V_1 &= -\chi, & V_2 &= -\chi/5, \\ V_3 &= -\chi/5, & V_4 &= -\chi/5. \end{aligned} \quad (2.6)$$

For both sets of parameters we have chosen  $2\Omega = 20$ .

We show in the upper part of Figs. 1 and 2 some excitation energies calculated by diagonalizing the fermion hamiltonian  $H_F$  in the space  $F$ , Eq. (2.4), with the two sets of parameters (2.5) and (2.6), respectively, as function of the parameter  $\tau \equiv 2\Omega\chi/\epsilon$ . We report only the energies of those states which are pure  $1p-1h$  and  $2p-2h$  states at  $\tau=0$ ; in this way, we simplify our analysis looking only at those states that in RPA are pure one-phonon ( $|\nu\rangle$ ) and two-phonon ( $|\nu_1\nu_2\rangle$ ) states. One can observe that the two reported spectra are slightly different. In the second case, the stronger attractive interaction terms in the three-particle-

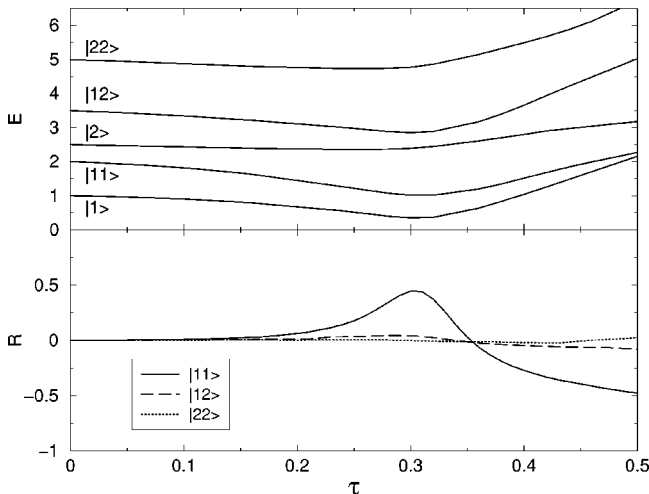


FIG. 2. Same as in Fig. 1 for the set of parameters (2.6).

one-hole ( $V_2$ ), four particle ( $V_3$ ), and four hole ( $V_4$ ) channels have the general effect (except for the state  $|2\rangle$ ) of pushing the excitation energies towards higher values. We observed that the results do not depend on the sign of  $V_2$ , due to the structure of the matrix to be diagonalized. Changing the signs of the interaction terms  $V_3$  and  $V_4$  we got a lowering of the excitation energies; in particular, the term with strength  $V_3$  starts to be important at high values of the strength  $\tau$ , while the term with strength  $V_4$  is important already at low values of  $\tau$ . This is related to the fact that the four hole term affects the ground state energy also when the correlations are absent or small, while the other term is effective only when the correlations are well developed.

Although not clearly visible at a first glance, the spectra of Figs. 1 and 2 show marked anharmonicities. In order to quantify these, in the lower part of Figs. 1 and 2 we show, for the two sets of parameters, respectively, the following ratios:

$$R_{\nu_1\nu_2} = \frac{E_{\nu_1\nu_2} - (E_{\nu_1} + E_{\nu_2})}{E_{\nu_1} + E_{\nu_2}}, \quad (2.7)$$

where by  $E_\nu$  and  $E_{\nu_1\nu_2}$  we mean the exact excitation energies of the states  $|\nu\rangle$  and  $|\nu_1\nu_2\rangle$ . One notices a well different behavior of the plotted ratios. In both figures the ratio  $R$  is very small for the states  $|12\rangle$  and  $|22\rangle$  showing that the corresponding exact states can be quite well described as pure two-phonon states for all the considered values of the parameter  $\tau$ . On the contrary, the ratio  $R_{11}$  changes rapidly with increasing  $\tau$  showing stronger anharmonicities for the state  $|11\rangle$ . Thus, for both sets of parameters the spectrum is found to exhibit some levels with a clear harmonic nature and other levels which do not display this nature and whose anharmonicities depend on the strength of the interaction terms of the Hamiltonian. These results resemble to some extent those of Ref. [26] where a realistic two-electron system was examined. The existence of anharmonicities represents an evident limit to the harmonic picture of RPA that cannot be a good approximation to reproduce the multiphonon spectrum of the model.

### III. THE BOSON MAPPING

Let us define the space

$$B \equiv \left\{ |n_1 n_2\rangle = \frac{1}{\sqrt{n_1! n_2!}} (b_1^\dagger)^{n_1} (b_2^\dagger)^{n_2} |0\rangle \right\}_{0 \leq n_1 + n_2 \leq 2\Omega}, \quad (3.1)$$

where the operators  $b_i^\dagger$  obey the standard boson commutation relations

$$[b_i, b_j^\dagger] = \delta_{ij}, \quad [b_i, b_j] = 0 \quad (3.2)$$

and  $|0\rangle$  is the vacuum of the  $b_i$ 's operators. A one-to-one correspondence exists between the states of  $F$  and  $B$ , the boson operators  $b_i^\dagger$  playing the role of the excitation operators  $K_{i0}$  and the boson vacuum  $|0\rangle$  replacing the HF state  $|0\rangle$ .

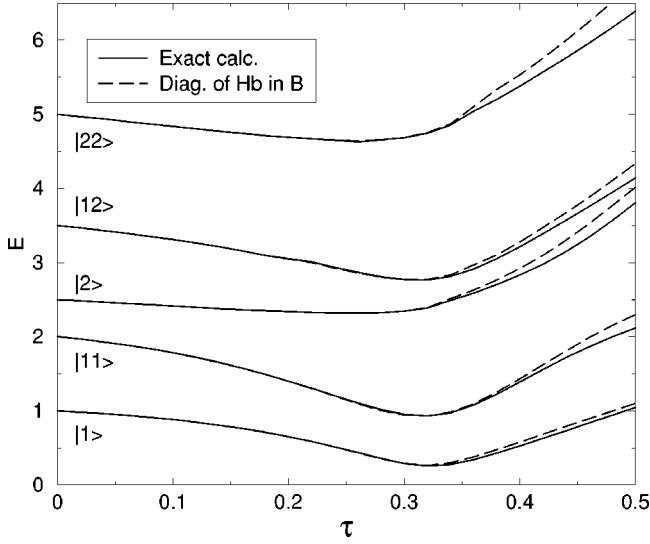


FIG. 3. Comparison between the exact one-phonon and two-phonon spectrum and the corresponding one obtained by diagonalizing  $H_B$  in the whole boson space  $B$  for the set of parameters (2.5). The energies are expressed in units of  $\epsilon$ .

The mapping procedure to construct boson images of fermion operators is the same discussed in previous works (see, for instance, Ref. [18]) and, due to the orthonormality of both sets of states  $|n_1, n_2\rangle$  and  $|n_1, n_2\rangle$ , it is simply based on the requirement that corresponding matrix elements in  $F$  and  $B$  be equal. Therefore, the procedure is of Marumori type. We refer to Refs. [18,28] for more details. Here, we simply say that, in correspondence with the Hamiltonian  $H_F$  (2.3), we introduce a hermitian boson Hamiltonian  $H_B$  which contains up to four-boson terms and whose general form is

$$\begin{aligned}
 H_B = & \alpha + \sum_i \beta_i (b_i^\dagger + \text{H.c.}) + \sum_{ij} \gamma_{ij} b_i^\dagger b_j \\
 & + \sum_{i \leq j} \phi_{ij} (b_i^\dagger b_j^\dagger + \text{H.c.}) + \sum_{i \leq j} \sum_k \epsilon_{ijk} (b_i^\dagger b_j^\dagger b_k + \text{H.c.}) \\
 & + \sum_{i \leq j} \sum_{k \leq l} \delta_{ijkl} b_i^\dagger b_j^\dagger b_k b_l \\
 & + \sum_{i \leq j \leq k} \sum_l \rho_{ijkl} (b_i^\dagger b_j^\dagger b_k^\dagger b_l + \text{H.c.}), \quad (3.3)
 \end{aligned}$$

with the coefficients depending on the parameters  $\epsilon(i), V_0, V_1, V_2, V_3, V_4$  of Eq. (2.3).

For the two sets of parameters, Eqs. (2.5) and (2.6), we show in Figs. 3 and 4, respectively, the comparison between the exact excitation energies and those obtained by diagonalizing  $H_B$  in the space  $B$  in order to check the validity of the four-boson truncation of the boson Hamiltonian. We can observe that the agreement between the two spectra is rather good for both sets of parameters. Differences between boson and fermion spectra start to be significant only for rather large values of  $\tau$  ( $\geq 0.35$ ) and are more evident for the set (2.6). This means that in the chosen range of values of  $\tau$  the considered truncation of the Hamiltonian is sufficient. We

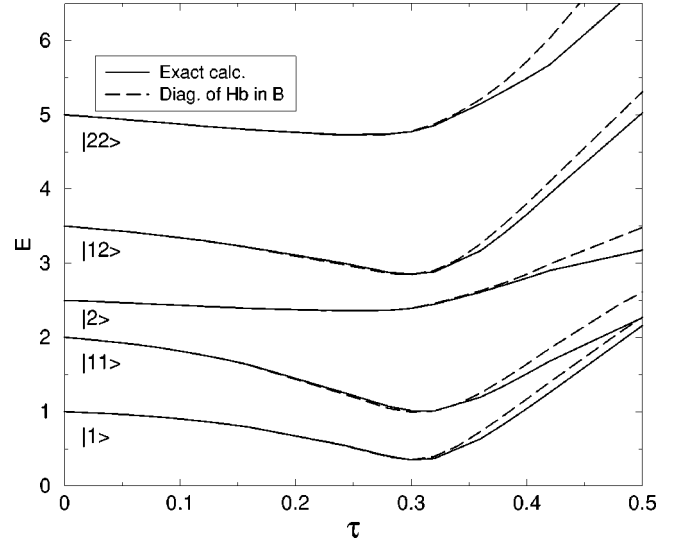


FIG. 4. Same as in Fig. 3 for the set of parameters (2.6).

have also verified that the inclusion of an additional five-boson term of the type  $b^\dagger b^\dagger b^\dagger b b$  considerably reduces the above differences in the spectra but we have nevertheless preferred to keep the boson Hamiltonian in the form (3.3) since this more closely reflects a realistic case (where the evaluation of the five-boson term would likely become rather difficult and would therefore be avoided).

In the next section we will show and comment some results obtained by diagonalizing  $H_B$  in restricted spaces, containing up to two, three, and four bosons. The quality of the results will be judged by comparing them with those obtained by diagonalizing  $H_B$  in the full boson space  $B$ . We will denote the latter as reference spectrum.

#### IV. EXTENSION OF RPA AND DIAGONALIZATION OF $H_B$ IN RESTRICTED SPACES

The calculation in the full bosonic space  $B$  is not feasible for realistic many-body systems and one has to resort to restricted spaces where only states containing up to a certain number of bosons are considered. In Fig. 5 we compare the reference spectrum for the set of parameters (2.5) with those obtained by limiting the number of bosons to two, three, and four. These calculations correspond to diagonalizations in spaces constructed by acting with two-particle–two-hole, three-particle–three-hole, and four-particle–four-hole excitation operators on the Hartree-Fock state  $|0\rangle$ . We see that the results obtained by limiting the number of bosons to two are very poor even for those states which at zero interaction strength are pure 1 boson states. Enlarging the space the quality of the results improves. However, even for the largest space it is satisfactory only for strength  $\tau \leq 0.25$ . One may expect that by introducing collective bosons (phonons) the agreement becomes better.

Let us now introduce the operators

$$Q_\nu^\dagger = \sum_i (X_i^{(\nu)} b_i^\dagger - Y_i^{(\nu)} b_i), \quad (4.1)$$

and let the state  $|\Psi_0\rangle$  satisfy the condition

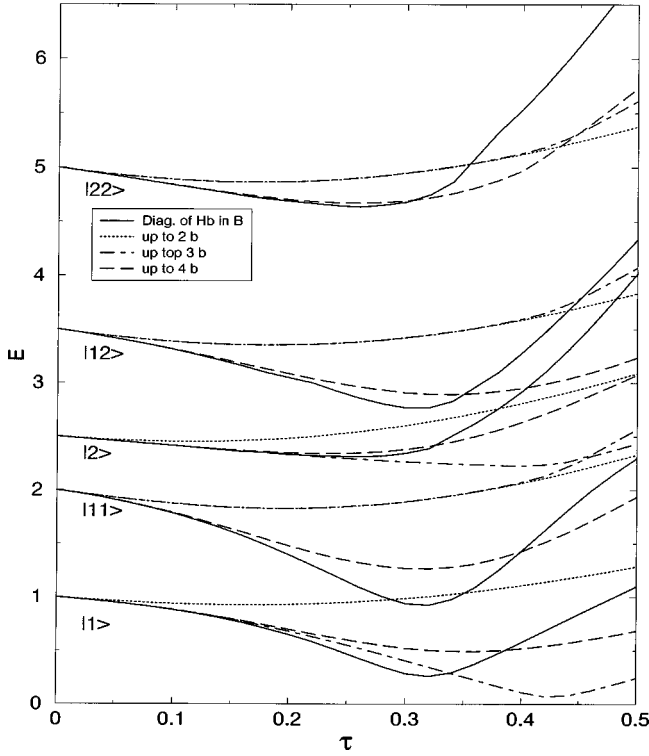


FIG. 5. Comparison between the reference spectrum and those obtained by limiting the bosonic space up to two, three, and four bosons  $b$  for the set of parameters (2.5). The energies are expressed in units of  $\epsilon$ .

$$Q_\nu |\Psi_0\rangle = 0. \quad (4.2)$$

By using the equations of motion method [29] one finds that the amplitudes  $X$  and  $Y$  are solutions of

$$\begin{pmatrix} A & B \\ -B^* & -A^* \end{pmatrix} \begin{pmatrix} X^{(\nu)} \\ Y^{(\nu)} \end{pmatrix} = \omega^{(\nu)} \begin{pmatrix} X^{(\nu)} \\ Y^{(\nu)} \end{pmatrix}, \quad (4.3)$$

where

$$A_{ij} = \langle \Psi_0 | [b_i, [H_B, b_j^\dagger]] | \Psi_0 \rangle, \quad (4.4)$$

$$B_{ij} = -\langle \Psi_0 | [b_i, [H_B, b_j]] | \Psi_0 \rangle. \quad (4.5)$$

As anticipated in Sec. I, the form of Eqs. (4.3) is strictly related to the degree of truncation of the boson Hamiltonian. In the hypothesis that  $H_B$  contains up to two-boson terms, the double commutators in Eqs. (4.4) and (4.5) are just numbers which, therefore, are also the values of the matrices  $A$  and  $B$ . This is the simplest case which can be realized in this formalism and represents the boson counterpart of the standard RPA. One limitation of RPA is that it collapses at a given strength of the interaction and imaginary energies are found. This problem is not present in spherical closed shell nuclei, while it shows up in other many-body systems as, for example, in metallic clusters. This degree of approximation can be improved by introducing a Hamiltonian with higher-order terms such as, for instance, Eq. (3.3). These terms originate on one hand from those parts of the fermionic

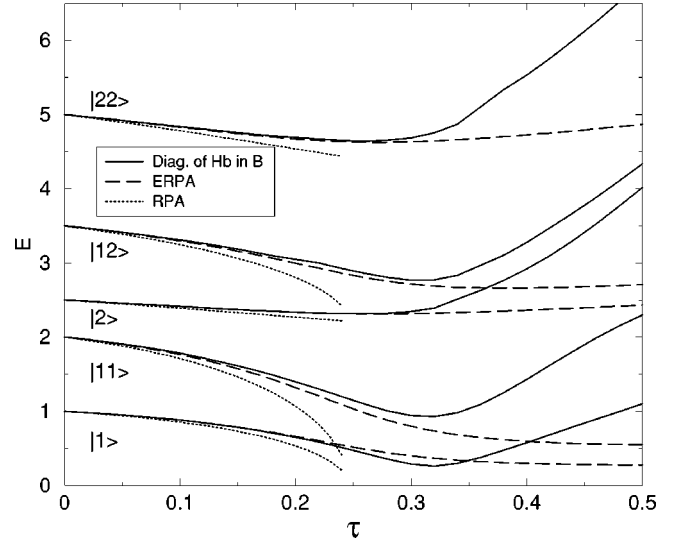


FIG. 6. Excitation energies of the states  $|\nu\rangle$  and  $|\nu_1\nu_2\rangle$  calculated within RPA (dotted lines) and ERPA (dashed lines) compared with the corresponding reference states (full lines) for the set of parameters (2.5). The energies are in units of  $\epsilon$ .

Hamiltonian, proportional to  $V_2$ ,  $V_3$ , and  $V_4$ , which do not enter in the RPA equations. On the other hand, they take into account some corrections to the violation of the Pauli principle. In this case the double commutators are operators. In order to calculate their expectation values in  $|\Psi_0\rangle$ , as required in Eqs. (4.4) and (4.5), one can express the operators  $b$  and  $b^\dagger$  in terms of  $Q$  and  $Q^\dagger$ , by reversing Eq. (4.1) (and its adjoint) and using the orthonormality conditions

$$\delta_{\nu\nu'} = \sum_{ij} (X_i^\nu X_j^{\nu'} - Y_i^{\nu'} Y_j^\nu). \quad (4.6)$$

This procedure gives, however, matrices  $A$  and  $B$  which depend on the  $X$  and  $Y$  amplitudes and, consequently, equations of motion (4.3) which are nonlinear. In what follows this nonlinear extension of RPA will be called ERPA [16].

Having determined the amplitudes  $X$  and  $Y$  within RPA or ERPA, one can express the Hamiltonian  $H_B$  in terms of the operators  $Q$  and  $Q^\dagger$ . In the case of RPA, namely, when the boson Hamiltonian Eq. (3.3) is truncated at two-boson terms only,  $H_B$  can be rewritten simply as

$$H_B = E_0 + \sum_\nu \omega^{(\nu)} Q_\nu^\dagger Q_\nu, \quad (4.7)$$

where  $\omega^{(\nu)}$  are the energies solutions of the RPA equations (4.3). This Hamiltonian obviously does not mix states with different phonon numbers and so its eigenstates are pure zero-, one-, ...,  $m$ -phonon states. For a higher-level truncation in the boson Hamiltonian, such as for instance, that of Eq. (3.3),  $H_B$  acquires instead the more general form

$$\begin{aligned} H_B = & E_0 + H_{10}(Q^\dagger + \text{H.c.}) + H_{11}Q^\dagger Q + H_{20}(Q^\dagger Q^\dagger + \text{H.c.}) \\ & + H_{21}(Q^\dagger Q^\dagger Q + \text{H.c.}) + H_{30}(Q^\dagger Q^\dagger Q^\dagger + \text{H.c.}) \\ & + H_{22}Q^\dagger Q^\dagger Q Q + H_{31}(Q^\dagger Q^\dagger Q^\dagger Q + \text{H.c.}) \\ & + H_{40}(Q^\dagger Q^\dagger Q^\dagger Q^\dagger + \text{H.c.}), \end{aligned} \quad (4.8)$$

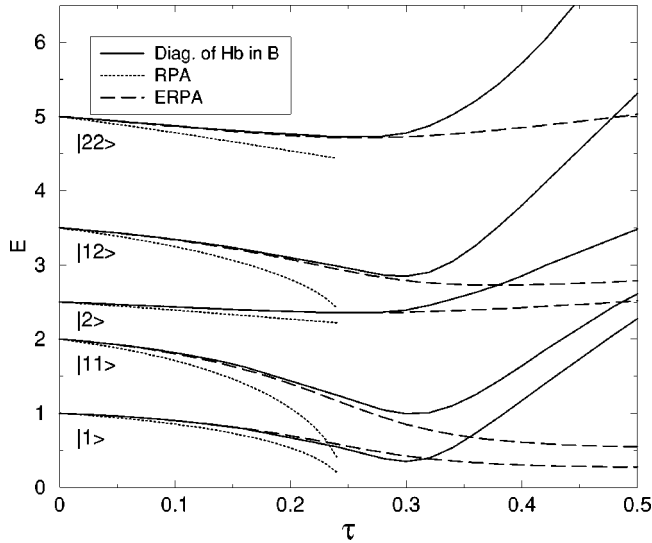


FIG. 7. Same as in Fig. 6 for the set of parameters (2.6).

where the coefficients  $H_{ij}$  are functions of  $X$  and  $Y$  (for simplicity, we have dropped all the indices). Also in this case, as in RPA, the term  $H_{20}$  as well as the nondiagonal terms  $H_{11}$  vanish, as can be easily shown using the fact that the amplitudes  $X$  and  $Y$  are solutions of the ERPA equations. However, the remaining terms of Eq. (4.8) mix different multiphonon states so that the eigenstates of the full Hamiltonian become combinations of these states. This fact introduces an evident difference with RPA since the energies which result from the

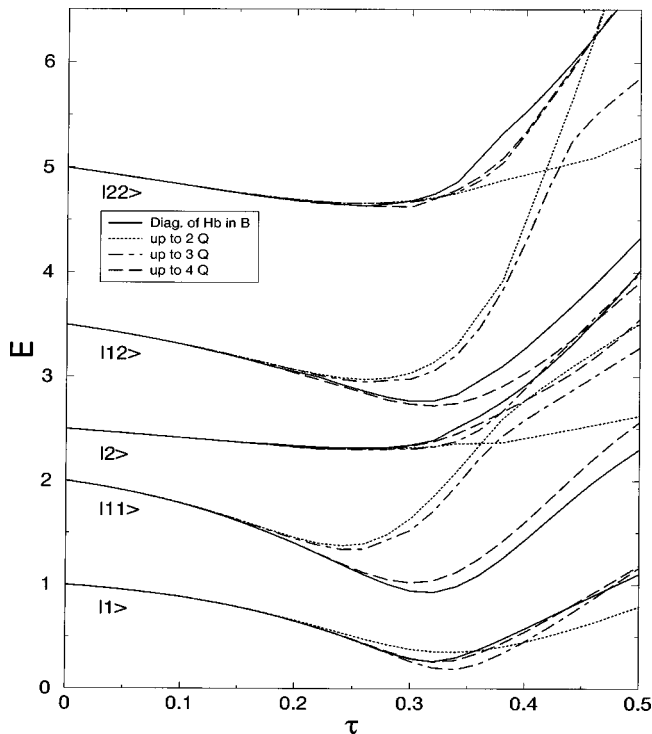


FIG. 8. Comparison between the reference spectrum and those obtained by diagonalizing  $H_B$  in the spaces containing up to two, three and four ERPA phonons for the set of parameters (2.5). The energies are expressed in units of  $\epsilon$ .

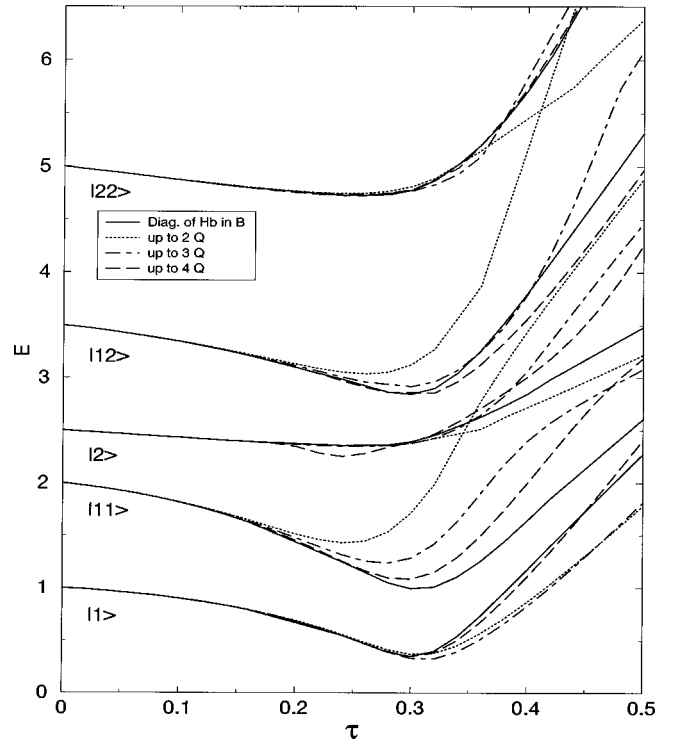


FIG. 9. Same as in Fig. 8 for the set of parameters (2.6).

ERPA equations are not eigenvalues of the boson Hamiltonian in the phonon space as it is in the case of RPA (where they provide the excitation energies of the one-phonon eigenstates).

With the chosen parameters RPA collapses at  $\tau=0.24$ . On the contrary, we found real solutions of the ERPA equations of motion in the whole considered strength range. Moreover, the so obtained energies for the states  $|1\rangle$  and  $|2\rangle$  are in good agreement with the reference ones for strength up to  $\tau=0.3$ . This shows that these states can be quite well described as pure one-phonon states. However, we want to stress that this does not imply a harmonic spectrum. Indeed, as already shown in Figs. 1 and 2, anharmonicities are present for  $\tau \geq 0.2$ . We show in Figs. 6 and 7, for the two sets of parameters (2.5) and (2.6), respectively, the excitation energies of the states  $|\nu\rangle$  and  $|\nu_1\nu_2\rangle$  calculated within RPA and ERPA. They are compared with the corresponding reference states.

In Figs. 8 and 9 we show the spectra obtained by diagonalizing  $H_B$  in spaces containing up to two, three, and four ERPA phonons. By comparing them with the reference results (shown as full lines) one sees that the agreement improves by enlarging the space and is satisfactory in the whole range of the interaction strength when the mixing of states up to four phonons is taken into account. It is worthwhile noting that the results with the phonons  $Q$  are much better than those obtained with the bosons  $b$ . The comparison is shown in Fig. 10 in the case of the largest spaces and with the parameters (2.5).

### V. CONCLUSIONS

In this paper we have analyzed some of the lowest excited states of the spectrum of a solvable three-level model,

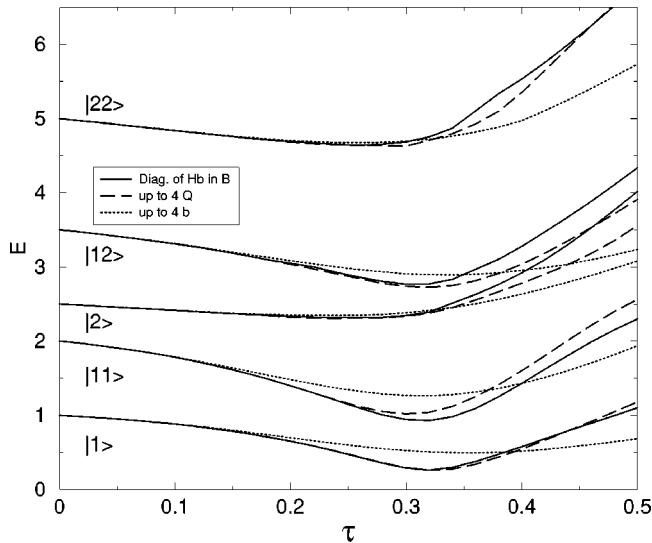


FIG. 10. Comparison between the reference spectrum, that obtained by limiting the boson space up to four bosons  $b$  and that obtained by limiting the space up to four ERPA phonons for the set of parameters (2.5). The energies are in units of  $\epsilon$ .

namely, those that in RPA would be described as one- and two-phonon states. We have worked in a boson formalism. As a preliminary step we have constructed a boson image of the fermion Hamiltonian whose expansion has been truncated at four-boson terms. The procedure followed in such a

derivation has been of Marumori type. The quality of the boson Hamiltonian has been tested by comparing its eigenvalues with the exact ones. Within the considered range of variation of the interaction strength the agreement between fermion and boson energies has always been found rather good.

By making use of this boson Hamiltonian we have introduced an extension of the RPA. The resulting equations of motion have the same form as the RPA ones but are nonlinear. They have been solved iteratively. The new solutions have gained in stability with respect to the RPA ones and, in particular, around the RPA collapse point the new energies have exhibited a good agreement with the exact ones. This extension of RPA, while introducing corrections to the Pauli principle violations present in RPA, naturally leads to a Hamiltonian which mixes states with a different number of phonons. We have performed diagonalizations in spaces containing up to two-, three-, and four-phonon states and observed an improved quality of the approximate spectra with increasing the size of the spaces.

Special attention has also been addressed to the problem of the anharmonicity of the spectrum. This has been found relevant for the state which, in RPA, is described as the double excitation of the lowest one-phonon state. On the contrary, for the other states, a less pronounced anharmonicity has been found. These findings agree with those of Ref. [26] and point to the necessity of considering together all the possible elementary excitations of a many-body system when discussing the anharmonicity of its spectrum.

- 
- [1] P. Ring and P. Schuck, *The Nuclear Many-Body Problem* (Springer, New York, 1980).
- [2] M. N. Harakeh and A. van der Woude, *Giant Resonances* (Clarendon, Oxford, 2001).
- [3] J. Dukelsky and P. Schuck, Nucl. Phys. **A512**, 466 (1990).
- [4] D. Janssen and P. Schuck, Z. Phys. A **339**, 43 (1991).
- [5] A. Klein, N. R. Walet, and G. Do Dang, Nucl. Phys. **A535**, 1 (1991).
- [6] D. Karadjov, V. V. Voronov, and F. Catara, Phys. Lett. B **306**, 166 (1993).
- [7] F. Catara, N. Dinh Dang, and M. Sambataro, Nucl. Phys. **A579**, 1 (1994).
- [8] J. Dukelsky and P. Schuck, Phys. Lett. B **387**, 233 (1996).
- [9] F. Catara, G. Piccitto, M. Sambataro, and N. Van Giai, Phys. Rev. B **54**, 17 536 (1996).
- [10] A. A. Raduta, C. M. Raduta, A. Faessler, and W. A. Kamiński, Nucl. Phys. **A634**, 497 (1998).
- [11] F. Catara, M. Grasso, G. Piccitto, and M. Sambataro, Phys. Rev. B **58**, 16 070 (1998).
- [12] F. Krmpotić, E. J. V. de Passos, D. S. Delion, J. Dukelsky, and P. Schuck, Nucl. Phys. **A637**, 295 (1998).
- [13] F. Šimković, A. A. Raduta, M. Veselsky, and A. Faessler, Phys. Rev. C **61**, 044319 (2000).
- [14] M. Grasso and F. Catara, Phys. Rev. C **63**, 014317 (2001).
- [15] N. Dinh Dang and A. Arima, Phys. Rev. C **62**, 024303 (2000).
- [16] D. Beaumel and Ph. Chomaz, Ann. Phys. (N.Y.) **213**, 405 (1992).
- [17] M. Sambataro and F. Catara, Phys. Rev. C **51**, 3066 (1995).
- [18] M. Sambataro and J. Suhonen, Phys. Rev. C **56**, 782 (1997).
- [19] F. Catara, Ph. Chomaz, and N. Van Giai, Phys. Lett. B **233**, 6 (1989).
- [20] E. G. Lanza, M. V. Andres, F. Catara, Ph. Chomaz, and C. Volpe, Nucl. Phys. **A613**, 445 (1997).
- [21] C. Volpe, Ph. Chomaz, M. V. Andres, F. Catara, and E. G. Lanza, Nucl. Phys. **A647**, 246 (1999).
- [22] M. Sambataro and N. Dinh Dang, Phys. Rev. C **59**, 1422 (1999).
- [23] R. Schlipper, R. Kusche, B. von Issendorf, and H. Haberland, Phys. Rev. Lett. **80**, 1194 (1998); (unpublished).
- [24] K. Hagino, Phys. Rev. B **60**, R2197 (1999).
- [25] F. Catara, Ph. Chomaz, and N. Van Giai, Phys. Rev. B **48**, 18 207 (1993).
- [26] F. Catara and M. Sambataro, J. Phys.: Condens. Matter **13**, L705 (2001).
- [27] S. Y. Li, A. Klein, and R. M. Dreizler, J. Math. Phys. **11**, 975 (1970).
- [28] M. Sambataro, Phys. Rev. C **60**, 064320 (1999).
- [29] D. J. Rowe, *Nuclear Collective Motion* (Methuen, London, 1970).

## Extension of the second random-phase approximation

D. Gambacurta, M. Grasso, F. Catara, and M. Sambataro

*Dipartimento di Fisica ed Astronomia, Via Santa Sofia 64, I-95123 Catania, Italy, and  
INFN, Sezione di Catania, Via Santa Sofia 64, I-95123 Catania, Italy*

(Received 4 October 2005; published 28 February 2006)

The second random-phase approximation (SRPA) is the simplest and most natural extension of the RPA. It enlarges the space of the elementary modes introduced to describe the collective states by adding 2 particle - 2 hole excitations to the 1 particle - 1 hole ones of the RPA. In deriving the SRPA equations, use is made, as in the RPA, of the so-called quasi-boson approximation (QBA) where expectation values in the ground state of the system are approximated by their values in the uncorrelated reference state. This, however, has been shown to imply a degree of approximation worse than that in the RPA. It is, therefore, necessary to improve the QBA by considering a reference state which contains some correlations. Having in mind to perform such calculations for realistic systems, we consider a simple extension of the SRPA in which the reference state contains 2 particle - 2 hole correlations. The quality of such an extension is tested by applying it to a solvable three-level model and found to be good.

DOI: [10.1103/PhysRevC.73.024319](https://doi.org/10.1103/PhysRevC.73.024319)

PACS number(s): 21.60.Jz, 21.10.Re

### I. INTRODUCTION

Collective excitations are one of the most common and interesting features of many-body systems. Of particular interest are the collective modes which can be interpreted in terms of vibrations. Nuclei show a large variety of such vibrations, both low lying and high lying [1]. In particular, the giant dipole resonance is due to the coherent motion of protons against neutrons. The analog of the giant dipole resonance in metal clusters is the dipole plasmon excitation which is well known [2,3] and is interpreted as the collective vibration of the electrons against the ions. The random-phase approximation (RPA) has been extensively used as a microscopic theory to study the basic properties of these collective excitations. In this framework, one introduces a set of phonon operators  $Q_v^\dagger$  whose action on the ground state  $|0\rangle$ , defined as the vacuum of the  $Q_v$  operators, creates the collective states  $|\nu\rangle$ . The excitation energies  $E_\nu$  are solutions of a system of equations which can be derived by using the equations of motion method [4,5]. In the derivation of the standard RPA, use is made of the quasi-boson approximation (QBA), which entails replacing the expectation value in the ground state  $|0\rangle$  of any operators with the corresponding value in the uncorrelated reference state. Strictly related to the QBA is the RPA property of predicting a harmonic spectrum with regularly spaced multiphonon states. On the other hand, the existence of anharmonicities in the multiphonon spectra of nuclei and their influence on various physical processes are well established [1,6–8]. Overcoming the QBA has been the starting point of many attempts aimed at improving the RPA.

One line of investigation in such a direction has been based on the reformulation of the whole theory in a boson formalism [9,10]. Along this line, an extension of RPA was presented in Ref. [10] within a three-level Lipkin model [11]. The phonon operators  $Q_v^\dagger$  were defined from the beginning in terms of true boson operators, and all the fermion operators of interest were replaced by their boson images via a mapping procedure. The RPA-type equations that one constructs in this

formalism depend on the degree of the expansion of the boson Hamiltonian. Standard RPA is obtained when the expansion of the boson image of the Hamiltonian is truncated at the lowest order, i.e., at the two boson terms only. Considering higher-order terms provides a natural way to reach a higher level of approximation and so go beyond the standard RPA. In Ref. [10], the boson Hamiltonian was diagonalized within the space containing up to two, three, and four phonon excitations. An important conclusion of such a study was that in order to reproduce the energies of states which in the harmonic limit correspond to two quanta excitations, it is necessary to diagonalize the Hamiltonian in the space of the states including up to four phonons. Such a calculation would not be feasible for a realistic system. Therefore, one has to look for a more affordable approach.

A natural extension of the RPA for the study of two-phonon states is the second RPA (SRPA). However, in its derivation, QBA is still used [12]; and as shown in Refs. [13,14], this is an even more severe approximation than that in the RPA. In the present paper, we introduce an extension of the RPA and SRPA obtained by improving the QBA along the lines indicated in Refs. [13–15]. The quality of the corresponding results is studied by performing calculations within the three-level Lipkin model. We calculate several physical quantities such as excitation and ground state correlation energies, occupation numbers, strength functions, and sum rules. From the comparison of our results with the exact ones, we conclude that the present approach gives a good description of the ground state and of those excited states which in the harmonic limit would correspond to one and two phonon excitations. This approach does not require a very heavy computational effort, and we plan to apply it to the study of realistic systems. Work in this direction is in progress.

The paper is organized as follows. In Sec. II, the formalism associated with the RPA and SRPA is shortly reviewed and the extensions of the two approaches are presented. In Sec. III, the exact and approximate results are compared

and in Sec. IV, our conclusions are drawn. In Appendix A, we show the explicit form of some matrices used in the calculations.

## II. FORMALISM

In this section, we present the derivation of the extensions of the RPA and SRPA mentioned in the Introduction and obtained by improving on the QBA. Let us define the operators  $Q_v^\dagger$  and  $Q_v$  such that

$$Q_v |0\rangle = 0, \quad (1)$$

$$|\nu\rangle = Q_v^\dagger |0\rangle, \quad (2)$$

where  $|0\rangle$  and  $|\nu\rangle$  are, respectively, the ground state and a generic excited state of the Hamiltonian  $H$ . It is easy to show [4,5] that the following equations hold for an arbitrary operator  $\delta Q$

$$\langle 0 | [\delta Q, [H, Q_v^\dagger]] | 0 \rangle = \omega_\nu \langle 0 | [\delta Q, Q_v^\dagger] | 0 \rangle, \quad (3)$$

with  $\omega_\nu = E_\nu - E_0$ .

Let  $|\text{HF}\rangle$  be the Hartree-Fock (HF) ground state of the system where the hole states below the Fermi energy are filled and the particle states above are empty. In the following, we use the indices  $m, n, p, q$  and  $i, j, k, l$  to indicate, respectively, particle and hole states. To derive the RPA equations, two approximations are made. The first one restricts the operators  $Q_v^\dagger$  to the space of 1 particle - 1 hole (1p1h) operators, i.e.,

$$Q_v^\dagger = \sum_{pi} (X_{pi}^{(v)} a_p^\dagger a_i - Y_{pi}^{(v)} a_i^\dagger a_p). \quad (4)$$

The second one is the QBA which amounts to substituting the ground state  $|0\rangle$  in Eq. (3) with the uncorrelated state  $|\text{HF}\rangle$ . An evident inconsistency is introduced since Eq. (3) is obtained assuming that  $|0\rangle$  is the vacuum of  $Q_v$ . By using the QBA, the system of Eq. (3), with the elementary excitations  $\delta Q \in \{a_i^\dagger a_p, a_p^\dagger a_i\}$ , becomes

$$\begin{pmatrix} A & B \\ B^* & A^* \end{pmatrix} \begin{pmatrix} X^{(v)} \\ Y^{(v)} \end{pmatrix} = \omega_\nu \begin{pmatrix} G & 0 \\ 0 & -G^* \end{pmatrix} \begin{pmatrix} X^{(v)} \\ Y^{(v)} \end{pmatrix}, \quad (5)$$

where  $X^{(v)}$  and  $Y^{(v)}$  is a short-hand notation for the vectors  $X_{pi}^{(v)}$  and  $Y_{pi}^{(v)}$ ; the RPA matrices are

$$A_{mi,pk} = \langle \text{HF} | [a_i^\dagger a_m, [H, a_p^\dagger a_k]] | \text{HF} \rangle, \quad (6)$$

$$B_{mi,pk} = -\langle \text{HF} | [a_i^\dagger a_m, [H, a_k^\dagger a_p]] | \text{HF} \rangle, \quad (7)$$

and the elements of the norm matrix  $G$  are

$$G_{mi,pk} = \langle \text{HF} | [a_i^\dagger a_m, a_p^\dagger a_k] | \text{HF} \rangle = \delta_{ik} \delta_{mp}. \quad (8)$$

A well-known feature of the RPA is that it predicts a harmonic spectrum. It is therefore clear that the RPA is not able to explain the existence of anharmonicities in multiphonon spectra.

One way to obtain a better description of the double excitations of the system is to use the SRPA, where the

excitation operators also contain 2p2h terms

$$Q_v^\dagger = \sum_{pi} (X_{pi}^{(v)} a_p^\dagger a_i - Y_{pi}^{(v)} a_i^\dagger a_p) + \sum_{pimj} (X_{pimj}^{(v)} a_p^\dagger a_i a_m^\dagger a_j - Y_{pimj}^{(v)} a_i^\dagger a_p a_j^\dagger a_m). \quad (9)$$

Starting from the equations of motion (3) and using the QBA, one gets in this case

$$\begin{pmatrix} \mathcal{A} & \mathcal{B} \\ \mathcal{B}^* & \mathcal{A}^* \end{pmatrix} \begin{pmatrix} \mathcal{X}^{(v)} \\ \mathcal{Y}^{(v)} \end{pmatrix} = \omega_\nu \begin{pmatrix} \mathcal{G} & 0 \\ 0 & -\mathcal{G}^* \end{pmatrix} \begin{pmatrix} \mathcal{X}^{(v)} \\ \mathcal{Y}^{(v)} \end{pmatrix}, \quad (10)$$

where

$$\mathcal{A} = \begin{pmatrix} A_{mi,pk} & A_{mi,pqkl} \\ A_{mnij,pk} & A_{mnij,pqkl} \end{pmatrix},$$

$$\mathcal{B} = \begin{pmatrix} B_{mi,pk} & B_{mi,pqkl} \\ B_{mnij,pk} & B_{mnij,pqkl} \end{pmatrix},$$

$$\mathcal{G} = \begin{pmatrix} G_{mi,pk} & 0 \\ 0 & G_{mnij,pqkl} \end{pmatrix},$$

and

$$\mathcal{X}^{(v)} = \begin{pmatrix} X_{mi}^{(v)} \\ X_{mnij}^{(v)} \end{pmatrix}, \quad \mathcal{Y}^{(v)} = \begin{pmatrix} Y_{mi}^{(v)} \\ Y_{mnij}^{(v)} \end{pmatrix}.$$

The elements  $A_{mi,pk}$ ,  $B_{mi,pk}$ , and  $G_{mi,pk}$  of  $\mathcal{A}$ ,  $\mathcal{B}$ , and  $\mathcal{G}$  are equal to those defined in Eqs. (6), (7), and (8), while the others are

$$A_{mi,pqkl} = \langle \text{HF} | [a_i^\dagger a_m, [H, a_p^\dagger a_q^\dagger a_l a_k]] | \text{HF} \rangle, \quad (11)$$

$$A_{mnij,pk} = \langle \text{HF} | [a_i^\dagger a_j^\dagger a_n a_m, [H, a_p^\dagger a_k]] | \text{HF} \rangle, \quad (12)$$

$$A_{mnij,pqkl} = \langle \text{HF} | [a_i^\dagger a_j^\dagger a_n a_m, [H, a_p^\dagger a_q^\dagger a_l a_k]] | \text{HF} \rangle, \quad (13)$$

$$B_{mi,pqkl} = -\langle \text{HF} | [a_i^\dagger a_m, [H, a_k^\dagger a_l^\dagger a_q a_p]] | \text{HF} \rangle, \quad (14)$$

$$B_{mnij,pk} = -\langle \text{HF} | [a_i^\dagger a_j^\dagger a_n a_m, [H, a_k^\dagger a_p]] | \text{HF} \rangle, \quad (15)$$

$$B_{mnij,pqkl} = -\langle \text{HF} | [a_i^\dagger a_j^\dagger a_n a_m, [H, a_k^\dagger a_l^\dagger a_q a_p]] | \text{HF} \rangle, \quad (16)$$

$$G_{mnij,pqkl} = \langle \text{HF} | [a_i^\dagger a_j^\dagger a_n a_m, a_p^\dagger a_q^\dagger a_l a_k] | \text{HF} \rangle. \quad (17)$$

One can show that

$$G_{mnij,pqkl} = \mathcal{Q}(ij) \mathcal{Q}(mn) \delta_{ik} \delta_{jl} \delta_{mp} \delta_{nq}, \quad (18)$$

where  $\mathcal{Q}(ij)$  is the antisymmetrizer for the indices  $i, j$  and

$$B_{mi,pqkl} = B_{mnij,pk} = B_{mnij,pqkl} = 0. \quad (19)$$

It has been shown in Refs. [13,14] that QBA is even more severe in SRPA than in RPA. In this work, in order to improve on QBA, we have searched for a correlated state to replace  $|\text{HF}\rangle$  in Eqs. (6), (7), and (11)–(16).

In order to get indications on how to improve the QBA, we notice that the standard form of the RPA ground state [i.e., the vacuum of the operators  $Q_v$  of Eq. (4)] is derived under the

approximation that the particle-hole operators  $a_m^\dagger a_i$  behave as ideal boson operators, namely,

$$[a_i^\dagger a_p, a_n^\dagger a_j] \approx \delta_{ij} \delta_{pn}, \quad (20)$$

and has the form

$$|\text{RPA}\rangle \propto \exp\left(\frac{1}{2} \sum_{minj} Z_{minj} a_m^\dagger a_i a_n^\dagger a_j\right) |\text{HF}\rangle, \quad (21)$$

where the coefficients  $Z$  are determined by

$$\sum_{mi} X_{mi}^{(v)*} Z_{minj} = Y_{nj}^{(v)*}. \quad (22)$$

An explicit expression of the vacuum  $|\text{RPA}\rangle$  cannot be found without resorting to Eq. (20). Wishing to avoid such a bosonic approximation while keeping the correlated state simple enough to be used in realistic calculations, we consider the approximation

$$|\text{RPA}\rangle \approx \mathcal{N} \left(1 + \frac{1}{2} \sum_{minj} Z_{minj} a_m^\dagger a_i a_n^\dagger a_j\right) |\text{HF}\rangle, \quad (23)$$

where  $\mathcal{N}$  is a normalization factor, and the operators  $a_m^\dagger a_i$  are treated without any bosonic approximation of the type (20). Equation (23) can be viewed as a truncation of Eq. (21). In such a spirit, we make the ansatz that the coefficients  $Z$  in Eq. (23) are still determined by Eq. (22). The matrices  $A$ ,  $B$ , and  $G$  of both the RPA equations (5) and the SRPA ones (10) are evaluated, in this approximation, by replacing the  $|\text{HF}\rangle$  state with the  $|\text{RPA}\rangle$  state (23) in Eqs. (6)–(8) and (11)–(17). We notice that when this is done, Eq. (19) is no longer valid. Furthermore, since the matrices  $A$ ,  $B$ , and  $G$  depend on  $Z$ , i.e., on  $X$  and  $Y$ , the problem is nonlinear. The procedure we adopt entails solving self-consistently the RPA equations (5) and (22), and keeping the so obtained  $Z$  coefficients when we solve the SRPA equations (10).

The present extension of the SRPA shares some similarities with those discussed in Refs. [13,15]. However, in Ref. [13] the  $Z$ -coefficients were calculated using the  $X$  and  $Y$  solutions of the standard RPA, and the matrix elements of  $A$  and  $B$  connecting 1p1h and 2p2h configurations were neglected. Furthermore, bosonic-type approximations were made when evaluating the matrices  $A$ ,  $B$ , and  $G$ . The main difference with respect to Ref. [15] is, that there the  $Z$  coefficients were evaluated in first-order Rayleigh-Schrödinger perturbation theory, i.e.,

$$Z_{minj}^{(\text{per})} = \frac{\langle \text{HF} | \hat{V} a_m^\dagger a_i a_n^\dagger a_j | \text{HF} \rangle}{-E_{minj}}, \quad (24)$$

where  $E_{minj}$  are the unperturbed energies of the 2p2h excitations and  $\hat{V}$  is the residual interaction.

### III. MODEL AND RESULTS

In this section, we apply the extensions of the RPA and SRPA discussed in the previous section to an exactly solvable three-level model [11,16]. We check the quality of the results obtained within such extensions by comparing them with the exact ones. Our main aim is to judge to what extent the

extended SRPA is adequate to reproduce the anharmonicities present in the two-phonon spectrum. The model consists of three levels of energy  $\epsilon_0$ ,  $\epsilon_1$ , and  $\epsilon_2$ . Each of them is  $2\Omega$ -fold degenerate, and  $N = 2\Omega$  is the total number of fermions in the system. Therefore, in the absence of interaction, the lowest level is fully occupied while the others are empty. This lowest level represents the HF ground state of the system  $|\text{HF}\rangle$ . A single-particle state is denoted by two quantum numbers  $j$  and  $m$ , where  $j$  labels the shells ( $j = 0, 1, 2$ ) and  $m$  specifies the  $2\Omega$  substates within each shell. Let us define the operators

$$K_{ij} = \sum_{m=1}^{2\Omega} a_{im}^\dagger a_{jm} \quad (i, j = 0, 1, 2), \quad (25)$$

where  $a_{jm}^\dagger$  and  $a_{jm}$  are, respectively, the creation and annihilation operators of a fermion in the state  $(jm)$ .

The operators  $K$  satisfy the relations

$$[K_{ij}, K_{kl}] = \delta_{jk} K_{il} - \delta_{il} K_{kj}, \quad (26)$$

$$N = \sum_i K_{ii}, \quad (27)$$

thus forming an  $\text{SU}(3)$  algebra.

We introduce the Hamiltonian of the system as

$$\begin{aligned} H_f = & \sum_{i \neq 0} \epsilon_i K_{ii} + V_0 \sum_{i, j \neq 0} K_{i0} K_{0j} \\ & + V_1 \sum_{i, j \neq 0} (K_{i0} K_{j0} + K_{0j} K_{0i}) \\ & + V_2 \sum_{i, j, k \neq 0} (K_{i0} K_{jk} + K_{kj} K_{0i}) \\ & + V_3 \sum_{i, j, k, l \neq 0} K_{ij} K_{kl}. \end{aligned} \quad (28)$$

The eigenstates and the eigenvalues of the system can be obtained either by using the properties of the  $\text{SU}(3)$  algebra or by diagonalizing  $H$  in the space

$$\left\{ |n_1 n_2\rangle = \frac{1}{\sqrt{\mathcal{N}_{n_1 n_2}}} (K_{10})^{n_1} (K_{20})^{n_2} |\text{HF}\rangle \right\}_{0 \leq n_1 + n_2 \leq 2\Omega}, \quad (29)$$

where  $\mathcal{N}_{n_1 n_2}$  are normalization factors.

The results presented in this paper refer to the same set of parameters used in Ref. [16], that is,

$$\begin{aligned} \epsilon_0 = 0 & & \epsilon_1 = \epsilon & & \epsilon_2 = 2.5\epsilon \\ V_0 = -\chi & & V_1 = \chi & & V_2 = -\chi/2 \\ V_3 = \chi/10 & & 2\Omega = 10. & & \end{aligned} \quad (30)$$

In this model, the excitation operators of the RPA and SRPA are, respectively (in all formulas below,  $i$  and  $j$  are greater than zero),

$$Q_v^\dagger = \sum_i (X_i^{(v)} K_{i0} - Y_i^{(v)} K_{0i}), \quad (31)$$

$$\begin{aligned} Q_v^\dagger = & \sum_i (X_i^{(v)} K_{i0} - Y_i^{(v)} K_{0i}) \\ & + \sum_{i < j} (X_{ij}^{(v)} K_{i0} K_{j0} - Y_{ij}^{(v)} K_{0i} K_{0j}). \end{aligned} \quad (32)$$

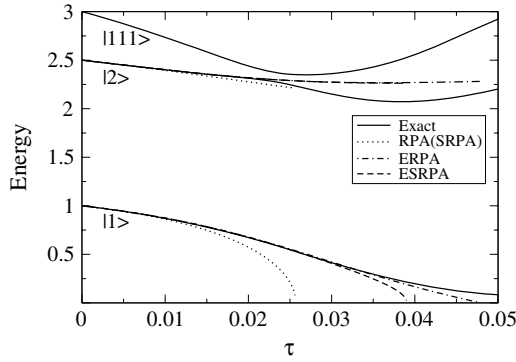


FIG. 1. Excitation energies of the states  $|\nu\rangle$  as functions of the strength  $\tau$  for the set of parameters (30). The results obtained within RPA-SRPA, ERPA, and ESRPA are compared with the exact ones. Energies are expressed in units of  $\epsilon$ . Also shown are the energies of the state  $|111\rangle$  discussed in the text.

In the following, we indicate with the RPA and SRPA the results obtained by using the QBA, namely, by evaluating the matrices in Eqs. (5) and (10) in the  $|\text{HF}\rangle$  state. In the present approximation, these matrices are calculated instead in the state

$$|\text{RPA}\rangle = \mathcal{N} \left( 1 + \frac{1}{2} \sum_{ij} Z_{ij} K_{i0} K_{j0} \right) |\text{HF}\rangle. \quad (33)$$

The corresponding extensions of the RPA and SRPA that we introduce in this way will be denoted in the following by ERPA and ESRPA, respectively.

In Figs. 1 and 2 we show the excitation energies as functions of the parameter  $\tau = \chi/\epsilon$ , calculated within RPA, ERPA, SRPA, and ESRPA. They are compared with the exact excitation energies. It is worth noticing that the exact excitation spectrum in the range of energy considered in Figs. 1 and 2 is actually richer than that shown in these figures. For simplicity, however, with the exception of the state  $|111\rangle$  defined below, we only show those states which at  $\tau = 0$  are pure 1p1h ( $|1\rangle$  and  $|2\rangle$ ) and 2p2h ( $|11\rangle$ ,  $|12\rangle$ , and  $|22\rangle$ ). In the following, we will refer to them just as 1p1h and 2p2h states. The state  $|111\rangle$  of Fig. 1 is instead a state which, at  $\tau = 0$ , is a pure

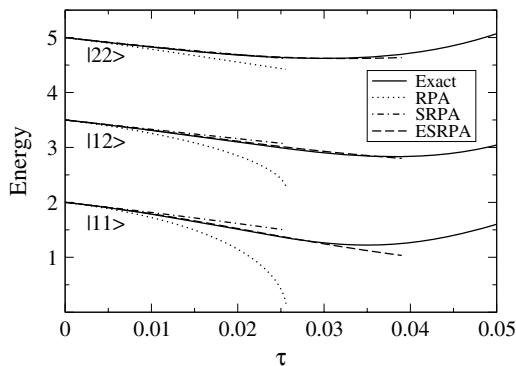


FIG. 2. Same as Fig. 1, but for the states  $|\nu_1\nu_2\rangle$ . RPA energies are calculated as the sum of the energies of the states  $|\nu_1\rangle$  and  $|\nu_2\rangle$ , namely  $E_{\nu_1\nu_2} = E_{\nu_1} + E_{\nu_2}$ .

3p3h state. For increasing values of  $\tau$ , this state gets closer and closer to the 1p1h state  $|2\rangle$  up to almost crossing it at  $\tau \sim 0.025$ . Although not shown in Fig. 2 in order not to make the figure too confusing, several other states lie quite close in energy to the 2p2h states  $|11\rangle$ ,  $|12\rangle$ , and  $|22\rangle$ . The presence of these extra states of a more complex nature “perturbs” these 2p2h states by leading, for large values of  $\tau$ , to a more relevant contribution of higher-order ph components. This makes the theoretical description of these states in a RPA-like or SRPA-like formalism more difficult.

As a first result, we notice that going from RPA to SRPA, the energies of the 1p1h states change very little. In Fig. 2, these energies are indistinguishable, and we have plotted them by using the same symbol. Both RPA and SRPA, therefore, are seen to collapse at  $\tau \sim 0.026$ ; but already for  $\tau > 0.02$ , the energies predicted for the lowest 1p1h state  $|1\rangle$  start to deviate significantly from the exact values. A better agreement is found instead in the case of the state  $|2\rangle$ . As far as the 2p2h states are concerned, we have evaluated the RPA energies of the states  $|\nu_1\nu_2\rangle$  as the sum of the energies of the states  $|\nu_1\rangle$  and  $|\nu_2\rangle$ , namely  $E_{\nu_1\nu_2} = E_{\nu_1} + E_{\nu_2}$ . In these cases, RPA and SRPA show marked differences, the latter approximation leading to a better agreement with the exact results.

Turning now to the extended versions of RPA and SRPA discussed in Sec. II, we notice that both ERPA and ESRPA improve significantly the quality of the approximated results. In particular, the collapse point is now shifted to a considerably larger value of  $\tau$  (0.047 for ERPA and 0.039 for ESRPA), and the energy of the first excited state is reproduced much better than in RPA (SRPA). With reference to this state, we show in Fig. 3 a comparison with the results obtained by the perturbative approach of Ref. [15], both in the case of RPA-like (ERPA-PER) and SRPA-like (ESRPA-PER) calculations. In this approximation, the  $Z$  coefficients are evaluated using (24). Similar to what was found in the case of standard RPA and SRPA calculations, the difference between ERPA-PER and ESRPA-PER results for the state  $|1\rangle$  is very small and cannot be appreciated in the figure (where we explicitly show only the ERPA-PER results). One observes in this case that the perturbative calculation improves upon RPA (SRPA) by

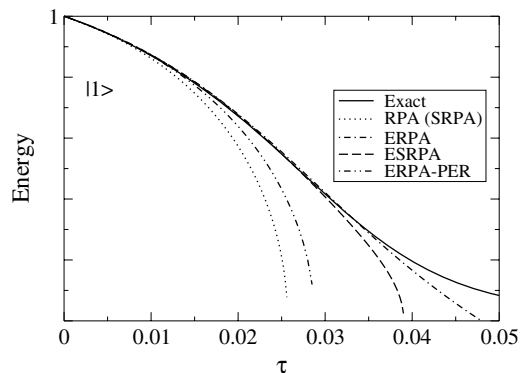


FIG. 3. Excitation energies of the  $|1\rangle$  state as functions of the strength  $\tau$  for the set of parameters (30). The results obtained within RPA (SRPA), ERPA, ESRPA, and ERPA-PER are compared with the exact ones. Energies are expressed in units of  $\epsilon$ .

exhibiting, in particular, a collapse point at  $\tau \sim 0.028$  without reaching, however, the quality of our results. As far as the remaining 1p1h and 2p2h states are concerned, the difference between our approach and the perturbative one is less evident (it is well understood that our calculations extend over a wider range of  $\tau$ ).

It is of interest to look also at the energy weighted sum rules (EWSR). Let us recall that if  $|\nu\rangle$  and  $|0\rangle$  are exact eigenstates of the Hamiltonian  $H$  with energies  $E_\nu$  and  $E_0$ , then for any one-body operator  $F$  the following identity holds:

$$\sum_\nu (E_\nu - E_0) |\langle \nu | F | 0 \rangle|^2 = \frac{1}{2} \langle 0 | [F^\dagger, [H, F]] | 0 \rangle. \quad (34)$$

The well-known Thouless theorem [17] states that the above equality is satisfied if one evaluates the l.h.s. within the RPA and the mean value of the double commutator in the r.h.s. in the |HF) state. In this sense, the RPA preserves the EWSR. The same is true for the SRPA (Ref. [12]). One can easily show that the identity (34) is exactly satisfied in our approximation if one keeps only the particle-hole components of the operator  $F$ . Vice versa, when one uses its complete expression

$$F = \sum_{\alpha\beta} f_{\alpha\beta} K_{\alpha\beta} \quad (35)$$

with  $\alpha$  and  $\beta$  running over all single-particle states (below and above the Fermi level), some violations are present. In Fig. 4, we show, as a function of  $\tau$ , the r.h.s. of Eq. (34) calculated in the correlated state (33) and the l.h.s. in ERPA and ESRPA. The calculations are done by assuming that all  $f_{\alpha\beta} = 1$ .

One sees that the violations increase with  $\tau$ . At the ERPA level, they reach quite large values, for instance,  $\sim 35\%$  at  $\tau = 0.035$ . A significant improvement is obtained within the ESRPA, the violation being  $\sim 10\%$  at the same interaction strength. This is very satisfactory in view of the fact that within other extensions of the RPA, the violations are more severe [16]. The large violations of the EWSR found in the ERPA can be traced back to the fact that, as discussed in Ref. [16], all components of  $F$  enter in the r.h.s. of Eq. (34), while when the excitation operators  $Q_\nu^\dagger$  are of the RPA type, only 1p1h terms of  $F$  contribute to the l.h.s. This is no longer true when  $Q_\nu^\dagger$  is of the SRPA type. The approach proposed in Ref. [16] entailed considering RPA-type operators  $Q_\nu^\dagger$  which also included  $K_{\alpha\beta}$

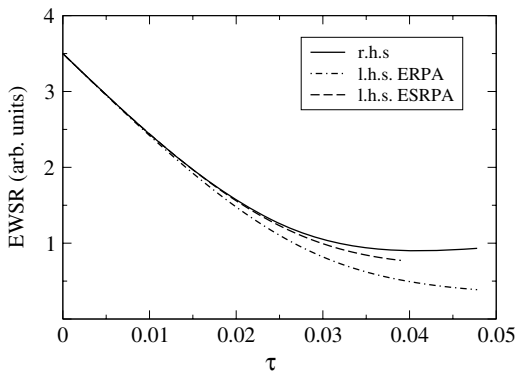


FIG. 4. R.h.s. of Eq. (34) calculated in the correlated state (33) and the l.h.s. evaluated in ERPA and ESRPA.

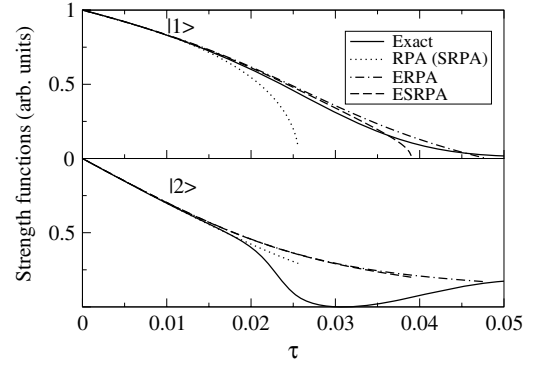


FIG. 5. Strength functions, as functions of the strength  $\tau$  for the set of parameters (30), for the states  $|1\rangle$  and  $|2\rangle$ . Results obtained within the RPA-SRPA, ERPA, and ESRPA are compared with the exact ones.

terms. It was found that the EWSR were exactly satisfied, but one could not avoid the appearance of a spurious state.

In Figs. 5 and 6, we show the strength functions  $|\langle \nu | F | 0 \rangle|^2$ . As far as the 1p1h states are concerned (Fig. 5), the RPA (SRPA) results show large deviations from the exact ones only for  $\tau$  approaching the collapse point. In the case of 2p2h states (Fig. 6), the SRPA predictions are instead very poor already for values of  $\tau$  well below the collapse point. The agreement within the ERPA and ESRPA is considerably better although significant deviations are observed also in this case for large  $\tau$ . As already noticed, however, in this region the structure of these 1p1h and 2p2h states is influenced by the presence of other states of a more complex nature which lie quite close in energy. This could also explain the “odd” behavior exhibited by the exact results relative to the states  $|2\rangle$ ,  $|12\rangle$ , and  $|22\rangle$  for large  $\tau$ . A more appropriate treatment of these high-lying states would involve diagonalizing the Hamiltonian in a multiphonon space. In Ref. [10], an approach of this kind was attempted, although in a bosonic formalism, within the same model. The conclusion was that in order to reproduce the energies of states which in the harmonic limit would correspond to two quanta excitations, it was necessary to perform a diagonalization in a space which included up to four phonons. Calculations of this kind would be quite difficult in a realistic case, so we did not perform them in the present work.

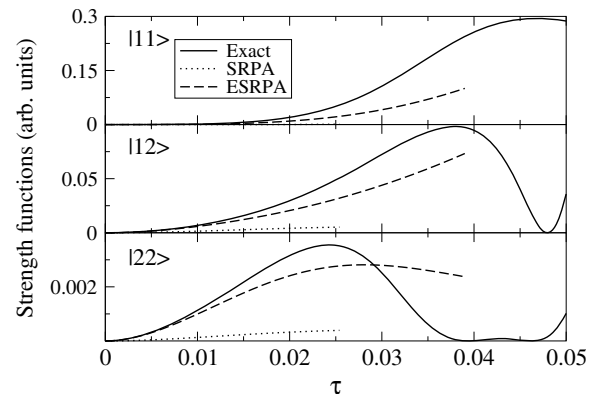


FIG. 6. Same as Fig. 5, but for states  $|11\rangle$ ,  $|12\rangle$ , and  $|22\rangle$ .

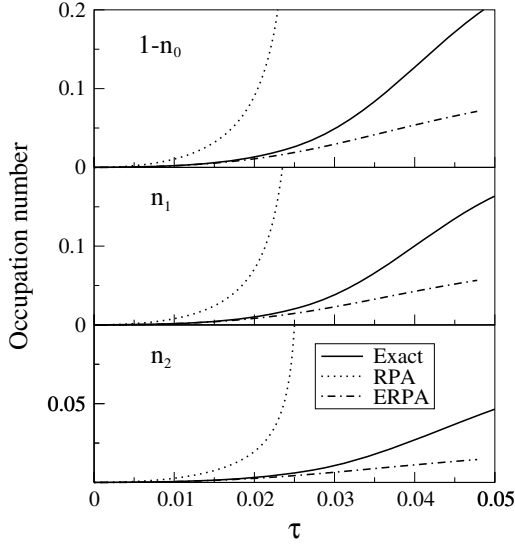


FIG. 7. Exact occupation numbers compared with the RPA and ERPA ones.

Further information on the quality of our approach can be obtained by looking at the occupation numbers. In Fig. 7, we compare the exact values with the RPA and ERPA ones. For the RPA occupation numbers, we used the expressions

$$n_0 = 1 - \frac{1}{2} \sum_{v,i} |Y_i^{(v)}|^2 \quad (36)$$

and

$$n_i = \frac{1}{2} \sum_v |Y_i^{(v)}|^2, \quad (37)$$

where the factor  $\frac{1}{2}$ , not present in the standard RPA expression, has been introduced following the suggestion of Refs. [18,19]. Within the ERPA, they have been evaluated as the expectation values of  $K_{\alpha\alpha}$  in the ground state (33) with the  $Z$  coefficients determined using Eq. (22). We notice that the RPA results deviate greatly from the exact ones already for  $\tau$  well below the collapse point. Within the ERPA, the quality of the agreement improves considerably. It is worthy remarking that while the RPA strongly overestimates the correlations in the

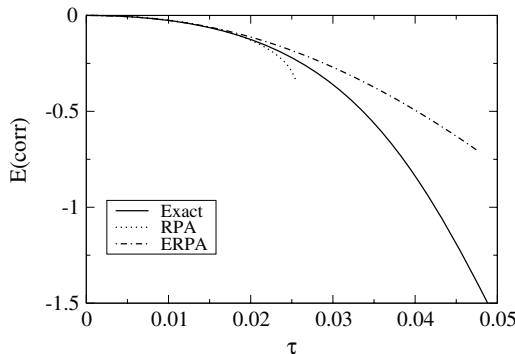


FIG. 8. Exact ground state correlation energy compared with the RPA and the ERPA ones. Energies are in units of  $\epsilon$ .

ground state, the ERPA underestimates them but to a much less extent.

This is also evident in Fig. 8, where we plot the RPA ground state correlation energy [4] together with the ERPA and exact ones.

#### IV. SUMMARY AND CONCLUSIONS

In this work, we have discussed an extension of the RPA and SRPA. The key point of such an extension has been the overcoming of the QBA by replacing the (uncorrelated) |HF> state with a correlated one in the derivation of the RPA and SRPA equations. The latter state has been assumed to contain up to 2p-2h configurations, whose amplitudes have been determined by self-consistently solving new extended RPA-type equations. In this sense, the correlated state so introduced can be viewed as a truncation of the RPA ground state. Unlike the RPA case, however, no bosonic-type approximations have been introduced when handling particle-hole operators. We have investigated, both in the RPA and SRPA, the effects of releasing the QBA in the way just described. As a testing ground, we have taken the three-level Lipkin model and compared exact calculations with those performed within the RPA, SRPA, and their extensions ERPA and ESRPA, respectively. The comparison has concerned ground state correlation energies, excitation energies, strength functions, and occupation numbers.

Furthermore, we have also examined sum rules. As a general result, we have observed that the ERPA considerably improves the RPA by leading, in particular, to a relevant shift of the collapse point to higher values of the interaction strength as well as to a better description of the spectrum. ESRPA calculations are characterized by a collapse point close to the ERPA one but exhibit a much richer spectrum, being able, in particular, to reproduce also those states which, in the standard RPA formalism, would correspond to double phonon excitations. A significant improvement of the ESRPA over the ERPA has also been observed at the level of the EWSR. As far as the ground state (identical by construction in the ERPA and ESRPA) is concerned, the exact occupation numbers are much better reproduced in the ERPA than in the RPA. One observes, in particular, a tendency of the present approximation to underestimate the ground state correlations (differently from the RPA, which severely overestimates them). This is also evidenced in the behavior of the correlation energies. In conclusion, all the results emerging from the present analysis testify to the good quality of the extension of the SRPA that we have discussed and, thanks to the not very heavy computational effort that it requires, encourage its application to more realistic systems.

#### APPENDIX A

As discussed in Sec. II, the extension proposed in this paper entails the evaluation of the matrices  $A$ ,  $B$ , and  $G$  in the |RPA> state (33). Of course, the new expressions of these matrices become more involved. As an example, in the following we report the explicit expression of the norm matrix  $G$  in the case of the three-level Lipkin model. In the standard RPA and

SRPA, we have

$$G_{i,j} = \frac{1}{2\Omega} \langle \text{HF} | [K_{0i}, K_{j0}] | \text{HF} \rangle = \delta_{ij}, \quad (\text{A1})$$

and

$$\begin{aligned} G_{ij,kl} &= \frac{1}{2\Omega(2\Omega-1)} \langle \text{HF} | [K_{0i}K_{0j}, K_{k0}K_{l0}] | \text{HF} \rangle \\ &= \mathcal{S}(ij)\delta_{ij}\delta_{ik}, \end{aligned} \quad (\text{A2})$$

where  $\mathcal{S}(ij)$  is the symmetrizer for the indices  $i, j$ .

In the ERPA and ESRPA, we evaluate the above matrices by replacing  $|\text{HF}\rangle$  with the  $|\text{RPA}\rangle$  state (33) and obtain

$$\begin{aligned} G_{i,j} &= \frac{1}{2\Omega} \langle \text{RPA} | [K_{0i}, K_{j0}] | \text{RPA} \rangle \\ &= \frac{1}{2\Omega} (\delta_{ij}N_{00} - N_{ij}), \end{aligned} \quad (\text{A3})$$

and

$$\begin{aligned} G_{ij,kl} &= \frac{1}{2\Omega(2\Omega-1)} \langle \text{RPA} | [K_{0i}K_{0j}, K_{k0}K_{l0}] | \text{RPA} \rangle \\ &= \frac{1}{2\Omega(2\Omega-1)} \mathcal{S}(ij)\mathcal{S}(kl)(\delta_{ij}(N_{0ik000} + N_{k100}) - N_{0ik0j} \\ &\quad - \frac{1}{2}(\delta_{li}\delta_{kj}(N_{0000} + N_{00}) + N_{kjli} - \delta_{li}N_{kj})), \end{aligned} \quad (\text{A4})$$

where

$$N_{\alpha\beta} = \langle \text{RPA} | K_{\alpha\beta} | \text{RPA} \rangle,$$

$$N_{\alpha\beta\gamma\delta} = \langle \text{RPA} | K_{\alpha\beta}K_{\gamma\delta} | \text{RPA} \rangle,$$

$$N_{\alpha\beta\gamma\delta\sigma\nu} = \langle \text{RPA} | K_{\alpha\beta}K_{\gamma\delta}K_{\sigma\nu} | \text{RPA} \rangle,$$

with  $\alpha, \beta, \gamma, \delta, \sigma, \nu = 0, 1, 2, \dots$

For example, we have

$$N_{00} = \langle \text{RPA} | K_{00} | \text{RPA} \rangle$$

$$= 2\Omega\mathcal{N}^2 \left( 1 + \frac{\Omega}{2\Omega-1} \sum_{kl} |Z_{kl}|^2 \right),$$

$$N_{ij} = \langle \text{RPA} | K_{ij} | \text{RPA} \rangle$$

$$= \frac{2\Omega}{2\Omega-1} \mathcal{N}^2 \sum_{kl} Z_{il}^* Z_{kj},$$

$$N_{ij00} = \langle \text{RPA} | K_{ij}K_{00} | \text{RPA} \rangle$$

$$= \frac{4\Omega(\Omega-1)}{2\Omega-1} \mathcal{N}^2 \sum_k Z_{ik}^* Z_{kj},$$

where  $i, j = 1, 2$ .

- [1] A. Bohr and B. Mottelson, *Nuclear Structure*, Vol. II (Benjamin, New York, 1975).  
 [2] W. A. de Heer, *Rev. Mod. Phys.* **65**, 611 (1993).  
 [3] M. Brack, *Rev. Mod. Phys.* **65**, 677 (1993).  
 [4] P. Ring and P. Schuck, *The Nuclear Many-Body Problem* (Springer, New York, 1980).  
 [5] D. J. Rowe, *Rev. Mod. Phys.* **40**, 153 (1968).  
 [6] P. Chomaz and N. Frascaria, *Phys. Rep.* **252**, 275 (1995).  
 [7] M. N. Harakeh and A. van der Woude, *Giant Resonances* (Clarendon, Oxford, 2001).  
 [8] M. Fallot *et al.*, *Nucl. Phys.* **A729**, 699 (2003).  
 [9] A. Klein and E. R. Marshalek, *Rev. Mod. Phys.* **63**, 375 (1991); M. Sambataro and F. Catara, *Phys. Rev. C* **51**, 3066 (1995), and references therein.

- [10] M. Grasso, F. Catara, and M. Sambataro, *Phys. Rev. C* **66**, 064303 (2002).  
 [11] S. Y. Li, A. Klein, and R. M. Dreizler, *J. Math. Phys.* **11**, 975 (1970).  
 [12] C. Yannouleas, *Phys. Rev. C* **35**, 1159 (1986).  
 [13] G. Lauritsch and P. G. Reinhard, *Nucl. Phys.* **A509**, 287 (1990).  
 [14] K. Takayanagi *et al.*, *Nucl. Phys.* **A477**, 205 (1988).  
 [15] A. Mariano, F. Krmpotic, and A. F. R. de Toledo Piza., *Phys. Rev. C* **49**, 2824 (1994).  
 [16] M. Grasso and F. Catara, *Phys. Rev. C* **63**, 014317 (2001).  
 [17] D. J. Thouless, *Nucl. Phys.* **21**, 225 (1960).  
 [18] D. J. Rowe, *Phys. Rev.* **175**, 1283 (1968).  
 [19] H. Lenske and J. Wambach, *Phys. Lett.* **B249**, 377 (1990).

# **Chapitre 4**

## **Les paires de Cooper dans les gaz atomiques ultra-froids**

## 4.1 Les gaz fermioniques ultra-froids piégés

Depuis une quinzaine d'années, un intérêt croissant a été focalisé sur les propriétés des gaz atomiques ultra-froids piégés. En 1995 la condensation de Bose-Einstein (BEC) d'atomes bosoniques piégés ( $^{87}\text{Rb}$ ,  $^{23}\text{Na}$ ,  $^7\text{Li}$ ) a été réalisée dans différents laboratoires [An95, Da95, Br95]. Le succès de ces expériences a encouragé à analyser aussi les propriétés des gaz d'atomes fermioniques ( $^6\text{Li}$ ,  $^{40}\text{K}$ ) et de nombreuses étapes ont été franchies depuis, grâce aussi à l'amélioration des techniques de piégeage et de refroidissement. Des gaz de Fermi dégénérés ont été obtenus [DM99, Gra02]. Des mélanges ont été réalisés [Sc01, Tu01, Ha02, Ha03] et le crossover BCS-BEC (où le BEC est réalisé avec des quasi-molécules) a été exploré en utilisant des résonances de Feshbach [Ba04, Re04, Zw04, Gi08]. Les gaz dits de dimensions quasi petites (Quasi Low Dimension, QLD) ont été aussi étudiés dans des pièges super anisotropiques [Pi03, Pe06].

Les gaz atomiques ultra-froids sont des systèmes très dilués, avec des densités de l'ordre de  $10^{14}$  atomes/cm<sup>3</sup> (huit ordres de grandeur plus petites par rapport à la densité de  $^4\text{He}$ ) ; ils sont piégés magnétiquement et/ou optiquement, contiennent environ  $10^4 - 10^7$  atomes, ont une taille de l'ordre de dizaines ou centaines de  $\mu\text{m}$  et sont refroidis à des températures de l'ordre de dizaines de nK.

Les gaz d'atomes fermioniques sont des systèmes de taille finie constitués par  $N$  fermions comme les noyaux atomiques. Cependant, ils ne sont pas auto-liés comme les noyaux mais existent seulement dans des pièges. Dans certaines conditions, l'interaction entre les atomes est attractive et les modèles théoriques prévoient que, au-dessous d'une température critique  $T_C$ , une transition vers la phase BCS ait lieu avec formation de paires de Cooper [Le80]. Cette superfluidité est tout à fait analogue à celle qu'on peut retrouver dans les noyaux et qui est due à l'appariement des nucléons. Grâce à cette analogie, nous avons étudié la superfluidité de ces gaz avec les mêmes approches microscopiques HFB + QRPA [Gr03, Gr05a, Ca05, Gr05b] déjà adoptées pour les noyaux, mais formulées cette fois à température finie. Nous avons fait des comparaisons entre les résultats microscopiques et les résultats obtenus en approximation de densité locale (LDA) à différentes températures et nous avons montré les limites de validité de la méthode semiclassique LDA par rapport à l'approche quantique microscopique, qui est, dans beaucoup de cas, nécessaire pour pouvoir décrire correctement les effets de taille finie dans ces systèmes.

## 4.2 Champ moyen à température finie et procédure de régularisation

Les gaz d'atomes peuvent être décrits dans un modèle théorique où le potentiel piégeant est simulé par un oscillateur harmonique et l'interaction entre les atomes est approximée par une interaction de portée nulle caractérisée par la longueur de diffusion en onde  $s$ . Ce choix est justifié par le fait que ces gaz sont typiquement très dilués. Pour simplifier ultérieurement le problème, on peut imposer une symétrie sphérique (dans les cas réels les gaz ont des formes de cigares).

Si on imagine de peupler de manière égale deux états de spin différents que nous notons comme  $\uparrow$  et  $\downarrow$  (deux états différents de structure hyperfine), l'Hamiltonien qui décrit le système de  $N$  atomes, avec  $N=N_{\uparrow}+N_{\downarrow}$ , est écrit comme :

$$H = T + \sum_{j=1}^N \frac{1}{2} m \omega^2 \bar{r}_j^2 + \frac{4\pi\hbar^2 a}{m} \sum_{i<j} \delta^3(\bar{r}_i - \bar{r}_j), \quad (4.1)$$

où  $T$  est le terme cinétique et  $a$  la longueur de diffusion en onde  $s$ .

Nous adoptons les unités  $m = \omega = \hbar = K_B = 1$ . Les équations HFB et les expressions pour les potentiels de champ moyen et d'appariement valables dans ce modèle ont été dérivées dans la Section 1.3. Puisque l'interaction utilisée est de portée nulle, l'expression pour le champ d'appariement  $\Delta(R)$  est divergente (divergence ultraviolette).

Dans l'article [Gr03], qui suit, nous avons analysé et amélioré la procédure de régularisation proposée en [Br99, Bu02], basée sur le concept de pseudopotentiel [Hu87]. Nous avons aussi effectué des comparaisons entre les résultats microscopiques et les résultats semiclassiques LDA et nous avons montré les limites de validité de la LDA en fonction de la taille et de la température du système.

# Hartree-Fock-Bogoliubov theory versus local-density approximation for superfluid trapped fermionic atoms

Marcella Grasso and Michael Urban

*Institut de Physique Nucléaire, F-91406 Orsay Cedex, France*

(Received 26 May 2003; published 19 September 2003)

We investigate a gas of superfluid fermionic atoms trapped in two hyperfine states by a spherical harmonic potential. We propose a regularization method to remove the ultraviolet divergence in the Hartree-Fock-Bogoliubov equations caused by the use of a zero-range atom-atom interaction. Compared with a method used in the literature, our method is simpler and has improved convergence properties. Then we compare Hartree-Fock-Bogoliubov calculations with the semiclassical local-density approximation. We observe that for systems containing a small number of atoms shell effects, which cannot be reproduced by the semiclassical calculation, are very important. For systems with a large number of atoms at zero temperature, the two calculations are in quite good agreement, which, however, is deteriorated at nonzero temperature, especially near the critical temperature. In this case, the different behavior can be explained within the Ginzburg-Landau theory.

DOI: 10.1103/PhysRevA.68.033610

PACS number(s): 03.75.Ss, 21.60.Jz, 05.30.Fk

## I. INTRODUCTION

In the last few years an increasing interest has been directed towards ultracold gases of trapped fermionic atoms. Many experimental efforts are made to develop and improve the techniques for trapping and cooling fermionic atoms, for instance,  $^{40}\text{K}$  and  $^6\text{Li}$ . An interesting aspect of trapped fermionic atoms in comparison with other Fermi systems is that parameters such as the temperature, the density, the number of particles, and even the interaction strength are tunable experimentally. By tuning the magnetic field in the vicinity of a Feshbach resonance [1], the scattering length, which is related to the interaction strength, can be changed. This offers a wide range of possibilities to investigate the behavior of these systems in different experimental conditions. By using optical or magnetic traps, temperatures of about  $\frac{1}{4}T_F$  have been achieved [2–4], where  $T_F = \epsilon_F/k_B$  is the Fermi temperature.

All these efforts are mainly directed to the realization and detection of a phase transition to the superfluid phase below some critical temperature  $T_C$ . In order to have a  $s$ -wave attractive interaction among the atoms, which can give rise to  $s$ -wave pairing correlations below  $T_C$ , the atoms have to be trapped and cooled in two different hyperfine states. This has been achieved in a recent experiment [5], where also the Feshbach resonance in the  $^6\text{Li}$  scattering amplitude has been used to enhance the scattering length. It seems that in the same experiment some signals indicating a superfluid phase transition have been observed.

From the theoretical point of view, many calculations have been performed in order to predict and study the equilibrium properties of the trapped system when the phase transition takes place. So far all these calculations are based on the mean-field approach. In Ref. [6], the trapped Fermi gas was treated in local-density approximation (LDA), where the system is locally treated as infinite and homogeneous. In Ref. [7], some corrections to the LDA for temperatures near  $T_C$  were obtained in the framework of the Ginzburg-Landau (GL) theory. The first approach fully taking into account the

finite system size was introduced in Ref. [8] and studied further in Refs. [9,10]. It consists of a Hartree-Fock-Bogoliubov (HFB) calculation, analogous to calculations done in nuclear physics, where the mean field and the pairing properties of the system are treated self-consistently. In Ref. [8] also a regularization prescription for the pairing field was developed: Since the densities in the traps are very low, the atom-atom interaction can be approximated by a zero-range interaction. However, this leads to an unphysical ultraviolet divergence of pairing correlations which has to be removed.

In spite of the possibility to perform full HFB calculations, it should be mentioned that these calculations are numerically very heavy and therefore limited to moderate numbers of particles. Another shortcoming of present HFB calculations is that they are restricted to the case of spherical symmetry, while the traps used in the experiments are usually strongly deformed. Hence, to describe trapped systems under realistic conditions, one has to rely on calculations within the LDA. This is a quite embarrassing situation, since even for large numbers of particles the results of HFB and LDA calculations have not always been in good agreement (see results shown in Ref. [8]).

In this paper, we will present a detailed comparison between HFB and LDA calculations. In particular, we will show that the disagreement between HFB and LDA calculations, which has been found in Ref. [8], is to a certain extent caused by the use of an unsuitable regularization prescription for the pairing field in the HFB calculations. We will present a modified regularization prescription which was originally developed for HFB calculations in nuclear physics [11] and is much easier to implement numerically. (As we learned after sending the first version of our manuscript, Nygaard *et al.* used the same prescription in their calculation of a vortex line in a dilute superfluid Fermi gas [12], without giving a description of this scheme.) Due to its improved convergence properties, this scheme leads to more precise results for the pairing field, which in the case of large numbers of atoms agree rather well with the results of the LDA at least at zero temperature. At non-zero temperature, however, the differences between HFB and LDA results turn out to be

important even for very large numbers of particles. For example, we find that the critical temperature obtained within the LDA is too high, and that the pairing field profile near the critical temperature is not well described by a LDA calculation: we show with the HFB approach that it actually has a Gaussian shape, as it was predicted in the framework of the GL theory in Ref. [7].

The paper is organized as follows. In Sec. II, we will present the adopted formalism with a particular attention on the description of the regularization techniques. In Sec. III, we will show some comparisons between HFB and LDA calculations and illustrations of the results obtained with different choices for the regularization method. We will also discuss results obtained for nonzero temperatures and verify the quantitative predictions of the GL theory. Finally, in Sec. IV we will draw our conclusions.

## II. THE FORMALISM

In this paper, we will consider a spherically symmetric harmonic trap with trapping frequency  $\omega$ , where  $N$  atoms of mass  $m$  populate equally two different spin states  $\uparrow$  and  $\downarrow$ , i.e.,  $N_\uparrow = N_\downarrow$ . As mentioned in the Introduction, the low density of the system allows us to introduce a contact interaction for the atoms, characterized by the  $s$ -wave scattering length  $a$ . The Hamiltonian reads

$$H = T + \sum_{j=1}^N \frac{1}{2} m \omega^2 r_j^2 + \frac{4\pi\hbar^2 a}{m} \sum_{i < j} \delta^3(\mathbf{r}_i - \mathbf{r}_j), \quad (1)$$

where  $T$  is the kinetic term. For convenience let us introduce a coupling constant  $g$  defined as

$$g = \frac{4\pi\hbar^2 a}{m}. \quad (2)$$

Since we are considering attractive interactions, we have  $a < 0$  and, consequently,  $g < 0$ . To simplify the notation, we will use in what follows the ‘‘trap units,’’ i.e.,

$$m = \omega = \hbar = k_B = 1. \quad (3)$$

Thus, energies will be measured in units of  $\hbar\omega$ , lengths in units of the oscillator length  $l_{ho} = \sqrt{\hbar/(m\omega)}$ , and temperatures in units of  $\hbar\omega/k_B$ .

Before describing the HFB approach, let us add some comments on the validity of Hamiltonian (1). The parametrization of the interaction in terms of the free-space  $s$ -wave scattering length  $a$  is valid at very low densities, where the distance between particles is much larger than  $|a|$ . However, if the distance between particles becomes comparable with  $|a|$ , the bare interaction has to be replaced by a density-dependent effective interaction, as it is done in nuclear physics (see also Ref. [13]). This is particularly important in the vicinity of a Feshbach resonance, where  $|a|$  becomes very large. In this case it might be necessary to include the Feshbach resonance as a new degree of freedom into the Hamiltonian [14].

## A. HFB approach and regularization procedure

Hamiltonian (1) will be treated within the mean-field approximation. We will not go into details here as the formalism has been introduced and extensively illustrated in Ref. [8]. The HFB or Bogoliubov–de Gennes [15,16] equations read

$$\begin{aligned} [H_0 + W(\mathbf{R})]u_\alpha(\mathbf{R}) + \Delta(\mathbf{R})v_\alpha(\mathbf{R}) &= E_\alpha u_\alpha(\mathbf{R}), \\ \Delta(\mathbf{R})u_\alpha(\mathbf{R}) - [H_0 + W(\mathbf{R})]v_\alpha(\mathbf{R}) &= E_\alpha v_\alpha(\mathbf{R}), \end{aligned} \quad (4)$$

where  $\alpha$  collects all quantum numbers except spin ( $n, l, m$ ),  $u_\alpha$  and  $v_\alpha$  are the two components of the quasiparticle wave function associated to the energy  $E_\alpha$ , and  $H_0$  is the following single-particle Hamiltonian:

$$H_0 = T + U_0 - \mu, \quad (5)$$

where  $U_0 = \frac{1}{2}r^2$  is the harmonic trapping potential and  $\mu$  is the chemical potential. The Hartree-Fock mean field  $W(\mathbf{R})$  in Eq. (4) is expressed by

$$W(\mathbf{R}) = g \sum_{\alpha} \{|v_\alpha(\mathbf{R})|^2 [1 - f(E_\alpha)] + |u_\alpha(\mathbf{R})|^2 f(E_\alpha)\}, \quad (6)$$

where  $f(E_\alpha)$  is the Fermi function:

$$f(E_\alpha) = \frac{1}{e^{E_\alpha/T} + 1}. \quad (7)$$

With a zero-range interaction the pairing field  $\Delta(\mathbf{R})$  appearing in Eq. (4) would usually be defined as  $\Delta(\mathbf{R}) = -g \langle \Psi_\uparrow(\mathbf{R}) \Psi_\downarrow(\mathbf{R}) \rangle$ , where  $\Psi_{\downarrow\uparrow}$  is the field operator associated with the spin states  $\downarrow$  and  $\uparrow$ . However, this expression is divergent and must be regularized. The regularization prescription proposed in Ref. [8] consists of using the pseudo-potential prescription [17]:

$$\Delta(\mathbf{R}) = -g \lim_{r \rightarrow 0} \frac{\partial}{\partial r} \left[ r \left\langle \Psi_\uparrow \left( \mathbf{R} + \frac{\mathbf{r}}{2} \right) \Psi_\downarrow \left( \mathbf{R} - \frac{\mathbf{r}}{2} \right) \right\rangle \right]. \quad (8)$$

In practice, Eq. (8) is evaluated as follows: It is possible to show that the expectation value  $\langle \Psi_\uparrow(\mathbf{R} + \mathbf{r}/2) \Psi_\downarrow(\mathbf{R} - \mathbf{r}/2) \rangle$  diverges as  $\Delta/(4\pi r)$  when  $r \rightarrow 0$  if a zero-range interaction is used. Now one adds and subtracts from this expectation value the quantity  $\frac{1}{2} \Delta(\mathbf{R}) G_\mu^0(\mathbf{R}, \mathbf{r})$ , where  $G_\mu^0$  is Green's function associated to the single-particle Hamiltonian  $H_0$ , Eq. (5), and calculated for the chemical potential  $\mu$ :

$$G_\mu^0(\mathbf{R}, \mathbf{r}) = \sum_{\alpha} \frac{\phi_\alpha^0 \left( \mathbf{R} + \frac{\mathbf{r}}{2} \right) \phi_\alpha^{0*} \left( \mathbf{R} - \frac{\mathbf{r}}{2} \right)}{\epsilon_\alpha^0 - \mu}, \quad (9)$$

where  $\phi_\alpha^0$  denotes the eigenfunction of  $H_0$  with eigenvalue  $\epsilon_\alpha^0 - \mu$ . One can demonstrate that this Green's function di-

verges as  $1/(2\pi r)$  when  $r \rightarrow 0$ . Expressing  $\langle \Psi_{\uparrow} \bar{\Psi}_{\downarrow} \rangle$  in terms of the wave functions  $u$  and  $v$ , one can write the pairing field  $\Delta$  as

$$\begin{aligned} \Delta(\mathbf{R}) = & -g \lim_{r \rightarrow 0} \frac{\partial}{\partial r} \left[ r \sum_{\alpha} \left( u_{\alpha} \left( \mathbf{R} + \frac{\mathbf{r}}{2} \right) v_{\alpha}^* \left( \mathbf{R} - \frac{\mathbf{r}}{2} \right) \right. \right. \\ & \times [1 - f(E_{\alpha})] - v_{\alpha}^* \left( \mathbf{R} + \frac{\mathbf{r}}{2} \right) u_{\alpha} \left( \mathbf{R} - \frac{\mathbf{r}}{2} \right) f(E_{\alpha}) \\ & \left. \left. - \frac{\Delta(\mathbf{R})}{2} \frac{\phi_{\alpha}^0 \left( \mathbf{R} + \frac{\mathbf{r}}{2} \right) \phi_{\alpha}^{0*} \left( \mathbf{R} - \frac{\mathbf{r}}{2} \right)}{\epsilon_{\alpha}^0 - \mu} \right) \right. \\ & \left. + \frac{\Delta(\mathbf{R})}{2} G_{\mu}^0(\mathbf{R}, r) \right]. \end{aligned} \quad (10)$$

The sum over  $\alpha$  is no longer divergent for  $r \rightarrow 0$ , since the divergent part of  $-\frac{1}{2}\Delta G_{\mu}^0$  cancels the divergent part of  $\langle \Psi_{\uparrow} \bar{\Psi}_{\downarrow} \rangle$ . Thus, we can take the limit  $r \rightarrow 0$  of this sum. On the other hand, the divergence of the last term is removed by the pseudopotential prescription, which selects only the regular part of Green's function  $G_{\mu}^0$ :

$$\lim_{r \rightarrow 0} \frac{\partial}{\partial r} [r G_{\mu}^0(\mathbf{R}, r)] \equiv G_{\mu}^{0 \text{ reg}}(\mathbf{R}). \quad (11)$$

Finally,  $\Delta$  can be expressed as follows:

$$\begin{aligned} \Delta(\mathbf{R}) = & -g \sum_{\alpha} \left( u_{\alpha}(\mathbf{R}) v_{\alpha}^*(\mathbf{R}) [1 - 2f(E_{\alpha})] \right. \\ & \left. - \frac{\Delta(\mathbf{R})}{2} \frac{|\phi_{\alpha}^0(\mathbf{R})|^2}{\epsilon_{\alpha}^0 - \mu} \right) - \frac{g\Delta(\mathbf{R})}{2} G_{\mu}^{0 \text{ reg}}(\mathbf{R}). \end{aligned} \quad (12)$$

Once the regular part of Green's function is calculated for a given chemical potential  $\mu$  [8], the HFB equations are solved self-consistently.

In practice, it is of course impossible to extend the sum over all states  $\alpha$  and one has to introduce some cutoff. However, since the sum over  $\alpha$  converges, the cutoff should not affect the results if it is chosen sufficiently high. We will discuss about the rapidity of convergence of the regularization procedure presented here with respect to the introduced energy cutoff. We will show that the convergence is quite slow. Moreover, the calculations can become heavy when systems with a large number of atoms are treated, as the function  $G_{\mu}^{0 \text{ reg}}$  has to be calculated for a large value of the chemical potential. A way to simplify the regularization procedure and to avoid calculation of  $G_{\mu}^{0 \text{ reg}}$  is proposed in Ref. [11], where the procedure of [8] is extended to calculations for nuclear systems. We will describe this method in following subsection.

## B. Thomas-Fermi approximation in the regularization procedure

In Ref. [11], a simpler regularization procedure was proposed where the Thomas-Fermi approximation (TFA) is used to calculate the regular part of Green's function. To that end, let us write Green's function  $G_{\mu}^0$  by adopting the TFA for the sum over the states corresponding to oscillator energies  $\epsilon_{nl}^0$  above some sufficiently large value  $\epsilon_C = N_C + \frac{3}{2}$ :

$$\begin{aligned} G_{\mu}^0(\mathbf{R}, r) \approx & \sum_{\substack{nlm \\ \epsilon_{nl}^0 \leq \epsilon_C}} \frac{\phi_{nlm}^0 \left( \mathbf{R} + \frac{\mathbf{r}}{2} \right) \phi_{nlm}^{0*} \left( \mathbf{R} - \frac{\mathbf{r}}{2} \right)}{\epsilon_{nl}^0 - \mu} \\ & + \int_{k_C(R)}^{+\infty} \frac{d^3 k}{(2\pi)^3} \frac{e^{i\mathbf{k} \cdot \mathbf{r}}}{k^2 + \frac{R^2}{2} - \mu}, \end{aligned} \quad (13)$$

where

$$k_C(R) = \sqrt{2\epsilon_C - R^2} = \sqrt{2N_C + 3 - R^2}. \quad (14)$$

Observing that

$$\int_0^{+\infty} \frac{d^3 k}{(2\pi)^3} \frac{e^{i\mathbf{k} \cdot \mathbf{r}}}{k^2} = \frac{1}{2} \frac{1}{\pi r} \quad (15)$$

and using Eq. (13), we can write the regular part of Green's function as follows:

$$\begin{aligned} G_{\mu}^{0 \text{ reg}}(\mathbf{R}) = & \lim_{r \rightarrow 0} \left( G_{\mu}^0(\mathbf{R}, r) - \frac{1}{2\pi r} \right) \\ \approx & \sum_{\substack{nlm \\ \epsilon_{nl}^0 \leq \epsilon_C}} \frac{\phi_{nlm}^0(\mathbf{R}) \phi_{nlm}^{0*}(\mathbf{R})}{\epsilon_{nl}^0 - \mu} + \int_{k_C(R)}^{+\infty} \frac{d^3 k}{(2\pi)^3} \\ & \times \left( \frac{1}{k^2 + \frac{R^2}{2} - \mu} - \frac{1}{k^2} \right) - \int_0^{k_C(R)} \frac{d^3 k}{(2\pi)^3} \frac{1}{k^2}. \end{aligned} \quad (16)$$

Evaluating the integrals over  $\mathbf{k}$  and summing over the magnetic quantum number  $m$ , we obtain

$$\begin{aligned} G_{\mu}^{0 \text{ reg}}(r) \approx & \sum_{\substack{nl \\ \epsilon_{nl}^0 \leq \epsilon_C}} \frac{(2l+1)R_{nl}^2(r)}{4\pi(\epsilon_{nl}^0 - \mu)} + \frac{k_F^0(r)}{2\pi^2} \\ & \times \ln \frac{k_C(r) + k_F^0(r)}{k_C(r) - k_F^0(r)} - \frac{k_C(r)}{\pi^2}, \end{aligned} \quad (17)$$

where  $R_{nl}$  are the radial parts of the oscillator wave functions and

$$k_F^0(r) = \sqrt{2\mu - r^2} \quad (18)$$

is the local Fermi momentum. As noted in Ref. [11], this method can be used beyond the classical turning point [characterized by  $k_F^0(r) = 0$ ] by allowing for imaginary values of  $k_F^0(r)$ . The case where  $k_C(r)$  becomes imaginary will not be considered, because we assume that  $N_C$  is sufficiently large such that the pairing field can be neglected in the regions where  $k_C(r)$  is imaginary. It should also be pointed out that already for, say,  $N_C \geq \mu + 10$ , Eq. (17) is an extremely accurate approximation to  $G_\mu^{0\text{reg}}$ , and gives results which are almost undistinguishable from those obtained by the numerically heavy algorithm proposed in Ref. [8].

Now let us substitute Eq. (17) into Eq. (12). We have to choose a cutoff for the sum over single-particle states. Instead of choosing a cutoff for the quasiparticle energies  $E_\alpha$ , as it is done in Ref. [11], we can likewise restrict the sum in Eq. (12) to the states corresponding to those appearing in the sum in Eq. (17). This is a natural choice if one obtains the wave functions  $u_\alpha$  and  $v_\alpha$  and the quasiparticle energies  $E_\alpha$  by solving Eq. (4) in a truncated harmonic oscillator basis containing the states satisfying  $\epsilon_{nl}^0 \leq \epsilon_C = N_C + \frac{3}{2}$ . In this way, we obtain the following simple formula for the gap:

$$\begin{aligned} \Delta(r) = & -g \sum_{\substack{nl \\ \epsilon_{nl}^0 \leq \epsilon_C}} \frac{2l+1}{4\pi} u_{nl}(r)v_{nl}(r)[1-2f(E_{nl})] \\ & -g \frac{\Delta(r)}{2} \left( \frac{k_F^0(r)}{2\pi^2} \ln \frac{k_C(r) + k_F^0(r)}{k_C(r) - k_F^0(r)} - \frac{k_C(r)}{\pi^2} \right). \end{aligned} \quad (19)$$

Finally, this can be rewritten in terms of a position dependent effective coupling constant:

$$\Delta(r) = -g_{\text{eff}}(r) \sum_{\substack{nl \\ \epsilon_{nl}^0 \leq \epsilon_C}} \frac{2l+1}{4\pi} u_{nl}(r)v_{nl}(r)[1-2f(E_{nl})], \quad (20)$$

where

$$\frac{1}{g_{\text{eff}}(r)} = \frac{1}{g} + \frac{1}{2\pi^2} \left( \frac{k_F^0(r)}{2} \ln \frac{k_C(r) + k_F^0(r)}{k_C(r) - k_F^0(r)} - k_C(r) \right). \quad (21)$$

We stress again that the results obtained with this regularization prescription, from now on called prescription (a), coincide with the results obtained with the prescription introduced in Ref. [8].

However, it will turn out that it is useful to introduce the following modification of the method: Let us replace everywhere  $k_F^0(r)$  by the local Fermi momentum taking into account the full potential (trapping potential  $U_0$  plus Hartree-Fock potential  $W$ ):

$$k_F(r) = \sqrt{2\mu - r^2 - 2W(r)}. \quad (22)$$

Formally this replacement does not change anything: Instead of adding and subtracting the term  $\frac{1}{2}\Delta(\mathbf{R})G_\mu^0(\mathbf{R},\mathbf{r})$  from the divergent expectation value  $\langle \Psi_\uparrow(\mathbf{R}+\mathbf{r}/2)\Psi_\downarrow(\mathbf{R}-\mathbf{r}/2) \rangle$  with  $G_\mu^0$  being Green's function corresponding to the harmonic oscillator potential  $U_0$ , we can also add and subtract a similar term involving Green's function  $G_\mu$  corresponding to the full potential  $U_0 + W$ . Also from Eq. (21), it is evident that in the limit  $N_C \rightarrow \infty$  [i.e.,  $k_C(r) \rightarrow \infty$ ] the results will be independent of the choice of  $k_F$ . However, we will see that the convergence of this modified scheme, from now on referred to as scheme (b), is very much improved. Thus, it is possible to use a much smaller cutoff  $N_C$  without having a strong cutoff dependence of the results.

### C. Local-density approximation

If the number of particles becomes very large, it is natural to assume that the system can be treated locally as infinite matter with a local chemical potential given by  $\mu - U_0(\mathbf{r})$ . This assumption leads directly to the LDA. Formally, the LDA corresponds to the leading order of the Wigner-Kirkwood  $\hbar$  expansion, which is at the same time an expansion in the gradients of the potential [15]. Thus it is the generalization of the standard TFA, which also corresponds to the leading order of an  $\hbar$  or gradient expansion, to the superfluid phase. Here we will adopt the name LDA in order to avoid confusion with the full HFB calculations using the TFA only in the regularization prescription, as discussed in Sec. II B. But in the literature also the name TFA is adopted.

In the case of a zero-range interaction, the LDA (or TFA) amounts to solving at each point  $\mathbf{r}$  the following nonlinear equations for the mean field  $W(\mathbf{r})$  and the pairing field  $\Delta(\mathbf{r})$ :

$$\begin{aligned} W(\mathbf{r}) &= \frac{g}{2} \rho(\mathbf{r}) \\ &= g \int \frac{d^3k}{(2\pi)^3} \left( \frac{1}{2} - [1 - 2f(E(\mathbf{r},\mathbf{k}))] \frac{\epsilon(\mathbf{r},\mathbf{k}) - \mu}{2E(\mathbf{r},\mathbf{k})} \right), \end{aligned} \quad (23)$$

$$\begin{aligned} \Delta(\mathbf{r}) &= -g \int \frac{d^3k}{(2\pi)^3} \left( [1 - 2f(E(\mathbf{r},\mathbf{k}))] \frac{\Delta(\mathbf{r})}{2E(\mathbf{r},\mathbf{k})} \right. \\ &\quad \left. - \frac{\Delta(\mathbf{r})}{2[\epsilon(\mathbf{r},\mathbf{k}) - \mu]} \right), \end{aligned} \quad (24)$$

where

$$\epsilon(\mathbf{r},\mathbf{k}) = \frac{k^2}{2} + U_0(\mathbf{r}) + W(\mathbf{r}), \quad (25)$$

$$E(\mathbf{r},\mathbf{k}) = \sqrt{[\epsilon(\mathbf{r},\mathbf{k}) - \mu]^2 + \Delta^2(\mathbf{r})}. \quad (26)$$

The last term in Eq. (24) has been introduced in order to regularize the ultraviolet divergence. In fact, the pseudopotential prescription used in the previous sections was originally motivated by the fact that it reduces to such a term if it

is applied to a homogeneous system [8,11]. A more rigorous justification of this term is that it appears if one renormalizes the scattering amplitude of two particles in free space [18].

Let us first consider the case of zero temperature,  $T=0$ . In this case, and if the gap  $\Delta$  is small compared with the local Fermi energy  $\epsilon_F = \frac{1}{2}k_F^2$ , Eqs. (23) and (24) can be solved (almost) analytically. Under these conditions, the density practically coincides with the density obtained for  $\Delta = 0$ , where Eqs. (23), (25), and (26) can be transformed into a cubic equation for the local Fermi momentum:

$$g \frac{k_F^3(\mathbf{r})}{6\pi^2} + \frac{k_F^2(\mathbf{r})}{2} + U_0(\mathbf{r}) - \mu = 0. \quad (27)$$

For a given local Fermi momentum and under the assumption that corrections of higher order in  $\Delta/\epsilon_F$  are negligible, Eq. (24) can be solved analytically. The result is the well-known formula

$$\Delta(\mathbf{r}) = 8\epsilon_F(\mathbf{r}) \exp\left(-2 - \frac{\pi}{2k_F(\mathbf{r})|a|}\right). \quad (28)$$

Now we turn to the case of nonzero temperature, but we want to consider only temperatures below the critical temperature, i.e.,  $0 < T < T_C$ . Therefore, we can neglect the influence of the temperature on the density and have to consider only the temperature dependence of  $\Delta$ . Let us denote the gap at  $T=0$  by  $\Delta_0$ . Then the gap at nonzero temperature can be obtained from the approximate relation [19]

$$-\ln \frac{\Delta(\mathbf{r})}{\Delta_0(\mathbf{r})} = \int d\xi \frac{f(\sqrt{\xi^2 + \Delta^2(\mathbf{r})})}{\sqrt{\xi^2 + \Delta^2(\mathbf{r})}}. \quad (29)$$

The solution of this equation leads to a universal function which gives the ratio  $\Delta/\Delta_0$  as a function of  $T/T_C$ , with  $T_C \approx 0.57\Delta_0$ . Note that, within the LDA, the critical temperature is a local quantity,  $T_C = T_C(\mathbf{r})$ .

In order to compare the LDA with the HFB theory, with special emphasis on the regularization prescription, we introduce a regularization scheme for the gap equation within LDA which is slightly different from Eq. (24). First of all, if we want to investigate the cutoff dependence, we have to introduce a cutoff in Eq. (24). Second, the regularization term introduced in Eq. (24) corresponds to regularization prescription (b) described at the end of the preceding section, which is different from that introduced in Ref. [8] and from regularization scheme (a). If we want to compare the LDA results with HFB results obtained with the original prescription or with prescription (a), which involves Green's function  $G_\mu^0$  of the potential  $U_0$  and not Green's function  $G_\mu$  of the full potential  $U_0 + W$ , we have to replace the energy  $\epsilon(\mathbf{r}, \mathbf{k})$  appearing in the regularization term by

$$\epsilon^0(\mathbf{r}, \mathbf{k}) = \frac{k^2}{2} + U_0(\mathbf{r}). \quad (30)$$

Thus, the gap equation within LDA suitable for comparison with the regularization scheme (a) reads

$$\Delta(\mathbf{r}) = -g \int_0^{k_C(\mathbf{r})} \frac{d^3k}{(2\pi)^3} \left( [1 - 2f(E(\mathbf{r}, \mathbf{k}))] \right. \\ \left. \times \frac{\Delta(\mathbf{r})}{2E(\mathbf{r}, \mathbf{k})} - \frac{\Delta(\mathbf{r})}{2[\epsilon^0(\mathbf{r}, \mathbf{k}) - \mu]} \right). \quad (31)$$

At zero temperature,  $T=0$ , it is again possible to solve this equation analytically, with the result

$$\Delta(\mathbf{r}) = 8\epsilon_F(\mathbf{r}) \sqrt{\frac{k_C(\mathbf{r}) - k_F(\mathbf{r})}{k_C(\mathbf{r}) + k_F(\mathbf{r})}} \exp\left(-2 - \frac{\pi}{2k_F(\mathbf{r})|a|}\right) \\ - \frac{k_F^0(\mathbf{r})}{2k_F(\mathbf{r})} \ln \frac{k_C(\mathbf{r}) - k_F^0(\mathbf{r})}{k_C(\mathbf{r}) + k_F^0(\mathbf{r})}. \quad (32)$$

The result corresponding to regularization scheme (b), Eq. (28), is recovered from this result by replacing  $k_F^0$  by  $k_F$ . In this case, there is no cutoff dependence at all, but one should remember that in deriving Eq. (32) we have implicitly assumed that the cutoff lies above the Fermi surface. A weak cutoff dependence would appear only if corrections to Eq. (32) of higher order in  $\Delta/\epsilon_F$  were included.

### III. NUMERICAL RESULTS

In this section, we will present some numerical results. In particular, we will investigate the convergence properties of the different renormalization methods. Then, we will discuss the validity of the LDA at zero temperature. Finally, we will compare HFB and LDA calculations at nonzero temperature.

In our numerical calculations, we will use for the coupling constant the value  $g = -1$  (in units of  $\hbar^2 l_{ho}/m$ ). If we consider  ${}^6\text{Li}$  atoms with scattering length  $a = -2160a_0$  [20], where  $a_0 = 0.53 \text{ \AA}$  is the Bohr radius, this value of  $g$  corresponds to a trap with  $\omega = (2\pi)817 \text{ Hz}$ . (Before relating this to real experimental conditions, one should however remember that in the experiments the trap is usually axially deformed, with a low longitudinal trapping frequency  $\omega_z$  and a high transverse trapping frequency  $\omega_\perp$ . For example, in the experiment described in Ref. [5], the trapping frequencies were given by  $\omega_z = (2\pi)230 \text{ Hz}$  and  $\omega_\perp = (2\pi)6625 \text{ Hz}$ .) The choice  $g = -1$  also facilitates the comparison of our results with those from Ref. [8], where the same value for  $g$  was used.

#### A. Convergence of the regularization methods

In this section, we will discuss the convergence rates with respect to the cutoff used in the numerical calculations for different choices for the regularization procedure. As in Sec. II, we denote by (a) the HFB calculations made with the choice of  $k_F^0$  given by Eq. (18), and by (b) the calculations made with the choice where  $k_F^0$  is replaced by  $k_F$  as given by Eq. (22). For our comparison, we use a chemical potential  $\mu = 32\hbar\omega$ , the corresponding number of atoms in the trap is  $N \approx 1.7 \times 10^4$ .

In Figs. 1 and 2, we present the pairing field  $\Delta$  calculated at zero temperature within the HFB and LDA formalisms for

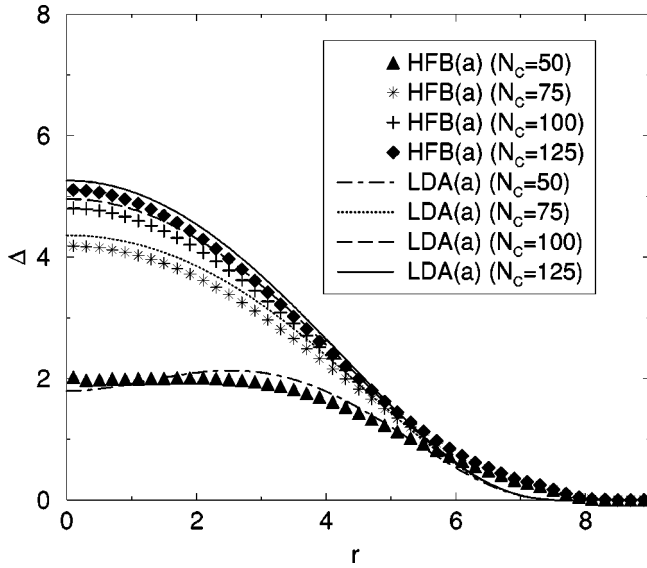


FIG. 1. Pairing field  $\Delta$  (in units of  $\hbar\omega$ ) as a function of the distance  $r$  (in units of  $l_{ho}$ ) from the center of the trap, calculated for the parameters  $\mu = 32\hbar\omega$  and  $g = -1\hbar^2 l_{ho}/m$ , corresponding to  $N \approx 1.7 \times 10^4$  particles in the trap. The different curves have been obtained within the HFB and LDA formalisms using regularization prescription (a) for different values of the cutoff  $N_C$ .

different values of the cutoff  $N_C$  from 50 up to 125. The results shown in Fig. 1 have been obtained with the choice (a) for the regularization for both the HFB and LDA calculations. We verified that the HFB calculations with the exact Green's function  $G_\mu^{0reg}$  (without TFA) give practically the same results as the method HFB (a) for all the values of the cutoff. This means that the TFA in the regularization procedure is very satisfying and reproduces well the regular part of the oscillator Green's function.

We observe in Fig. 1 that the agreement between LDA and HFB is reasonable for all values of the cutoff  $N_C$ . We

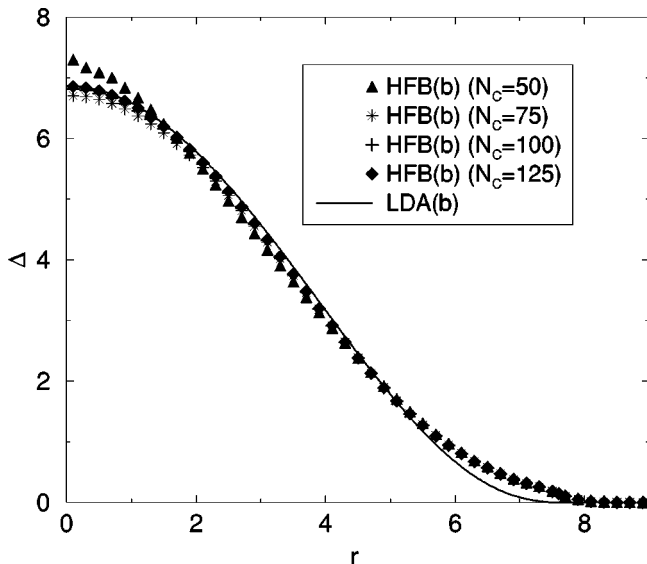


FIG. 2. Same as Fig. 1, but with regularization prescription (b). Remember that with this prescription the LDA result [Eq. (32)] is independent of the cutoff  $N_C$ .

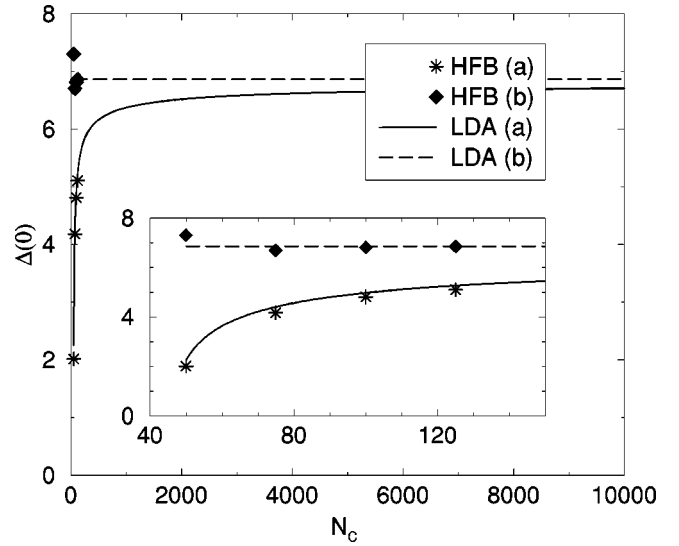


FIG. 3. Value of the pairing field in the center of the trap,  $\Delta(0)$  (in units of  $\hbar\omega$ ), as a function of the cutoff  $N_C$ , obtained from HFB calculations with regularization methods (a) (stars) and (b) (diamonds), and from the LDA, methods (a) (solid line) and (b) (dashed line). The parameters  $\mu$  and  $g$  are the same as in Fig. 1.

also notice that for  $N_C = 125$ , which is the maximum value that we considered, the convergence has not yet been reached and therefore the pairing field would grow further if we could increase the cutoff above 125. In Fig. 2, we present the same calculations made with choice (b) for the regularization. Remember that with this choice, the pairing field within LDA is independent of  $N_C$  once  $N_C$  lies above the Fermi surface. On the other hand, the HFB results saturate quite fast and are already very close to convergence for  $N_C = 75$ . Again, the LDA and HFB results are in reasonable agreement.

By comparing Figs. 1 and 2, one observes clearly that the calculations (a), Fig. 1, are still quite far from convergence even for the highest considered cutoff. We argue that the convergence rate of method (a), which is the same convergence rate as that of HFB without TFA in the regularization prescription [8], is much slower than that of method (b). This is more evident in Fig. 3 where we plot the HFB values of the pairing field in the center of the trap,  $\Delta(0)$ , for two regularization prescriptions (a) (stars) and (b) (diamonds) as a function of the cutoff  $N_C$ . We also plot the results obtained within the LDA (a) (full line) and LDA (b) (dashed line) up to a cutoff of  $N_C = 10^4$ . In the inset of the figure, we magnify the region of cutoff values between 50 and 150. We can observe in the inset that the LDA (a) curve fits well the calculated points for HFB (a). We noticed that the LDA (a) results converge slowly towards a pairing field of about  $6.86\hbar\omega$ , at a very high cutoff,  $N_C = 10^6$ . For  $N_C = 10^3$ , the pairing field in LDA(a) is still only  $6.37\hbar\omega$ . This very slow convergence rate can be understood within the LDA by taking the ratio of the pairing fields corresponding to methods (a) and (b). Using Eq. (32) in the limit of very large  $k_C$ , one can derive the relation

$$\frac{\Delta_{LDA(a)}(\mathbf{r})}{\Delta_{LDA(b)}(\mathbf{r})} \approx 1 - \frac{|g|\sqrt{2}[\mu - W(\mathbf{r})]}{3\pi^2\sqrt{N_C}} + \dots, \quad (33)$$

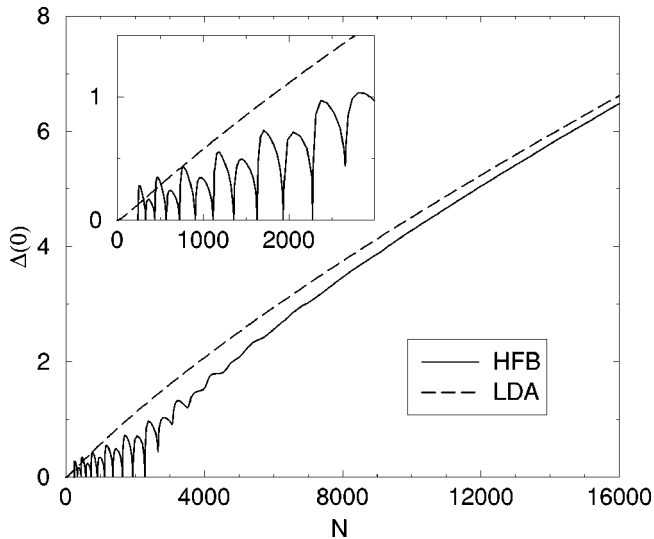


FIG. 4. Value of the pairing field in the center of the trap,  $\Delta(0)$  (in units of  $\hbar\omega$ ), as a function of the number of particles  $N$  obtained from HFB (solid line) and LDA (dashed line) calculations [regularization method (b), cutoff  $N_C=100$ , coupling constant  $g=-1$  in trap units].

where  $W(r)$  represents the Hartree field [in the present case,  $W(0) \approx -16\hbar\omega$ ].

As the agreement between LDA (a) and HFB (a) is good in the region up to  $N_C=125$ , we suppose that the convergence rate for HFB (a) is the same as for LDA (a). On the contrary, within HFB (b) the values of the pairing field in the center of the trap are  $6.81\hbar\omega$  for  $N_C=100$  and  $6.86\hbar\omega$  for  $N_C=125$ : we conclude that the convergence in this case is much faster. In what follows we will always use method (b) for the regularization procedure.

### B. Validity of the LDA at zero temperature

As mentioned before, the parameters used for the calculations shown in Figs. 1–3 correspond to a trap with about  $1.7 \times 10^4$  atoms. In this case, we found a good agreement between the numerical HFB results and the results obtained from the LDA. However, one might wonder under which conditions the LDA is valid. To study this question, one has to look at systems containing smaller numbers of particles, since in smaller systems the quantum effects (in particular shell effects) which are neglected in the LDA, are supposed to be more important.

In Fig. 4, we present the HFB (full line) and LDA (dashed line) results for the pairing field in the center of the trap,  $\Delta(0)$ , as a function of the number of atoms  $N$ . The calculations are done again at zero temperature and with a coupling constant  $g=-1$  in trap units. We observe that the two calculations are in reasonable agreement for number of atoms greater than about 5000, which confirms the expectation that the LDA is a valid approximation for systems with a large number of atoms.

What is particularly interesting to look at in this figure is the region  $N \lesssim 3000$ . In this region the HFB results clearly show the shell structure: the pairing field becomes zero for

$N=240,330,440, \dots$ , which are the harmonic oscillator “magic numbers.” One also realizes that the central value of the pairing field is smaller if the outer shell corresponds to odd-parity states, than in the case where the outer shell corresponds to even-parity states. This can be understood easily, since the main contribution to the pairing field comes from the states near the Fermi surface, and only  $s$  states can contribute to the pairing field at  $r=0$ . Usually one expects that the LDA should at least reproduce the value of the pairing field if the fluctuations due to shell effects are averaged out, but our results show that the pairing field calculated within the LDA is systematically too high. This might be related to the fact that we are looking at the pairing field at one particular point ( $r=0$ ) rather than at the average gap at the Fermi surface, as proposed in Ref. [21].

When the number of atoms increases, above a value of about 2500 the shell structure starts to be washed out and gradually disappears due to the stronger and stronger pairing correlations. This happens in the region where the pairing field grows up to a value of about  $\hbar\omega$ : when the pairing field becomes comparable with the oscillator level spacing, the pairing correlations in a closed-shell system can diffuse pairs of atoms towards the higher-energy empty shell, resulting in a nonzero pairing field. Globally, we observe that for  $N > 5000$  the agreement between HFB and LDA is acceptable, even if the LDA systematically overestimates the value of the pairing field at the center.

Of course, the number of particles needed for the validity of the LDA depends on the strength of the interaction; the true criterion which has to be fulfilled reads  $\Delta_{LDA} > \hbar\omega$ . This criterion can even be applied locally, as one can see in Fig. 2: there the HFB and LDA results are in perfect agreement except in the region of  $r \gtrsim 5.5l_{ho}$ , where  $\Delta$  becomes smaller than  $\hbar\omega$ .

### C. Results for nonzero temperature

Now we will discuss some results for temperatures different from zero. We are particularly interested in the following question: Within the LDA, the critical temperature  $T_C$  is different at each point  $r$ , i.e., when the temperature increases, the order parameter vanishes at last in the center of the trap, where the local critical temperature is the highest. In contrast to this, within the HFB theory, the gap and the critical temperature are global properties, and naively one would expect that, as long as the temperature is below  $T_C$ , the pairing field extends over the whole volume of the system. We will see that even in cases where the LDA works well at zero temperature, it fails at nonzero temperature. On the other hand, also the notion that the gap vanishes globally at  $T=T_C$  has to be revised in these cases.

In Figs. 5 and 6, we show the HFB and LDA pairing fields obtained at different temperatures, again for  $g=-1$  (in trap units) and regularization method (b). The chemical potentials chosen are  $\mu=32\hbar\omega$  in Fig. 5 and  $\mu=40\hbar\omega$  in Fig. 6, corresponding to approximately  $1.7 \times 10^4$  and  $4 \times 10^4$  particles, respectively. We observe that the good agreement obtained at zero temperature is deteriorated at higher temperatures. In Fig. 5, already at  $T=2\hbar\omega/k_B$ , the LDA reproduces badly

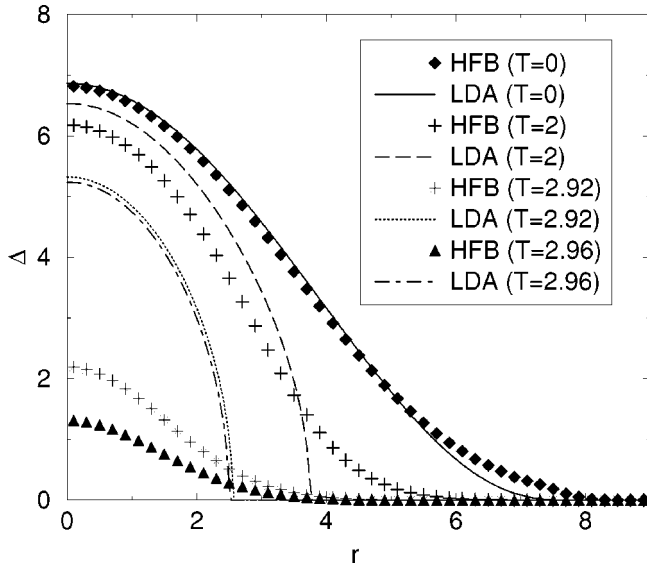


FIG. 5. Pairing field  $\Delta$  (in units of  $\hbar\omega$ ) as a function of the distance  $r$  (in units of  $l_{ho}$ ) from the center of the trap, for a chemical potential  $\mu = 32\hbar\omega$ , corresponding to about  $1.7 \times 10^4$  atoms in the trap [regularization method (b), cutoff  $N_C = 100$ , coupling constant  $g = -1$  in trap units]. Results obtained within numerical HFB calculations (symbols) are compared with LDA results (lines) for different temperatures  $T$ .

not only the tail of the pairing field profile, but also the pairing field in the central region of the trap, in spite of the fact that the pairing field is still large compared with  $\hbar\omega$  at this temperature. The LDA description gets worse and worse for higher temperatures and results in an overestimation of the central pairing field and in a too drastic cut of the queue of the profiles at large distances. Finally, the LDA method predicts a higher critical temperature than the one predicted by HFB. We observed that  $T_C$  is equal to 3.89 (in units of  $\hbar\omega/k_B$ ) for LDA and to 2.98 for HFB. In Fig. 6, the agreement is somewhat better. Since the critical temperature is

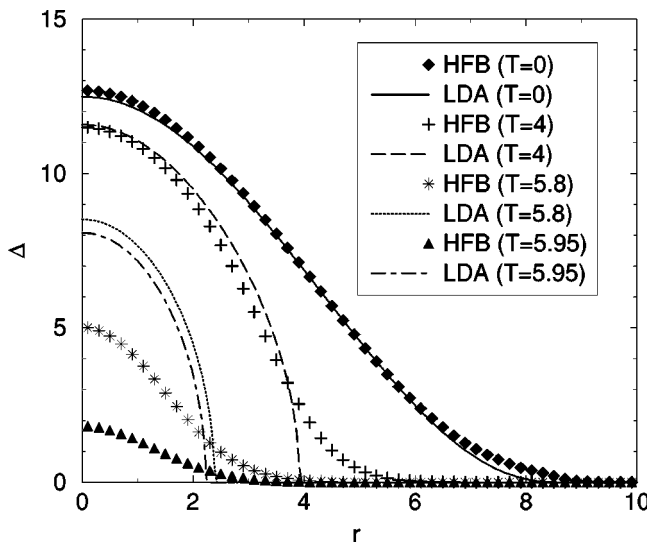


FIG. 6. Same as Fig. 5, but for a chemical potential of  $\mu = 40\hbar\omega$ , corresponding to  $N \approx 4 \times 10^4$  atoms in the trap.

TABLE I. Comparison of results (in trap units) obtained from HFB calculations for the two cases  $\mu = 32$  and  $\mu = 40$  shown in Figs. 5 and 6 [coupling constant  $g = 1$  in trap units, regularization method (b),  $N_C = 100$ ] and the corresponding results obtained from the GL theory.

$\mu$	$k_F(0) a $	$T_C^{(0)}$	$T_C$	$\delta T_C$	$\delta T_C^{(GL)}$	$l_\Delta$	$l_\Delta^{(GL)}$
32	0.78	3.89	2.98	0.91	1.12	1.44	1.23
40	0.91	7.08	5.97	1.11	1.29	1.28	0.95

higher than in the previous case, the agreement between LDA and HFB is maintained in a wider range of temperatures. Up to  $T = 4$ , one can see that at least the central region of the trap is well described by LDA. For higher temperatures, we observe the same kind of deterioration of the LDA results shown in Fig. 5. Again, the critical temperature is higher in LDA (7.08) than in HFB (5.97).

It is evident that the LDA does not correctly describe the phase transition in both cases. On the other hand, also within the HFB calculations, one finds that with increasing temperature the pairing field becomes more and more concentrated in the center of the trap. Such a behavior has been predicted in Ref. [7] using the GL theory, the only assumption being that the critical temperature is large compared with the trapping frequency,  $k_B T_C \gg \hbar\omega$ . Let us briefly review the main results from this theory and compare them with the results obtained from our HFB calculations (the corresponding numbers are listed in Table I).

In the GL theory the critical temperature  $T_C$  is predicted to be lower than the critical temperature  $T_C^{(0)}$  obtained from the LDA. The difference can be written as

$$\delta T_C = T_C^{(0)} - T_C = \frac{3\hbar\Omega}{k_B} \sqrt{\frac{7\zeta(3)}{48\pi^2} \left(1 + \frac{\pi}{4k_F(0)|a|}\right)}, \quad (34)$$

where  $\zeta$  denotes the Riemann zeta function [ $\zeta(3) = 1.202 \dots$ ]. In the derivation of Eq. (34) in Ref. [7], the Hartree potential has been neglected. Here we will include the Hartree potential by using an effective oscillator frequency  $\Omega > \omega$ . Since near  $T_C$  the pairing field is concentrated in the center of the trap, we define  $\Omega$  by expanding the potential around  $r = 0$ :

$$\Omega = m \sqrt{\nabla^2 [U_0(r) + W(r)]_{r=0}}. \quad (35)$$

Within the Thomas-Fermi approximation, for the density profile the effective oscillator frequency can be written as

$$\Omega = \frac{\omega}{1 - \frac{2k_F(0)|a|}{\pi}}. \quad (36)$$

The estimates for  $\delta T_C$  obtained by inserting the numerical values for  $k_F(0)|a|$  given in Table I into Eqs. (34) and (36) are very reasonable. This can be seen by comparing them with the  $\delta T_C$  values obtained from the HFB calculations, which are also listed in Table I. If one considers that these

numbers can only be a rough estimate, since  $k_B T_C$  is not really very large compared with  $\hbar\Omega$ , the agreement with the HFB results is very satisfying.

Not only the critical temperature, also the shape of the order parameter near the critical temperature can be obtained from the GL theory. It can be shown that for temperatures very close to  $T_C$  the pairing field has the form of a Gaussian,

$$\Delta(\mathbf{r}) = \Delta(0) \exp\left(-\frac{r^2}{2l_\Delta^2}\right). \quad (37)$$

In contrast to the LDA result, the radius  $l_\Delta$  of this Gaussian is predicted to stay finite in the limit  $T \rightarrow T_C$ , as it is the case for the solution of the HFB equations. Its value is given by

$$l_\Delta^2 = R_{TF}^2 \frac{\hbar\Omega}{k_B T} \sqrt{\frac{7\xi(3)}{48\pi^2} \frac{1}{1 + \frac{\pi}{4k_F(0)|a|}}}. \quad (38)$$

In Ref. [7], the quantity  $R_{TF}$  was defined as the Thomas-Fermi radius of the cloud,  $R_{TF} = \sqrt{2\mu/(m\omega^2)}$ . Generalizing the derivation of Eq. (38) to the case of a nonvanishing Hartree field, we see that the corresponding parameter for the pairing field near the center of the trap is given by

$$R_{TF} \rightarrow \sqrt{\frac{2[\mu - W(0)]}{m\Omega^2}} = \left(1 - \frac{2k_F(0)|a|}{\pi}\right) k_F(0) l_{ho}^2. \quad (39)$$

On the other hand, the HFB pairing fields corresponding to the temperatures next to  $T_C$ , shown in Figs. 5 and 6, are also perfectly fitted by Gaussians. As shown in Table I, the agreement between the radii obtained from this fit are again in reasonable agreement with the radii obtained from Eqs. (38) and (39). The deviations are of the order of 30%, which is even better than one could have expected, since the parameter  $\hbar\Omega/(k_B T_C)$  is not very small in the present case.

Finally, let us look more closely at the critical behavior near  $T_C$ . Again, from the GL theory one can derive that for  $T \rightarrow T_C$  the value of the pairing field in the center should go to zero like

$$\Delta(0) = \sqrt{\frac{16\pi^2\sqrt{2}}{7\xi(3)} T_C(T_C - T)}. \quad (40)$$

As shown in Figs. 7 and 8, this formula is very well satisfied by the HFB results in both cases,  $\mu = 32$  and  $\mu = 40$  (in trap units). Note that the prefactor in Eq. (40) differs from the prefactor in LDA. In LDA one finds for  $T \approx T_C^{(0)}$ ,

$$\Delta_{LDA}(0) = \sqrt{\frac{8\pi^2}{7\xi(3)} T_C^{(0)}(T_C^{(0)} - T)}. \quad (41)$$

The different prefactor as well as the different critical temperature and the finite radius of the pairing field are due to the ‘‘kinetic’’ term  $\propto \Delta \nabla^2 \Delta$  in the GL energy functional,

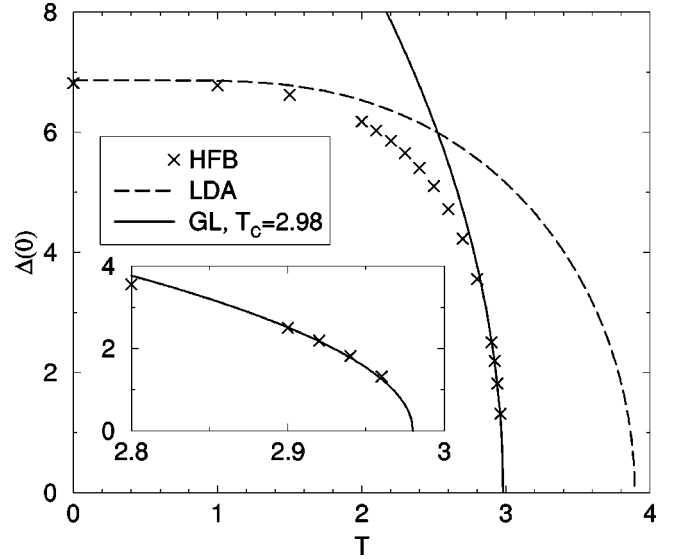


FIG. 7. Value of the pairing field in the center of the trap,  $\Delta(0)$  (in units of  $\hbar\omega$ ), as a function of temperature  $T$  (in units of  $\hbar\omega/k_B$ ) for a chemical potential  $\mu = 32\hbar\omega$ , corresponding to about  $1.7 \times 10^4$  atoms in the trap [regularization method (b), cutoff  $N_C = 100$ , coupling constant  $g = -1$  in trap units]. Results obtained within numerical HFB calculations (symbols) are compared with the LDA result (dashed line) and with formula (40) obtained from the GL theory (solid line).

which is absent in the LDA and is very important for the description of the strongly  $r$  dependent pairing field near the critical temperature.

As a final remark let us mention that the different calculations which we have compared in this paper are all based on mean-field theory, and therefore we do not take into account fluctuations of the order parameter  $\Delta$ . It is well known that fluctuations are very important near the phase transition, and in particular in a situation where  $k_F|a|$  is not small, as it is the case here, they can lead to a considerable change of the

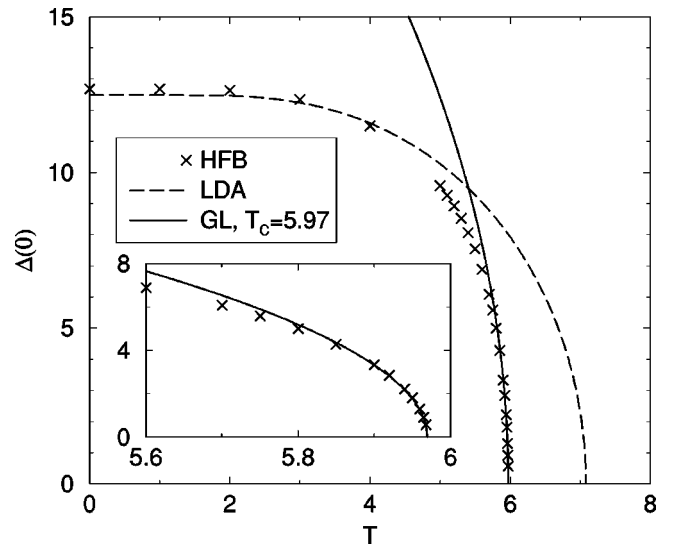


FIG. 8. Same as Fig. 7, but for a chemical potential of  $\mu = 40\hbar\omega$ , corresponding to  $N \approx 4 \times 10^4$  atoms in the trap.

critical temperature. Anyway, what we wanted to point out here is that the LDA gives the wrong  $T_C$  as compared with a theory taking into account the inhomogeneity of the system. From this result we conclude that in order to have a reliable prediction of  $T_C$  for the trapped system, it is not sufficient to do a reliable calculation of  $T_C$  (even including fluctuations) for a homogeneous gas and then apply the LDA.

#### IV. CONCLUSIONS

In this paper, we have shown a detailed comparison between HFB and LDA calculations at  $T=0$  and at  $T\neq 0$  for a low density gas of superfluid fermionic atoms trapped by a spherical harmonic potential. We have used a zero-range interaction for the atoms and we have proposed an improvement of the regularization method adopted to remove the ultraviolet divergence [8]. This improvement is a modification of a procedure proposed for nuclear systems in Ref. [11], where the Thomas-Fermi approximation is used in the calculation of the regular part of Green's function  $G_\mu^{0\text{reg}}$ , Eq. (16). The use of the Thomas-Fermi approximation allows us to treat systems with a large number of atoms much easier than in the calculations of Ref. [8]. On the other hand, our modification considerably improves the convergence rate of the procedure with respect to the numerical cutoff. By using this regularization method, we have observed that the LDA results are in quite good agreement with the corresponding HFB results at zero temperature and for systems with a relatively large number of atoms, where the shell structure effects are washed out. The shell effects, which are important for small systems where the pairing field is smaller than the harmonic level spacing  $\hbar\omega$ , cannot obviously be reproduced by a LDA calculation.

For nonzero temperatures, the agreement between HFB

and LDA is deteriorated even in those cases where it was good at  $T=0$ . In general, LDA overestimates the value of the pairing field in the center of the trap, cuts too drastically the tail of the radial profile of the pairing field at large distances, and overestimates the critical temperature with respect to HFB. We have verified that this discrepancy between the HFB and LDA which results at  $T$  different from zero can be nicely predicted by using the GL theory [7] in cases where the critical temperature is much larger than the harmonic level spacing.

In this paper, we considered only spherical traps. However, the traps used in experiments are usually cigar shaped with a low longitudinal and a high transverse trapping frequency,  $\omega_z \ll \omega_\perp$ . In this case, it is possible that the pairing field, even if it is larger than  $\hbar\omega_z$ , is still smaller than  $\hbar\omega_\perp$ , and the LDA would probably not work. Therefore in principle one should also perform deformed HFB calculations, but at the moment this seems to be numerically very difficult. On the other hand, as noted above, even in the case where  $\Delta$  is large compared with both trapping frequencies, the LDA is not adequate at a nonzero temperature. Therefore a first step to study nonspherical traps could be to generalize the GL theory of Ref. [7] to the deformed case.

#### ACKNOWLEDGMENTS

The authors wish to thank Elias Khan, Peter Schuck, and Nguyen Van Giai for useful discussions. We thank Yvan Castin for supplying us the code for the numerical calculation of Green's function  $G_\mu^{0\text{reg}}$  which we used to check the TF approximation. M. G. acknowledges financial support by the European Commission. M.U. acknowledges support by the Alexander von Humboldt Foundation.

- 
- [1] J.L. Roberts *et al.*, Phys. Rev. Lett. **86**, 4211 (2001).
  - [2] B. De Marco and D.S. Jin, Science **285**, 1703 (1999); B. De Marco, S.B. Papp, and D.S. Jin, Phys. Rev. Lett. **86**, 5409 (2001).
  - [3] A.G. Truscott *et al.*, Science **291**, 2570 (2001).
  - [4] F. Schreck, G. Ferrari, K.L. Corwin, J. Cubizolles, L. Khaykovich, M.-O. Mewes, and C. Salomon, Phys. Rev. A **64**, 011402(R) (2001).
  - [5] K.M. O'Hara, S.L. Hemmer, M.E. Gehm, S.R. Granade, and J.E. Thomas, Science **298**, 2179 (2002).
  - [6] M. Houbiers, R. Ferwerda, H.T.C. Stoof, W.I. McAlexander, C.A. Sackett, and R.G. Hulet, Phys. Rev. A **56**, 4864 (1997).
  - [7] M.A. Baranov and D.S. Petrov, Phys. Rev. A **58**, R801 (1998).
  - [8] G. Bruun, Y. Castin, R. Dum, and K. Burnett, Eur. Phys. J. D **7**, 433 (1999).
  - [9] G.M. Bruun and H. Heiselberg, Phys. Rev. A **65**, 053407 (2002).
  - [10] G.M. Bruun, Phys. Rev. A **66**, 041602(R) (2002).
  - [11] A. Bulgac and Y. Yu, Phys. Rev. Lett. **88**, 042504 (2002).
  - [12] N. Nygaard, G.M. Bruun, C.W. Clark, and D.L. Feder, Phys. Rev. Lett. **90**, 210402 (2003).
  - [13] H. Heiselberg, Phys. Rev. A **63**, 043606 (2001).
  - [14] E. Timmermans, K. Furuya, P.W. Milonni, and A.K. Kerman, Phys. Lett. A **285**, 228 (2001).
  - [15] P. Ring and P. Schuck, *The Nuclear Many-Body Problem* (Springer-Verlag, Berlin, 1980).
  - [16] P.-G. de Gennes, *Superconductivity of Metals and Alloys* (Benjamin, New York, 1966).
  - [17] K. Huang, *Statistical Mechanics* (Wiley, New York, 1987).
  - [18] C.A.R. Sá de Melo, M. Randeria, and J.R. Engelbrecht, Phys. Rev. Lett. **71**, 3202 (1993).
  - [19] E.M. Lifshitz and L.P. Pitaevskii, *Statistical Physics, Part 2: Theory of the Condensed State* (Pergamon, Oxford, 1980).
  - [20] E.R.I. Abraham, W.I. McAlexander, J.M. Gerton, R.G. Hulet, R. Côté, and A. Dalgarno, Phys. Rev. A **55**, R3299 (1997).
  - [21] M. Farine, F.W.I. Hekking, P. Schuck, and X. Viñas, e-print cond-mat/0207297.

### 4.3 Appariement non – standard : la phase LOFF

Il est possible de contrôler expérimentalement les populations dans les différents états de structure hyperfine et des mélanges avec des populations asymétriques peuvent être obtenus [Zw03]. Si le système est très asymétrique, les énergies de Fermi associées aux diverses polarisations de spin deviennent très différentes et le couplage à moment zéro qui caractérise la formation de paires de Cooper standard est supprimé. Par contre, d'autres couplages à moments non nuls peuvent se réaliser donnant lieu à des phénomènes d'appariement plus exotiques, comme par exemple la phase Larkin-Ovchinnikov-Fulde-Ferrel (LOFF) [Co04] ou la phase Sarma [Li03].

Nous avons résolu les équations HFB dans le cas d'un système asymétrique. Les équations à résoudre ont la forme suivante :

$$\begin{aligned} u_{\eta\sigma}(\vec{r})E_{\eta\sigma} &= W_{\sigma}u_{\eta\sigma}(\vec{r}) + \Delta(\vec{r})v_{\eta-\sigma}(\vec{r}), \\ v_{\eta-\sigma}(\vec{r})E_{\eta\sigma} &= -W_{-\sigma}v_{\eta-\sigma}(\vec{r}) + \Delta(\vec{r})u_{\eta-\sigma}(\vec{r}), \end{aligned} \quad (4.2)$$

avec,

$$W_{\sigma} = H_0 + g\rho_{-\sigma} - \mu_{\sigma}. \quad (4.3)$$

$\mu_{\sigma}$  et  $\rho_{\sigma}$  sont le potentiel chimique et la densité associés au spin  $\sigma$ ,  $g$  est la constante de couplage égale à  $(4\pi\hbar^2 a)/m$  ;  $H_0$  contient le terme cinétique et le potentiel piégeant et  $\Delta$  représente le champ d'appariement. Le cas où les deux potentiels chimiques sont différents décrit un gaz avec deux populations différentes dans les deux états de spin. Quand les deux potentiels chimiques sont égaux,  $\mu_{\uparrow} = \mu_{\downarrow}$ , les équations (4.2) ont la forme des équations HFB standard.

Dans l'article qui suit, [Ca05], nous étudions les solutions de ces équations HFB généralisées en fonction de l'asymétrie des populations et de la température. Dans certaines conditions, nous prédisons des oscillations du gap d'appariement, ce qui serait une indication de la réalisation d'une phase LOFF.

## Nonstandard pairing in asymmetric trapped Fermi gases

Paolo Castorina,<sup>1</sup> Marcella Grasso,<sup>1,2,3</sup> Micaela Oertel,<sup>4</sup> Michael Urban,<sup>3</sup> and Dario Zappalà<sup>2</sup>

<sup>1</sup>*Dipartimento di Fisica e Astronomia, Via Santa Sofia 64, I-95123 Catania, Italy*

<sup>2</sup>*INFN, Sezione di Catania, Via Santa Sofia 64, I-95123 Catania, Italy*

<sup>3</sup>*Institut de Physique Nucléaire, 15 rue Georges Clémenceau, F-91406 Orsay Cedex, France*

<sup>4</sup>*Service de Physique Nucléaire, CEA-DAM Ile-de-France, BP 12, F-91680 Bruyères-le-Châtel, France*

(Received 18 April 2005; published 15 August 2005)

We study an ultracold trapped Fermi gas of atoms in two hyperfine states with unequal populations. In this situation the usual BCS pairing is suppressed and nonstandard pairing mechanisms become important. These are treated by solving the Bogoliubov–de Gennes equations, which at the same time correctly take into account the finite size of the trapped system. We find results which can be viewed as generalization of the LOFF (Larkin-Ovchinnikov-Fulde-Ferrel) phase to finite systems.

DOI: [10.1103/PhysRevA.72.025601](https://doi.org/10.1103/PhysRevA.72.025601)

PACS number(s): 03.75.Ss, 21.60.Jz

In the past years much progress has been made in improving the techniques used to trap and cool dilute gases of bosonic and fermionic atoms [1,2]. One of the interesting aspects of the properties of ultra-cold gases is that the interatomic interaction can be modified, both in its intensity and in its sign, by changing the applied magnetic field around a Feshbach resonance. Due to the very low densities and temperatures in these systems the details of the interatomic interaction are unimportant and the interaction can be characterized by one single parameter, the  $s$ -wave scattering length  $a$ . In this article we consider Fermi gases trapped and cooled in two hyperfine states with an attractive interaction, i.e.,  $a < 0$ . We will concentrate on the weakly interacting case ( $k_F|a| \ll 1$ , where  $k_F$  denotes the Fermi momentum). In this region, BCS superfluidity with formation of Cooper pairs is expected below a certain critical temperature. So far, some experimental signals have been found which would indicate the existence of superfluidity in this region, [2] but a clear evidence is still missing.

Besides the interaction, also the population of the two hyperfine states can experimentally be controlled. Usually mixtures with equal populations are created, but controlled asymmetric mixtures have also been obtained [3]. Unequal populations of the two hyperfine states can lead to very interesting phenomena. For instance, the BCS pairing mechanism is supposed to become suppressed [4] since the two Fermi momenta associated with the two spin polarizations become different: The formation of zero-momentum Cooper pairs built of two atoms at their respective Fermi surface becomes difficult. Instead, other more exotic pairing phenomena have been suggested for the case of unequal populations, like the Larkin-Ovchinnikov-Fulde-Ferrel (LOFF) phase [5], the Sarma (interior gap) phase [6,7], or a phase with deformed Fermi surfaces (DFS) [8]. Many of these nonstandard pairing mechanisms have already been discussed in other domains of physics where asymmetric two-component fermion systems can be found: Superconductors in a magnetic field [9,10], neutron-proton pairing in asymmetric nuclear matter [11], color superconductivity in high density QCD [12]. The experimental observation of the LOFF phase in the case of superconductivity is a subject of debate. It seems that quite recently an oscillating supercon-

ducting order parameter has been observed in a ferromagnetic thin film [13].

In the literature [4–8] these nonstandard pairing types in ultracold Fermi gases are usually discussed for the case of infinite and homogeneous systems, or for trapped systems in local-density approximation (LDA) which again amounts to treating the system locally as homogeneous. However, as we are going to show, in certain cases the LDA can become a very poor approximation and we therefore want to analyze this problem within a fully microscopic mean field Bogoliubov–de Gennes (BdG) approach [14] taking into account the inhomogeneity and finite size of the trapped system. Recently the solution of the BdG equations has been considered in Ref. [15], where the authors discuss also possibilities for the experimental detection of a spatially modulated pairing gap.

In the present article we study two systems: a small one where shell effects still play a role and a relatively large one, where one could expect the LDA to be a reasonable approximation. As we will show, this is not always the case, although the LDA describes roughly the qualitative features. In addition, we examine the temperature dependence of the nonstandard pairing phase, since this is important in connection with the experimental realization of such a phase.

Let us briefly recall the BdG formalism. We consider a system containing  $N = N_+ + N_-$  atoms of mass  $m$  trapped by a spherical harmonic potential in two hyperfine states denoted by  $+$  and  $-$ . The many-body Hamiltonian of the system can be written as

$$H = \sum_{\sigma} \int d^3r [\Psi_{\sigma}^{\dagger}(\mathbf{r}) H_0 \Psi_{\sigma}(\mathbf{r}) + g \Psi_{+}^{\dagger}(\mathbf{r}) \Psi_{-}^{\dagger}(\mathbf{r}) \Psi_{-}(\mathbf{r}) \Psi_{+}(\mathbf{r})], \quad (1)$$

where  $H_0 = -\hbar^2 \nabla^2 / (2m) + m\omega^2 r^2 / 2$  denotes the harmonic oscillator single-particle Hamiltonian,  $\Psi_{\sigma}(\mathbf{r})$  is the field operator which annihilates a particle at the position  $\mathbf{r}$  in the spin state  $\sigma$  ( $+$  or  $-$ ),  $g = 4\pi\hbar^2 a / m$  is the coupling constant. In mean-field approximation, one can derive the following BdG equations corresponding to the Hamiltonian (1):

$$u_{\eta\sigma}(\mathbf{r})E_{\eta\sigma} = W_{\sigma}u_{\eta\sigma}(\mathbf{r}) + \Delta(\mathbf{r})v_{\eta-\sigma}(\mathbf{r}),$$

$$v_{\eta-\sigma}(\mathbf{r})E_{\eta\sigma} = -W_{-\sigma}v_{\eta-\sigma}(\mathbf{r}) + \Delta(\mathbf{r})u_{\eta\sigma}(\mathbf{r}), \quad (2)$$

where  $W_{\sigma} = H_0 + g\rho_{-\sigma}(\mathbf{r}) - \mu_{\sigma}$ ,  $\mu_{\sigma}$  and  $\rho_{\sigma}$  being the chemical potential and the density, respectively.  $\Delta(\mathbf{r})$  denotes the pairing field (gap) and  $E_{\eta\sigma}$ ,  $u_{\eta\sigma}$  and  $v_{\eta\sigma}$  are the quasiparticle energy and wave functions, respectively, corresponding to the quantum numbers  $\eta = n, l, m$  and spin  $\sigma$ . In order to have different populations, the two chemical potentials  $\mu_+$  and  $\mu_-$  must be different. It is convenient to introduce the average chemical potential  $\bar{\mu}$  and to write  $\mu_{\sigma} = \bar{\mu} + \sigma\delta\mu/2$  where  $\delta\mu$  determines the asymmetry. Equations (2) reduce to the usual BdG equations in the symmetric case  $\mu_+ = \mu_-$ . They are solved numerically employing the same regularization method for the pairing field as described in Ref. [16] for the symmetric case.

Eqs. (2) are general enough to describe rather complicated types of nonstandard pairing. In the case of usual BCS pairing, the dominant matrix elements of the pairing field are the diagonal ones, i.e., each state  $|n, l, m, +\rangle$  is paired with its time-reversed counterpart  $|n, l, -m, -\rangle$ . However, the nondiagonal matrix elements of  $\Delta$  are also included, which amounts to taking into account also the pairing of states  $|n, l, m, +\rangle$  and  $|n', l, -m, -\rangle$  with different principal quantum numbers  $n' \neq n$ . In our present calculation, we still keep the restriction that the Cooper pairs have total angular momentum zero. To release this constraint would mean to allow for a spontaneous breakdown of spherical symmetry, which would be numerically very heavy. The effect of strong nondiagonal matrix elements of  $\Delta$  in fact corresponds closely to the LOFF phase in the case of a uniform system. There, the states are labeled by their momentum  $\mathbf{k}$ . In the simplest version of the LOFF phase, the Cooper pairs have total momentum  $\mathbf{q}$ , i.e., each state  $|\mathbf{k}, +\rangle$  is paired with  $|-\mathbf{k} + \mathbf{q}, -\rangle$ . The corresponding gap is oscillating with wave vector  $\mathbf{q}$  and its matrix elements are therefore of the form  $\Delta_{\mathbf{k}\mathbf{k}'} = \Delta \delta_{\mathbf{k}-\mathbf{q}, \mathbf{k}'}$  (in contrast to the BCS phase, where  $\Delta_{\mathbf{k}\mathbf{k}'} = \Delta \delta_{\mathbf{k}\mathbf{k}'}$ ) [17].

In the discussion of our results all quantities will be given in harmonic oscillator units. We use the same coupling constant as in Ref. [16], i.e.,  $g = -\hbar^2 l_{ho}/m$ , where  $l_{ho} = \sqrt{\hbar/(m\omega)}$  denotes the harmonic oscillator length, and we consider two values for the average chemical potential,  $\bar{\mu} = 22 \hbar\omega$  (small system with  $N \approx 4900$ ) and  $32 \hbar\omega$  (large system with  $N \approx 17000$ ).

In Fig. 1 we show the values of the pairing gap  $\Delta(0)$  at the center of the trap for increasing asymmetry  $\delta\mu$  at  $T=0$ . Let us first look at the lowest line, corresponding to the small system with  $\bar{\mu} = 22 \hbar\omega$ . When both spin states are equally populated ( $\delta\mu=0$ ), we find  $\Delta(0) \approx 2 \hbar\omega$ , i.e., we are no more in the intrashell-pairing regime, but shell effects are still important [16]. If we increase  $\delta\mu$ , the two Fermi surfaces become more and more separated, i.e., if the state  $|n, l, m, +\rangle$  lies close to the Fermi level for spin  $+$ , the state  $|n, l, -m, -\rangle$  lies far from the Fermi level for spin  $-$ , making BCS pairing less and less favorable. As a consequence, at  $\delta\mu \approx 1.2 \hbar\omega$ , corresponding to a particle number asymmetry  $\alpha = (N_+ - N_-)/N \approx 0.06$ , the pairing disappears (shell closure effect). But then, near  $\delta\mu \approx 2 \hbar\omega$  ( $\alpha \approx 0.07$ ), the states

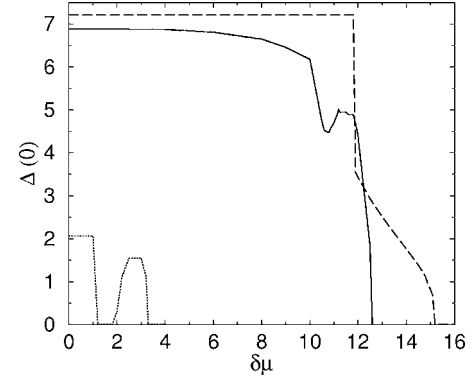


FIG. 1. Value of the pairing gap at the center of the trap (in units of  $\hbar\omega$ ) as a function of the asymmetry  $\delta\mu$  (in units of  $\hbar\omega$ ). The lowest line corresponds to  $\bar{\mu} = 22\hbar\omega$ . The two upper lines correspond to  $\bar{\mu} = 32\hbar\omega$  and show the BdG (solid line) and the LDA result (dashed line).

$|n, l, m, +\rangle$  near the Fermi level for spin  $+$  approach the states  $|n', l, -m, -\rangle$  near the Fermi level for spin  $-$  if  $n' = n - 1$ . Therefore, pairing becomes again possible, but now the Cooper pairs are built of two wave functions with different numbers of nodes, leading to a gap  $\Delta(r)$  which as a function of  $r$  has exactly one node.

Let us now turn to the investigation of the larger system,  $\bar{\mu} = 32 \hbar\omega$ . Here it seems to be appealing to estimate if and where the LOFF phase could appear by using the LDA, which should be exact in an infinite system. In order to do this, we calculate at each point  $R$  the thermodynamic potential  $\Omega$  of a uniform gas with effective average chemical potential  $\bar{\mu}_{eff}(R) = \bar{\mu} - m\omega^2 R^2/2$ , assuming a gap of the form  $\Delta(\mathbf{r}) = \Delta \exp(i\mathbf{q} \cdot \mathbf{r})$ , and minimize  $\Omega$  with respect to  $\Delta$  and  $q$ . To be more precise, we should have taken a more sophisticated expression for the order parameter, but we stress here that we use the LDA just to have some indications about what kind of behavior one should expect. Let us again look at  $\Delta(0)$  as a function of the asymmetry (dashed line in Fig. 1). We find that LDA gives the BCS solution  $q=0$  as the most favorable solution up to  $\delta\mu = 11.9 \hbar\omega$ . At that asymmetry we find a first-order phase transition [i.e., a discontinuity in  $\Delta(0)$ ] to the LOFF phase with  $q \sim l_{ho}^{-1}$  which means that the order parameter oscillates with a wavelength of  $\sim 6.2 l_{ho}$ . This behavior is different from the microscopic (BdG) result (solid line in Fig. 1), which shows a smooth behavior of  $\Delta(0)$ . Nevertheless, also in the BdG calculation there is a rapid change of  $\Delta(0)$  between  $\delta\mu = 10 \hbar\omega$  ( $\alpha \approx 0.25$ ) and  $\delta\mu = 11 \hbar\omega$  ( $\alpha \approx 0.29$ ), where the system goes from the BCS-type to the LOFF-type phase, as discussed above. The minimum that one observes for the BdG gap at  $\delta\mu \approx 10.8 \hbar\omega$  and the subsequent enhancement are due to shell effects which still persist even in this large system and which cannot be reproduced by the semiclassical LDA calculation.

In Fig. 2 we plot the radial profile of the pairing field  $\Delta(r)$  for  $\delta\mu = 12 \hbar\omega$ , corresponding to  $\alpha \approx 0.3$ , at  $T=0$ . The microscopic (solid line) and the LDA (dashed line) results are shown. Within LDA, in this case, the LOFF phase is more favorable than BCS for all values of  $r$ . We observe in Fig. 2 that the LDA gap goes abruptly to zero at a radius of  $\sim 2 l_{ho}$ ,

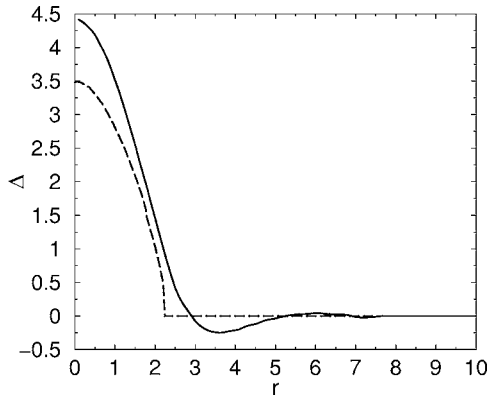


FIG. 2. Radial profile of the pairing gap  $\Delta(r)$  (in units of  $\hbar\omega$ ) for  $\delta\mu=12 \hbar\omega$ . The radial coordinate  $r$  is expressed in units of  $l_{ho}$ . The microscopic (solid line) and the LDA (dashed line) results are plotted.

which is smaller than the LDA wavelength of  $\sim 6.2 l_{ho}$ . Thus, the region where the gap is nonzero does not even contain one wavelength of the oscillation and therefore the validity of LDA seems to be very questionable. As expected from the symmetric case [16], the LDA fails to describe the tail of the pairing field: The LDA gap goes abruptly to zero while in the microscopic case the gap has a smooth profile. We finally observe that the microscopic order parameter makes an oscillation and that a node is situated at  $\approx 3 l_{ho}$ : The modulation of the order parameter and the presence of a node are signals which indicate that the system is in a LOFF-type phase.

Let us consider now the case of a smaller asymmetry,  $\delta\mu=6 \hbar\omega$ , corresponding to  $\alpha \approx 0.15$ . We show in Fig. 3 the radial profiles of the gap  $\Delta(r)$  (top) and of the densities (bottom) at  $T=0$ . In the upper panel we report the microscopic (BdG) gap (solid line) and the LDA result (dashed line). In this case, according to the LDA, the BCS phase ( $q=0$ ) would be energetically preferred in the center of the gas (as we have shown in Fig. 1) and up to  $r=3.8 l_{ho}$ , while the LOFF phase with  $q \sim 0.7 l_{ho}^{-1}$  would be more favorable in the interval

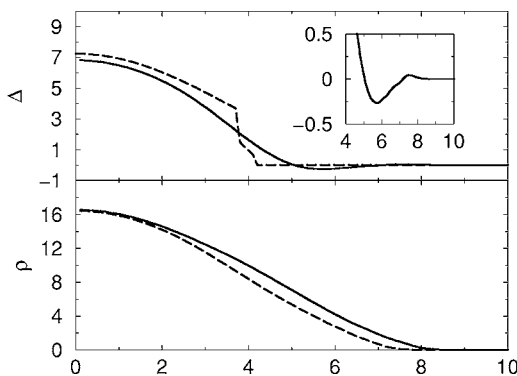


FIG. 3. Radial profiles of the pairing gap  $\Delta(r)$  in units of  $\hbar\omega$  (top) and of the densities in units of  $l_{ho}^{-3}$  (bottom) for  $\delta\mu=6 \hbar\omega$  as a function of the radial coordinate  $r$  in units of  $l_{ho}$ . In the upper panel the solid and dashed lines correspond to the BdG and LDA results, respectively. In the lower panel, the solid and the dashed lines refer to the BdG results for the + and - densities, respectively.

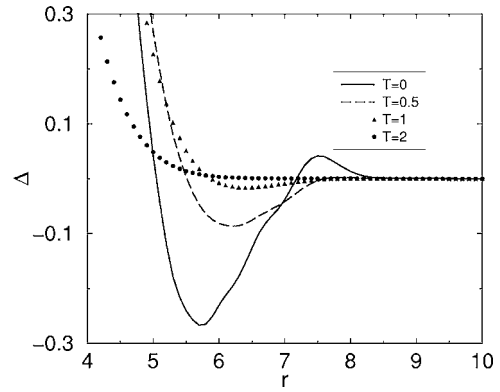


FIG. 4. Radial profile of the pairing gap  $\Delta(r)$  (in units of  $\hbar\omega$ ) for  $\delta\mu=6 \hbar\omega$ . The radial coordinate  $r$  is expressed in units of  $l_{ho}$ . Results at  $T=0$  (solid line),  $T=0.5 \hbar\omega/k_B$  (dashed line),  $T=\hbar\omega/k_B$  (triangles), and  $T=2 \hbar\omega/k_B$  (circles) are reported.

$3.8 l_{ho} < r < 4.1 l_{ho}$ . For larger values of  $r$ , the LDA predicts that the gap should be zero. The wavelength of the oscillation of the order parameter in the LOFF phase ( $\sim 8.9 l_{ho}$ ) would again be much larger than the region where the gap is nonzero. Contrary to the LDA, the microscopic BdG calculation gives a smooth behavior of the order parameter. Near the center, it corresponds rather well to the LDA prediction, indicating that the pairing is more or less of BCS type. Between  $r=4 l_{ho}$  and  $10 l_{ho}$ , the gap is oscillating (see inset in the upper panel of Fig. 3), indicating the appearance of the LOFF-type phase. Although within the BdG calculation there is no sharp transition from one phase to the other, qualitatively it seems that both phases can be present at the same time in different regions of the system.

In the lower panel of Fig. 3 the BdG results for the two densities ( $\rho_+$  and  $\rho_-$ ) are shown. One observes that in the center of the gas the two densities are equal. This is coherent with the fact that in the BCS phase at  $T=0$  the LDA always gives  $\rho_+ = \rho_-$  if  $\Delta > \delta\mu/2$ , as is the case here.

All the results shown so far refer to  $T=0$ . However, in real experiments with trapped atomic gases the temperature is always nonzero. Let us therefore raise the temperature in the case of asymmetry  $\delta\mu=6 \hbar\omega$  in order to analyze what happens to the gap modulation when the temperature is finite. In Fig. 4 we show the order parameter in the radial interval from  $4 l_{ho}$  to  $10 l_{ho}$  (where we observed an oscillation in the case  $T=0$ ) for four values of temperature,  $T=0$  (solid line),  $T=0.5 \hbar\omega/k_B$  (dashed line),  $T=\hbar\omega/k_B$  (triangles), and  $T=2 \hbar\omega/k_B$  (circles). One observes that the oscillation has a smaller and smaller amplitude with increasing temperature and that it disappears between  $T=\hbar\omega/k_B$  and  $T=2 \hbar\omega/k_B$ . Our interpretation of this result is that the critical temperature of the LOFF-type phase is smaller than the BCS critical temperature. Therefore, the LOFF-type phase disappears at some temperature between  $\hbar\omega/k_B$  and  $2 \hbar\omega/k_B$ , while the BCS gap in the central region of the gas is still different from zero at  $T=2 \hbar\omega/k_B$ . In this case the LDA results (not shown) are very different from the BdG ones (the gap is much too large), as one could expect from the fact that already in the symmetric case the agreement between LDA and BdG calculations becomes quite poor at finite temperature [16]. Nev-

ertheless, qualitatively the LDA gives again the right indication: Also within LDA the LOFF phase is absent at  $T=2 \hbar\omega/k_B$ . Instead, at that temperature the Sarma phase becomes more favorable in certain regions within the LDA: This phase is characterized by zero momentum Cooper pairs, a gap  $\Delta$  smaller than  $\delta\mu/2$ , different densities  $\rho_+$  and  $\rho_-$  and typical occupation number distributions as shown in Ref. [6].

To summarize, we have solved the BdG equations for an atomic Fermi gas with different populations of two hyperfine states. It is well known that an increasing asymmetry of the populations renders BCS pairing difficult, and nonstandard pairing mechanisms become possible. In this article we showed that the BdG formalism automatically includes such nonstandard pairing mechanisms through the nondiagonal matrix elements of the gap. For example, in the case of a small system, we found that the usual pairing disappears at a certain asymmetry, but when the asymmetry is strong enough such that the single-particle energies of states with opposite spin and different principal quantum numbers start to match, pairing becomes again possible, but now with an oscillating order parameter. This is very similar to the LOFF phase in-

roduced for the case of a homogeneous system. In the case of a larger system, there is no longer a sharp separation between the BCS pairing and the LOFF-type pairing: As a function of asymmetry, but also as a function of the distance from the center of the trap, the system undergoes smooth transitions from one kind of pairing to the other. This result is qualitatively different from that obtained with LDA calculations, where the transition between the BCS and the LOFF phase is a first order phase transition. We also observe that even a system containing 17000 atoms is still much too small for the LDA to be applicable, since the wavelength of the LOFF oscillations is of the same order of magnitude as the whole system. Finally we looked at the temperature dependence of the LOFF-type phase. We observe that it disappears already at temperatures where the BCS phase is still present. This, of course, can be a problem if one tries to observe the LOFF phase in experiments.

We acknowledge discussions with M. Baldo, F. Cataliotti, and A. Sedrakian.

- 
- [1] B. De Marco and D. S. Jin, *Science* **285**, 285 (1999); M. Greiner, C. A. Regal, and D. S. Jin, *Nature (London)* **426**, 537 (2003); M. W. Zwierlein *et al.*, *Phys. Rev. Lett.* **91**, 250401 (2003); C. A. Regal, M. Greiner, and D. S. Jin, *Phys. Rev. Lett.* **92**, 040403 (2004); M. W. Zwierlein *et al.*, *Phys. Rev. Lett.* **92**, 120403 (2004); M. Bartenstein *et al.*, *Phys. Rev. Lett.* **92**, 120401 (2004); T. Bourdel *et al.*, *Phys. Rev. Lett.* **93**, 050401 (2004).
- [2] J. Kinast, S. L. Hemmer, M. E. Gehm, A. Turlapov, and J. E. Thomas, *Phys. Rev. Lett.* **92**, 150402 (2004); C. Chin *et al.*, *Science* **305**, 1128 (2004).
- [3] M. W. Zwierlein *et al.*, *Phys. Rev. Lett.* **91**, 250404 (2003).
- [4] M. Houbiers *et al.*, *Phys. Rev. A* **56**, 4864 (1997).
- [5] R. Combescot and C. Mora, *Europhys. Lett.* **68**, 79 (2004).
- [6] W. V. Liu and F. Wilczek, *Phys. Rev. Lett.* **90**, 047002 (2003).
- [7] P. F. Bedaque, H. Caldas, and G. Rupak, *Phys. Rev. Lett.* **91**, 247002 (2003); J. Carlson and Sanjay Reddy, *cond-mat/0503256*.
- [8] A. Sedrakian *et al.*, *cond-mat/0404577*.
- [9] P. Fulde and R. A. Ferrel, *Phys. Rev.* **135**, A550 (1964); A. I. Larkin and Yu. N. Ovchinnikov, *Sov. Phys. JETP* **20**, 762 (1965).
- [10] G. Sarma, *J. Phys. Chem. Solids Suppl.* **24**, 1029 (1963).
- [11] A. Sedrakian and U. Lombardo, *Phys. Rev. Lett.* **84**, 602 (2000).
- [12] J. A. Bowers and K. Rajagopal, *Phys. Rev. D* **66**, 065002 (2002); I. Shovkovy and M. Huang, *Phys. Lett. B* **564**, 205 (2003); R. Casalbuoni and G. Nardulli, *Rev. Mod. Phys.* **76**, 263 (2004).
- [13] T. Kontos, M. Aprili, J. Lesueur, and X. Grison, *Phys. Rev. Lett.* **86**, 304 (2001).
- [14] P.-G. de Gennes, *Superconductivity of Metals and Alloys* (Benjamin, New York, 1966).
- [15] T. Mizushima, K. Machida, and M. Ichioka, *Phys. Rev. Lett.* **94**, 060404 (2005).
- [16] M. Grasso and M. Urban, *Phys. Rev. A* **68**, 033610 (2003).
- [17] Note, however, that this analogy between the trapped and the homogeneous system is not perfect, since in the trapped system with  $\delta\mu \neq 0$  even pairing between states  $|n, l, m, +\rangle$  and  $|n, l, -m, -\rangle$  includes pairing of states with different wave functions due to the different mean fields felt by atoms with different spin projections.

## 4.4 Les états excités dans les gaz superfluides

Des modes collectifs appelés modes de respiration sont observés dans les gaz atomiques [Ki04a, Ki04b]. Nous avons réalisé une étude microscopique basée sur la QRPA à température finie [Br01] pour analyser les propriétés de ces modes d'excitation et décrire leur évolution autour de la température critique. Cette analyse est présentée dans l'article qui suit [Gr05b].

## Temperature dependence and finite-size effects in collective modes of superfluid-trapped Fermi gases

M. Grasso,<sup>1,2</sup> E. Khan,<sup>2</sup> and M. Urban<sup>2</sup><sup>1</sup>*Dipartimento di Fisica ed Astronomia and INFN, Via Santa Sofia 64, I-95123 Catania, Italy*<sup>2</sup>*Institut de Physique Nucléaire, Université Paris-Sud, IN2P3-CNRS, 91406 Orsay Cedex, France*

(Received 29 July 2005; published 26 October 2005)

We discuss collective monopole and quadrupole excitations of a collisionless gas of trapped Fermionic atoms in the superfluid BCS phase, comparing the fully microscopic Bogoliubov–de Gennes and quasiparticle random-phase approximation method with widely used semiclassical methods. In particular, the microscopic treatment allows us to address the questions of temperature dependence and nontrivial dependence on the trap parameters, which cannot be answered within the semiclassical approach. The main result concerning the temperature dependence is a strong Landau damping at intermediate temperature, which disappears in the limits of zero and critical temperature. However, even at zero temperature, considerable deviations from superfluid hydrodynamics are found if the trap frequency is of the same order of magnitude as the pairing gap.

DOI: [10.1103/PhysRevA.72.043617](https://doi.org/10.1103/PhysRevA.72.043617)

PACS number(s): 03.75.Ss, 21.60.Jz

### I. INTRODUCTION

Dilute gases of alkaline-metal Fermionic and Bosonic atoms are superfluid at very low temperature: Bose-Einstein condensates (BEC's) have been obtained in the case of Bosonic atoms [1], while condensation of molecules (made out of two atoms) has been observed in the case of Fermionic atoms [2]. For Fermionic atoms in the weakly interacting regime ( $k_F|a| \ll 1$ , where  $k_F$  is the Fermi momentum and  $a$  is the  $s$ -wave scattering length) BCS superfluidity is expected in the case of attractive interatomic interaction ( $a < 0$ ).

A striking experimental evidence for BCS superfluidity is still missing, even though various signals which would be coherent with a superfluid behavior have been observed in some experiments: the anisotropic expansion of the gas after releasing it from the trap [3], the measurement of the gap [4], the measurement of the frequencies and damping rates of the breathing modes [5,6].

However, the gap has been actually measured only in the strongly interacting regime and no experimental values exist for the weakly interacting case. The anisotropic expansion on the one hand and the frequencies of the breathing modes on the other hand can be predicted within a hydrodynamic approach for a superfluid gas [7–9]. In both cases the experimental observations agree very well with the hydrodynamic predictions, and this could actually be considered as an evidence for superfluidity. However, the predictions for a superfluid gas are the same as those for a normal gas in the presence of collisions. It is true that at the very low temperatures achieved in these experiments the Pauli principle is expected to inhibit collisions. However, the experimental measurements have been performed during the expansion of the gas after releasing it from the trap. In such a situation momentum space deformations are possible and collisions can survive even at very low temperatures. So far, it has not been possible to completely control this problem from an experimental point of view and, for this reason, no firm conclusions about superfluidity can actually be drawn.

Another limitation is related to the hydrodynamic approach: hydrodynamics can be safely applied only within the

limits of validity of semiclassical approaches,  $\Delta \gg \hbar\Omega$ , where  $\Delta$  is the pairing gap and  $\Omega$  is the trapping frequency. Effects from the finite size and inhomogeneity, governed by the finite trap frequency  $\Omega$ , are neglected. Moreover, the hydrodynamic formalism has been developed so far only for the case of zero temperature ( $T=0$ ).

In this paper we deal with the excitation spectra in the normal and superfluid phases of a dilute Fermi gas and we analyze how these spectra are affected by superfluidity, both in hydrodynamic and microscopic descriptions. In order to study excitations similar to those observed experimentally (the breathing modes) we focused our attention on the monopole and quadrupole modes. However, while the breathing modes have been observed for a cigar-shaped gas (and the radial and axial frequencies have been measured), we restrict our analysis to a spherical gas for the sake of numerical tractability. Moreover, while the experiments of Refs. [5,6] have been done for strongly interacting gases, we treat a weakly interacting system.

We analyze the excitation spectra within a finite-temperature mean-field approach which provides a microscopic treatment for the system. The Bogoliubov–de Gennes (BdG) equations [10] are solved for the ground state and the excitations are treated within the quasiparticle random-phase approximation (QRPA) [11]. This approach has already been developed for atomic Fermi gases in Ref. [12], where the spin-dipole and the quadrupole modes have been analyzed. On the other hand, the monopole modes have already been studied and compared to a schematic model in Ref. [13].

In the present work we want to study systematically the effects related to the temperature and to the trap frequency of the system. In particular, we compare our results with the corresponding hydrodynamic ones in order to check the validity of the semiclassical approach. In addition to the strength distributions related to the excitation spectra, we also present the transition densities which can give important information on nature of the collective modes.

The paper is organized as follows. In Sec. II we briefly sketch the quantum-mechanical and semiclassical formal-

isms to describe collective modes in the superfluid phase and in the normal phase in the collisionless limit. In Sec. III results for the monopole and quadrupole excitations are shown: the dependence on the temperature and on the frequency of the trap are studied. In Sec. IV we draw our conclusions.

## II. QUANTUM-MECHANICAL AND SEMICLASSICAL FORMALISM

In this section we will briefly review the theoretical description of collective modes in trapped Fermi gases. As already mentioned in the introduction, one has to distinguish between quantum-mechanical (“microscopic”) and semiclassical approaches. The fully quantum-mechanical calculation consists in solving the QRPA equations, which are the small-amplitude limit of the time-dependent BdG equations. At present such calculations are available only for systems containing up to  $\sim 10^4$  atoms in the case of a spherically symmetric trap. These conditions are quite far from the experimental ones, corresponding to particle numbers of  $\sim 10^5$ – $10^6$  particles in a cigar-shaped trap. Up to now, the “realistic” conditions can only be treated within semiclassical approaches. The simplest semiclassical approach is the hydrodynamic theory. This theory is valid in the superfluid phase at zero temperature, since the pairing correlations keep the Fermi surface spherical during the collective motion of the system. However, hydrodynamics fails at nonzero temperature, unless the local equilibrium can be ensured by collisions. Since we are interested in the weakly interacting regime, the collision rate  $1/\tau$  is very small compared to the frequency of the trap. In this “collisionless” regime, the Fermi surface becomes locally deformed during the collective oscillation. This cannot be described by hydrodynamics, but requires a description in the framework of the Vlasov equation. The latter is valid in the normal phase, i.e., above the critical temperature  $T_c$ . In the intermediate temperature range  $0 < T < T_c$ , a semiclassical theory is still missing.

### A. Quantum-mechanical formalism (QRPA)

The QRPA method has already been applied to trapped Fermi gases in the weakly [12] as well as in the strongly interacting regime [14] and here we will only give a short summary.

We consider a gas of atoms with mass  $m$  in a spherical harmonic trap with frequency  $\Omega$ , assuming that the atoms equally occupy two hyperfine states  $\sigma = \uparrow, \downarrow$ . Because of the low temperature and density of the gas, the interaction between the atoms can be chosen as a zero-range interaction and parametrized by the  $s$ -wave atom-atom scattering length  $a$ . In order to simplify the notation, we will express all quantities in harmonic oscillator (HO) units, i.e., frequencies in units of  $\Omega$ , energies in units of  $\hbar\Omega$ , temperatures in units of  $\hbar\Omega/k_B$ , and lengths in units of the oscillator length  $l_{HO} = \sqrt{\hbar/(m\Omega)}$ . Furthermore, instead of the scattering length we will use the coupling constant  $g = 4\pi a/l_{HO}$  as parameter of the interaction strength.

As mentioned above, the QRPA describes small-amplitude oscillations around the equilibrium state within the BdG formalism. Therefore the first step consists in solving the BdG equations [10]

$$[H_0 + W(r)]u_{nlm}(\mathbf{r}) + \Delta(r)v_{nlm}(\mathbf{r}) = E_{nl}u_{nlm}(\mathbf{r}),$$

$$\Delta(r)u_{nlm}(\mathbf{r}) - [H_0 + W(r)]v_{nlm}(\mathbf{r}) = E_{nl}v_{nlm}(\mathbf{r}) \quad (1)$$

for the static case. In this way we obtain a set of quasiparticle energies  $E_{nl}$  and wave functions  $u_{nlm}$  and  $v_{nlm}$ . In Eq. (1),  $H_0$  denotes the Hamiltonian of the noninteracting HO minus the chemical potential  $\mu$ ,

$$H_0 = \frac{1}{2}(-\nabla^2 + r^2) - \mu, \quad (2)$$

while the interaction is accounted for in a self-consistent way through the Hartree potential  $W$  and the pairing field  $\Delta$ . Due to spherical symmetry, the wave functions can be written as

$$u_{nlm}(\mathbf{r}) = u_{nl}(r)Y_{lm}(\theta, \phi), \quad (3)$$

$$v_{nlm}(\mathbf{r}) = v_{nl}(r)Y_{lm}(\theta, \phi). \quad (4)$$

The quantum numbers  $l$  and  $m$  are the angular momentum and its projection, while  $n$  numbers different states having the same  $l$  and  $m$ . In practice, the diagonalization of Eq. (1) is done in a truncated harmonic oscillator basis, containing the eigenfunctions of the trapping potential up to a certain HO energy  $E_C = N_C + \frac{3}{2}$ , i.e.,

$$2(n-1) + l \leq N_C. \quad (5)$$

The self-consistency relates  $W$  and  $\Delta$  to the wave functions  $u$  and  $v$ . The mean field  $W$  is just proportional to the density, i.e.,

$$W(\mathbf{r}) = g \sum_{nl}^{N_C} \frac{2l+1}{4\pi} \{v_{nl}^2(r)[1 - f(E_{nl})] + u_{nl}(r)f(E_{nl})\}, \quad (6)$$

where

$$f(E) = \frac{1}{e^{E/T} + 1} \quad (7)$$

denotes the Fermi function. The Hartree field is independent of the cutoff  $N_C$  if the latter is taken sufficiently large. The calculation of the pairing field  $\Delta$ , however, is more complicated. The zero-range interaction leads to a divergence which in the case of uniform systems can be regularized in a standard way by renormalizing the scattering length. This regularization method has been generalized to the case of trapped systems by Bruun *et al.* [15] and developed further by Bulgac and Yu [16] and two of the authors [17]. As a result, the pairing field can be written as

$$\Delta(\mathbf{r}) = -g_{eff}(r) \sum_{nl}^{N_C} \frac{2l+1}{4\pi} u_{nl}(r)v_{nl}(r)[1 - 2f(E_{nl})], \quad (8)$$

with an effective coupling constant  $g_{eff}$  which allows to include the contribution from states beyond the cutoff  $N_C$  within the Thomas-Fermi approximation (TFA). The explicit expression for  $g_{eff}$  reads

$$\frac{1}{g_{\text{eff}}(r)} = \frac{1}{g} + \frac{1}{2\pi^2} \left( \frac{k_F(r)}{2} \ln \frac{k_C(r) + k_F(r)}{k_C(r) - k_F(r)} - k_C(r) \right), \quad (9)$$

where  $k_F$  and  $k_C$  denote the local Fermi and cutoff momenta, respectively:

$$k_F(r) = \sqrt{2\mu - r^2 - 2W(r)}, \quad (10)$$

$$k_C(r) = \sqrt{2N_C + 3 - r^2}. \quad (11)$$

Once the static BdG equations are solved, we can calculate the linear response of the system to a small time-dependent perturbation. Following Ref. [12], we have to compute the QRPA response function  $\Pi$ , which is a  $4 \times 4$  matrix built out of 16 correlation functions:

$$\Pi(\omega, \mathbf{r}, \mathbf{r}') = \begin{pmatrix} \langle\langle \hat{\rho}_\uparrow \hat{\rho}_\uparrow \rangle\rangle & \langle\langle \hat{\rho}_\uparrow \hat{\rho}_\downarrow \rangle\rangle & \langle\langle \hat{\rho}_\uparrow \hat{\chi} \rangle\rangle & \langle\langle \hat{\rho}_\uparrow \hat{\chi}^\dagger \rangle\rangle \\ \langle\langle \hat{\rho}_\downarrow \hat{\rho}_\uparrow \rangle\rangle & \langle\langle \hat{\rho}_\downarrow \hat{\rho}_\downarrow \rangle\rangle & \langle\langle \hat{\rho}_\downarrow \hat{\chi} \rangle\rangle & \langle\langle \hat{\rho}_\downarrow \hat{\chi}^\dagger \rangle\rangle \\ \langle\langle \hat{\chi} \hat{\rho}_\uparrow \rangle\rangle & \langle\langle \hat{\chi} \hat{\rho}_\downarrow \rangle\rangle & \langle\langle \hat{\chi} \hat{\chi} \rangle\rangle & \langle\langle \hat{\chi} \hat{\chi}^\dagger \rangle\rangle \\ \langle\langle \hat{\chi}^\dagger \hat{\rho}_\uparrow \rangle\rangle & \langle\langle \hat{\chi}^\dagger \hat{\rho}_\downarrow \rangle\rangle & \langle\langle \hat{\chi}^\dagger \hat{\chi} \rangle\rangle & \langle\langle \hat{\chi}^\dagger \hat{\chi}^\dagger \rangle\rangle \end{pmatrix}, \quad (12)$$

with the shorthand notation

$$\langle\langle \hat{A} \hat{B} \rangle\rangle = -i \int_0^\infty \frac{dt}{2\pi} e^{i\omega t} \langle [\hat{A}(t, \mathbf{r}), \hat{B}(0, \mathbf{r}')] \rangle, \quad (13)$$

where  $\langle \rangle$  means the thermal average. The operators of the normal and anomalous densities,  $\hat{\rho}$  and  $\hat{\chi}$ , are defined in terms of the field operators  $\hat{\psi}$  and  $\hat{\psi}^\dagger$  as follows:

$$\hat{\rho}_\sigma(t, \mathbf{r}) = \hat{\psi}_\sigma^\dagger(t, \mathbf{r}) \hat{\psi}_\sigma(t, \mathbf{r}), \quad (14)$$

$$\hat{\chi}(t, \mathbf{r}) = \hat{\psi}_\uparrow(t, \mathbf{r}) \hat{\psi}_\downarrow(t, \mathbf{r}). \quad (15)$$

In order to obtain  $\Pi$ , we first compute the free or unperturbed response function  $\Pi_0$ , which is defined analogously to Eq. (12), but which does not include the effect of interactions between the quasiparticles. Thus  $\Pi_0$  can be obtained by replacing the field operators  $\hat{\psi}$  in Eqs. (14) and (15) by

$$\hat{\psi}_\sigma(t, \mathbf{r}) = \sum_{nlm} [b_{nlm\sigma} u_{nlm}(\mathbf{r}) e^{iE_{nl}t} - \sigma b_{nlm-\sigma}^* v_{nlm}^*(\mathbf{r}) e^{-iE_{nl}t}], \quad (16)$$

where  $\hat{b}$  and  $\hat{b}^\dagger$  are annihilation and creation operators of noninteracting quasiparticles. Inserting the resulting expressions into Eq. (12) and using the relations  $\{b_\alpha, b_\beta\} = \{b_\alpha^\dagger, b_\beta^\dagger\} = 0$ ,  $\{b_\alpha, b_\beta^\dagger\} = \delta_{\alpha\beta} [1 - f(E_\alpha)]$ , and  $\langle b_\alpha^\dagger b_\beta \rangle = f(E_\alpha) \delta_{\alpha\beta}$ , we obtain explicit expressions for the 16 functions contained in  $\Pi_0$  in terms of the  $u$  and  $v$  functions and the quasiparticle energies obtained from Eq. (1).

Due to the spherical symmetry of the trap and the rotational invariance of the interaction, excitations with different angular momenta do not mix. Therefore it is useful to decompose  $\Pi_0$  into contributions of different angular momenta:

$$\Pi_0(\omega, \mathbf{r}, \mathbf{r}') = \sum_{LM} \Pi_{0L}(\omega, r, r') Y_{LM}(\theta, \phi) Y_{LM}^*(\theta', \phi'). \quad (17)$$

The QRPA response  $\Pi_L$  for angular momentum  $L$  can now be obtained from the quasiparticle response  $\Pi_{0L}$  by solving the Bethe-Salpeter integral equation

$$\begin{aligned} \Pi_L(\omega, r, r') &= \Pi_{0L}(\omega, r, r') \\ &+ \int_0^\infty dr'' r''^2 \Pi_{0L}(\omega, r, r'') G \Pi_L(\omega, r'', r'), \end{aligned} \quad (18)$$

where  $G$  accounts for the residual interaction between the quasiparticles:

$$G = \begin{pmatrix} 0 & g & 0 & 0 \\ g & 0 & 0 & 0 \\ 0 & 0 & 0 & g \\ 0 & 0 & g & 0 \end{pmatrix}. \quad (19)$$

When calculating the 16 functions contained in  $\Pi_{0L}$ , one observes that two of them, namely those related to  $\langle\langle \hat{\chi}^\dagger \hat{\chi} \rangle\rangle$  and  $\langle\langle \hat{\chi} \hat{\chi}^\dagger \rangle\rangle$ , are divergent for  $N_C \rightarrow \infty$ . This divergence has the same origin as that of the pairing field. Bruun and Motelson [12] therefore suggested to use the same pseudopotential method as for the regularization of the pairing field in order to remove the divergence. However, it is not clear how in their prescription, Eq. (7) in Ref. [12], the contribution of states beyond the cutoff  $N_C$  can be approximated (as we did in the case of the pairing field by using the TFA), which is crucial for having convergence at reasonable values of the cutoff  $N_C$ . We therefore propose a simplified prescription: when calculating  $\Pi_{0L}$ , we have to restrict the sum to states below the cutoff,  $2(n-1) + l \leq N_C$ . To compensate the resulting cutoff dependence, the interaction in the pairing channel must be replaced by the effective coupling constant given in Eq. (9). Thus we replace  $G$  in Eq. (18) by  $G_{\text{eff}}(r'')$ , which is defined by

$$G_{\text{eff}}(r) = \begin{pmatrix} 0 & g & 0 & 0 \\ g & 0 & 0 & 0 \\ 0 & 0 & 0 & g_{\text{eff}}(r) \\ 0 & 0 & g_{\text{eff}}(r) & 0 \end{pmatrix}. \quad (20)$$

One can show that, in the case of a uniform system, this simplified prescription coincides with the pseudopotential method in the limit of excitations with long wavelengths and low frequencies. We have checked the convergence of the results using this regularization prescription.

Finally, we have to say how physical quantities of interest can be extracted from the correlation function  $\Pi$ . To that end it is useful to look at the spectral representation

$$\sum_{\sigma\sigma'} \langle\langle \hat{\rho}_\sigma \hat{\rho}_{\sigma'} \rangle\rangle = \int d\omega' \frac{S(\omega', \mathbf{r}, \mathbf{r}')}{\omega - \omega' + i\epsilon}, \quad (21)$$

(17) with

$$S(\omega, \mathbf{r}, \mathbf{r}') = -\frac{1}{\pi} \sum_{\sigma\sigma'} \text{Im} \langle \langle \hat{\rho}_{\sigma} \hat{\rho}_{\sigma'} \rangle \rangle = (1 - e^{-\omega/T}) \sum_{ij} \frac{e^{-E_j/T}}{Z} \delta(\omega - E_j + E_i) \times \sum_{\sigma\sigma'} \langle i | \hat{\rho}_{\sigma}(\mathbf{r}) | j \rangle \langle j | \hat{\rho}_{\sigma'}(\mathbf{r}') | i \rangle, \quad (22)$$

where  $|i\rangle$  and  $|j\rangle$  are eigenstates of the many-body Hamiltonian with total energies  $E_i$  and  $E_j$ , respectively, and  $Z = \sum_i \exp(E_i/T)$ . In the present QRPA formalism Eq. (22) is evaluated using the four upper left elements of the  $\Pi$  response function (12), obtained with Eq. (18).

In this paper we will consider excitation operators of the form

$$V_1(t, \mathbf{r}) \propto r^2 Y_{LM}(\theta, \phi) e^{-i\omega t}, \quad (23)$$

with  $L=0$  (monopole excitations) and  $L=2$  (quadrupole excitations). The corresponding strength function  $S_L(\omega)$ , which gives the excitation spectrum, is defined by

$$S_L(\omega) = \int_0^\infty dr r^4 \int_0^\infty dr' r'^4 \sum_{\sigma\sigma'} S_L(\omega, r, r'). \quad (24)$$

Another interesting quantity is the transition density  $\delta\rho = \rho - \rho_0$ , where  $\rho_0$  denotes the density in equilibrium and  $\rho$  is the density of the excited system. In the case of zero temperature, where the stationary system is in the ground state  $|0\rangle$ , the transition density for  $\omega = E_j - E_0$  is proportional to

$$\delta\rho(\omega = E_j - E_0, \mathbf{r}) \propto \sum_{\sigma} \langle j | \hat{\rho}_{\sigma}(\mathbf{r}) | 0 \rangle. \quad (25)$$

In this case, the sum over  $i$  in Eq. (22) reduces to one term ( $i=0$ ), and therefore the transition density can be obtained from

$$[\delta\rho(\omega = E_j - E_0, \mathbf{r})]^2 \propto \int_{\omega-\delta}^{\omega+\delta} d\omega' S(\omega', \mathbf{r}, \mathbf{r}), \quad (26)$$

where  $\delta$  is supposed to be sufficiently small to avoid that other states than the selected one ( $|j\rangle$ ) contribute.

## B. Superfluid hydrodynamics

At zero temperature, superfluid hydrodynamics provides the equations of motion for the density (per spin state)  $\rho(t, \mathbf{r})$  and the irrotational collective velocity field  $\mathbf{v}(t, \mathbf{r})$  of the superfluid current (continuity and Euler equations) [18]:

$$\dot{\rho} + \nabla \cdot (\rho \mathbf{v}) = 0, \quad (27)$$

$$\dot{\mathbf{v}} = -\nabla \left( \frac{\mathbf{v}^2}{2} + \frac{V_{ext}}{m} + \frac{\mu_{loc}}{m} \right). \quad (28)$$

These equations can equally be used for Fermionic and Bosonic systems, only the equation of state, relating the local chemical potential  $\mu_{loc}$  to the density  $\rho$ , must be adapted correspondingly. In the case of weakly interacting fermions, where the density can be regarded as independent of the pairing gap, this equation of state is given by the Thomas-Fermi relation

$$\mu_{loc}(\rho) = \frac{p_F^2}{2m} + g\rho = \frac{\hbar^2 (6\pi^2 \rho)^{2/3}}{2m} + g\rho. \quad (29)$$

In the static (equilibrium) case, Eq. (28) together with this equation of state gives immediately the usual Thomas-Fermi equation for the density profile  $\rho_0(\mathbf{r})$ ,

$$\mu_{loc}[\rho_0(\mathbf{r})] + V_0(\mathbf{r}) = \mu, \quad (30)$$

which is valid in both the normal and the superfluid phase. While the TFA in the normal phase is valid if  $\mu_{loc}$  is much larger than the discrete level spacing of the trapped system ( $\hbar\Omega$  in our case), superfluid hydrodynamics requires in addition that also the pairing gap  $\Delta$  is large compared with the level spacing, which is much more difficult to satisfy.

Since the superfluid velocity field  $\mathbf{v}$  is irrotational, it can be written as a gradient. In order to establish a connection with microscopic quantities, we write it in the form

$$\mathbf{v}(\mathbf{r}) = \frac{\hbar}{m} \nabla \varphi(\mathbf{r}), \quad (31)$$

where  $\varphi$  is related to the phase of the pairing field by  $\Delta(\mathbf{r}) = |\Delta(\mathbf{r})| \exp[2i\varphi(\mathbf{r})]$ .

In this paper we are interested in small-amplitude motion. We therefore split the density and the external potential into their equilibrium values and small deviations,  $\rho = \rho_0 + \delta\rho$  and  $V_{ext} = V_0 + V_1$ , and expand Eqs. (27) and (28) up to linear order in the deviations. In addition, as we did in the preceding subsection, we will specialize to the case of a spherically symmetric harmonic trap and use the corresponding HO units ( $\hbar = m = \Omega = 1$ ), i.e.,  $V_0 = r^2/2$ . We know that for an excitation of the type (23) the solution must be of the form

$$\varphi(t, \mathbf{r}) = \varphi(r) Y_{LM}(\theta, \phi) \exp(-i\omega t) \quad (32)$$

and analogous for  $\delta\rho$ . Furthermore, we are interested in the eigenmodes of the system, which persist even if  $V_1=0$ . Then Eqs. (27) and (28) can be transformed into an eigenvalue equation for the eigenfrequencies  $\omega$  and the corresponding eigenfunctions  $\varphi(r)$ ,

$$\frac{d\mu_{loc}}{d\rho} \bigg|_{\rho_0} \left( \frac{1}{r^2} (r^2 \rho_0 \varphi')' - L(L+1)\varphi \right) = -\omega^2 \varphi, \quad (33)$$

where  $f'$  means  $df/dr$ , and an equation for the transition density,

$$\delta\rho = -i\omega \left( \frac{d\mu_{loc}}{d\rho} \bigg|_{\rho_0} \right)^{-1} \varphi = \frac{-i\omega}{r} \rho_0' \varphi. \quad (34)$$

The numerical solution of Eq. (33) is not difficult. However, in the present paper we are only interested in the lowest monopole ( $L=0$ ) and quadrupole ( $L=2$ ) modes. For these two modes, the velocity field  $\mathbf{v}$  is practically linear in  $\mathbf{r}$ , and we can thus obtain a very accurate analytic approximation to the numerical solution. Let us start with the quadrupole mode ( $L=2$ ). We insert the ansatz  $\varphi \approx ar^2$  into Eq. (33), multiply the equation by  $\rho_0(r)$ , and integrate over  $d^3r$ . By this integration the small deviations of the quadratic ansatz from the exact solution of Eq. (33) are averaged out and one thus obtains a very precise prediction for the frequency. After a

lengthy calculation we reproduce the well-known result

$$\omega_{L=2} = \sqrt{2}, \quad (35)$$

which is independent of the interaction.

In a similar way we can find an approximation for the eigenfrequency of the lowest monopole mode ( $L=0$ ). In this case the function  $\varphi$  has the form  $\varphi(r) \approx a - br^2$ . Inserting this ansatz into Eq. (33), taking the derivative with respect to  $r$  in order to get rid of the constant  $a$ , multiplying by  $r$ , and proceeding in the same way as in the case of the quadrupole mode, we finally obtain

$$\omega_{L=0} = 2 \sqrt{1 + \frac{3E_{int}}{8E_{pot}}}, \quad (36)$$

where  $E_{int}$  and  $E_{pot}$  are the interaction and potential energies,

$$E_{int} = \int d^3r g \rho_0^2(\mathbf{r}), \quad E_{pot} = \int d^3r r^2 \rho_0(\mathbf{r}). \quad (37)$$

Contrary to the quadrupole frequency, the monopole frequency depends on the interaction. Since  $E_{int}$  is negative, the frequency  $\omega_{L=0}$  is slightly lower than twice the trap frequency,  $2\Omega$ . Finally, the ratio of the constants  $a$  and  $b$ , which is needed in order to compute the transition density  $\delta\rho$ , can be determined from the condition that the integral over  $\delta\rho$  must vanish, since the total number of particles stays constant.

### C. Vlasov description

Let us now consider a normal Fermi gas just above  $T_c$ . In the weakly interacting limit,  $T_c$  is very small as compared with the Fermi energy, i.e., except for the fact that the system is not superfluid, we can neglect temperature effects. We will also assume that the effect of collisions can be neglected. Under this condition the system cannot come to local equilibrium during the collective motion. In order to describe this effect, we will use the Wigner function  $f(t, \mathbf{r}, \mathbf{p})$ . In equilibrium and within the TFA, this function simply describes a Fermi sphere:

$$f_0(\mathbf{r}, \mathbf{p}) = \Theta(p_F(\mathbf{r}) - p). \quad (38)$$

Out of equilibrium, if the particles do not undergo enough collisions to restore the isotropic momentum distribution, the local Fermi surface will assume a more complicated shape. The equation of motion for the Wigner function is the Vlasov equation

$$\dot{f} = (\nabla V) \cdot (\nabla_p f) - \frac{\mathbf{p}}{m} \cdot (\nabla_r f), \quad (39)$$

where  $V(t, \mathbf{r}) = V_{ext}(t, \mathbf{r}) + g\rho(t, \mathbf{r})$  is the total (external + mean-field) potential and  $\nabla_r$  and  $\nabla_p$  are acting in coordinate and momentum space, respectively.

Contrary to the hydrodynamic equations in the superfluid phase, it is very difficult to solve the Vlasov equation directly. We are therefore again looking for approximate solutions for the special case of small-amplitude monopole and quadrupole oscillations in a spherical harmonic trap. We will

employ the ‘‘generalized scaling ansatz’’ [19], which has been used with great success to describe giant resonances in atomic nuclei and which has also been applied to trapped atomic Fermi gases [7]. In this approach, the possible deformations of the local Fermi surface are restricted to quadrupolar shape. Introducing a small displacement field  $\xi(t, \mathbf{r})$ , one can write

$$f(t, \mathbf{r}, \mathbf{p}) = f_0(\mathbf{r}', \mathbf{p}'), \quad (40)$$

with

$$\mathbf{r}' = \mathbf{r} - \xi(t, \mathbf{r}), \quad (41)$$

$$\mathbf{p}' = \mathbf{p} - m\dot{\xi}(t, \mathbf{r}) + \nabla_r[\mathbf{p} \cdot \xi(t, \mathbf{r})]. \quad (42)$$

The velocity field is then simply given by  $\mathbf{v} = \dot{\xi}$ , and the last term in Eq. (42) describes the deformation of the Fermi sphere. For the form of the velocity field we make the same ansatz as before, i.e.,

$$\xi(t, \mathbf{r}) = a \nabla r^2 Y_{LM}(\theta, \phi) e^{-i\omega t}, \quad (43)$$

with  $L=0$  (monopole mode) or  $L=2$  (quadrupole mode). In analogy to the procedure in the preceding subsection, we linearize the Vlasov equation (39) with respect to  $\xi$ , multiply by  $\mathbf{p} \cdot \xi^*$  and integrate over  $d^3p$  and  $d^3r$ . Using Eqs. (30) we reproduce after a tedious calculation the results originally derived in Ref. [7],

$$\omega_{L=0} = 2\Omega \sqrt{1 + \frac{3E_{kin}}{8E_{pot}}}, \quad \omega_{L=2} = 2\Omega \sqrt{1 - \frac{3E_{kin}}{4E_{pot}}}. \quad (44)$$

Note that the monopole mode has the same frequency in the normal phase as in the superfluid phase. This can be understood as follows. If the displacement field is purely radial ( $\xi \propto \mathbf{r}$ ), as it is the case for the monopole mode, one can see from Eq. (40) that the Fermi surface stays spherical. Therefore hydrodynamics gives the same frequency as the Vlasov equation. The frequency of the quadrupole mode in the normal phase, however, is higher than in the superfluid phase by a factor of approximately  $\sqrt{2}$ . From Eq. (40) one can see that in this case the Fermi surface gets a quadrupole deformation perpendicular to the deformation of the density profile in coordinate space. This deformation costs energy and therefore increases the frequency of the mode as compared to hydrodynamics.

### III. RESULTS

In this section we will compare QRPA and semiclassical results for monopole and quadrupole oscillations in a spherical trap. We are mainly interested in the limits of validity of superfluid hydrodynamics, since this theory is widely used in order to analyze experimental results. For instance, a recent experiment of the Innsbruck group showed that the axial breathing mode in a cigar-shaped trap follows the hydrodynamic behavior throughout the BCS-BEC crossover, while the radial breathing mode deviates considerably from the hydrodynamic predictions [6], especially on the BCS side of the crossover region. This contrasts a similar experiment at

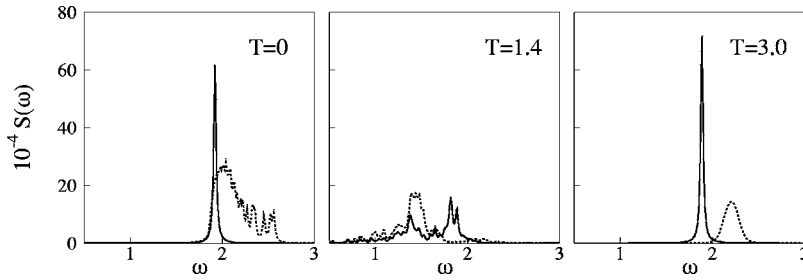


FIG. 1. Free quasiparticle response (dashed line) and QRPA response (solid line) of the monopole excitation as a function of the frequency  $\omega$  (in units of the trap frequency  $\Omega$ ), for three different temperatures:  $k_B T=0$ ,  $1.4\hbar\Omega$ , and  $3\hbar\Omega$  (from left to right).

Duke University [5], of course with different trap parameters, where the frequency of the radial breathing mode was in reasonable agreement with hydrodynamics. In both experiments the systems were still very strongly interacting even on the BCS side of the crossover (in the Innsbruck experiment, the strongest deviations happened when  $k_F|a|$  was of the order of 2), such that our weak-coupling theory (valid for  $k_F|a| \ll 1$ ) cannot directly be compared to these experiments. Nevertheless, it is clear that the limits of validity of hydrodynamics should be clarified.

It is known that hydrodynamics works at zero temperature and if the level spacing  $\hbar\Omega$  is much smaller than the gap  $\Delta$ , but both conditions are generally not fulfilled in the experiments. Since experiments cannot be done at zero temperature, it is interesting to see what kind of temperature effects can arise below the critical temperature  $T_c$ . The second condition is also very strong, especially if the trap is strongly deformed and the transverse trap frequency is large, and it is therefore important to know up to which ratio  $\hbar\Omega/\Delta$  hydrodynamics can be trusted.

### A. Temperature dependence

In this subsection we will study how the properties of collective modes change in the small temperature range from zero to the critical temperature  $T_c$ . For this investigation we are using the parameter set  $\mu=32\hbar\Omega$  and  $g=-0.965$  (in HO units). With these parameters, the number of particles is approximately 17 000 and the gap in the center of the trap at zero temperature is approximately  $6\hbar\Omega$ ; one can therefore expect that at least at zero temperature hydrodynamics should work very well.

In Figs. 1 and 2 we show the monopole and quadrupole response functions, respectively, for three different values of the temperature. The figures on the left show the response at zero temperature. The solid lines correspond to the QRPA results while the dashed lines represent the free quasiparticle response. In principle, the response function consists of a very large number of discrete levels. For the purpose of

graphical presentation, these delta functions must be smeared out, and we therefore introduce a small imaginary part of  $\epsilon = 0.015\Omega$  in the denominators of the correlation functions [see Eq. (22)]. For  $T=0$ , the QRPA quadrupole response shows one single collective peak whose frequency is very close to that predicted by hydrodynamics (see Table I). The QRPA response is completely different from the free quasiparticle response, which has a broad and almost continuous distribution of strength between  $\sim 1.8\Omega$  and  $\sim 2.7\Omega$ . As has been realized before [12,14], the threshold of the two-quasiparticle strength is related to the energy of the lowest-lying quasiparticles which are located near the surface of the atomic cloud.

In the case of the monopole mode the good agreement between QRPA and hydrodynamics (Table I) is even more surprising than in the case of the quadrupole mode, since the frequency of the monopole mode is so high that it lies in the two-quasiparticle continuum (see dashed line in Fig. 1) and one would therefore expect a certain amount of Landau damping.

Apart from the study of the frequencies of the collective modes, the comparison between hydrodynamics and QRPA can be extended also to the analysis of the character of such modes. We display in Fig. 3 the transition densities of the two collective modes, which, since the density profile is known, can be related to the velocity field [see Eq. (34)]. The normalization of the QRPA transition density is obtained from the integral of the corresponding peak in the strength function, while that of the semiclassical transition density has been adjusted to the QRPA one. We see that the simple formulas from Sec. II B are in good agreement with the QRPA transition densities. However, the QRPA transition densities exhibit small Friedel-like oscillations, especially near the surface where the gap is small and the local Fermi surface is therefore relatively sharp.

Let us now consider an intermediate temperature between 0 and  $T_c$ . For the present set of parameters the critical temperature is  $T_c \approx 2.8\hbar\Omega/k_B$ ; we therefore choose  $T = 1.4\hbar\Omega/k_B \approx T_c/2$ . As can be seen in the middle of Figs. 1

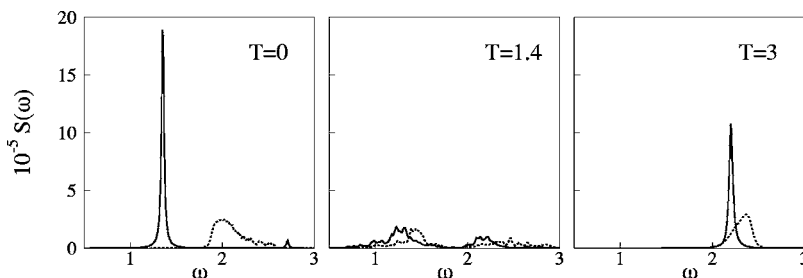


FIG. 2. Free quasiparticle response (dashed line) and QRPA response (solid line) of the quadrupole excitation as a function of the frequency  $\omega$  (in units of the trap frequency  $\Omega$ ) for three different temperatures:  $k_B T=0$ ,  $1.4\hbar\Omega$ , and  $3\hbar\Omega$  (from left to right).

TABLE I. Frequencies (in units of the trap frequency  $\Omega$ ) of monopole ( $L=0$ ) and quadrupole ( $L=2$ ) modes for  $\mu=32\hbar\Omega$  and  $g=-0.965$  (in HO units) at zero temperature and above  $T_c$ . The QRPA results for  $T>T_c$  were obtained with  $T=3\hbar\Omega/k_B$ .

	$T=0$		$T>T_c$	
	QRPA	Hydro.	(Q)RPA	Vlasov
$L=0$	1.9	1.88	1.9	1.88
$L=2$	1.4	$\sqrt{2}$	2.2	2.22

and 2, due to the presence of thermally excited quasiparticles the free quasiparticle response starts now already at  $\omega=0$ . As a consequence, both the collective monopole and quadrupole modes become strongly fragmented and damped. Qualitatively, this strong Landau damping at temperatures between zero and  $T_c$  could be related to the damping mechanism which is responsible for the experimentally observed damping of breathing modes on the BCS side of the BEC-BCS crossover [5,6]. Interesting is also the double-peak structure which can be seen in the quadrupole response, as if there were two damped modes, one corresponding to the hydrodynamic mode and another one corresponding to the quadrupole mode in the collisionless normal phase (see below). This can be interpreted in the sense of the two-fluid model [20], which states that between  $T=0$  and  $T=T_c$  the system effectively behaves as if it consisted of a mixture of normal and superfluid components.

Now we increase the temperature further to  $T=3\hbar\Omega/k_B$ , which lies slightly above  $T_c$ , i.e., the system reaches the normal phase, but still the temperature is very low compared with the Fermi energy. In the normal phase, the BdG equations become identical to the usual Hartree-Fock equations, and the QRPA becomes equal to the usual RPA. In the case of the monopole mode (right panel of Fig. 1), the QRPA response is almost identical to that at zero temperature (left panel of Fig. 1), although the free quasiparticle response is quite different. Again there is one collective mode having the same frequency as at  $T=0$ . This is not very surprising. As mentioned in the preceding section, the Vlasov equation predicts the same frequency as superfluid hydrodynamics, since in the case of the monopole mode there is no deformation of the local Fermi surface. This is different in the case of the quadrupole mode (right panel of Fig. 2). Also here a collective mode reappears, but it is situated at a different frequency

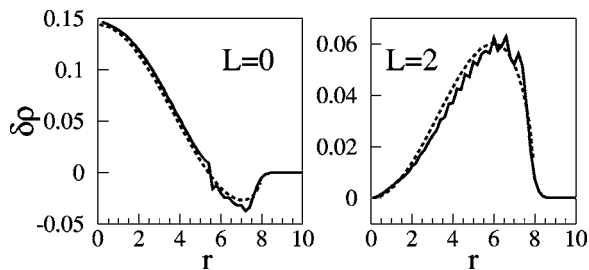


FIG. 3. Transition densities for the collective monopole (left panel) and quadrupole (right panel) modes as a function of  $r$  (in units of the oscillator length  $l_{HO}$ ), at  $T=0$ . Solid and dashed lines represent the QRPA and the semiclassical results, respectively.

TABLE II. Chosen values of the coupling constant  $g$  (first column; in HO units) and corresponding results for the number of particles,  $N$  (second column), and for the gap at the center of the trap,  $\Delta(0)$  (third column; in units of  $\hbar\Omega$ ). The remaining parameters were fixed to  $\mu=32\hbar\Omega$  and  $T=0$ .

$g$	$N$	$\Delta(0)$
-0.965	16500	6.0
-0.8	15000	2.9
-0.7	14300	1.4
-0.636	13900	0.7

than at zero temperature. The higher frequency in the normal phase compared with the superfluid phase is due to the Fermi-surface deformation and is well described by the Vlasov equation (cf. Table I).

### B. Dependence on the size of the system

Let us now investigate the importance of the discrete level spacing at zero temperature. In the case without superfluidity, the semiclassical  $\hbar \rightarrow 0$  limit (TFA in equilibrium and the Vlasov equation in the dynamical case) is known to work very well if the number of particles is sufficiently large. The reason is very simple: The only dimensionless parameter on which corrections can depend is  $\hbar\Omega/\mu$ , which becomes very small for large numbers of particles. In the current experiments involving  $\sim 10^5$ – $10^6$  atoms this type of corrections is completely negligible. For our study we choose, as in the preceding subsection, a chemical potential of  $\mu=32\hbar\Omega$ . This is large enough to make these corrections small, and the numerical calculations are still tractable. The corresponding numbers of atoms lie between  $\sim 14\,000$  and  $\sim 17\,000$  depending on the chosen values of the coupling constant  $g$  due to the Hartree field (see Table II).

In the case of superfluidity, however, another dimensionless parameter becomes important, which is  $\hbar\Omega/\Delta$ . Since in the BCS phase  $\Delta \ll \mu$ , this parameter is not necessarily small even if the number of particles is very large. In order to study the validity of hydrodynamics as a function of  $\hbar\Omega/\Delta$ , we change  $\Delta$  by varying the coupling constant  $g$  between  $-0.636$  and  $-0.965$  (in HO units). As a measure for  $\Delta$  we take its value at the center of the trap,  $\Delta(0)$ . The values of  $\Delta(0)$  corresponding to the different coupling constants are listed in Table II.

We are now going to analyze the finite-size effects on the quadrupole response function by using the different values of the coupling constant listed in Table II. Note that, since we are using HO units, changing the coupling constant  $g \propto a/l_{HO}$  is equivalent to changing the oscillator length  $l_{HO}$  and thus the radius of the cloud  $R = \sqrt{2\mu/\hbar\Omega}l_{HO}$ . Anyway, as argued above, the important parameter for finite-size effects is the ratio  $\hbar\Omega/\Delta(0)$  and not the cloud size itself.

For the strongest coupling,  $g=-0.965$  (in HO units), the central value of the gap,  $\Delta(0)$ , is large compared with  $\hbar\Omega$ , and hydrodynamics works almost perfectly at zero temperature, as we have already seen in the preceding subsection.

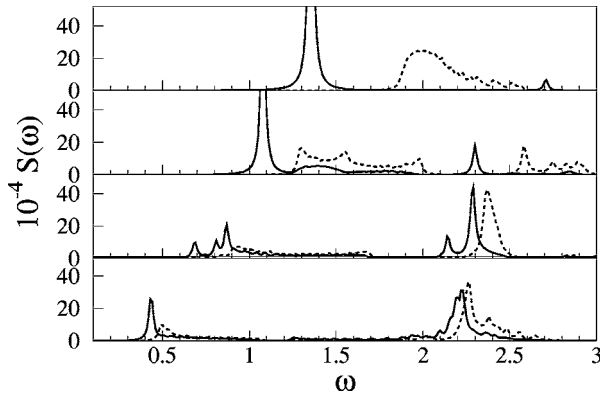


FIG. 4. Unperturbed response (dashed line) and QRPA response (solid line) of the quadrupole excitation as a function of the frequency  $\omega$  (in units of the trap frequency  $\Omega$ ) for  $T=0$  and  $\mu = 32\hbar\Omega$  and four different values of the coupling constant:  $g = -0.965$ ,  $g = -0.8$ ,  $g = -0.7$ , and  $g = -0.636$  (in HO units; from top to bottom).

Figure 4 shows, from top to bottom, the evolution of the quadrupole response at  $T=0$  for decreasing coupling constant  $g$ , i.e., for increasing importance of the discrete level spacing. Besides the QRPA response (solid lines), we also show the free quasiparticle response (dashed lines). For  $g = -0.8$  (in HO units), the gap at the center is still larger than  $\hbar\Omega$  by a factor of 3, but now we find considerable deviations of the QRPA response from the hydrodynamic result. Since the free quasiparticle response is now shifted to lower frequencies, the hydrodynamic mode becomes fragmented, which experimentally would show up as damping effect, and its frequency ( $\omega \approx 1.1\Omega$ ) lies below the hydrodynamic prediction ( $\sqrt{2}\Omega$ ). For  $g = -0.7$  and  $g = -0.636$  (in HO units), the central value of the gap is comparable to  $\hbar\Omega$  and it is clear that hydrodynamics must fail. Indeed, the QRPA response becomes more and more similar to the free quasiparticle response which in the case of weak pairing looks very different from the strong-pairing case. The double-peak structure is a consequence of the two types of transitions which are allowed by the selection rules of the harmonic oscillator, i.e., transitions inside an oscillator shell ( $\delta N=0$ , where  $N$  denotes the number of oscillator quanta) and transitions with  $\delta N=2$ . As the interaction decreases, the strength of the  $\delta N=0$  transitions becomes less important while the  $\delta N=2$  transitions become stronger. This can be understood from the fact that in the limit of a noninteracting harmonic oscillator without pairing ( $g \rightarrow 0$ ) the  $\delta N=0$  transitions are forbidden by Pauli principle and only the  $\delta N=2$  transitions survive. In this limit the response has a single peak at  $\omega=2\Omega$ , in exact agreement with the prediction from the Vlasov equation. In the semiclassical language, one can say that in this case the pairing is too weak to restore the spherical shape of the Fermi sphere during the oscillation, and therefore one finds the normal collisionless frequency instead of the hydrodynamical one.

#### IV. SUMMARY AND CONCLUSIONS

In this paper we have studied the properties of collective monopole and quadrupole modes in superfluid Fermi gases

in the BCS phase ( $k_F|a| \ll 1, a < 0$ ) in a spherical harmonic trap. Having briefly recalled the quantum-mechanical and semiclassical formalisms (QRPA, hydrodynamics, Vlasov equation), we presented numerical results and compared the different formalisms. Our main interest was focused on two types of effects: temperature and finite-size effects. Both cannot be treated within the semiclassical approaches available in the present literature, and they can therefore only be studied in the framework of the fully microscopic QRPA formalism.

In the case of a sufficiently large system (large meaning  $\Delta \gg \hbar\Omega$ ), superfluid hydrodynamics can be used to describe the properties of collective modes at zero temperature. Our results confirm earlier findings [12] which show that already for parameters which lead to  $\Delta(0) = 6\hbar\Omega$  the extremely simple theory of superfluid hydrodynamics is in almost perfect agreement with the numerically heavy QRPA method. This is not only true for the frequencies, but also for the transition densities, i.e., the velocity fields associated with the collective modes. However, experiments can never be done at zero temperature. The critical temperature  $T_c$  being extremely low, it is clear that already at very low temperatures between 0 and  $T_c$  the properties of the collective modes must undergo dramatic changes. This is evident if the hydrodynamic frequency ( $T=0$ ) is different from that in the collisionless normal phase ( $T=T_c$ ), like in the case of the quadrupole mode. In the case of the monopole mode we also find a strong temperature dependence, although its frequency at  $T=0$  is the same as at  $T=T_c$ . In the intermediate temperature range between 0 and  $T_c$  the collective modes exhibit strong Landau damping. When the critical temperature is reached, the damping disappears and the collective modes can be very well described by the semiclassical Vlasov equation within the generalized scaling approximation.

It is interesting to compare these temperature effects with those found previously in the case of the twist mode [21], which is an excitation where the upper hemisphere rotates against the lower one. Near  $T_c$ , the behavior is rather similar: At  $T=T_c$  the twist mode is a collective mode which can be described by the generalized scaling approximation to the Vlasov equation and whose frequency is slightly higher than the trap frequency. If the temperature is lowered, the twist mode becomes strongly damped, like the quadrupole and monopole modes. However, an important qualitative difference appears near zero temperature. Since the velocity field of the twist mode cannot be written as a gradient, the twist mode disappears completely at zero temperature, whereas the quadrupole and monopole modes have an irrotational velocity field and they reappear at zero temperature as hydrodynamic modes. In the case of the twist mode, the disappearance of the  $1/\omega$  weighted integrated strength could be well described within a rather simple two-fluid model [21,22]. It remains to be studied if a generalization of the two-fluid model to the dynamical case can also explain the damping of the quadrupole and monopole modes and the two-peak structure in the quadrupole response function at temperatures between 0 and  $T_c$ .

In addition to temperature effects, we studied how the properties of the quadrupole mode change at zero temperature when the condition for the validity of the hydrodynamic

approach,  $\Delta \gg \hbar\Omega$ , is no longer satisfied. For parameters leading to  $\Delta(0) \approx 3\hbar\Omega$  the QRPA already shows considerable deviations from the hydrodynamic theory. In the case of the quadrupole mode, the frequency for these parameters is found to be lower by 20% than the hydrodynamic prediction, and a certain fragmentation of the excitation spectrum (i.e., damping of the collective mode) can be observed. If  $\Delta(0) \approx \hbar\Omega$ , the hydrodynamic mode has more or less disappeared. At the same time, a fragmented strength appears in the excitation spectrum near the frequency of the collec-

tive quadrupole mode in the normal collisionless phase.

These results should be kept in mind when frequencies of collective modes measured in experiments with strongly deformed traps are compared with the hydrodynamic predictions. Due to the strong deformation, the radial trap frequency  $\Omega_r$  is often much higher than the axial one,  $\Omega_z$ . Even in the case of strong pairing, the gap might be of the order of, say,  $3\hbar\Omega_z$ , and considerable deviations from hydrodynamics are possible.

We thank Nguyen Van Giai for fruitful discussions.

- 
- [1] M. H. Anderson *et al.*, *Science* **269**, 198 (1995); K. B. Davis *et al.*, *Phys. Rev. Lett.* **75**, 3969 (1995); C. C. Bradley, C. A. Sackett, J. J. Tollett, and R. G. Hulet, *ibid.* **75**, 1687 (1995).
- [2] M. W. Zwierlein *et al.*, *Phys. Rev. Lett.* **91**, 250401 (2003)
- [3] K. M. O'Hara *et al.*, *Science* **298**, 2179 (2002).
- [4] C. Chin *et al.*, *Science* **305**, 1128 (2004).
- [5] J. Kinast, S. L. Hemmer, M. E. Gehm, A. Turlapov, and J. E. Thomas, *Phys. Rev. Lett.* **92**, 150402 (2004); J. Kinast, A. Turlapov, and J. E. Thomas, *Phys. Rev. A* **70**, 051401(R) (2004).
- [6] M. Bartenstein *et al.*, *Phys. Rev. Lett.* **92**, 203201 (2004).
- [7] C. Menotti, P. Pedri, and S. Stringari, *Phys. Rev. Lett.* **89**, 250402 (2002).
- [8] S. Stringari, *Europhys. Lett.* **65**, 749 (2004).
- [9] M. A. Baranov and D. S. Petrov, *Phys. Rev. A* **62**, 041601(R) (2000).
- [10] P.-G. de Gennes, *Superconductivity of Metals and Alloys* (Benjamin, New York, 1966).
- [11] P. W. Anderson, *Phys. Rev.* **112**, 1900 (1958).
- [12] G. M. Bruun and B. R. Mottelson, *Phys. Rev. Lett.* **87**, 270403 (2001).
- [13] G. M. Bruun, *Phys. Rev. Lett.* **89**, 263002 (2002).
- [14] Y. Ohashi and A. Griffin, cond-mat/0503641.
- [15] G. Bruun, Y. Castin, R. Dum, and K. Burnett, *Eur. Phys. J. D* **7**, 433 (1999).
- [16] A. Bulgac and Y. Yu, *Phys. Rev. Lett.* **88**, 042504 (2002).
- [17] M. Grasso and M. Urban, *Phys. Rev. A* **68**, 033610 (2003).
- [18] M. Cozzini and S. Stringari, *Phys. Rev. Lett.* **91**, 070401 (2003).
- [19] P. Ring and P. Schuck, *The Nuclear Many-Body Problem* (Springer-Verlag, Berlin, 1980).
- [20] A. J. Leggett, *Phys. Rev.* **140**, A1869 (1965); *Phys. Rev.* **147**, 119 (1966).
- [21] M. Grasso, M. Urban, and X. Viñas, *Phys. Rev. A* **71**, 013603 (2005).
- [22] M. Urban, *Phys. Rev. A* **71**, 033611 (2005).

# **Chapitre 5**

## **Conclusions et perspectives pour les études de physique nucléaire**

## 5.1 Contexte actuel

Depuis une vingtaine d'années, la physique nucléaire renouvelle et restructure ses thématiques autour de la physique des noyaux exotiques, domaine très dynamique et en pleine expansion qui se développe de plus en plus grâce surtout à la construction des nouvelles installations. Avec ces accélérateurs de nouvelle génération qui fonctionneront dans les années à venir, nous pourrons effectuer des études plus systématiques des états fondamentaux et excités des noyaux instables et explorer des régions plus exotiques de la carte nucléaire. Spiral2 dans le contexte national, ainsi que FAIR, RIBF et Eurisol dans le contexte international, permettront d'accroître nos connaissances sur les propriétés des noyaux instables.

Les noyaux exotiques sont des systèmes quantiques de fermions faiblement liés ; un certain nombre de travaux expérimentaux ont mis en évidence l'existence de propriétés particulières qui les caractérisent. Entre autres, des phénomènes nouveaux comme les halos dans certains noyaux légers, les excitations pygmées de basse énergie ou la modification des nombres magiques sont désormais bien établis expérimentalement.

D'un point de vue théorique, beaucoup d'efforts sont consacrés à la description de ces phénomènes, ainsi qu'à la prédiction d'autres propriétés dans les régions encore inexplorées de la carte des noyaux. Au cours des dernières années, l'évidence s'est imposée de la nécessité d'améliorer et d'étendre les outils théoriques actuellement disponibles. Plusieurs directions sont explorées en France et dans la communauté internationale de physique nucléaire dans l'effort commun pour raffiner les approches théoriques existantes et augmenter leur pouvoir de prédiction. Un grand nombre de travaux sont consacrés à l'étude de l'interaction nucléaire, en ce qui concerne à la fois les interactions réalistes (citons par exemple l'introduction de l'interaction de bas moment  $V_{\text{low-k}}$ ) et les interactions effectives. Dans ce cadre, des pistes pour améliorer les paramétrisations et pour introduire de nouveaux termes (par exemple le terme tenseur) dans les interactions effectives standards (comme celle de Skyrme) sont analysées.

Les liens avec la QCD, qui permettent d'analyser l'interaction d'un point de vue plus fondamental, sont aussi étudiés dans le cadre de la formulation des théories de champ effectives et le développement des calculs de QCD sur réseau.

L'interaction d'appariement, qui joue un rôle très important pour décrire les noyaux superfluides, est aussi l'objet de nombreuses études pour mieux comprendre sa nature et ses propriétés. Ses fondements plus microscopiques ainsi que l'amélioration des fonctionnelles empiriques couramment utilisées sont analysés.

Parallèlement à ces travaux sur l'interaction nucléaire, raffinements et extensions des approches traditionnelles sont proposés. Mentionnons les efforts autour des méthodes qui vont au-delà du champ moyen (introduction des mélanges de configurations, couplage particule-vibration,...), les extensions du modèle en couches avec, par

exemple, le modèle en couches avec continuum ou le modèle en couches auto-consistant, les travaux autour des modèles *ab initio* comme le 'Coupled Cluster Method' ou le modèle en couches sans cœur.

La nécessité d'aller au-delà du champ moyen s'impose face à l'existence de différents phénomènes nouveaux qui caractérisent certains noyaux exotiques. Par exemple, les prédictions sur l'évolution de la structure en couches loin de la stabilité nécessitent une évaluation plus sophistiquée des énergies des états individuels (couplage particule-vibration). Par ailleurs, l'existence des modes d'excitation dipolaires pygmées de basse énergie indiquerait que les noyaux exotiques sont des systèmes plus complexes que les noyaux stables où les corrélations jouent un rôle peut-être plus important.

Les propriétés des noyaux instables déjà connus ainsi que les scénarios qui seront prochainement accessibles grâce aux nouvelles installations expérimentales interpellent les théoriciens et nous encourageant à explorer d'autres pistes et démarches par rapport à celles habituelles.

Je me sens fortement impliquée dans ce cadre de travail. En ce qui concerne les études sur l'interaction nucléaire, j'ai récemment exploré deux directions qui ont été discutées dans le Chapitre 2. D'une part, j'ai effectué une étude plus systématique de l'interaction d'appariement avec l'analyse de la réponse associée aux modes de transfert de paires de neutrons. Différentes interactions d'appariement (différents mélanges volume/surface) ont été considérées. Ce travail se poursuit actuellement avec l'objectif d'analyser la sensibilité des sections efficaces associées aux différents modes de transfert par rapport au choix de l'interaction d'appariement. D'autre part, l'enrichissement de la fonctionnelle de Skyrme dans le canal de champ moyen a été exploré suivant deux directions différentes : des estimations de l'effet du terme tenseur (Section 2.4), très important quand l'évolution des spectres à une particule est étudiée le long d'une chaîne isotopique, et des estimations des effets reliés à des termes additionnels dépendant de la densité de spin (Section 2.7).

Avec des projets à plus long terme, je me sens impliquée dans la formulation et la réalisation de méthodes théoriques plus raffinées par rapport au champ moyen standard. Dans ce mémoire, la plupart des résultats que nous avons présentés et discutés (non seulement dans le domaine de la physique nucléaire, mais aussi pour les gaz atomiques) ont été obtenus avec des modèles basés sur le champ moyen. Le Chapitre 3 représente une exception dans ce sens, puisque, dans ce chapitre, des travaux sur des modèles qui vont au-delà du champ moyen ont été décrits.

C'est le moment de faire un bilan qui sera présenté sous forme de quelques perspectives dans la section suivante.

## 5.2 Au-delà du champ moyen. Quelques perspectives

Aller au-delà du champ moyen signifie prendre en compte un certain nombre de corrélations absentes dans une approche basée sur une représentation de particules ou quasiparticules indépendantes. L'introduction des corrélations peut être formalisée de différentes manières.

Un cas où l'introduction des corrélations est importante est l'étude des énergies des états individuels. L'analyse des états individuels est très délicate dans le cadre du champ moyen employant des interactions phénoménologiques. Les paramètres des interactions phénoménologiques sont en effet ajustés pour reproduire des propriétés globales (énergies de liaison et rayons) de certains noyaux et les énergies des états individuels ne rentrent pas dans ces procédures de fit (sauf dans l'ajustage des paramètres pour le terme de spin-orbite).

Cette manière de procéder est raisonnable puisque le champ moyen est une approche insuffisante pour fournir des prédictions quantitatives précises des énergies des états individuels. Cela pour deux raisons. La première est que, dans le modèle HF, les facteurs spectroscopiques ne peuvent pas être prédits puisqu'ils sont tous égaux à 1 ou 0 par construction. En ajoutant les corrélations d'appariement avec HFB, les occupations autour de l'énergie de Fermi sont éventuellement modifiées mais seulement à cause de l'appariement (les autres corrélations sont exclues). De plus, une correction non négligeable aux énergies individuelles de champ moyen vient du couplage entre les degrés de liberté individuels et les degrés de liberté collectifs. Ce couplage particule-vibration [Be80, Co01, Br05, Li07], décrit dans le cadre de la RPA en tenant compte seulement des excitations  $ph^1$ , modifie l'opérateur de masse HF :

$$M(E) = M^{HF} + \Sigma(E) , \quad (5.1)$$

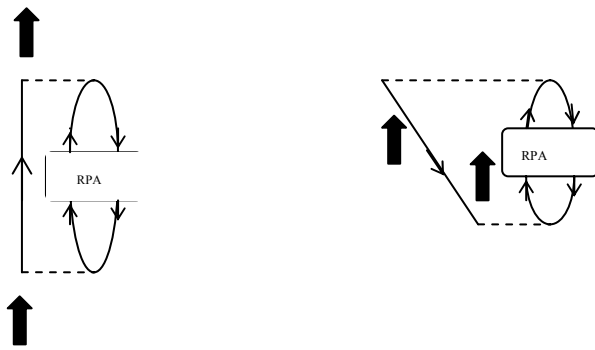
où :

$$\Sigma(E) = \Sigma^{RPA}(E) - \Sigma^{(2)}(E) . \quad (5.2)$$

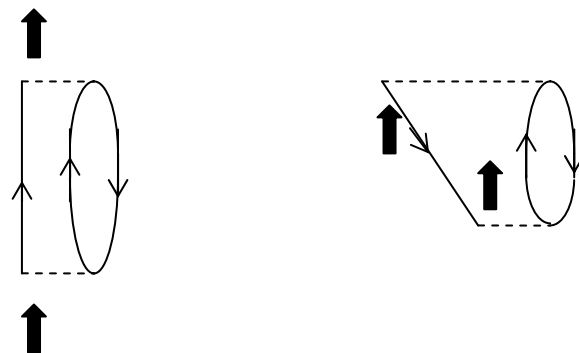
La correction due au premier terme à droite de l'éq. (5.2) est décrite par les deux diagrammes suivants :

---

<sup>1</sup> Il a été montré par Berstch et collaborateurs [Be79] que les vibrations  $pp$  contribuent moins que les excitations  $ph$  à la modification des états individuels



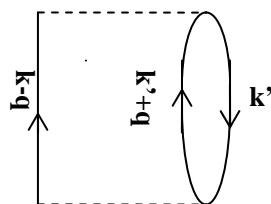
Le diagramme de gauche est dit de polarisation et celui de droite de corrélation. Les diagrammes du second ordre,



doivent être soustraits pour corriger le double comptage dû à l'utilisation de la RPA dans la description du couplage particule-phonon.

Ce couplage provoque un décalage des énergies individuelles (et aussi de celles des modes d'excitation de basse énergie) et une fragmentation des états individuels (ainsi que des modes collectifs) qui permet de décrire de manière pertinente les facteurs spectroscopiques.

Nous sommes en train d'analyser de manière plus détaillée et systématique cette problématique du couplage particule-vibration dans le cadre des modèles employant l'interaction de Skyrme. Dans ce cas, une divergence ultraviolette (qui est visible quand le cutoff numérique introduit dans les calculs est modifié) se manifeste à cause de la portée nulle de l'interaction. Considérons par exemple le digramme de polarisation du second ordre :



écrit comme :

$$\Sigma = \frac{2}{\hbar^2} \frac{1}{(2\pi)^8} \int d^3k' \int d^3q d\omega' d\omega_q v^2(q) G_p(k - q, \omega - \omega_q) G_p(k' + q, \omega' + \omega_q) G_h(k', \omega'). \quad (5.3)$$

Une manière de montrer la divergence est de choisir pour l'interaction  $v$  une forme gaussienne :

$$v(q) = g e^{-\frac{1}{4}\mu^2 q^2}, \quad (5.4)$$

où  $g$  est une constante de couplage. Après un certain nombre de manipulations, il est possible de montrer que  $\Sigma$  est la somme de deux termes dont le premier est proportionnel à :

$$\frac{1}{\mu^2} \left( \frac{2m}{k_F} - \frac{\sqrt{2\pi}}{\mu} - \frac{2}{\mu^2 k_F} \right). \quad (5.5)$$

Dans la limite où la portée de la gaussienne tend vers zéro, ce terme est fortement divergent et cette divergence n'est pas atténuée par le deuxième terme.

À cause de cette divergence, seulement une renormalisation pourrait éliminer la forte dépendance du cutoff numérique choisi. Sans renormalisation, le cutoff devient donc un paramètre très important dans ce type de calculs.

L'idée vers laquelle nos travaux sont orientés est d'ajuster une interaction de Skyrme à utiliser pour des calculs qui vont au-delà d'HF et qui prennent en compte le couplage particule-phonon (avec éventuellement un paramètre supplémentaire donné par le cutoff si aucune renormalisation n'est effectuée).

Dans le même sens, mon activité s'oriente aussi vers la réalisation d'extensions de la RPA de type seconde RPA (SRPA). En effet, une façon d'inclure le couplage particule-vibration de manière pour ainsi dire plus globale est de réaliser des calculs de seconde RPA (SRPA). Les configuration 2p-2h sont incluses dans le formalisme de SRPA et, donc, le couplage entre 1p-1h et 2p-2h est pris en compte. Dans une forme compacte, les équations SRPA s'écrivent comme [Ya86] :

$$\begin{pmatrix} \Phi & \Gamma \\ -\Gamma^* & -\Phi^* \end{pmatrix} \begin{pmatrix} \theta(\omega_v) \\ \tau(\omega_v) \end{pmatrix} = \hbar \omega_v \begin{pmatrix} \theta(\omega_v) \\ \tau(\omega_v) \end{pmatrix}, \quad (5.6)$$

avec :

$$\Phi = \begin{pmatrix} A_{ph,p'h'} & A_{ph,p'p''h'h''} \\ A_{p\bar{p}h\bar{h},p'h'} & A_{p\bar{p}h\bar{h},p'p''h'h''} \end{pmatrix}, \quad (5.7)$$

$$\Gamma = \begin{pmatrix} B_{ph,p'h'} & B_{ph,p'p''h'h''} \\ B_{p\bar{p}h\bar{h},p'h'} & B_{p\bar{p}h\bar{h},p'p''h'h''} \end{pmatrix}, \quad (5.8)$$

et :

$$\theta(\omega_v) = \begin{pmatrix} Y_{ph}(\omega_v) \\ Y_{p\bar{p}h\bar{h}}(\omega_v) \end{pmatrix} \quad \tau(\omega_v) = \begin{pmatrix} Z_{ph}(\omega_v) \\ Z_{p\bar{p}h\bar{h}}(\omega_v) \end{pmatrix}. \quad (5.9)$$

L'opérateur d'excitation de la SRPA est défini comme :

$$Q_v^+ \equiv \sum_{ph} \left[ Y_{ph}(\omega_v) a_p^+ a_h - Z_{ph}(\omega_v) a_h^+ a_p \right] + \sum_{p < p', h < h'} \left[ Y_{pp'hh'}(\omega_v) a_p^+ a_{p'}^+ a_h a_{h'} - Z_{pp'hh'}(\omega_v) a_h^+ a_{h'}^+ a_p a_{p'} \right] \quad (5.10)$$

et les équations pour les matrices A et B sont données dans la référence [Ya86] (eqs. (6a) – (7)).

Comme déjà mentionné dans ce mémoire, pour l'étude des états excités dans le cadre des méthodes de type RPA, une manière possible d'aller au-delà du champ moyen est de ne pas utiliser l'approximation de quasibosons et de respecter donc le Principe de Pauli qui est violé avec la QBA (Chapitre 3). Cet aspect s'applique aussi à la SRPA.

L'introduction de corrélations dans un modèle rigoureux peut d'ailleurs se révéler cruciale dans le développement de la nouvelle physique des noyaux exotiques. Par exemple, pour les prédictions théoriques des résonances dipolaire pygmées, le fait de satisfaire le Principe de Pauli peut apporter des avantages considérables si l'on considère que ces modes de basse énergie sont typiquement moins collectifs (moins de configurations y participent) que, par exemple, les résonances géantes.

Une manière d'inclure de manière globale et cohérente le couplage particule-vibration et les extensions de la RPA qui satisfont le Principe de Pauli, pourrait se réaliser avec la formalisation et la mise au point d'une seconde RPA pour les noyaux avec des corrélations explicitement introduites dans l'état fondamental.

Ce programme de recherche envisagé pour les années à venir est assez vaste et complexe et prévoit un certain nombre d'étapes qui demandent différents niveaux de compétences et d'expertise. Une partie de ce travail se prête donc de manière naturelle à

constituer de possibles sujets de stages et de thèses qui pourraient être développés prochainement dans notre groupe de physique théorique de l'IPN-Orsay.

## Références

- [Ad05] P. Adrich, et al., Phys. Rev. Lett. 95 (2005), 132501
- [AM76] N.W. Ashcroft and N.D. Mermin, *Solid State Physics*, Harcourt, Orlando, 1976
- [An95] M. H. Anderson, et al., Science, 269 (1995), 198
- [An02] M.V. Andres, F. Catara, E.G. Lanza, Ph. Chomaz, M. Fallot, and J.-A. Scarpaci, Phys. Rev. C 65 (2002), 014608
- [Av08] B. Avez, C. Simenel, and Ph. Chomaz, Phys. Rev. C 78 (2008), 044318
- [Ba99] M. Baldo, in *Nuclear Methods and the Nuclear Equation of State*, ed. M. Baldo Singapore, World Scientific, 1999
- [Ba04] M. Bartenstein, et al., Phys. Rev. Lett. 92 (2004), 120401
- [BCS57] J. Bardeen, L.N. Cooper, and J.R. Schrieffer, Phys. Rev. 108 (1957), 1175
- [Be79] G.F. Bertsch, P.F. Bortignon, R.A. Broglia, and C.H. Dasso, Phys. Lett. B 80 (1979), 161
- [Be80] V. Bernard and N. Van Giai, Nucl. Phys. A 348 (1980), 75
- [Be92] D. Beaumel and Ph. Chomaz, Ann. Phys. (N.Y) 213 (1992), 405
- [Be06] E. Becheva, et al., Phys. Rev. Lett. 96 (2006), 012501
- [Be08] M. Bender, Th. Duguet, and D. Lacroix, arXiv:0809.2045
- [Be09] G.F. Bertsch, C.A. Bertulani, W. Nazarewicz, N. Schunck, and M.V. Stoitsov, Phys. Rev. C 79 (2009), 034306
- [BM01] G.M. Bruun and B.R. Mottelson, Phys. Rev. Lett. 87 (2001), 270403
- [Bo84] I.N. Borzov, S.V. Tolokonnikov, and S.A. Fayans, Sov. J. Nucl. Phys. 40 (1984), 732
- [Bo01] S.K. Bogner, A. Schwenk, T.T.S. Kuo, G.E. Brown, nucl-th/0111042
- [Bo03] K. Boretzsky, et al., Phys. Rev. C 68 (2003) 024317
- [Bo03a] S.K. Bogner, T.T.S. Kuo, A. Schwenk, D.R. Entem, and R. Machleidt, Phys. Lett. B 576 (2003), 265
- [Bo03b] S.K. Bogner, T.T.S. Kuo, and A. Schwenk, Phys. Rep. 386 (2003), 1
- [Bo06] I.N. Borzov, Nucl. Phys. A 777 (2006), 645
- [BP52] D. Pines and D. Bohm, Phys. Rev. 85 (1952), 338

- [Br73] R.A. Broglia, O. Hansen, and C. Riedel, *Advances in Nuclear Physics*, NY Plenum 6 (1973), 287
- [Br95] C.C. Bradley, et al., *Phys. Rev. Lett.* 75 (1995), 1687
- [Br99] G. Bruun, Y. Castin, R. Dum, and K. Burnett, *Eur. Phys. J. D* 7 (1999), 433
- [Br05] R.A. Broglia, F. Barranco, P.F. Bortignon, G. Colò, and E. Vigezzi, *Nucl. Phys. A* 752 (2005), 345
- [Br07] D.M. Brink, and Fl. Stancu, *Phys. Rev. C* 75 (2007), 064311
- [Bu02] A. Bulgac and Y. Yu, *Phys. Rev. Lett.* 88 (2002), 042504
- [Ca89] F. Catara, Ph. Chomaz, and N. Van Giai, *Phys. Lett. B* 233 (1989), 6
- [Ca93] F. Catara, Ph. Chomaz, and N. Van Giai, *Phys. Rev. B* 48 (1993), 18207
- [Ca98] F. Catara, M. Grasso, G. Piccitto, and M. Sambaturo, *Phys. Rev. B* 58 (1998), 16070
- [Ca05] Paolo Castorina, Marcella Grasso, Micaela Oertel, Michael Urban, and Dario Zappalà, *Phys. Rev. A* 72 (2005), 025601
- [Ca06] F. Catara, D. Gambacurta, M. Grasso, and M. Sambaturo, *Phys. Lett. A* 349 (2006), 345
- [Ca08] B.G. Carlsson, J. Dobaczewski, and M. Korteleinen, *Phys. Rev. C* 78 (2008), 044326
- [Ch95] Ph. Chomaz and N. Frascaria, *Phys. Rep.* 252 (1995), 275
- [Ch98] E. Chabanat, P. Bonche, P. Haensel, J. Meyer, and R. Schaeffer, *Nucl. Phys. A* 635 (1998), 231
- [Co01] G. Colò and P.F. Bortignon, *Nucl. Phys. A* 696 (2001), 427
- [Co04] R. Combescot and C. Mora, *Europhys. Lett.* 68 (2004), 79
- [Co07] G. Colò, H. Sagawa, S. Fracasso, and P.F. Bortignon, *Phys. Lett B* 646 (2007), 227
- [Da95] K.B. Davis, et al., *Phys. Rev. Lett.*, 75 (1995), 3969
- [dG66] P.G. de Gennes, *Superconductivity of Metals and Alloys*, Perseus Books Publishing, L.L.C. 1966
- [DM99] B. DeMarco and D.S. Jin, *Science* 285 (1999), 1703
- [Do84] J. Dobaczewski, H. Flocard, and J. Treiner, *Nucl. Phys. A* 422 (1984), 103

- [Do94] J. Dobaczewski, I. Hamamoto, W. Nazarewicz, and J. A. Sheikh, Phys. Rev. Lett. 72, 981 (1994)
- [Do95] J. Dobaczewski and J. Dudek, Phys. Rev. C 52 (1995), 1827
- [Do97] J. Dobaczewski and J. Dudek, Phys. Rev. C 55 (1997), 3177(E)
- [Do07] J. Dobaczewski, M.V. Stoitsov, W. Nazarewicz, and P.-G. Reinhard, Phys. Rev. C 76 (2007), 054315
- [Dr90] R.M. Dreizler and E.K.U Gross, *Density Functional Theory*, Springer, Berlin (1990)
- [Du90] J. Dukelsky and P. Schuck, Nucl. Phys. A 512 (1990), 466
- [Du96] J. Dukelsky and P. Schuck, Phys. Lett. B 387 (1996), 233
- [Du08] Th. Duguet, M. Bender, K. Bennaceur, D. Lacroix, and Th. Lesinski, arXiv:0809.2049
- [DV87] Società Italiana di Fisica, Conference Proceedings, *Collective aspects in Pair-Transfer Phenomena*, Varenna 1987, edited by C.H. Dasso and A. Vitturi
- [Ep08] E. Epelbaum, H.-W. Hammer, and Ulf.G. Meissner, arXiv:0811.1338 [nucl-th]
- [Fa03] M. Fallot, et al., Nucl. Phys. A 729 (2003), 699
- [Fa06] M. Fallot, et al., Phys. Rev. Lett. 97 (2006), 242502
- [Fa07] M. Fallot, M. Grasso, E. Khan, and J. Margueron, Nucl. Phys. News 17, n. 4 (2007), 31
- [Fi03] P. Finelli, N. Kaiser, D. Vretenar, and W. Weise, Eur. Phys. J. A 17 (2003), 573
- [Fi04] P. Finelli, N. Kaiser, D. Vretenar, and W. Weise, Nucl. Phys. A 735 (2004), 449
- [Fi06] P. Finelli, N. Kaiser, D. Vretenar, and W. Weise, Nucl. Phys. A 770 (2006), 1
- [Fi07] P. Finelli, N. Kaiser, D. Vretenar, and W. Weise, Nucl. Phys. A 791 (2007), 57
- [Fo05] C. Forssén, P. Navrátil, W.E. Ormand, and E. Caurier, Phys. Rev. C 71 (2005), 044312
- [Fr85] M.A. Franey and W.G. Love, Phys. Rev. C 31 (1985), 488; W.G. Love and M.A. Franey, Phys. Rev. C 24 (1981), 1073
- [Fr07] S. Fracasso and G. Colò, Phys. Rev. C 76 (2007), 044307
- [FW71] A.L. Fetter and J.D. Walecka, *Quantum Theory of Many-Particle Systems*, San Francisco, Mc Graw-Hill, 1971

- [Ga00] J.E. Garcia Ramos, J.M. Arias, and P. van Isacker, Phys. Rev. C 62 (2000), 064309
- [Ga06a] D. Gambacurta, M. Sambataro, and F. Catara, Phys. Rev. C 66 (2006), 014310
- [Ga06b] D. Gambacurta, M. Grasso, F. Catara, and M. Sambataro, Phys. Rev. C 73 (2006), 024319
- [Ga06c] L. Gaudefroy, et al., Phys. Rev. Lett. 97 (2006), 092501
- [Ga09] D. Gambacurta, F. Catara, and M. Grasso, Phys. Rev. C 80 (2009), 014303
- [Ge02] L.G. Gerchikov, C. Guet, and A.N. Ipatov, Phys. Rev. A 66 (2002), 053202
- [Gi08] S. Giorgini, L.P. Pitaevskii, and S. Stringari, Rev. Mod. Phys. 80 (2008), 1215
- [Go75] D.Gogny, Proceedings of the International Conference on Nuclear Selfconsistent Fields, Trieste, 1975. G. Ripka and M. Porneuf, Eds. North Holland, Amsterdam, 1975
- [Go09] S. Goriely, N. Chamel, and J.M. Pearson, in press Phys. Rev. Lett. (2009)
- [Gra02] S.R. Granade, M.E. Gehm, K.M. O'Hara, and J.E. Thomas, Phys. Rev. Lett. 88 (2002), 120405
- [Gr00] M. Grasso and F. Catara, Phys. Rev. C 63 (2000), 014317
- [Gr01] M. Grasso, N. Sandulescu, N. Van Giai, and R.J. Liotta, Phys. Rev. C 64 (2001), 064321
- [Gr02] M. Grasso, F. Catara, and M. Sambataro, Phys. Rev. C 66 (2002), 064303
- [Gr03] Marcella Grasso and Michael Urban, Phys. Rev. A 68 (2003), 033610
- [Gr05a] Marcella Grasso, Michael Urban, and Xavier Viñas, Phys. Rev. A 71 (2005), 013603
- [Gr05b] Marcella Grasso, Elias Khan, and Michael Urban, Phys. Rev. A 72 (2005), 043617
- [Gr06] M. Grasso, S. Yoshida, N. Sandulescu, and N. Van Giai, Phys. Rev. C 74 (2006), 064317
- [Gr07a] M. Grasso, Z.Y. Ma, E. Khan, J. Margueron, and N. Van Giai, Phys. Rev. C 76 (2007), 044319
- [Gr07b] M. Grasso, S. Yoshida, N. Sandulescu, and N. Van Giai, Nucl. Phys. A 788 (2007), 337c

- [Gr08] M. Grasso, E. Khan, J. Margueron, and N. Van Giai, Nucl. Phys. A 807 (2008), 1
- [Gr09] M. Grasso, L. Gaudefroy, E. Khan, T. Nikšić, J. Piekarewicz, O. Sorlin, N. Van Giai, and D. Vretenar, Phys. Rev. C 79 (2009), 034318
- [Gr09a] M. Grasso, E. Khan, and J. Margueron, Proceedings of the Conference NSD09, Dubrovnik, Croatia, May 2009
- [Ha64] K. Hara, Prog. Theor. Phys. 32 (1964), 88
- [Ha97] K. Hagino, N. Takigawa, and S. Kuyucak, Phys. Rev. Lett. 79 (1997), 2943
- [Ha99] K. Hagino, Phys. Rev. B 60 (1999), R2197
- [Ha01] M.N. Harakeh and A. van der Woude, *Giant Resonances*, Clarendon, Oxford, 2001
- [Ha02] Z. Hadzibabic, et al., Phys. Rev. Lett. 88 (2002), 160401
- [Ha03] Z. Hadzibabic, et al., Phys. Rev. Lett. 91 (2003), 160401
- [Ha08] G. Hagen, T. Papenbrock, D.J. Dean, and M. Hjorth-Jensen, Phys. Rev. Lett. 101 (2008), 092502
- [He09] K. Hebeler, T. Duguet, T. Lesinski, and A. Schwenk, arXiv:0904.3152
- [HK64] P. Hohenberg and W. Kohn, Phys. Rev. 136 (1964), B864
- [Hu87] K. Huang, *Statistical Mechanics*, Wiley, New York, 1987
- [Ic06] M. Ichimura, H. Sakai, and T. Wakasa, Prog. Part. Nucl. Phys. 56 (2006), 446
- [Ka93] D. Karadjov, V.V. Voronov, and F. Catara, Phys. Lett. B 306 (1993), 166
- [Kh02] E. Khan, N. Sandulescu, M. Grasso, and N. V. Giai, Phys. Rev. C 66 (2002), 024309
- [Kh04] E. Khan, N. Sandulescu, N. V. Giai, and M Grasso, Phys. Rev. C 69 (2004), 014314
- [Kh07] E. Khan, M. Grasso, and J. Margueron, Proceedings of the international Symposium EXOCT07, Catania, Italy, June 2007
- [Kh08] E. Khan, M. Grasso, J. Margueron, and N. Van Giai, Nucl. Phys. A 800 (2008), 37
- [Kh09] E. Khan, M. Grasso, and J. Margueron, arXiv:0905.4108, soumis Phys. Rev. C, rapport reçu, quelques modifications apportées, version resoumise

- [Kho03] Dao T. Khoa, Hoang Sy Than, and Marcella Grasso, Nucl. Phys. A 722 (2003), 92c
- [Kho04] Dao T. Khoa, Hoang Sy Than, Tran Hoai Nam, M. Grasso, and N. Van Giai, Phys. Rev. C 69 (2004), 044605
- [Ki04a] J. Kinast, et al., Phys. Rev. Lett. 92 (2004), 150402
- [Ki04b] J. Kinast, A. Turlapov, and J.E. Thomas, Phys. Rev. A 70 (2004), 051401(R)
- [Kl91] A. Klein, N.R. Walet, and G. Do Dang, Nucl. Phys. A 535 (1991), 1
- [Kn84] W.D. Knight, et al., Phys. Rev. Lett. 52 (1984), 2141
- [Ko06] G. Kotliar, S.Y. Savrasov, K. Haule, V.S. Oudovenko, O. Parcollet, and C.A. Marianetti, Rev. Mod. Phys. 78 (2006), 865
- [Ko08] M. Korteleinen, J. Dobaczewski, K. Mizuyama, and J. Toivanen, Phys. Rev. C 77 (2008), 064307
- [Kr98] F. Krmpotić, E.J.V. De Passos, D.S. Delion, J. Dukelsky, and P. Schuck, Nucl. Phys. A 637 (1998), 295
- [KS65] W. Kohn and L.J. Sham, Phys. Rev. 140 (1965), A1133
- [La90] G. Lauritsch and P.G. Reinhard, Nucl. Phys. A 509 (1990), 287
- [La97] E.G. Lanza, M.V. Andres, F. Catara, Ph. Chomaz, and C. Volpe, Nucl. Phys. A 613 (1997), 445
- [La06] E.G. Lanza, F. Catara, M.V. Andres, Ph. Chomaz, M. Fallot, and J.-A. Scarpaci, Phys. Rev. C 74 (2006), 064614
- [La08] Lattice 2008, Conference Website: <http://conferences.jlab.org/lattice2008/>
- [La08] D. Lacroix, Th. Duguet, and M. Bender, Phys. Rev. C 79 (2009), 044318
- [Le80] A.G. Leggett, J. Phys. (Paris) C7 (1980), 19
- [Le07] T. Lesinski, M. Bender, K. Bennaceur, T. Duguet, and J. Meyer, Phys. Rev. C 76 (2007), 014312
- [Le09] T. Lesinski, T. Duguet, K. Bennaceur, and J. Meyer, arXiv:0809.2895
- [Li03] W.V. Liu and F. Wilczek, Phys. Rev. Lett. 90 (2003), 047002
- [Li07] E. Litvinova, P. Ring, and V. Tselyaev, Phys. Rev. C 75 (2007), 064308
- [Lo06] W.H. Long, N. Van Giai, and J. Meng, Phys. Lett. B 640 (2006), 150
- [Ma67] N.H. March, W.H. Young, and S. Sapanthar, *The Many-Body Problem in Quantum Mechanics*, Cambridge University Press, 1967

- [Ma94] A. Mariano, F. Krmpotic, and A.F.R. de Toledo Piza, Phys. Rev. C 49 (1994), 2824
- [Ma02] J. Margueron, J. Navarro, and N.V. Giai, Phys. Rev. C 66 (2002), 014303
- [Ma05] M. Matsuo, K. Mizuyama, and Y. Serizawa, Phys. Rev. C 71 (2005), 047302
- [Ma06] M. Matsuo, Phys. Rev. C 71 (2006), 044309
- [Ma08] J. Margueron, H. Sagawa, and K. Hagino, Phys. Rev. C 77 (2008), 054309
- [Ma09] M. Matsuo, Private Communication and COMEX3 Proceedings
- [Ma09a] J. Margueron and H. Sagawa, soumis J. Phys. G
- [Ma09b] J. Margueron, S. Goriely, M. Grasso, G. Colò, and H. Sagawa, arXiv:0906.3508, soumis J. Phys. G, rapport reçu, quelques modifications apportées, version resoumise
- [Me02] J. Meng, H. Toki, J.Y. Zeng, S.Q. Zhang, and S.-G. Zhou, Phys. Rev. C 65 (2002), 041302
- [Me03] J. Meyer, Ann. Phys. Fr. 28, n. 3, 2003
- [MR98] J. Meng and P. Ring, Phys. Rev. Lett. 80 (1998), 460
- [Ne82] J.W. Negele, Rev. Mod. Phys. 54 (1982), 913
- [Ni08] T. Nikšić, D. Vretenar, and P. Ring, Phys. Rev. C 78 (2008), 034318
- [NV72] J.W. Negele and D. Vautherin, Phys. Rev. C 5 (1972), 1472
- [Os92] F. Osterfeld, Rev. Mod. Phys. 64 (1992), 491
- [Ot05] T. Otsuka, T. Suzuki, R. Fujimoto, H. Grawe, and Y. Akaishi, Phys. Rev. Lett. 95, 232502 (2005)
- [OV01] W. von Oertzen and A. Vitturi, Rep. Prog. Phys. 64 (2001), 1247
- [Pa01] D.T. de Paula, T. Aumann, L.F. Canto, B.V. Carlson, H. Hemling, and M.S. Hussein, Phys. Rev. C 64 (2001), 064605
- [Pe06] D.S. Petrov, D.M. Gangardt, and G.V. Shlyapnikov, J. Phys. IV 116 (2006), 3
- [Pi03] L. Pitaevskii and S. Stringari, *Bose-Einstein Condensation*, Clarendon Press, Oxford, 2003
- [Pi07] N. Pillet, N. Sandulescu, and P. Schuck, Phys. Rev. C 76 (2007), 024310
- [Po97] V. Yu Ponomarev, and C.A. Bertulani, Phys. Rev. Lett. 79 (1997), 3853
- [Ra98] A.A. Raduta, C. M. Raduta, A. Faessler, and W. A. Kaminski, Nucl. Phys. A 634 (1998), 497

- [Re04] C.A. Regal, M. Greiner, and D.S. Jin, Phys. Rev. Lett. 92 (2004), 040403
- [Ro68] D.J. Rowe, Rev. Mod. Phys. 40 (1968), 153
- [Ro09] R. Roth and P. Navratil, Phys. Rev. Lett. 99 (2007), 092501
- [RS80] P. Ring and P. Schuck, *The Nuclear Many-Body Problem*, Springer-Verlag Berlin Heidelberg New York, 1980
- [Sa95] M. Sambataro and F. Catara, Phys. Rev. C 51 (1995), 3066
- [Sa97] M. Sambataro and J. Suhonen, Phys. Rev. C 56 (1997), 782
- [Sa99] M. Sambataro and N. Dinh Dang, Phys. Rev. C 59 (1999), 1422
- [Sc98] R. Schlipper, R. Kutsche, B. von Issendorf, and H. Haberland, Phys. Rev. Lett. 80 (1998), 1194
- [Sc01] F. Schreck, et al., Phys. Rev. Lett. 87 (2001), 080403
- [Sk56] T.H.R. Skyrme, Phil. Mag. 1 (1956), 1043
- [Sk59] T.H.R. Skyrme, Nucl. Phys. 9 (1959), 615
- [So08] O. Sorlin and M.G. Porquet, Prog. Part. Nucl. Phys. 61 (2008), 602
- [St77] Fl. Stancu, D.M. Brink, and H. Flocard, Phys. Lett. B 68 (1977), 108
- [Su99] E.T. Suzuki and H. Sakai, Phys. Lett. B 455 (1999), 25
- [Ta85] I. Tanihata, et al., Phys. Rev. Lett. 55 (1985), 2675
- [Ta88] K. Takayanagi, et al., Nucl. Phys. A 477 (1988), 205
- [Ta04] S. Takahara, M. Tohyama, and P. Schuck, Phys. Rev. C 70 (2004), 057307
- [To04] B.G. Todd-Rudel, J. Piekarewicz, and P.D Cottle, Phys. Rev. C 69 (2004), 021301 (R)
- [To07] M. Tohyama, Phys. Rev. C 75 (2007), 044310
- [Tu01] A.G. Tuscott, et al., Science 291 (2001), 2570
- [VB72] D. Vautherin and D.M. Brink, Phys. Rev. C 5 (1972), 626
- [Vo99] C. Volpe, Ph. Chomaz, M.V. Andres, F. Catara, and E. Lanza, Nucl. Phys. A 647 (1999), 246
- [Wa74] J.D. Walecka, Ann. Phys. 83 (1974), 491
- [Wa05] T. Wakasa, M. Ichimura, and H. Sakai, Phys. Rev. C 72 (2005), 067303
- [Wi02] R.B. Wiringa and Steven C. Pieper, Phys. Rev. Lett. 89 (2002), 182501
- [Ya86] C. Yannouleas, Phys. Rev. C 35 (1986), 1159
- [Ya08] M. Yamagami, Y.R. Shimizu, T. Nakatsukasa, arXiv:0812.3197

[Zw03] M.W. Zwiernin, et al., Phys. Rev. Lett. 91 (2003), 250404

[Zw04] M.W. Zwiernin, et al., Phys. Rev. Lett. 92 (2004), 120403